

A minimal system to establish microtubule-based cell polarity in vitro

Taberner Carretero, Nuria

DOI

[10.4233/uuid:c87db99c-45f8-4ee9-bcf6-c0667c2be618](https://doi.org/10.4233/uuid:c87db99c-45f8-4ee9-bcf6-c0667c2be618)

Publication date

2016

Document Version

Final published version

Citation (APA)

Taberner Carretero, N. (2016). *A minimal system to establish microtubule-based cell polarity in vitro*. [Dissertation (TU Delft), Delft University of Technology]. <https://doi.org/10.4233/uuid:c87db99c-45f8-4ee9-bcf6-c0667c2be618>

Important note

To cite this publication, please use the final published version (if applicable). Please check the document version above.

Copyright

Other than for strictly personal use, it is not permitted to download, forward or distribute the text or part of it, without the consent of the author(s) and/or copyright holder(s), unless the work is under an open content license such as Creative Commons.

Takedown policy

Please contact us and provide details if you believe this document breaches copyrights. We will remove access to the work immediately and investigate your claim.

**A MINIMAL SYSTEM TO ESTABLISH
MICROTUBULE-BASED CELL POLARITY IN VITRO**



A MINIMAL SYSTEM TO ESTABLISH MICROTUBULE-BASED CELL POLARITY IN VITRO

Proefschrift

ter verkrijging van de graad van doctor
aan de Technische Universiteit Delft,
op gezag van de Rector Magnificus prof. ir. K. C. A. M. Luyben,
voorzitter van het College voor Promoties,
in het openbaar te verdedigen op dinsdag 11 oktober 2016 om 10:00 uur

door

Núria TABERNER CARRETERO

Master in Biophysics,
Universitat de Barcelona, Spain
geboren te Mataró, Catalonië.

Dit proefschrift is goedgekeurd door de promotor:

Prof. dr. M. Dogterom

Samenstelling promotiecommissie:

Rector Magnificus, voorzitter
Prof. dr. M. Dogterom, Technische Universiteit Delft, promotor

Onafhankelijke leden:

Prof. dr. C. Dekker, Technische Universiteit Delft
Dr. ir. L. Laan, Technische Universiteit Delft
Dr. P. Tran, University of Pennsylvania
Prof. dr. R. Carazo-Salas, University of Bristol
Prof. dr. A. Akhmanova, Utrecht University
Prof. dr. P. R. ten Wolde, Vrije Universiteit Amsterdam
Prof. dr. ir. S. Tans, Technische Universiteit Delft, reservelid



Keywords: Microtubules, +TIPs, polarity, reconstitution

Printed by: Ridderprint

Front & Back: Cover image made by Andreu Taberner displaying an artist impression of a microtubule depositing his-tagged Tip1 to a Tris-Ni(II)-NTA coated wall aided by Mal3 and Tea2.

Copyright © 2016 by N. Taberner

ISBN 978-94-6299-446-1

An electronic version of this dissertation is available at
<http://repository.tudelft.nl/>.

*To my parents:
Maria Carme Carretero Serra, Francesc Taberner Duràn.*

Núria Taberner Carretero



CONTENTS

1	Microtubule-based cell polarity	1
1.1	Cell polarity: How cells define directions	2
1.2	Motivation and thesis outline	14
2	Localization of polarity factors to microtubule plus ends	19
2.1	Introduction	20
2.2	Mal3, Tea2 and Tip1	21
2.3	Tea2 produces gliding of microtubules in the absence of Mal3 and Tip1	23
2.4	Mal3-dependent recruitment of Tea2-Tip1 to the microtubule and possible cluster formation	25
2.5	Tea2-Tip1 transfer between microtubules.	28
2.6	Motor distributions on microtubules	33
2.7	Discussion	38
2.8	Methods	40
2.9	Data analysis	42
3	Designing and building a minimal polarized cell	49
3.1	Introduction and Rationale	50
3.2	Materials	54
3.3	Micro-fabrication of glass micro-wells with chromium overhang	55
3.4	Selective surface functionalization	57
3.5	Microtubule assays	58
3.6	Discussion	60
4	Microtubule-based deposition of +TIPs to a bio-mimetic cortex	63
4.1	Introduction	64
4.2	Design and optimization of the bio-mimetic cortex.	64
4.3	Microtubule-based delivery of +TIPs to the bio-mimetic cortex.	67
4.4	Discussion	79
4.5	Sample preparation and data acquisition	82
4.6	Data analysis	83
5	Microtubule-based establishment of polarized patterns <i>in vitro</i>	89
5.1	Introduction	90
5.2	Polarity in the absence of microtubule organizing proteins	90
5.3	Polarity in the presence of microtubule organizing proteins	98
5.4	Discussion	102
5.5	Sample preparation and data acquisition	103
5.6	Data Analysis	104

6	Towards the establishment of polarity with a diffusing receptor	109
6.1	Introduction and Rationale	110
6.2	Materials	112
6.3	Methods	114
6.4	Discussion and perspectives	119
7	Control of microtubule dynamics by cortical proteins	121
7.1	Introduction	122
7.2	Microtubule dynamics regulation by Clasp	122
7.3	Microtubule 'end-on' interaction with Clasp	123
7.4	Discussion	130
7.5	Methods	130
7.6	Data analysis	131
	Bibliography	133
	Summary	161
	Samenvatting	165
	Dankwoord	169
	Curriculum Vitæ	171
	List of Publications	173

1

MICROTUBULE-BASED CELL POLARITY

*What I cannot create, I do not understand;
Know how to solve every problem that has been solved.*

Richard Feynman

Cells have to define directions in order to grow, migrate or divide. This ability is called cell polarity. Polarized cells typically exhibit asymmetric distributions of inner components or patterned distributions of proteins at their cortex. There are many ways by which cells can achieve those arrangements. All of them need to obey fundamental physics and chemistry principles. Therefore, understanding the principles of those mechanisms brings us closer to understanding how cells behave.

In this thesis we took on the challenge to get a better understanding of how cells can establish a polarized cortical pattern. We hypothesized the minimum set of components a cell may need to form the pattern and assessed its emergence in a controlled in vitro environment. By re-solving the problem of how to define directions with cellular tools, we learned about the principles of polarity.

The main cellular component used in our study are microtubules. These are dynamic filaments found in all eukaryotes used as tracks for cellular transport and force generation. In short, this thesis addresses the question 'How can microtubules establish a protein cortical pattern?'

*In this first chapter we give a general introduction on how cells establish polarity and the main tool we will use in our system: microtubules. Furthermore, we explain in detail a model system for microtubule-based establishment of polarity: *Schizosaccharomyces pombe*. We conclude exposing the approach used in this thesis to obtain in vitro a minimal microtubule-based polarized system.*

1.1. CELL POLARITY: HOW CELLS DEFINE DIRECTIONS

From unicellular organisms that migrate towards nutrients (chemotaxis), to tissue cells that define an inner and an outer side of organs, most cells need some sense of directionality (figure 1.1). This is usually done by asymmetric protein distributions at the cell periphery (cortical patterns) that serve as signalling cues or polarity markers to organize the inner components and drive directionally oriented actions. This ability of cells to form asymmetric distributions of proteins, cellular components or shape is called cell polarity and it is vital to nearly all cells [Nelson 2003, Macara and Mili 2010].

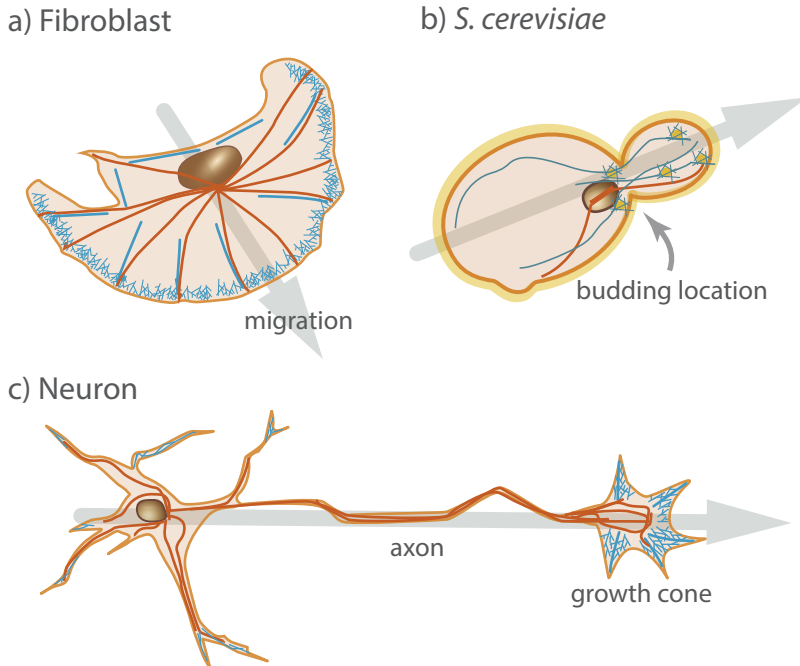


Figure 1.1: **Polarized cells.** Examples of polarized cells. (a) Migrating fibroblast on a flat surface, (b) *S. cerevisiae* budding a daughter cell, and (c) a neuron growing an axon. Microtubules are depicted in red and actin filaments in blue.

During the last decades, cell biologists have been identifying polarized patterns in a number of cell types. Those, are mainly involved in cell migration, organ formation, specialized cell shape and directional division. Each of this cellular adaptations increases the fitness of the cell or the one of the multicellular organism they belong to.

For instance, migrating cells like *Dictyostelium discoideum*, fibroblasts or growing neurons, define a leading edge with abundant actin-mediated cellular protrusions (pseudopodia, lamellipodia, and a growth cone, respectively) that produces directional traction force (figure 1.1 a and c). This, allows these cells to aggregate, move into wounds or search for synaptic partners [Wang 2009, Swaney et al. 2010, Stiess and Bradke 2011].

In the case of non-migrating cells, the cell shape itself may be polarized to better

undergo cellular functions. Neurons are a clear example. They consist of several short dendrites and a long axon. This highly polarized shape facilitates long-distance communication [Ramon y Cajal 1890, Inagaki et al. 2011, Sakakibara and Hatanaka 2015] (figure 1.1 c).

Also tissue cells, although not so clearly polarized in shape terms, exhibit a clear distinction between the apical and the baso-lateral sides. While the apical surface provides the luminal interface and regulates the exchange of nutrients, the basolateral surfaces provide attachment with adjacent cells and contact with the extracellular matrix and underlying blood vessels [Nelson 2003, Bryant and Mostov 2008, McCaffrey and Macara 2011].

Finally, in dividing cells, the division plane is often controlled upstream by cortical patterns of the partitioning defective (PAR) proteins, as it has been shown to be the case for epithelia, *Drosophila melanogaster* neural precursors or *Caenorhabditis elegans* embryos [Kemphues 2000, Doe 2001, St Johnston and Ahringer 2010, Nance and Zallen 2011].

How exactly each type of cell employs polarity to achieve different functions is very relevant to understanding unicellular and multicellular organisms. However, in this dissertation we focussed on the initial question: How can polarized or asymmetric cortical patterns be established?

The answer to this question is not unique, and depends on the type of cells and their environments. For instance, in migrating cells, the symmetry breaking is often triggered by an extrinsic signal which predetermines the axis of polarization. This signal can be an external gradient of a chemoattractant [Wang 2009]. The cell senses the gradient, integrates it, and produces a directional response [Iglesias and Devreotes 2008].

It has been shown that bacteria sense gradients by temporal integration while maintaining continuous migration [Macnab and Koshland 1972, Sourjik and Wingreen 2012]. Static eukaryotic cells sense very shallow spatial gradients [Devreotes and Zigmond 1988]. A recent model explains that this could be achieved by local activation and global inhibition of cortical receptors [Iglesias and Devreotes 2012].

Alternatively, cells are able to establish polarity without an external cue, based on intrinsic processes. In this case, the polarized distribution emerges from local short range molecular interactions. This, can be achieved via systems of diffusive proteins that can switch between active and inactive states, or via forming long protein scaffolds called the cytoskeleton that physically connect distant parts of the cell.

The first mechanism of switch-able proteins was introduced by Alan Turing in 1952 to explain macroscopic patterns such as animal stripes and spots. He showed mathematically that long range heterogeneous patterns can arise from an initially homogeneous distribution of two interacting morphogen species of different diffusivity. In living cells, reminiscent systems called reaction-diffusion systems are usually associated with GTPase or ATPase proteins [Perez and Rincon 2010]. These proteins switch from an active GTP/ATP-bound state (guanosine-5'-triphosphate and adenosine triphosphate respectively), to an inactive state triggered by hydrolysis and possible release of the GDP/ADP

(Guanosine-5'-diphosphate and Adenosine diphosphate respectively). Exchange of GDP for GTP and vice-versa is often mediated by guanine-nucleotide-exchange factors (GEFs) and GTPase-activating proteins (GAPs) respectively [Rossman et al. 2005].

Rho GTPases like the highly conserved cell division control protein 42 (Cdc42) can only bind to the plasma membrane and activate signaling pathways in the GTP-bound state. That way, the active membrane-bound proteins have slower diffusion than the inactive cytoplasmic ones, which is the basis for pattern formation in Turing systems. One of the most studied reaction-diffusion systems is cell polarity is the MinD-MinE system, found in many bacteria including the rod-shaped *Escherichia coli* (*E. coli* [Laloux and Jacobs-Wagner 2014]). See figure 1.2 and its caption.

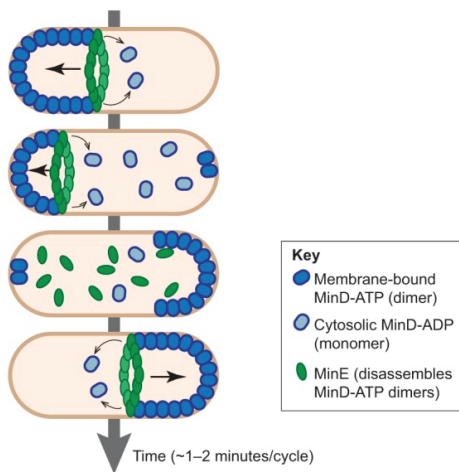


Figure 1.2: **Pole-to-pole MinD oscillation in *E. coli*.** This system causes a pole-to-pole oscillation of the proteins by the following cycle: cytoplasmic MinD dimerizes upon ATP binding and cooperatively binds to the plasma membrane [Hu et al. 2002-2003, Lackner et al. 2003]; MinE binds to MinD dimers and stimulates ATP hydrolysis [Hu and Lutkenhaus 2001], thereby promoting unbinding of MinD from the membrane; cytoplasmic MinD can dimerize again and bind to the other pole of the cell, free of MinE. This oscillation leaves the middle of the cell depleted of MinD particles, which is used as clue to determine the location of cytokinesis [Raskin and de Boer 1999, Hu and Lutkenhaus 1999]. Cartoon taken from Laloux and Jacobs-Wagner 2014.

Similar pattern formations occur at larger scale in development. In this case patterning of multiple cells defines body segmentation and cell fate decisions [Tabata and Takei 2004, Kutejova et al. 2009, Briscoe et al. 2010, Rogers and Schier 2011]. According to the Synthesis-Diffusion-Clearance model (SDC, or SDD from Synthesis-Diffusion-Degradation), a morphogen is produced from a localized source, diffuses through tissue, and is cleared from the diffusible pool by immobilization degradation or endocytosis [Crick 1970, Wartlick et al. 2009, Lander et al. 2009]. Target tissue cells interpret the received concentration of morphogen and modulate it, by for example endocytosis, and regulatory feedbacks, by producing new morphogens [Rogers and Schier 2011].

CYTOSKELETON-BASED ESTABLISHMENT OF POLARITY

Cells have found other methods to establish cortical patterns, by employing self-assembly of proteins into polarized macro-structures. In eukaryotes, those structures are microtubules and actin filaments, which are intrinsically polarized filaments formed by polymerization of the globular proteins tubulin and actin, respectively. See figure 1.3 for actin, and section 1.1 for microtubules. Another type of cytoskeleton filaments are septins [Bowen et al. 2011, Mostowy and Corrart 2012, Bi and Park 2012]. Their role in polarity has been less studied and seems to be more downstream as it is linked to en-

forcement of cell shape and restriction of organelle localization, rather than establishing polarity [Spiliotis and Gladfelter 2012]. The other element of the cytoskeleton are intermediate filaments. They are apolar and although they play a key role in establishing and maintaining the mechanical integrity of cells, in general they are not involved in cell polarity [Goldman et al. 2008].

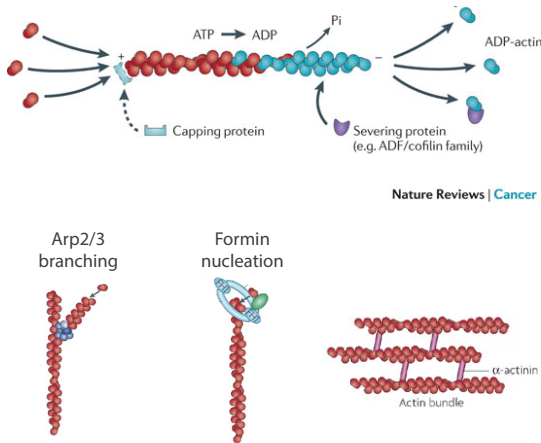


Figure 1.3: Actin filament polymerization. Actin filaments are double stranded filaments of 6-8 nm diameter nucleated from ATP-bound globular actin. Hydrolysis of ATP and later phosphate release, as well as severing proteins, promote actin filament disassembly. Actin filaments can nucleate from pre-existing filaments aided by Arp2/3, or from formin proteins, usually bound to the plasma membrane. They form higher order structures aided by actin-binding proteins such as α -actinin. Images taken from Nurnberg et al. 2011, Mattila and Lappalainen 2008, and Cingolani and Goda 2008.

Among many other functions, actin filaments are often effectors of polarity. For example, they form polarized networks at the leading edge of cells to drive migration. Such networks, which are aided by nucleating proteins at the front like Arp2/3 and severing proteins at the rear like Cofilin, have been shown to produce spontaneous polarization in uniform chemoattractant reservoirs [Wang et al. 2002, Weiner et al. 2002, Postma et al. 2003]. There, the chemoattractant may act as a 'compass' that directs the symmetry breaking. This is what is called an 'excitable system'. Such systems display wave-like behaviour, as it has been observed in *Dictyostelium discoideum*, fibroblasts, neutrophils, and mouse melanoma cells [Vicker et al. 1997-2000-2002, Bretschneider et al. 2004, Gerish et al. 2004, Weiner et al. 2007, Bretschneider et al. 2009].

Actin networks might not simply be passive followers of other cues. Here, we list some examples.

In motile neutrophils the dynamic formation of such structures amplifies and contributes to the maintenance of the polarized distribution of polarity markers [Wang et al. 2002]. Similarly, in mutant *S. cerevisiae* actin cables are responsible for maintaining the Cdc42 pattern by contributing to its focussing [Irazaqui et al. 2005].

In *C. elegans* embryos, actin filaments and nonmuscle Myosin II form dynamic contractile foci that drive the asymmetric localization of PAR3 and PAR6 to the anterior site of the plasma membrane (figure 1.4). The symmetry break in this case is induced by sperm entry at the posterior cortex, which inhibits actomyosin contractility there [Munro et al. 2004, Nance and Zallen 2011].

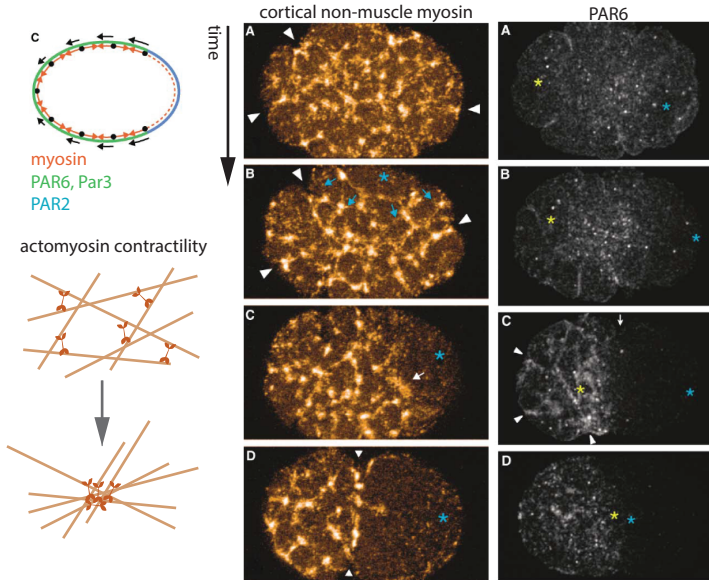


Figure 1.4: **Actomyosin-based polarization of PAR proteins in *C. elegans* embryo.** Images taken from Munro et al. 2004 showing the model diagram and fluorescence microscopy images of how actomyosin contractile networks may drag PAR6 and PAR3 proteins to the anterior side of the embryo (left side in the pictures).

MICROTUBULES: A MACRO PROTEIN ASSEMBLY TO ORGANISE CELLS

In the early 50s, it was a mystery how chromosomes could segregate. This is a vital process for eukaryotic life as it allows to pass the genetic information from the mother to the daughter cells. Thanks to the development of polarized microscopy, Shinya Inoué showed that the chromosomes are held by dynamic filaments nowadays known as microtubules, confirming earlier drawings of Walther Flemming from 1882 (figure 1.5, [Inoué 1953]). Those filaments are organized in two arrays growing in an aster-like configuration from nucleating centres located several micrometers apart from each other. In the middle, they arrange in an anti-parallel fashion and hold the chromosomes with their tips. At some moment in time, both asters shrink and pull back the chromosomes they are attached to, towards their sides of the cell.

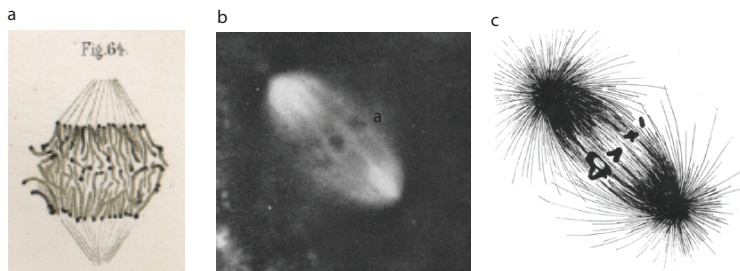


Figure 1.5: **First microtubule images.** (a) Drawings from a mitotic spindle by Flemming 1882. (b) Polarized microscopy image and (c) scheme of the first division spindle in *Chaetopterus pergamentaceus* taken from Inoué 1953.

Now we know that microtubules are formed by the globular proteins α and β tubulin, which assemble into hollow tubes of 25 nm diameter that can extend several microns. These tubes are typically formed by 13 parallel filaments composed of consecutive $\alpha - \beta$ dimers extending longitudinally (figure 1.6 [Tilney et al. 1973]), although the number of protofilaments can vary, at least *in vitro*, from 11 to 16 [Hyman et al. 1995, Chretien et al. 1996, Sui 2010].

Microtubules are highly dynamic structures that switch from phases of growth (polymerization) to shrinkage (depolymerization). This is an intrinsic property called dynamic instability [Mitchison and Kirschner 1984, Walker et al. 1988]. The side exposing a β subunit, called the plus end, has a fast growth rate. The other side, the minus end, has a slower growth rate. In cells, minus ends are often not dynamic, therefore most studies have focussed on plus ends. The transition from growth to shrinkage, termed *catastrophe*, is stochastic. *In vitro* studies characterised this stochasticity by growing microtubules from stable (non-depolymerizing) microtubule ‘seeds’ and measuring the time between the start of microtubule polymerization and catastrophe of multiple events. These times exhibit a distribution that can be better fitted with a gamma distribution than an exponential distribution [Odde et al. 1995, Gardner et al. 2011]. This means that microtubules exhibit some ‘ageing’ that causes an increase in catastrophe frequency during the first seconds of microtubule growth.

Growth occurs by the longitudinal addition of tubulin dimers with an exchangeable GTP bound to the β subunit and a non exchangeable one to the α subunit [Mitchison 1993, Nogales et al. 1999-2000]. After dimer addition, the exchangeable GTP hydrolyses and the phosphate is released [Jacobs et al. 1974, Weisenberg et al. 1976, David-Pfeuty et al. 1977]. Cryo-electron microscopy studies showed that hydrolysed lattices are longitudinally more compact than non-hydrolysed lattices, seen by GMPCPP nucleated microtubules [Alushin et al. 2014, Zhang et al. 2015] (figure 1.6). GTP hydrolysis and release of the phosphate also produces a twist tangential to the microtubule surface and perpendicular to the microtubule axis [Zhang et al. 2015]. Recent studies suggest that the hydrolysis process has an intermediate GDP-Pi state which is mimicked by GTP γ S-bound lattices or in the presence of beryllium fluoride [Carlier et al. 1989, Maurer et al. 2014, Zhang et al. 2015]. This state is compact but not twisted. Due to the GTP hydrolysis process the microtubule lattice is mostly composed of GDP-bound tubulin (blue in figure 1.6) except at the very growing tip where it contains GTP-bound dimers (red) [Carlier et al. 1987, Erickson and O'Brien 1992] and an intermediate region formed of GDP-Pi dimers [Zhang et al. 2015](pink).

Microtubule stability is highly linked to GTP hydrolysis. GDP microtubule lattices have been shown to be more unstable (prone to undergo catastrophe) than GTP lattices [Arai and Kaziro 1976, Hyman et al. 1995]. This is probably because their more compact lattice produces a destabilizing strain [Zhang et al. 2015]. Those lattices may be held together thanks to the lateral interactions [Caplow et al. 1994, Ravelli et al. 2004, Wang and Nogales 2005, Yajima et al. 2012, Alushin et al. 2014]. Protofilaments that lose the lateral interactions bend outwards and give rise to the canonical image of a shrinking microtubule of protofilaments peeling off (figure 1.6 [Kirschner et al. 1974, Melki et al. 1989, Mandelkow et al. 1991]). Due to the different stability between GTP and GDP lattices, microtubule catastrophe has been associated with the loss of the GTP region at

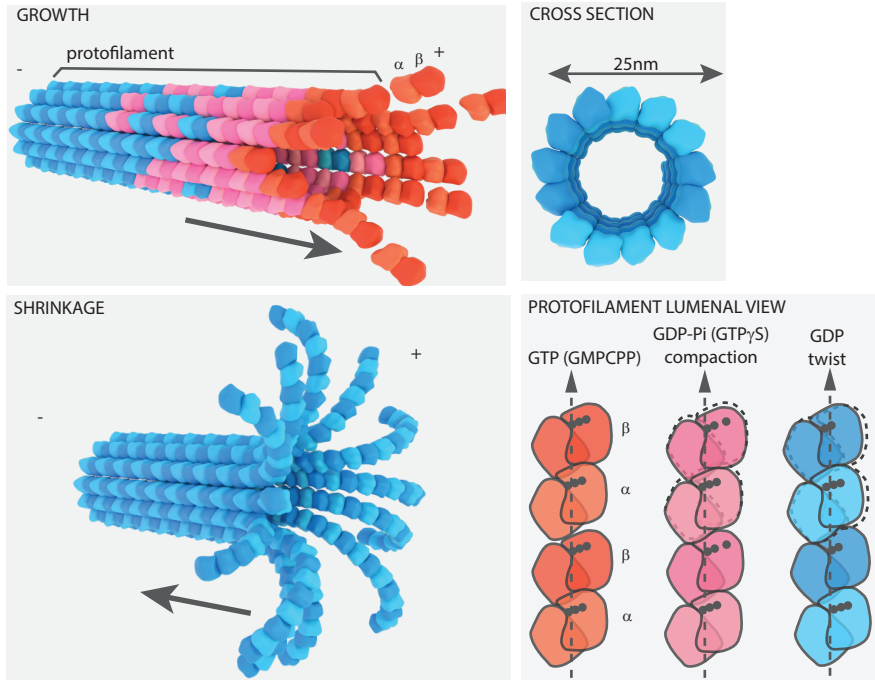


Figure 1.6: **Dynamic instability.** Cartoons illustrating microtubule morphology during growth (polymerization) and shrinkage (depolymerization). Figures redrawn from Zhang et al. 2015. Tubulin is colour coded according to hydrolysis state of the exchangeable GTP in the beta sub-unit.

the tip, 'GTP-cap', due to full hydrolysis [Mitchison and Kirschner 1984]. However, recent experiments show that the size of the intermediate GDP-Pi region correlates with microtubule stability [Duellberg et al. 2016].

Agents affecting microtubule dynamics (growth speed, or frequency of catastrophes) have been shown to affect tubulin compaction or bending. For example, Taxol, a microtubule stabilizing agent used in cancer treatment, reverses the compaction from GDP lattices [Alushin et al. 2014]. On the contrary, the microtubule destabilizer Colchicine prevents bent protofilaments from straightening, which inhibits growth [Panda et al. 1995, Ravelli et al. 2004].

Despite a large body of work done on microtubule dynamics, the precise intrinsic cause of catastrophe remains unclear [Brouhard 2015]. Recent brownian dynamic simulations taking into account the mechanics of protofilament bending and a thermal bath have shown to reproduce emergence of catastrophe with quantitative accuracy to experimental studies [Zakharov et al. 2015]. The model further predicts the emergence of microtubule 'ageing' as a slow evolution of stochastic reversible events occurring continuously at the tip.

MICROTUBULE ASSOCIATED PROTEINS: PUTTING THE REINS TO MICROTUBULES

In order to organize microtubules spatio-temporally, cells possess a variety of microtubule associated proteins (MAPs). These, are proteins that regulate microtubule dynamics. Microtubule associated proteins bind specifically to tubulin subunits, or in the protofilament grooves formed during microtubule assembly. By recognising features of different tubulin conformational states, including the nucleotide state and bending, MAPs can distinguish polymerized tubulin from non-polymerized, as well as different parts of the microtubule (the lattice of the plus or minus end). Here we present the most relevant ones.

The highly conserved proteins of the end binding (EB) family bind between protofilaments at the growing tips of microtubules. They recognise and promote an intermediate structural state generated during GTP hydrolysis [Maurer et al. 2012, Zhang et al. 2015]. This binding is very short-lived, around 300 ms. Imaged with fluorescence microscopy, EB intensity appears as a comet that follows the growing microtubule tip [Bieling et al. 2007, Dragestein et al. 2008, Seetapun et al. 2012]. Recently, EB intensity have been found to be an indicator of the instantaneous microtubule stability [Duellberg et al. 2016]. Proteins of the EB family serve as guide for other proteins to find the microtubule growing tip and exert their functions [Akhmanova and Steinmetz 2008-2010, Galjart 2010, Kumar and Wittmann 2012]. These proteins interacting with the microtubule tip are called +TIPs.

Other proteins that bind at the grooves between protofilaments are the Ndc80 complex and doublecortin (DCX) [Brouhard and Rice 2014]. Ndc80 binds along the longitudinal interfaces and connects microtubules to the outer kinetochore [Cheeseman et al. 2006, Wilson-Kubalek et al. 2008], therefore it is essential for proper chromosome segregation [McClelland et al. 2004, DeLuca et al. 2005]. Doublecortin is a neuron specific protein required for proper brain development which recognizes bent microtubules of 13 protofilaments [des Portes et al. 1998, Gleeson et al. 1998, Moores et al. 2004, Taylor et al. 2000, Bechstedt and Brouhard 2012, Bechstedt et al. 2014].

Depolymerases are MAPs that prevent microtubule growth or promote catastrophes. For instance, the highly conserved protein Stathmin/Op18 forces tubulin protofilaments into bent conformations making them unable to grow [Gigant et al. 2000, Steinmetz et al. 2000, Gupta et al. 2013]. Similarly, MCAK/kinesin-13/XKCM1 also bend protofilaments and even trigger tubulin unbinding from the microtubule [Desai et al. 1999, Moores et al. 2002, Hunter et al. 2003, Asenjo et al. 2013, Bruns et al. 2014]. These proteins are regulated spatio-temporally during the cell cycle. MCAK is involved in driving chromosome segregation by depolymerizing the minus ends of microtubules generating a poleward flux powered by ATP [Maney et al. 1998, Rogers et al. 2004, Ganem et al. 2005]. Stathmin is deactivated at the leading edge of migrating cells and close to the chromosomes by gradients of diffusive regulatory molecules [Niethammer et al. 2004].

Another depolymerase and spindle size regulator called Kinesin-8/Kip3p is able to depolymerise microtubules in a length-dependent manner without need for an external regulator [Goshima et al. 2005, Gupta et al. 2006, Varga et al. 2006, Varga et al. 2009, Rizk et al. 2014]. Kinesin-8, as most kinesin proteins, contains a motor domain which allows

it to walk on microtubules with high processivity, i.e. perform long runs. Thus, it can form traffic jams at the plus ends of microtubules and that way ‘measure’ microtubule length [Reese et al. 2011, Leduc et al. 2012].

Other MAPs can increase microtubule growth speed or prevent them from undergoing catastrophes. A very conserved family is the XMAP215 family, (Stu2p in *S. Cerevisiae*, Msp1 in *Drosophila*, Alp14 and Dis1 in *S. pombe*), which contribute to microtubule growth from spindle poles [Gard and Kirschner 1987, Wang and Huffaker 1997, Cullen et al. 1999]. These proteins contain several tumor overexpressed gene (TOG) domains that bind to $\alpha\beta$ -tubulin [Al-Bassam et al. 2006, Slep and Vale 2007, Widlund et al. 2011, Ayaz et al. 2012]. According to the current thinking, XMAP215 can promote addition of curved tubulin dimers while tethered to the microtubule plus end. Once the tubulin subunit forms lateral bonds, it straightens and promotes XMAP215 release [Ayaz et al. 2014]. Consistent with this idea, XMAP215 has been found at the extreme of the plus ends of growing microtubules [Nakamura et al. 2012, Maurer et al. 2014]. In addition, XMAP215 can diffuse along the microtubule to find the tip [Brouhard et al. 2008, Widlund et al. 2011].

Other TOG containing proteins are part of the cytoplasmic linker associated protein family (CLASP) [Pasqualone and Huffaker 1994, Akhmanova et al. 2001]. However, differences in the TOG domains between CLASPs and XMAP215 produce a different effect on microtubules [Leano et al. 2013]. CLASPs do not increase microtubule growth speed [Mimori-Kiyosue et al. 2006], but seem to promote rescues and reduce the probability of catastrophe [Al-Bassam et al. 2010]. However, the mechanism by which this effect is achieved is not yet understood [Brouhard and Rice 2014]. Recent experiments suggested that CLASP may modify microtubule lattices and regulate EB localization [Grimaldi et al. 2014].

Finally, microtubule reorganization in cells is also highly regulated by severing proteins (see Roll-Mecak and McNally 2010 for review).

FORCE PRODUCTION BY MICROTUBULES AND REGULATION OF MICROTUBULE DYNAMICS BY FORCES

Microtubule organization is further regulated by cell boundaries and interactions with large cellular components like the cell nucleus and the chromosomes. *In vitro* experiments have shown how confinement and cortical proteins regulate microtubule organization [Cosentino Lagomarsino et al. 2007, Laan et al. 2012a, Laan et al. 2012b]. Factors inducing microtubule organization due to cell boundary effects are microtubule alignment with the boundary and pushing or pulling forces generated by the microtubule. Here we give a brief introduction to microtubule force generation.

Force generation is an intrinsic property of microtubules that can be aided by molecular motors and other proteins. It is observed in spindle formation, nucleus centering, microtubule interactions with the cell cortex, or endoplasmic reticulum membrane tubule formation, among others [Inoue and Salmon 1995, Waterman-Storer and Salmon 1998, Tran et al. 2001].

In vitro experiments have shown that microtubule polymerization alone can produce pushing forces that deform liposomes [Miyamoto and Hotani 1988, Fygenson et al. 1997] and produce bending of the microtubule when growing against a hard barrier [Dogterom and Yurke 1997, Janson and Dogterom 2004]. Polymerisation-based pushing forces are also found in other biological polymers like actin [Footer et al. 2007]. They can be explained by a 'Brownian ratchet' model [Peskin et al. 1993, Howard 2001, Dogterom et al. 2005]. Since polymer thermal fluctuations are larger than the size of monomers, they allow for monomers to be added at the polymer tip, even while in contact with a barrier or any other physical structure. Then the polymerization on-rate is modified by the probability of opening a gap of the monomer addition size, δ , by thermal fluctuations. Assuming that off-rate is not affected by force, it can be shown that the polymerization velocity in the presence of a constant external load force, F , for a rigid single-strand filament follows:

$$v(F) = \delta(k_{\text{on}}e^{-F\delta/k_{\text{B}}T} - k_{\text{off}}) \quad (1.1)$$

where k_{on} and k_{off} are the on and off rate respectively, k_{B} the Boltzman constant and T the temperature. Then, the stall force at which this polymer neither polymerizes nor depolymerizes is

$$F_{\text{stall}} = \frac{k_{\text{B}}T}{\delta} \ln\left(\frac{k_{\text{on}}}{k_{\text{off}}}\right). \quad (1.2)$$

In vitro experiments have shown that microtubules stall at around 5 pN, in agreement with theoretical predictions [Fygenson et al. 1997, Dogterom and Yurke 1997, van Doorn et al. 2000]. These stalling events have been shown to promote catastrophes [Janson et al. 2003].

On the other hand, recent experiments showed that microtubules can pull physical elements like beads or kinetochore protein scaffolds while depolymerizing [Grishchuk et al. 2005, Akiyoshi et al. 2010, Volkov et al. 2013].

MICROTUBULE-BASED ESTABLISHMENT OF CELL POLARITY

Microtubules are typically connectors of distant parts of the cell. Due to microtubule intrinsic polarity, motor proteins like kinesins and dyneins can move on them with a specific direction [Valee and Sheetz 1996, Hirokawa 1998]. This leads to polarized transport of cellular components and polarity factors [Burack et al. 2000, Nakata and Hirokawa 2003, Kapitein and Hoogenraad 2011]. Microtubules play a key role in establishing polarity in systems such as neurons, migrating cells, and *S. pombe* as we will see below.

Undifferentiated hippocampal rat neurites, display several dendrites and only one of them extends longer and becomes the axon [Dotti et al. 1988]. Forced stabilization by photoactivation of caged taxol has shown that microtubule stability is a determinant factor to axon specificity [Witte et al. 2008]. Axon determination has also been associated with the motor protein Kif5 of the Kinesin-1 family as it gradually shifts its transport only to the dendrite that will become the axon [Jacobson et al. 2006]. This kinesin is in charge of promoting microtubule growth in the axon by transporting multiple proteins that promote axon growth such as collapsin response mediator protein-2 (CRMP-2) to the plus end, which in turn, carries tubulin dimers [Fukata et al. 2002b, Nariko et al.

2005, Kimura et al. 2005]. On the other hand, Kinesin-3 also promotes axon specification by transporting phosphatidylinositol-(3,4,5)-triphosphate (PIP₃), a second messenger implicated in signal transduction and membrane transport, to the tip of neurites [Horiguchi et al. 2006]. *In vivo*, neuronal polarity is inherited from apicobasal polarity of the progenitors or migration [Barnes and Polleux 2009, Hatanaka et al. 2012]. Then, the above mentioned microtubule regulation by MAPs contributes to steering the growth cone towards the appropriate direction (see Bearce et al. 2015 for review).

In mouse and human fibroblasts, microtubules are indispensable for establishment of directional migration [Vasilev et al. 1970, Bershafsky et al. 1991, Siegrist and Doe 2007]. They display a polarized organization by growing from the centrosome, close to the nucleus, with the plus ends facing towards the actin-rich leading edge of the cells (figure 1.1 a) [Small and Kaverina 2003]. At the leading edge, they activate Rac1 GTPase and Cdc42, leading to polymerization of actin to form microfilaments and lamellipodia [Ridley et al. 1992], by multiple tip touches with the cortex [Waterman-Storer et al. 1999]. Those activations are thought to be mediated by the signaling scaffold protein IQGAP1, which directly interacts with the +TIPs CLIP-170 and SKAP, although it does not localize with microtubule plus ends [Fukata et al. 2002a, Briggs and Sacks 2003, Watanabe et al. 2004, Cao et al. 2015]. Rac1, in turn, stabilizes microtubules, affecting microtubule organization, therefore promoting a feedback [Watanabe et al. 2004]. At the rear, microtubules promote focal adhesion disassembly [Kaverina et al. 1999, Ezratty et al. 2005].

In *S. pombe*, a rod-shaped unicellular eukaryote, microtubules deliver polarity factors to the poles of the cell and this creates a bi-polar pattern [Mata and Nurse 1997]. In this case, the pre-established elongated rigid cell shape produces the initial symmetry breaking [Terenna et al. 2008]. This is probably the best understood system on microtubule-based establishment of polarity and we will use this model organism for inspiration during this thesis.

POLARITY IN *Schizosaccharomyces pombe*

Schizosaccharomyces pombe is an ideal model organism to study microtubule-based polarity because it is able to form a polarized pattern, the Tea1-Tea4 protein complex pattern (figure 1.7), without relying on actin, septins, switch proteins or external cues. *S. pombe* has an inherited axial symmetry. *S. pombe* cells have a very regular rod shape of 4 μm diameter which grows longitudinally from 7 to 14 μm by cell end (pole) extension [Mitchison and Nurse 1985].

During interphase, microtubules are arranged in 2 to 6 anti-parallel bundles of 4-5 microtubules with overlapping minus ends at the centre of the cell, often associated with the perinucleus (figure 1.7) [Hagan and Hyams 1988, Tran et al. 2001, Sagolla et al. 2003, Carazo-Salas and Nurse 2006]. The microtubule plus ends face towards the poles of the cell. Roughly every two minutes a plus end tip reaches a pole of the cell and delivers the polarity markers Tea1 and Tea4 to the plasma membrane, where they accumulate in clusters displaying a bipolar pattern [Mata and Nurse 1997, Behrens and Nurse 2002, Feierbach et al. 2004, Martin et al. 2005, Tatebe et al. 2005, Tischer et al. 2009, Bicho et al. 2010, Dodgson et al. 2013]. The Tea1-Tea4 pattern initiates the cascade for cell growth by

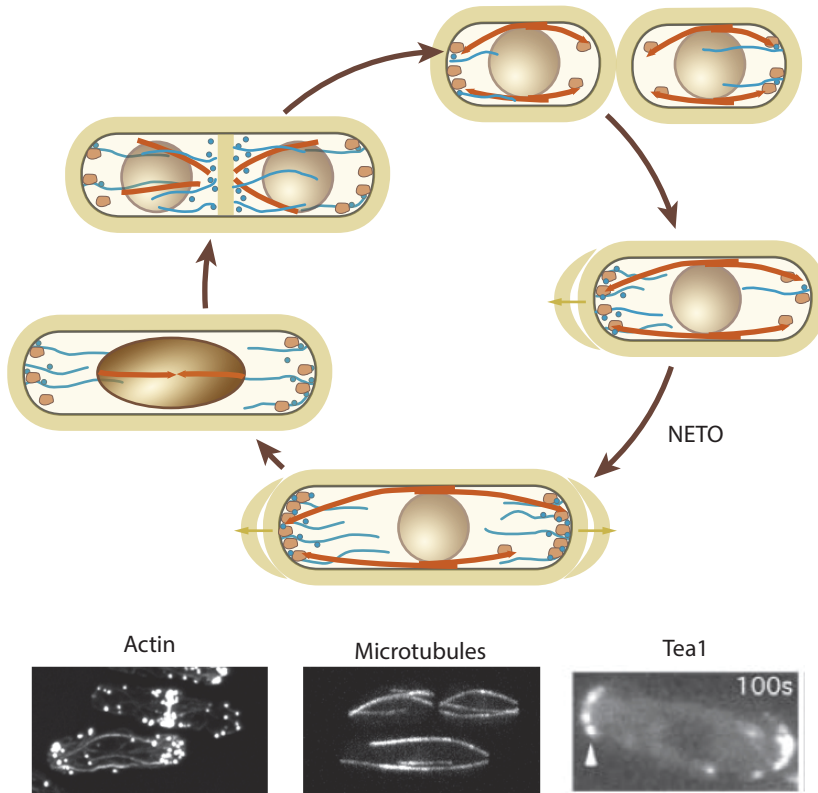


Figure 1.7: *Schizosaccharomyces pombe* cell cycle and distribution of polarity factors. Microtubules are represented as red arrows indicating the growth direction. Polarity markers are orange, actin cables and actin patches are blue. Figure redrawn from Chang and Martin 2009. **Below:** Fluorescent microscopy images taken from Chang and Martin 2009 and Behrens and Nurse 2002 of cells in interphase.

mediating recruitment of the formin For3 and the actin-associated protein Bud6 [Glynn et al. 2001, Feierbach and Chang 2001, Feierbach et al. 2004]. Recent findings suggest that Tea4 further promotes Cdc42 activation at the poles by local recruitment of the Cdc42 activator Gef1 and exclusion of the deactivator Rga4 [Kokkoris et al. 2014]. Active Cdc42 promotes polarized exocytosis of cell-wall-remodeling enzymes to drive polar cell growth [Martin et al. 2007, Rincón et al. 2009, Bendezú and Martin 2011, Estravís et al. 2011]. Moreover, Tea4 induces the DYRK kinase Pom1 gradient, which controls the location of the cell division site [Martin et al. 2005, Tatebe et al. 2005, Celton-Morizur et al. 2006, Padte et al. 2006, Hachet et al. 2011].

Schizosaccharomyces pombe divides by medial fission. Therefore, the daughter cells have an old pole containing polarity markers and a new pole without (figure 1.7). Accordingly, cells initially grow only from the old pole and, as the new pole gradually be-

comes enriched by microtubule-based depositions of Tea1-Tea4, the new end takes off (NETO), i. e. bipolar growth starts [Mitchison and Nurse 1985, Sawin and Snaith 2004].

During interphase, microtubules grow by plus end polymerization from several 'satellite' particles containing γ -tubulin complexes called γ -TuC and other proteins located at the lattice of pre-existing microtubules [Stearns et al. 1991, Vardy and Toda 2000, Fujita et al. 2002, Venkatram et al. 2004, Sawin et al. 2004, Zimmerman et al. 2004-2005, Samejima et al. 2005, Venkatram et al. 2005, Janson et al. 2005] (see figure 1.8). Short growing microtubules are then held anti-parallel by the action of the bundler Ase1 and transported towards the minus end of the template microtubule by the motor Klp2. After reaching the minus end tip, Ase1 acts as a brake and holds the microtubules together [Carazo-Salas and Nurse 2006, Janson et al. 2007]. The CLASP family protein Cls1 further stabilizes microtubules in this 'overlapping region' [Bratman and Chang 2007]. In wild type cells, microtubules grow long enough to reach the poles of the cell, where they stay in contact for around 100 seconds, and depolymerize [Drummond and Cross 2000, Tran et al. 2001], leaving behind the polarity markers. The Clip170 homologue protein Tip1 and Cls1 contribute to ensure proper microtubule length. Tip1 seems to stabilize microtubules, and Cls1 promotes rescues [Brunner and Nurse 2000, Kelkar and Martin 2015]. Microtubule catastrophes occur predominantly close to the cell poles or after contact with the pole cortex. This can be explained by a combination of compressive forces upon cortical contact and length-dependent catastrophe promotion by the Kinesin-8 family-member Klp5/6 [Tischer et al. 2009, Foethke et al. 2009].

Tea1-Tea4 transport at microtubule plus ends is performed by interaction with Tip1, which links Tea1 to the kinesin Tea2 [Behrens and Nurse 2002, Busch et al., 2004, Busch and Brunner 2004, Feierbach et al. 2004, Martin et al. 2005]. Binding to the microtubule and plus-end accumulation requires the transient interactions with the EB protein Mal3 [Bieling et al. 2007].

Transfer of Tea1, Tea4, Tip1, and Tea2 from the microtubule plus end to the plasma membrane is achieved via a combined interaction between Tea1 and the transmembrane prenylated anchor protein Mod5 and Tea3, from the Erzin-Radixin-Moesin (ERM) family [Browning et al. 2003, Snaith and Sawin 2003, Feierbach et al. 2004, Snaith et al. 2005]. It is still unclear how Tea1, Mod5 and Tea3 interact. Tip1 and Mod5 co-localise, forming around 20 dispersed clusters of sizes up to 100 nm at the plasma membrane [Dodgson et al. 2013]. Membrane cluster formation and even Tea1 retention at the cortex require Tea1 trimmerization [Dodgson et al. 2013, Bicho et al. 2010]. Furthermore, Tip1 depositions induce a polarized distribution of Mod5. This positive feedback is thought to add robustness to the Tea1-Tea4 pattern [Snaith and Sawin 2003]. Tea3 displays clusters co-localising with Mod5, that only co-localise with Tea1 during mitosis. Forced localization between Tea1 and Tea3 during interphase produces polarity defects [Dodgson et al. 2013].

Tea1-Tea4 recruit formin For3 and Bud6, which initiate actin cable formation [Feierbach and Chang 2001, Nakano et al. 2002, Martin et al. 2005]. These are very dynamic filaments, detached from Tea1-Tea4 polarisomes, that undergo retrograde flow while keeping initially attached to For3 at the plasma membrane [Martin et al. 2005]. They

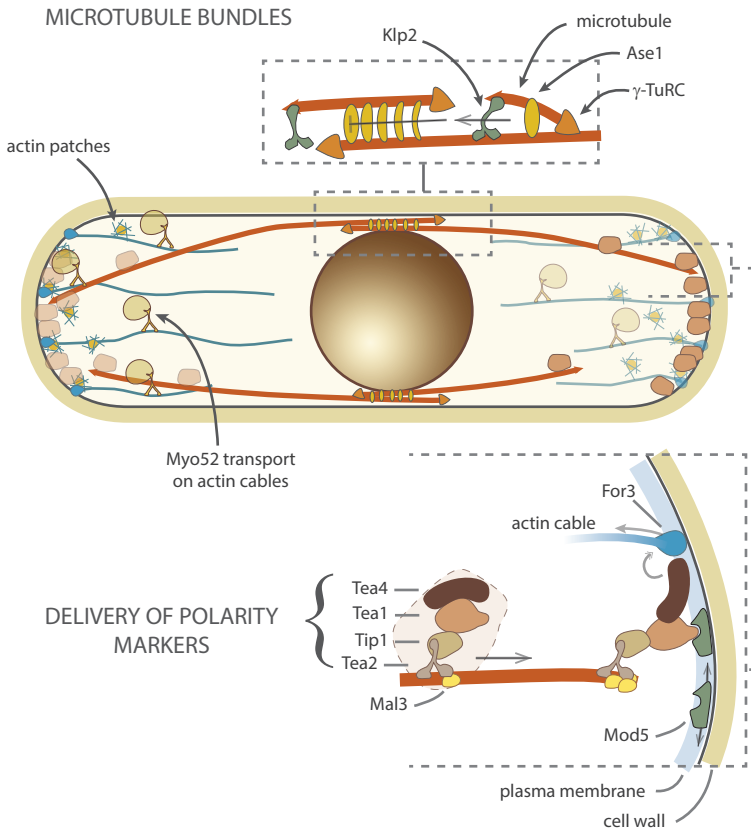


Figure 1.8: *Schizosaccharomyces pombe* cytoskeleton and establishment of Tea1-Tea4 pattern. Cartoon displaying the key proteins involved in the establishment of the Tea1-Tea4 cortical pattern and subsequent depositions of growth factors by myosin Myo52 in a cell in interphase. See the main text for explanations.

serve as tracks for Myosin V Myo52 to transport and tether exocytotic vesicles at the cell poles [Schott et al. 1999, Feierbach and Chang 2001, Motegi et al. 2001, Win et al. 2001, Lo Presti and Martin 2011]. Moreover, Myosin V contributes to shaping of the actin cables [Lo Presti et al. 2012].

1.2. MOTIVATION AND THESIS OUTLINE

Since polarity is such a vital mechanism for cells, it is not surprising that cells display redundancy in the polarity machineries to ensure it, as well as mechanisms to improve its robustness. One may ask however, what the minimal requirements are for the establishment of microtubule-based polarity.

In this thesis we took the challenge of exploring *in vitro* how a polarized pattern can

be formed by microtubule-based delivery of polarity markers. We took as a model system *S. pombe* because it is the best understood system of microtubule-based establishment of polarity. We restricted ourselves to minimal conditions, i. e. seek for the minimal set of components required to establish a polarized pattern. This means our system is not aiming for robustness, although future research into that topic would be very interesting.

Recently, minimal system approaches in the context of *S. pombe* polarity have been pursued. In our lab it was shown that a chimera protein containing affinity for both microtubule tips, via Mal3, and the cell cortex, via a Pom1[305-510] fragment, could be focussed to the cell poles in a microtubule-dependent manner (figure 1.9) [Recouvreur et al. 2016]. In this case, the chimera protein did not appear to be clearly transported by microtubules, but rather diffusing in the plasma membrane. Microtubule plus end contacts with the cortex induced the asymmetric localization of the protein. Due to being a minimal system, the chimera pattern is less pronounced and robust than the Tea1-Tea4 pattern.

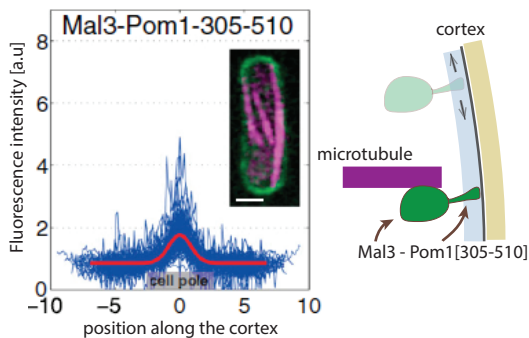


Figure 1.9: *S. pombe* polarity factors. Pictures taken from Recouvreur et al. 2016 showing the cortical distribution of the Mal3-Pom1[305-510] chimera (green) on the microtubule cortex. The graph shows the fluorescence intensity along the cell cortex with the pole in the origin.

Another study showed that a chimera protein containing the motor domain of Tea2 and the globular tail of Myo52 could transport Myosin cargoes on microtubules and restore polarized growth in mutant cells lacking actin [Lo Presti and Martin 2011].

These artificial chimera experiments in cells give important insights into what are the minimum mechanisms required for a cell to produce a pattern. Nevertheless, experiments in cells can not completely exclude that unknown protein interactions are contributing to the observed pattern. In this thesis, we follow a bottom up approach where we build a controllable cell-like environment where components are added one at a time.

In order to obtain a polarized pattern, there are two known requirements: control of microtubule dynamics and organization so that the tips reach the target location of delivery, and a good interplay between the polarity marker and the cortical receptor that ensures depositions. These two aspects are interconnected in two ways. First, the polarity markers themselves may affect microtubule dynamics and possibly organization. Second, microtubule dynamics play a role in facilitating deposition of polarity markers,

beyond the first step of reaching the cell cortex. For instance, pulse release of protein upon microtubule catastrophe may facilitate its deposition.

Moreover, due to the small size of *S. pombe*, polarity markers are homogeneously distributed in the cytoplasm from where they could potentially bind directly to the membrane receptor. This means that microtubule depositions to the correct cortical location have to be favoured over isotropic cytoplasmic bindings. To our knowledge, Tea1 does not have an active state that allows it to bind to Mod5 when it is associated with the microtubule, and an inactive state when it is in the cytoplasm. Therefore, we considered a polarity marker which is always able to interact with the cortex. In this case, it is not yet known how microtubule-based depositions to the plasma membrane are favoured against cytoplasmic binding. Given that protein binding to the cortical receptor is probably proportional to protein concentration, a receptor could distinguish between the protein concentrations in solution and the higher protein concentrations at the microtubule tip (figure 1.10).

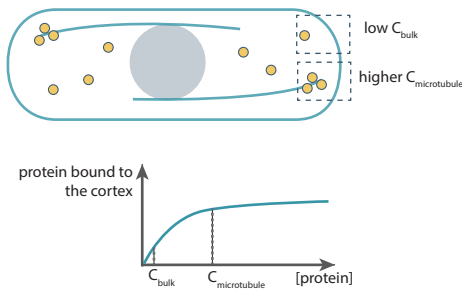


Figure 1.10: **Microtubule-induced specificity for polarity markers to bind to a cortical receptor.** Schematic cartoon showing how higher amounts of protein found at microtubule tips can facilitate protein deposition as opposed to free binding from solution. The graph below represents a schematic of a possible non-cooperative protein-cortical receptor binding curve in equilibrium. Nearly no protein binds to the receptor from solution (C_{bulk}), while the higher concentration at the microtubule tip ($C_{\text{microtubule}}$) is enough for cortical binding. It should be noted that cortical binding from the microtubule tip does not necessarily follow the same binding curve as from solution.

In our experiments, we form *S. pombe*-shape micro-cavities where microtubule plus-end tracking proteins can be delivered by microtubules to the boundaries of these cavities. As polarity markers, we used either Mal3 or Tip1 in the presence of Mal3 and Tea2. These proteins may form minimal versions of the polarity markers found in *S. pombe*. The Mal3 system corresponds to a minimal plus end tracking system, while the Tip1 system corresponds to a minimal Kinesin-cargo system. As we will see, both systems affect differently microtubule dynamics upon cortical contact and produce different delivery outcomes.

The thesis is structured as follows:

In **Chapter 2** we give a review on the proteins Mal3, Tea2 and Tip1 and characterize how Tip1 distributes on microtubules as a function of the other two proteins. The aim of this chapter is to better understand the system and find the best conditions in which Tip1 may act as a polarity marker. The data suggests that under some conditions Tip1-Tea2 can form complexes of high amounts of Tip1 particles at the microtubule tips.

In **Chapter 3** we describe in detail how we engineered a *S. pombe*-like *in vitro* envi-

ronment. In this case we used glass micro-wells that mimic the cell cortex by containing synthetic receptors for the chosen polarity marker, Mal3 or Tip1, fused to a tag that can bind to the receptor. Here, the cortical receptor is not mobile, as in *S. pombe* cells.

In **Chapter 4** we use the engineered cortex to test under which conditions microtubules can deposit tagged Mal3, or tagged Tip1 in the presence of Mal3 and Tea2. We show that only the tagged Tip1 complexes can be efficiently transferred to our cortices. These complexes can tether microtubule tips to the wall and their deposition efficiency is increased by microtubule catastrophe.

In **Chapter 5** we explore how elongated cavities can polarize microtubules and how this can produce a polarized Tip1 cortical pattern. We find that in the absence of microtubule organizing proteins like Ase1 and Klp2, microtubules tend to interfere with each other in finding the cavity poles with the plus ends. We then let dynamic anti-parallel microtubule bundles form by adding Ase1 and Dynein to the system. In this case, microtubules interfere much less with each other and are able to produce polarized Tip1 deliveries with higher frequency than in the absence of Ase1 and Dynein.

In **Chapter 6** we get a step closer to *S. pombe* by including motility of the cortical receptor and confinement. To do so, we developed a method to form elongated water-in-oil emulsion droplets where microtubules can grow inside and tagged Mal3 or tagged Tip1 can bind to a lipid receptor.

In **Chapter 7** we show some preliminary results on how cortical proteins can affect microtubule dynamics. In particular, we functionalise micro-fabricated glass barriers with CLASP and observe whether microtubules can sustain their tip contact with the barrier longer than in the presence of solely EB1.

2

LOCALIZATION OF POLARITY FACTORS TO MICROTUBULE PLUS ENDS

In cells, microtubule plus ends are decorated by the so called plus tip proteins (+TIPs). They regulate microtubule dynamics, organization, and interactions with other cellular components such as the chromosomes, mitochondria, and the cell cortex. It is, therefore, of great interest to understand how different +TIPs locate at microtubule plus ends.

*In *S. pombe*, the polarity markers *Tea1* and *Tea4* are deposited at the cell poles by microtubule plus ends. Their plus end localization depends on the kinesin *Tea2*, the CLIP-170 homologue *Tip1*, and the EB1 homologue *Mal3*. In this chapter we study *in vitro* how those three proteins work together to accumulate at microtubule ends in large amounts.*

*We extract the kinetics of *Tip1* binding to the different microtubule parts and the dynamics of kinesin mediated transport along the microtubule and possible jamming at the microtubule plus ends. This analysis provides input for the design of later assays of deposition of +TIPs to a bio-mimetic cortex.*

2.1. INTRODUCTION

Microtubules are often referred to as the highways of cells. They form paths along which motor proteins, such as kinesin and dynein, can walk and transport cellular components over long distances. That way, cells can distribute components spatially. It has been shown that microtubules in cells like *S. pombe* and fibroblasts deposit marker proteins from their tips to specific parts of the cortex (see Siegrist and Doe 2007 for a review). Those proteins initiate local signals that lead to global processes like cell growth or directed migration. It is likely that the way those proteins organize on the microtubule plus end may affect their ability to be transferred to the cortex. For instance, a high number of proteins at the tip may increase the chances of a transfer to happen (see figure 1.10).

In this chapter, we study how the plus end binding system from *S. pombe* composed of the EB1 homologue Mal3, the kinesin motor Tea2 and its cargo Tip1 bind to dynamic microtubules. In particular, we are interested in how the three proteins can act together to accumulate high amounts of Tip1 at microtubule plus ends.

The chapter starts with a literature review of the three proteins and their known interactions. Next, we describe how Tip1 is recruited to microtubule lattices *in vitro* as a function of Mal3 and Tea2 concentrations. We measure the dynamic properties of the complex directly, as well as using Fluorescence Recovery After Photobleaching (FRAP) measurements. Both analyses suggest that Tip1 localization at the microtubule plus end is both due to Mal3-based recruitment at the tip, and, at high protein densities, on short traffic jams of Tea2-Tip1 particles coming from the GDP microtubule lattice.

We further show that Tea2-Tip1 particles are able to steer a microtubule from its tip on another microtubule lattice and be transferred to the second microtubule. This data suggests that Tea2-Tip1 and Mal3 is able to form clusters on microtubule tips that behave as particles of long processivity. These transfer examples suggest that under the same conditions, transfers from a microtubule plus end to a cortical receptor might be possible.

To conclude the chapter, we performed a study on the ability of Tea2-Tip1 to form traffic jams at microtubule tips. We take a simple existing theoretical model that predicts the emergence of jams. The model consists of particles (for instance kinesins) binding and unbinding on a finite lattice (the microtubule) hopping in one direction to unoccupied lattice sites. We expand this model for the case of a growing lattice to take into account the effect of microtubule growth. Preliminary results show that the data, at least qualitatively, agrees with the theoretical predictions. Therefore, we expect that Tea2-Tip1 complexes under some conditions form jams on growing microtubule tips of a few hundreds of nanometres. The set of experiments analysed in study is scarce, therefore more experiments should be performed in order to better understand the system. Nevertheless, we hope this analysis sets a new method to understand protein distributions at microtubule tips. A systematic study using this method could yield motor dynamics parameters in non-single molecule conditions. This is interesting since properties like the run length (ℓ_r) or the number of proteins oligomerizing at a microtubule may vary upon protein concentration.

2.2. MAL3, TEA2 AND TIP1

MAL3

Mal3 belongs to the highly conserved family of autonomous end-binding proteins called EBs. It contains an EB homology domain (EBH) from where it dimerizes [Honnappa et al. 2005] and a calponin homology domain (CH, figure 2.2) [Hayashi and Ikura 2003, Slep and Vale 2007]. The latter domain has been shown to autonomously track microtubule growing ends by recognizing [Maurer et al. 2011] and affecting [Vitre et al. 2008, Zhang et al. 2015] the nucleotide state of growing microtubules. EB proteins bind to the groove between lateral protofilaments, accelerate GTP hydrolysis and promote a conformational state which is more compact than GDP-bound lattices but less compact than GTP-bound lattices [Maurer et al. 2012, Maurer et al. 2014, Zhang et al. 2015]. *In vitro* experiments have also shown that Mal3 promotes microtubules rescues (switch from shrinkage to growth) on a concentration dependent manner [Vitre et al. 2008, Munteanu 2008, Katsuki et al. 2009]. Single molecule experiments showed that Mal3 binds to the microtubule growing tip for a residence time of 0.282 ± 0.003 s [Bieling et al. 2007, Maurer et al. 2012]. As a result, Mal3 signal on the microtubule tips appears as a comet that follows the tip with a tail length that is directly proportional to the microtubule growth speed (figure 2.1a, [Bieling et al. 2007]).

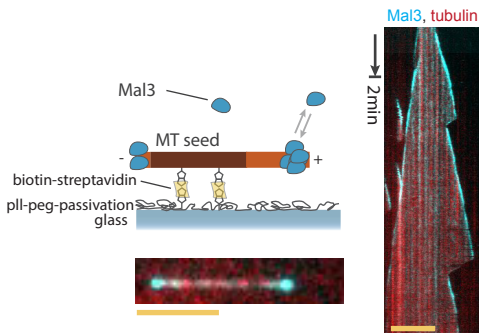


Figure 2.1: **Mal3 autonomous tip tracking.** Kymographs of a microtubule (red) in the presence of 100nM Mal3::mCherry (cyan). Imaged with TIRF microscopy. Scale bar 5 μ m.

The EBH domain can interact with many other proteins that 'hitchhike' on EB proteins to locate at microtubule ends [Akhmanova and Steinmetz 2008, Honnappa et al. 2009]. As compared to other EB proteins, Mal3 lacks a EEY/F domain at the C-terminus, to which other proteins like CLIP-170 and p150^{Glued} can bind from their Cap-Gly domains [Bieling et al. 2008a, Watson 2006, Dixit et al. 2008]. Mal3 does contain an EEA domain, which, to our knowledge, has not been studied yet.

TEA2

Tea2 is a 70KDa protein with a kinesin motor domain, an unstructured region at its N-terminal (*Nte*) and a short coil-coil region (28 a.a.) from where it dimerizes (figure 2.2) [Browning et al. 2000, Browning and Hackney 2005]. It was first found because it produced a tip elongation aberrant phenotype similar to Tea1 in *S. pombe* [Verde et al. 1995] and later identified as a *Klp4* motor protein [Browning et al. 2000].

In the absence of any other binding partner Tea2 can only perform walks on the mi-

cro-tubule lattice at low ionic strengths. In this case, the average speed is $4.8 \pm 0.3 \mu\text{m} \cdot \text{min}^{-1}$, about a factor of two slower than in the presence of Mal3 and Tip1 ($9.8 \pm 2.9 \mu\text{m} \cdot \text{min}^{-1}$) [Bieling et al. 2007]. This is in agreement with the observation that Mal3 stimulates the ATPase activity of Tea2 [Browning and Hackney 2005].

2

TIP1 TRANSPORT

As mentioned above, under physiological salt conditions, Tea2 cannot processively walk along microtubules autonomously. After several studies *in vivo* which identified multiple Tea2 binding partners [Brunner and Nurse 2000, Browning et al. 2003, Busch and Brunner 2004], Bieling et al. 2007 reconstituted the minimal system of Tea2-based protein transport *in vitro* with purified proteins. The authors showed that Mal3 and protein Tip1 were necessary and sufficient for Tea2 to become processive. Interestingly, it is via interaction with Tip1, and not Tea2, that the endogenous *S. pombe* polarity factor Tea1 travels towards the microtubule plus end [Feierbach et al. 2004].

In the presence of Mal3, Tea2 and Tip1 stably bind to each other and co-migrate along the microtubule lattice with velocities around $9 \mu\text{m} \cdot \text{min}^{-1}$ (figure 2.1c, [Bieling et al. 2007]). This is nearly 10 fold faster than microtubule growth under the same *in vitro* conditions. The average run length, which is the distance travelled on the microtubule before detachment, is around $1 \mu\text{m}$. Moreover, Tea2-Tip1 accumulate at higher concentrations at the growing microtubule plus end than on the lattice. Although it has been shown that Mal3 is required for processivity of the complex (figure 2.4 a), its interaction with the Tea2-Tip1 complex is transient, as observed from its short run length on the microtubule ($0.29 \pm 0.01 \mu\text{m}$ [Bieling et al. 2007]).

Bieling et al. 2007 answered many questions about Mal3-Tea2-Tip1 transport. However, it is not yet well understood how the three proteins interact. Figure 2.2 shows a schematic of the known interactions between the proteins.

Mal3 and Tea2 have two weak interactions. The primary interaction occurs between the EB1 domain of Mal3 and the *Nte* domain of Tea2. The secondary interaction is weaker and occurs via the motor domain. Experiments by Browning and Hackney 2005 suggested that Mal3 and Tea2 mutually recruit each other to the microtubule, rather than compete.

Tip1 is a dimerizing protein containing a Cap-Gly domain at its N-terminus, a serine-rich region, a long coiled-coil region and a metal binding site (ZnF domain) at its C-terminus (figure 2.2). Tip1 weakly interacts with the EB domain of Mal3 via the Cap-Gly domain [Busch and Brunner 2004]. Moreover, this domain together with the serine rich domain can interact with the EEY/F hook on alpha-tubulin [Weisbrich et al. 2007]. Nevertheless, those two binding sites are not sufficient for Tip1 to tip-track growing microtubules by hitch-hiking on Mal3 [Bieling et al. 2007]. It is interesting to note that the human homologue of Tip1, CLIP-170, which is a much larger protein (162KDa) and contains an extra Cap-Gly domain at the N-terminus, can tip-track growing microtubules with a fast turnover by hitch-hiking on EB1 [Bieling et al. 2008a, Dragestein et al. 2008].

Tip1 forms a stable complex with Tea2 via an unknown interaction at the coiled-coil regions of both proteins [Busch et al. 2004, Browning and Hackney 2005, Bieling et al. 2007]. Although as a complex, Tea2-Tip1 can bind to the microtubule via the motor do-

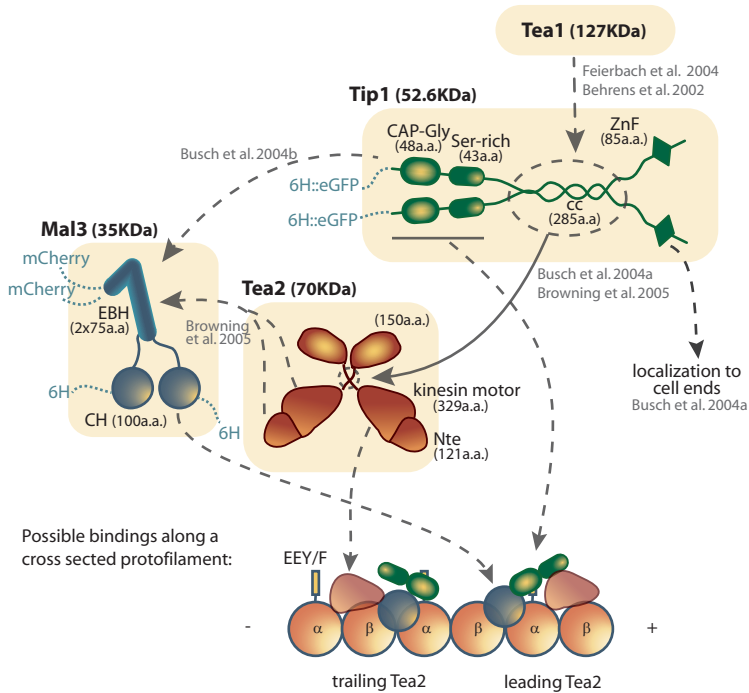


Figure 2.2: **Interactions between Tip1, Tea2 and Mal3.** Schematic of protein domains and their interactions. Dark lines represent unstructured or coiled-coil domains. Dashed arrows represent weak interactions between domains. Continuous lines represent strong interactions. For our *in vitro* assays, we have fused functional domains, indicated with dotted blue lines. They include the histidine tags (6H) used for protein binding to the biomimetic cortices in chapters 3-7 and the fluorophores eGFP and mCherry. The configuration of the three proteins on the microtubule lattice is not known. The cartoon portrays two possible bindings of all the protein domains to a microtubule protofilament section: one where Tea2 leads towards walking direction, and another one it trails.

main and the Cap-Gly and Serine-rich domains, they still require Mal3 to become processive (figure 2.4 a). Finally, the C-terminus of Tip1, containing a metal binding site, is not necessary for tip tracking but constructs with this terminus deleted show less Tip1 accumulation at microtubule growing ends and no accumulation at cell poles [Brunner and Nurse 2000, Busch et al. 2004].

The main known function of Tip1 in *S. pombe* is to recruit Tea1 to microtubule tips for subsequent deposition of the protein complex at the cell poles (see chapter 1, figure 1.8 [Behrens and Nurse 2002, Feierbach et al. 2004]).

2.3. TEA2 PRODUCES GLIDING OF MICROTUBULES IN THE ABSENCE OF MAL3 AND TIP1

We observed that Tea2 alone aspecifically bound to a glass slide produces microtubule gliding at normal ionic strength (50 mM KCl MRB80). Figure 2.3 b shows the maximum projection over a time lapse movie of a gliding assay using $\sim 3 \mu\text{m}$ long GMPCPP microtubule seeds.

2

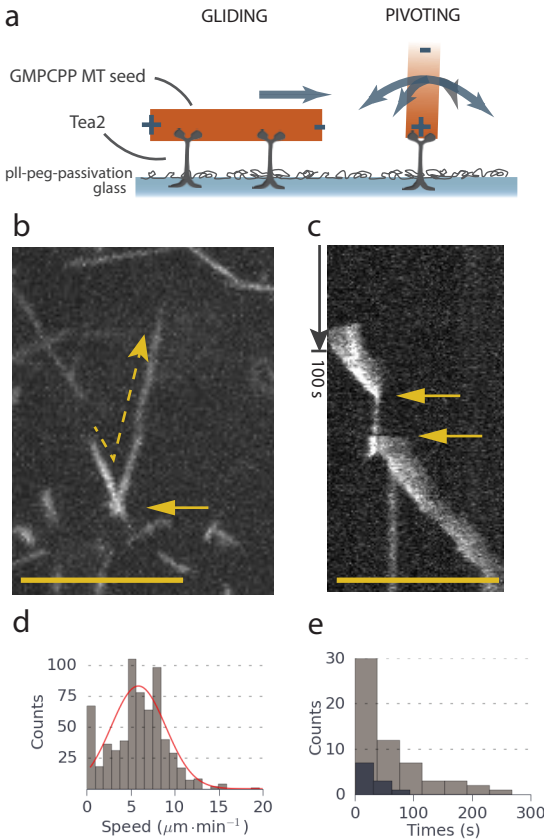


Figure 2.3: **Gliding of GMPCPP seeds by Tea2.** (a) Schematic of the gliding assay. (b) Maximum projection of a 5 min time-lapse movie of gliding GMPCPP seeds imaged with Spinning Disk Fluorescence Microscopy. Scale bar $10 \mu\text{m}$. Continuous arrow points at a pivoting event. (c) Kymograph along the path of the dashed arrow in (b). Scale bar $10 \mu\text{m}$. Arrows indicate the start and end of the pivoting event, where only the tip of the microtubule is in focus. (d) Time weighted histogram of gliding speeds and normal distribution fit (including all the data points). (e) Histograms of dwell times in pivoting states for seeds that completely detach from the surface, darker bars, and seeds that re-attach to continue gliding on the surface, brighter bars.

Gliding trajectories were short, with pauses, and sharp changes of direction. Measured mean gliding speed yielded $5.9 \pm 3.1 \mu\text{m}\cdot\text{min}^{-1}$ (figure 2.3 d), comparable to the motility assay of Tea2 in the absence of Mal3 and Tip1 from Bieling et al. 2007 ($4.8 \pm 0.3 \mu\text{m}\cdot\text{min}^{-1}$).

We observed that before changing direction, microtubules remained anchored for some seconds with the rear end stuck to the surface (presumably the plus end held by a motor) and the other end fluctuating out of focus. We conclude that the density of motors on the surface was low and therefore, seeds would often remain attached by only one motor in an 'end-on' configuration (figure 2.3 a right). We call this a *pivoting* state. Figure 2.3 c shows the kymograph along the trajectory of the seed indicated by the dashed

arrow in figure 2.3 b. In 11 out of 69 pivoting events (16%) the seeds eventually detached from the cover-slip surface. In the other cases, the seed restarted gliding in a new direction (the kymograph of figure 2.3 c is an example of such a trajectory). Seed detachment was only observed during pivoting events.

We estimated the pivoting dwell time by taking the total time of measured pivoting events, divided by the times we saw dissociation (11 times) gives $K_{\text{off}} = 0.0029 \text{ s}^{-1}$. This value corresponds to the dwell time of a Tea2 motor attached in an 'end-on' configuration.

It should be noted that similar pivoting events had been reported before for Tea2-based gliding of axonemes. In that case, addition of high concentrations of Mal3 to the system promoted those events as well as axoneme detachment from the surface [Brown-ing and Hackney 2005].

2.4. MAL3-DEPENDENT RECRUITMENT OF TEA2-TIP1 TO THE MICROTUBULE AND POSSIBLE CLUSTER FORMATION

We investigated the Mal3-dependent recruitment of Tea2-Tip1 complexes to the microtubule. For this, we conducted the plus-end tracking assay of Bieling et al. 2007 at different Mal3 concentrations. We grew dynamic microtubules from biotinylated GM-PCPP seeds bound to the cover-slip surface by biotin-streptavidin linkages. His-tagged eGFP::Tip1 trajectories on microtubules were observed with time lapse imaging using TIRF Microscopy (figure 2.4).

In previous exploratory experiments, we observed that high Tip1:Tea2 ratios produced higher signal of 6H::eGFP::Tip1 at the microtubule plus ends. This led us to the hypothesis that a single Tea2 could 'carry' several Tip1 proteins (data not shown). Therefore, we decided focus our analysis on when there is an excess of Tip1 proteins (150 nM Tip1, 10 nM Tea2, and 0-200 nM Mal3).

Figure 2.4 a shows 6H::eGFP::Tip1 kymographs for different assays. In agreement with Bieling et al. 2007, we observed almost no Tea2-Tip1 binding along the microtubule in the absence of Mal3 (figure 2.4 a). Addition of Mal3 caused Tea2-Tip1 recruitment at the microtubule lattice and at the growing plus end. However, recruitment was not linear with Mal3 concentration (figure 2.5). Between 10 and 100 nM, Mal3 caused a non-linear increase on the 6H::eGFP::Tip1 signal at the microtubule lattice and tip. At 200 nM Mal3, the signal decreased slightly. This observed decrease may be due to saturation of Mal3 binding at the microtubule tip.

According to the literature, Mal3 tip saturation is achieved at around 100-200 nM Mal3 and lattice saturation at around 500 nM [Munteanu, 2008, Maurer et al. 2011]. In our hands, Mal3::mCherry signal at the microtubule lattice and tip in the presence of Tea2 and 6H::eGFP::Tip1 was higher at 200 nM than 100 nM (figure 2.5 b). This variations may be due to different sample preparations, therefore repeated assays should be performed to discern whether samples at 200 nM Mal3 display less 6H::eGFP::Tip1 accumulation at the microtubule tip than 100 nM Mal3 samples.

We also looked at single Tea2-mediated Tip1 walks on the microtubule lattice. We defined a trace as a Tip1 walk observed in a kymograph along the microtubule from the

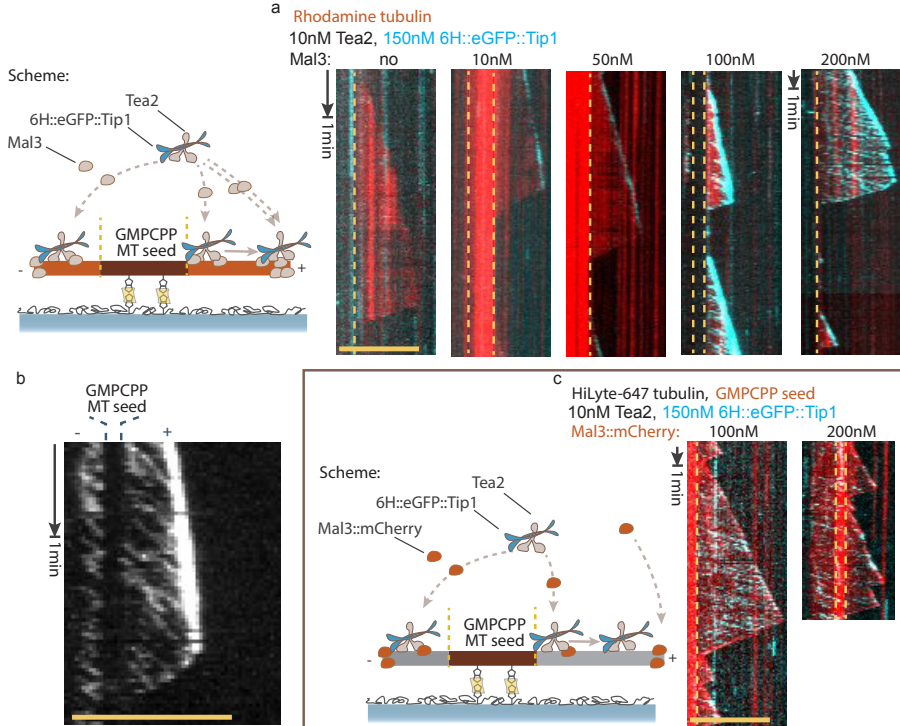


Figure 2.4: **Mal3 dependent recruitment of Tea2-Tip1.** (a) Kymographs of dynamic microtubules with 6H::eGFP::Tip1, Tea2 and Mal3 at the stated protein concentrations. The GMPCPP seed in the samples of 10 and 50nM Mal3 is labelled with rhodamine tubulin with higher ratio of fluorescent tubulin than the free tubulin, therefore it appears brighter. For the other samples, the GMPCPP seed was labelled with HiLyte-647 tubulin, not shown in the figure. (b) Close-up of the 6H::eGFP::Tip1 signal for 100nM 6H::eGFP::Tip1, 10nM Tea2 and 100nM Mal3. (c) Kymograph of 6H::eGFP::Tip1 and Mal3::mCherry in the presence of Tea2. The dashed line indicates the boundary between the GMPCPP seed (labelled with Rhodamine tubulin) and the GTP/GDP lattice. Scale bars 5 μm .

signal appearance to its disappearance. We measured the average intensity of such a trace on a kymograph (grey line in figure 2.5) and the range between the lowest and the highest mean intensities among the traces (yellow area). Intensity fluctuations of such a trace were not quantified. Interestingly all traces from the samples of 100 and 200 nM Mal3, were more intense than any trace in the samples at 10 and 50 nM Mal3 (lower side of the yellow area in figure 2.5 a). This means that every trace in the samples of 100 and 200 nM Mal3 had more Tip1 molecules than in the lower amount of Mal3 samples. The absence of low intensity traces, suggests that multiple Tip1 molecules co-migrate, presumably held together by a lower amount of Mal3 and Tea2 molecules.

For all Mal3 concentrations studied, Tea2-Tip1 showed nearly no binding to the GMPCPP microtubule seed (figure 2.4 b). This is consistent with a Mal3-dependent recruitment to the microtubule, since Mal3 has very low affinity for GMPCPP lattices as ob-

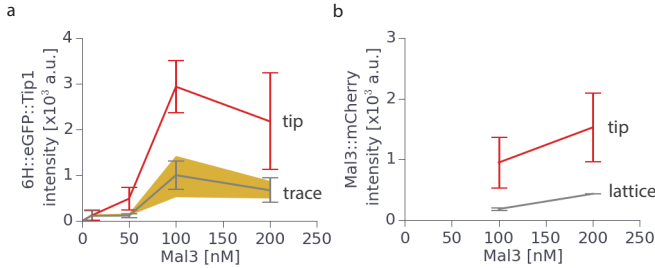


Figure 2.5: **Tip1 recruitment to microtubule lattices.** (a) 6H::eGFP::Tip1 mean fluorescence intensities at the tip of the growing microtubules (red) and on the lattice trajectories (grey). The grey data points indicate the average intensity value among all the pixels identified as a Tea2-Tip1 trace. The yellow area indicates the range between the average intensities of the least and the most intense trace. (b) Mal3::mCherry mean fluorescence intensity at tip and the lattice of the microtubule in the presence of 150 nM 6H::eGFP::Tip1 and 10 nM Tea2.

served in Maurer et al. 2011 and our own experiments with Mal3::mCherry (data not shown). Tea2-Tip1 complexes coming from the minus-end detached from the microtubule when encountering the GMPCPP seed (figure 2.4 b). This suggests that Mal3 is not only required for recruitment of complexes to the microtubule, but also for keeping them bound to the microtubule.

In assays with Mal3::mCherry, the 6H::eGFP::Tip1 signal at the microtubule was highly reduced (figure 2.4c). Kymographs from these assays displayed similar amounts of 6H::eGFP::Tip1 lattice traces, but with lower intensities than the ones from unlabelled Mal3 assays. His-tagged eGFP::Tip1 accumulation at the microtubule tip was caused mostly by lattice arrival instead of recruitment from the reservoir. Mal3::mCherry covered the whole microtubule with an enrichment at the plus end. Therefore, Mal3::mCherry can recruit 6H::eGFP::Tip1-Tea2 complexes at the lattice but not at the microtubule tip. We hypothesize that the two fluorophores fused in Mal3 and Tip1 interfere slightly in the binding between the two proteins, but without affecting their native bindings of each protein with Tea2 and the microtubule. Then, Mal3-Tip1 interaction is required for tip recruitment of Tea2-Tip1 complexes from the reservoir but not for lattice recruitment, for which Mal3-Tea2 interaction is then sufficient. This suggests that Mal3 can bind in two different configurations with Tip1 and Tea2, that are sensitive to the microtubule nucleotide state, characterized by different lattice compaction.

TEA2-TIP1 COMPLEX DYNAMICS

We wondered whether Tea2-Tip1 dynamics are affected by Mal3 in a concentration dependent manner. We measured the Tea2-Tip1 run length, velocity, and dissociation constant (inverse of the time of a run) by manual tracing of 6H::eGFP::Tip1 trajectories on kymographs of microtubules grown in the presence of untagged Mal3 (table 2.1). It should be noted that for kymographs with a high density of traces it is often not possible to determine where a trace starts and where it finishes (figure 2.6 a). Therefore, while velocities can be measured relatively accurately, parameters like the run length, or the time

of a run are much less accurate.

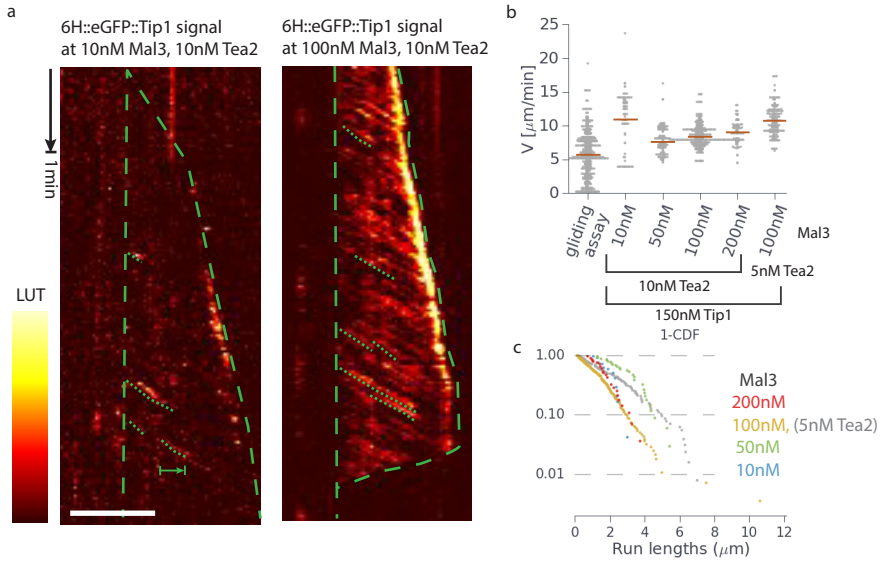


Figure 2.6: **6H::eGFP::Tip1 traces on growing microtubules and their dynamics.** (a) Kymographs of 6H::eGFP::Tip1 signal on growing microtubules at the stated protein concentrations. Green dashed lines indicate the GMPCPP seed and the growing tip. Dotted green lines indicate some Tea2-Tip1 traces with clear start and end. The arrow indicates the run length of a trace. Scale bar $5 \mu\text{m}$. (b) Histograms of Tea2-Tip1 complexes velocities. (c) Run length distributions in terms of 1-*cumulative distribution function*.

Tea2-Tip1 velocities were similar for all the samples (figure 2.6, table 2.1).

The expected run length distribution for a motor unbinding from the microtubule by a single event process, is an exponential decay. This distribution can be easily identified by plotting the 1-*cumulative distribution function* of all the observed run length times, which should exhibit a straight decreasing line in a logarithmic plot.

We only obtained a clear exponential decay for the measurements at 100nM Mal3, which contain the highest amount of data points. These measurements yielded an average run length of $1.51 \pm 0.44 \mu\text{m}$ for 10 nM Tea2 and $2.3 \pm 0.19 \mu\text{m}$ for 5 nM Tea2. The reason behind the other measurements not displaying an exponential distribution can come from the low amount of data points, miscount of short events due to similarity with the background noise signal, or Tea2-Tip1 detachment from the microtubule being caused by more than one event. This last case could correspond to, for example, two motors being linked together, therefore, complete detachment of the complex requires detachment of both motors. Given the amount of data points and the resolution of our measurements, we cannot determine that this is the case and we shall regard the measurements at 100 nM Mal3 as the most accurate. Nevertheless, it would be interesting to explore those parameters with data acquisition at higher time lapse rate.

The mean run lengths obtained are higher than the previously reported ones for three

Tea2	Tip1	150nM			
	Mal3	10nM	50nM	100nM	200nM
5nM	$\ell_r \pm \text{STD}$	-	-	2.30 ± 0.19	-
10nM	$[\mu\text{m}]$	1.95 ± 0.53	3.0 ± 1.2	1.51 ± 0.44	1.78 ± 0.79
5nM	$\omega_d \pm \text{STD}$	-	-	0.078 ± 0.017	-
10nM	$[\text{s}^{-1}]$	0.121 ± 0.075	0.064 ± 0.041	0.078 ± 0.054	0.098 ± 0.041
5nM	$v \pm \text{STD}$	-	-	10.8 ± 2.1	-
10nM	$[\mu\text{m} \cdot \text{min}^{-1}]$	11.0 ± 4.2	7.7 ± 2.0	8.4 ± 1.5	9.0 ± 1.7
5nM	$v_{\text{MT}} \pm \text{STD}$	-	-	1.15 ± 0.53	-
10nM	$[\mu\text{m} \cdot \text{min}^{-1}]$	1.03 ± 0.64	1.41 ± 0.60	0.86 ± 0.49	0.71 ± 0.37

Table 2.1: **Dynamic parameters measured from 6H::eGFP::Tip1 traces on kymographs.** Cells without a value, correspond to assays not performed. Histograms of the velocities can be found in figure 2.6 b. The *run lengths* and dissociation constants were only measured for clear distinguishable traces. The data presented corresponds to 22, 32, 278 and 27 traces for the samples of 10nM Tea2, and 10, 50, 100, and 200nM Mal3 respectively. For the sample at 5nM Tea2, 47 traces were used.

times lower Tip1 concentration (1 μm , for 100nM Mal3, 50nM Tip1, and 8nM Tea2 [Bieling et al. 2007]). This, could be due to different measurement conditions such as temperature (26°C in our assays versus 30°C in Bieling et al. 2007) or an effect of the higher Tip1 concentration.

2.5. TEA2-TIP1 TRANSFER BETWEEN MICROTUBULES

We found that at high Tip1 densities on microtubules (200 nM Mal3, 10 nM Tea2 and 150 nM 6H::eGFP::Tip1) apparent Tea2-Tip1 clusters could be transferred from a microtubule plus end to another microtubule lattice. Figures 2.7 a and b show two clear transfers. In these cases, the *donor* microtubule stayed connected to the *acceptor* microtubule for several minutes by a slowly advancing high density area of Tip1 proteins.

Kymographs along the *acceptor* microtubule show how the large amount of proteins transferred redistributed on the GDP or GMPCPP microtubule lattice (figure 2.7 c). After the transfer onto a GDP lattice (figure 2.7 c), three clear domains of different protein densities and velocities appeared.

- **Domain *i* of high density:** This corresponds to the location where particles were transferred. It had the slowest velocity of all the three domains, with $1.7 \pm 0.6 \mu\text{m} \cdot \text{min}^{-1}$ that lasted a few minutes until the domain started spreading. Figure 2.7 d shows the width of the domain (cyan) and how the position of the mean (location of the centre of mass) deviated from the mode (location of the highest density) of the particle distribution as the spreading started. This plot shows that this domain started spreading ~ 100 seconds after the start of protein transfer, and ~ 50 seconds prior release of the *donor* microtubule (detachment).
- **Domain *ii* of intermediate density:** This domain consists of particles which escaped domain *i*. It had a lower density, and particles moved faster than in domain *i*, $4.3 \pm 1.2 \mu\text{m} \cdot \text{min}^{-1}$.

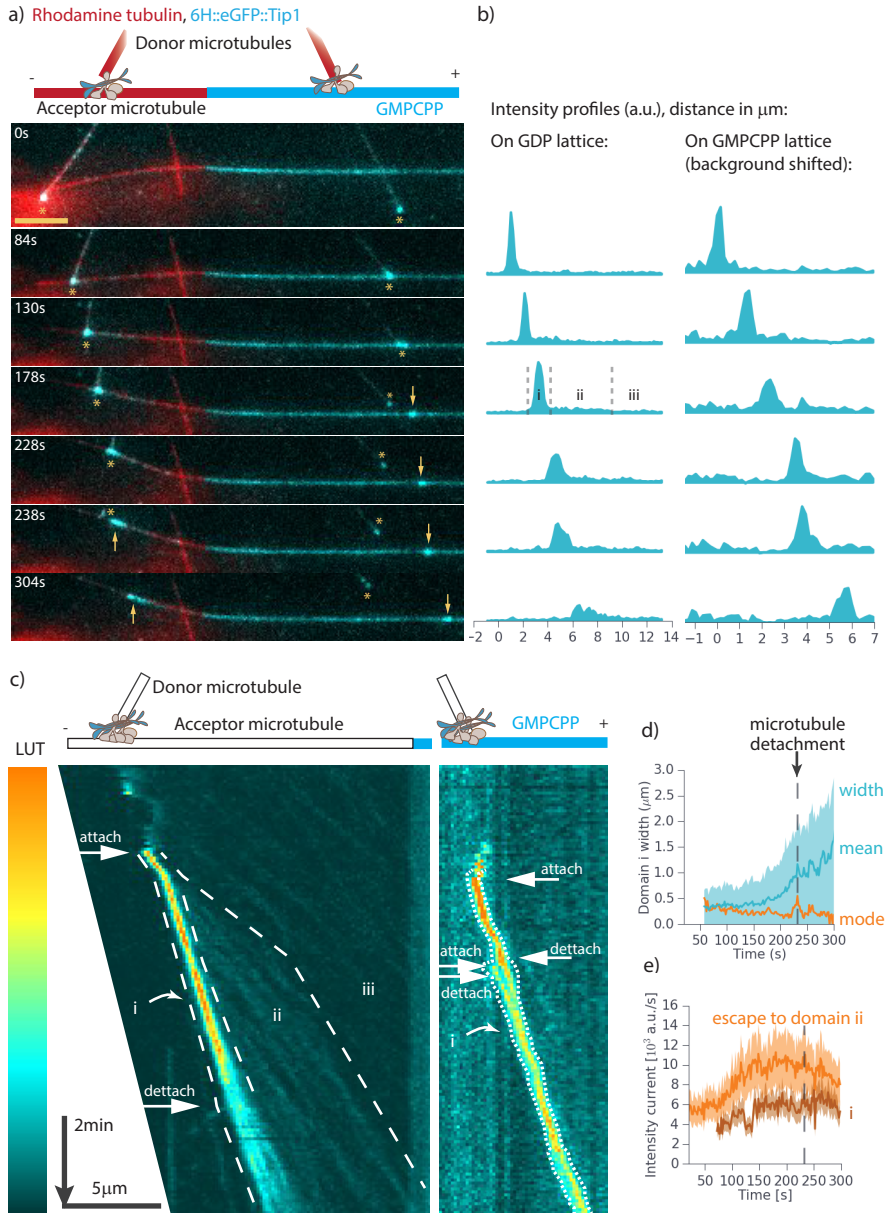


Figure 2.7: **Transfer of Tea2-Tip from a microtubule plus end to a microtubule lattice.** (a) Spinning disk fluorescent snapshots of 6H::eGFP::Tip1 steering a microtubule tip along another microtubule followed by protein transfer. GMPCPP biotinylated seeds appear also in cyan (HiLyte-488 tubulin). Asterisks indicate the plus ends of the *donor* microtubules and arrows indicate transferred 6H::eGFP::Tip1. (b) 6H::eGFP::Tip1 intensity profiles. (c) 6H::eGFP::Tip1 kymographs along the *acceptor* microtubule for the two shown transfers. LUT has been stretched for each image to better visualize intensity changes. White lines indicate the boundaries between different 6H::eGFP::Tip1 density domains formed. Arrows indicate the instants of clear microtubule attachment and detachment. (d) Fitting of a skewed Gaussian on *domain i*. (e) Intensity current of domains *i* and *ii* in c left.

- **Domain *iii* of low density:** This domain corresponds to a nearly unperturbed density of particles on a microtubule lattice. Particle velocities were faster than in the other two domains, $5.4 \pm 1.2 \mu\text{m}\cdot\text{min}^{-1}$, however, they were still lower than previously measured for a sample at this protein concentration ($9.0 \pm 1.7 \mu\text{m}\cdot\text{s}^{-1}$, table 2.1). Some of the Tip1 traces appeared during the very short contacts of the *donor* and the *acceptor* microtubules, before clear attachment of both. These transfers could be the reason behind the observed higher density of lower speed of this domain with respect to an unperturbed microtubule. They further indicate that Tea2-Tip1 transfer from one microtubule to another can occur in less than 5 seconds (frame rate), as no clear microtubule attachment is observed.

The high density domain *i* can be understood as a local jam of particles caused by a local sudden increase of particle density outside of equilibrium [Lighthill and Whitham 1955, Kolomeisky et al. 1998]. Since particles have a restricted space on the microtubule lattice, when most of the sites are occupied, motors, that do not walk synchronously, interfere with each other. Therefore, an increase in particle density causes a slow down of particle velocity, similar to observations in jams at microtubule plus ends [Leduc et al. 2012].

The motor at the leading edge of domain *i* can walk at its normal speed since it has no particles in front, and therefore escape domain *i* (figure 2.8 a). With a particle escaping, domain *i* shrinks by one site and the next particle can then in turn escape the domain. Particles escaping domain *i* cause an increment in the already existing particle density, and domain *ii* emerges. The high particle density difference between domains *i* and *ii* is termed domain wall.

One can define the current of particles in a domain by the flow of particles in that domain. This corresponds to the sum of all the particles in the domain times their velocities. If there are no particles entering or exiting the domain, the current of a domain remains constant and changes in the particle velocities would be linked to the domain size. In our case, particles coming from the *donor* microtubule enter domain *i* producing a current increase. In the same way, particles escaping domain *i* and entering domain *ii* produce an increase in the particle current of domain *ii*.

In order to determine the transfer of proteins from one microtubule to the other and from domains *i* to *ii*, we defined the intensity current over a certain microtubule length as the integral of the fluorescent signal over all the pixels of the considered length multiplied by the average velocity of particles. We calculated the time evolution of the intensity currents at domain *i* and at 1 micron right of domain *i* (escape to domain *ii*). Figure 2.7 e shows that the intensity currents of both domains increased from the instant of microtubule attachment up to around time 150 s, when they reached a plateau. This, indicates that, during this time, there was a continuous transfer of proteins from the *donor* microtubule to domain *i*, and from domains *i* to *ii*. Once the plateau value was reached, i.e. transfer of proteins from the *donor* microtubule stopped, domain *i* started spreading. Microtubule detachment occurred around 100 seconds after finishing the protein transfer.

It is interesting to wonder why domain *i* did not expand during the first seconds of transfer and remained as a high density compact domain. There could be different rea-

sons. Firstly, the particles could remain bound to the *donor* microtubule plus end. Alternatively, particles might interact to each other and have some transient bindings that limit particle escape.

2

Domain *ii* expanded up to $\sim 5 \mu\text{m}$. This is around 2 times larger than the mean run length of Tea2-Tip1 particles ($< 3 \mu\text{m}$, table 2.1). Therefore, particles escaping domain *i* were more processive than average.

We also observed transfer of particles to a GMPCPP lattice (figure 2.7). This finding is surprising since under normal conditions Tea2-Tip1 particles detached from GMPCPP lattices (2.4 b). However, in this case, the transferred high density domain *i* processively advanced even after the *donor* microtubule plus end detached from it. Advancing speed was the same as domain *i* on GDP lattices, $1.71 \pm 0.42 \mu\text{m} \cdot \text{min}^{-1}$.

In this case, domain *i* kept a relatively constant width with mean of $0.83 \mu\text{m}$ and STD of $0.23 \mu\text{m}$. Due to the fact that the GMPCPP lattice was labelled with the same fluorophore wavelengths as Tip1, it is difficult to accurately determine the current in domains *i* and *ii*. However, as observed in the kymograph of figure 2.7 c nearly no protein seem to have escaped from domain *i*, neither to the leading microtubule lattice, nor to the cytoplasm since the moment of microtubule detachment to the time-lapse end.

Both transfers observed exhibit a domain of high density 6H::eGFP::Tip1 particles that remains compact for a few minutes. Such domain does not behave as a Kolomeisky domain, as in that case, the domain should spread and decrease density. We hypothesize that the proteins form clusters aided by Mal3 bindings containing several Tea2 and Tip1 molecules. Such clusters travel as a whole on the microtubule lattice, even at GMPCPP lattices (where Mal3 has very low affinity). Clusters could attain a higher processivity than stoichiometric Tea2-Tip1 oligomers by disposing of several microtubule binding sites (figure 2.8 b). Moreover, the fact that such high densities of 6H::eGFP::Tip1 are not found in the assays containing Mal3 with a fused mCherry on its C-terminal, indicate that Mal3 interaction with Tip1 is needed for clusters to emerge. Being that the case, a fraction of Mal3 would be transported by the clusters.

Similar guidance of a microtubule plus end on a microtubule lattice have been observed recently *in vitro* for engineered versions of kinesin-2 with an added affinity for EB1 or directly fused to it [Doodhi et al. 2014, Chen et al. 2014]. In those cases, EB1 is required to keep the motor attached to the *donor* microtubule plus end. However, in those cases, clustering of proteins did not seem to occur. Therefore, clustering is not needed for steering per se, at least in other systems.

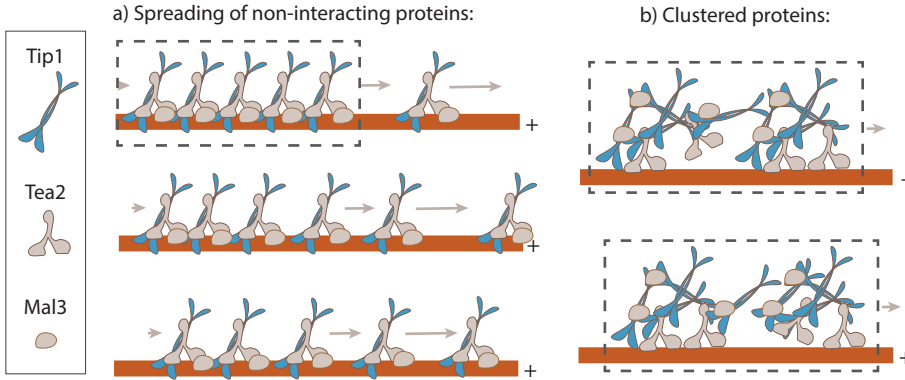


Figure 2.8: **Models for high densities of Tip1 on the microtubule.** (a) Case of non-interacting stoichiometric Tea2-Tip1 oligomers. An initial high density domain spreads out as oligomers at the front of the domain can scape at faster velocities than the ones inside the domain. (b) Case of cluster formation binding together multiple Tea2 and Tip1 molecules, aided by Mal3. The cluster remains compact and its processivity is higher than for single oligomers since extra microtubule bindings maintain detaching Tea2 being transported by the cluster.

2.6. MOTOR DISTRIBUTIONS ON MICROTUBULES

In the previous section, we observed that complexes of Tea2-Tip1 coming from the lattice accumulate at growing microtubule plus ends. This property resembles traffic jams as has been observed *in vitro* with highly processive kinesins [Leduc et al. 2012]. In this section we describe those jams by comparing our experimental data to an existing model on jamming, for static microtubules and an extension of these models for a growing microtubule.

Motor organization on microtubules has been described previously by the Parmeggiani model [Parmeggiani et al. 2003, Leduc et al. 2012]. This model combines *Langmuir kinetics* on a finite 1D lattice (stochastic binding and unbinding of particles from a reservoir) with a totally asymmetric simple exclusion process (TASEP), where particles can move in one direction to unoccupied lattice sites [MacDonald et al. 1968]. Since the lattice is finite, boundary effects including traffic jams at the last lattice sites and depletion of particles at the first lattice sites appear.

We will first describe the existing model. Then, expand it to the case of a growing 1D lattice, and compare it to our experimental data.

PARMEGGIANI MODEL FOR A SEMI-INFINITE 1D LATTICE

In this model, the microtubule is taken as a one-dimensional lattice where particles (motor proteins) from a reservoir can associate with empty lattice sites and dissociate with rates ω_a and ω_d respectively (figure 2.9 a). Particles on the lattice move in one direction with hopping rate u if the next site is empty. At the last site of the lattice (microtubule plus end), particles can detach with rate β , which can be different from ω_d .

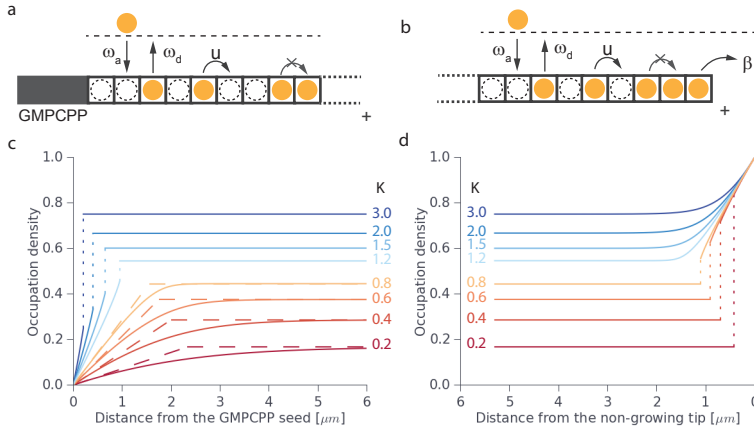


Figure 2.9: **TASEP with Langmuir kinetics model.** Model for particles hopping on a semi-infinite 1D lattice with excluded volumes. **(a)** Model applied to a lattice starting at the microtubule GMPCPP seed, and **(b)** at the microtubule plus end. **(c)** Occupation density profile of particles from the GMPCPP seed. **(d)** Occupation density profile from the non-growing microtubule plus end. Continuous lines correspond to the analytical solution (equations 2.27); dashed lines correspond to the linearised approximations (equations 2.17 and 2.18); and dotted lines correspond to the discontinuous jump in the particle density, *domain wall*. Parameters: $v = 8.4 \mu\text{ms}^{-1}$, $\omega_d = 0.05\text{s}^{-1}$, and variable $K \equiv \frac{\omega_a}{\omega_d}$.

Since a microtubule contains 13 protofilaments, adoption of the model supposes that motors do not hop from one protofilament to another and that the motors from adjacent protofilaments do not interact with each other except for body exclusion. This is the case for some kinesins [Ray et al. 1993, Schaap et al. 2011, Shibata et al. 2012]. However, other kinesins have been found to avoid obstacles by changing protofilament [Bormuth et al. 2012, Hoepflich et al. 2014, Buhel et al. 2015, Oriola et al. 2015]. We have no information about Tea2 regarding this point.

A typical *in vitro* assay allows us to restrict the study only to long microtubules. Then, the microtubule can be modelled as a semi-infinite 1D lattice, containing either a start (minus end) or an end (plus end) [Reese et al. 2011]. In our case, since Tea2-Tip1 particles in the presence of untagged Mal3 do not bind to GMPCPP lattices, a microtubule grown from a GMPCPP seed forms an ideal static start boundary between the GMPCPP and the GDP lattice.

Parmeggiani et al. showed that the equilibrium occupation density profile of particles on the lattice can be obtained analytically [Parmeggiani et al. 2003, Parmeggiani et al. 2004]. The equilibrium occupation density describes the probability of finding a particle at a certain location on the lattice. It depends on the association, dissociation and hopping rates of the particles. Figures 2.9 c and d show examples of occupation density profiles that the model predicts for different association constants, $K \equiv \frac{\omega_a}{\omega_d}$. The model predicts the following shapes:

- **Density profile from the GMPCPP seed:** For $K \leq 1$ the model predicts a density profile that increases nearly linearly with the distance from the boundary, *antenna*

profile, up to the *Langmuir isotherm* (ρ_{La}), where it is constant. The point of intersection between the two profiles is called the *wedge distance*.

However, for $K > 1$ the *antenna profile* does not catch up with the *Langmuir isotherm* and continuity of the current imposes a jump between the two regimes. This jump is termed *domain wall* (dashed lines in figure 2.9 c).

- **Density profile from the tip:** Interestingly, the Parmeggiani model has a *particle-hole* symmetry, i.e. it can be interpreted as particles hopping in one direction or holes hopping on the other. In this sense, the plus end can be understood as an *antenna* that collects holes that hop towards the minus end. Therefore, the occupation density exhibits a *wedge* profile for $K \geq 1$ and a *domain wall* for $K < 1$ (figure 2.9 d).

Note that in the Parmeggiani model, the microtubule plus end is defined by a single site with a different unbinding rate β . In the case of Tea2-Tip1 the tip could be defined as the extended region where Mal3 preferentially binds.

EXTENSION OF THE MODEL FOR A GROWING TIP

In our experiments, the microtubule plus end polymerises with average growth velocity v_{MT} . This is equivalent to addition of unoccupied lattice sites with rate $g = \frac{v_{MT}}{\epsilon}$, where ϵ corresponds to the distance between motor binding sites on the microtubule. We derived the analytical occupation density profile resulting from microtubule growth in an analogous way as in Reese et al. 2011 (see section 2.9). In this method, the profile is derived in the frame co-moving with the growing microtubule plus end, and all the particles experience an extra current equal to the microtubule growth speed in the opposite direction. Given the observations on our own data (discussed in the next section), we restricted the analysis to the case $K < 1$.

Analytical solutions of the equilibrium occupation density profiles for different microtubule growth velocities and dissociation constants at the tip, β , are plotted in figure 2.10 for $K = 0.5$. In this case, for a non-growing lattice the model predicts a traffic jam at the tip ~ 700 nm long. Addition of microtubule growth gradually reduces the length of the jam until there is no discontinuity in the occupation density profile.

Typical *in vitro* microtubule growth velocities (0.6 - $1.5 \mu\text{m}\cdot\text{min}^{-1}$) will still maintain the traffic jam, but reduce it by up to a factor of 2. In *S. pombe*, microtubules grow at ~ 2 - $4 \mu\text{m}\cdot\text{min}^{-1}$ [Behrens and Nurse 2002, Tran et al. 2001], therefore the jam could even disappear for $K = 0.5$. It is important to note here that we do not know the association and dissociation rates of Tip1 *in vivo*, which could vary from the ones measured *in vitro*.

Increase in the dissociation rate at the tip, β , linearly decreases the occupation at the tip and shifts the *domain wall* towards the tip (figure 2.10 b). At a critical dissociation rate, $\beta_c = \frac{v}{\epsilon} \rho_{La}$, the traffic jam at the tip disappears and the profile shows a single spike at the tip.

It is important to note that the possible traffic jam observed for these parameters has similar length to the GTP cap of a microtubule or the region where Mal3 preferentially binds. Therefore, proteins coming from the microtubule lattice may compete for

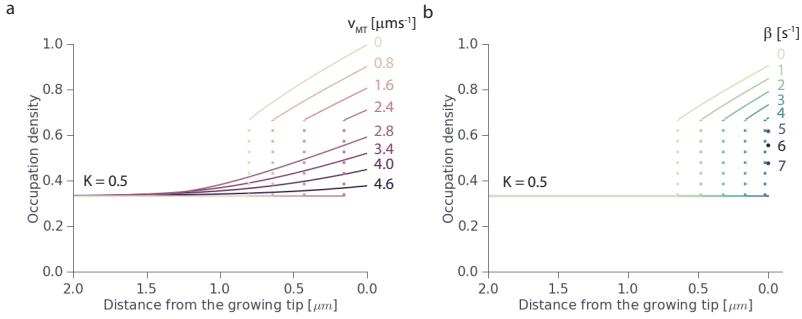


Figure 2.10: **Effect of microtubule growth and tip dissociation rate on the density profile at the tip.** Occupation density profiles from the analytical solution of the Parmeggiani model at the growing tip for (a) variable growth speed; (b) variable dissociation rate at the tip, β . Parameters: $v = 8.4 \mu\text{m}\cdot\text{s}^{-1}$, $K = 0.5$, $g = 0.8 \mu\text{m}\cdot\text{min}^{-1}$, and $\beta = 0.05$. For these conditions, the occupation density at the tip decreases linearly with β up to $\beta_c = 5.83$.

binding sites with proteins coming from solution due to the higher affinity of Mal3 in this region. However, since the GTP cap size fluctuates [Duellberg et al. 2016], protein jamming could help maintain a pull of Tea2-Tip1 complexes at the microtubule tip.

PROTEIN DENSITY PROFILES *in vitro*

We measured the average fluorescence intensity profile of 6H::eGFP::Tip1 in the presence of Tea2 and untagged Mal3 on microtubules as a function of distance from the GMPCPP seed and the growing microtubule plus end. If all Tea2-Tip1 particles have the same stoichiometry, and our fluorescence detection scales linearly with protein amounts, the fluorescence intensity measurement is, approximately proportional to the occupation density. Therefore, we can use the average fluorescence intensity as a proxy for the occupation density.

Indeed, intensity profiles at high concentrations of Tea2 and Mal3 samples proved very similar to the ones predicted by the Parmeggiani model. The examples in figure 2.11 display clear *antenna* and *Langmuir* regimes, as well as a big jump in intensity at the growing plus end which could be explained by a *domain wall*. This profile, as well as all the other obtained profiles, corresponds to $K < 1$. This means that, the *Langmuir isotherm* has less than half of the lattice sites occupied.

Figures 2.11 c and d show the average intensity profiles of the Mal3::mCherry signal. The profile from the seed only exhibits a *Langmuir isotherm* without *antenna profile*, as expected for non-asymmetrically hopping particles. Mal3::mCherry, however, displays a well known jump in the occupation density at the microtubule plus end. We note here that the width of the Mal3::mCherry and the 6H::eGFP::Tip1 signals are, within our resolution, the same (less than 500 nm). However, the peak intensities are inversely related, as mentioned before. Moreover, the signals of 6H::eGFP::Tip1 at the tip are much higher with respect to their respective lattice signals. Such increase in the 6H::eGFP::Tip1 signal is most likely due to jam contributions.

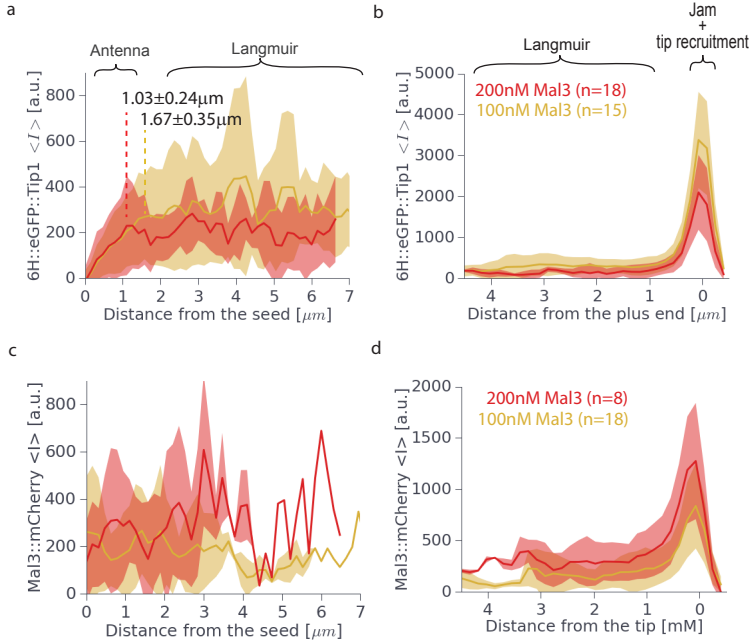


Figure 2.11: **Plus tips intensity profiles.** (a) Average 6H::eGFP::Tip1 intensity profiles from the seed, and (b) from the tip at 150nM 6H::eGFP::Tip1 in the presence of 10nM Tea2 and 100-200nM Mal3. The *wedge distances* in the *seed profile* obtained by linear regression fitting are indicated. (c) Average Mal3::mCherry intensity profiles from the seed, and (d) from the tip at 100-200nM Mal3::mCherry in the presence of 150nM 6H::eGFP::Tip1 and 10nM Tea2. Wide area corresponds to the standard deviations among n kymographs.

FITTING OF THE SEED PROFILES

We used the average 6H::eGFP::Tip1 intensity profile from the microtubule seed to extract dynamic properties of the Tea2-Tip1 complexes. The complete analytical solution gives a rather complex function of several parameters. Non-linear square fittings of the data to the analytical solution revealed that multiple combinations of parameters could lead to equally good fittings. This is because this profile can be roughly characterized by two parameters: the slope of the *antenna regime* and the *wedge distance* at which the profile switches to the *Langmuir isotherm*. Therefore a linearised solution was introduced by Reese et al. 2011. In this formulation, the *antenna profile* for $K < 1$ is given by

$$\rho(x) \approx \frac{\omega_a}{v} x \quad (2.1)$$

and the plateau value away from the boundaries is given by the *Langmuir isotherm* first described by Fowler 1929:

$$\rho_{La} = \frac{\omega_a}{\omega_a + \omega_d} = \frac{K}{1 + K}. \quad (2.2)$$

Then, the *wedge distance* follows

$$d_{\text{wedge}} \approx \frac{v}{\omega_a + \omega_d} = \frac{v}{\omega_d} \frac{1}{K + 1} = \ell_r \frac{1}{K + 1} \quad (2.3)$$

where ℓ_r is the mean run length of the particles. This expression can be written as

$$K = \frac{\ell_r - d_{wedge}}{d_{wedge}}. \quad (2.4)$$

Therefore, since $0 \leq K \leq 1$, the mean run length should fall in the interval $[d_{wedge}, 2d_{wedge}]$.

In this set of experiments, we do not dispose of a fluorescence calibration, therefore it is difficult to compare fluorescence intensity with density of particles. Alternatively, one could estimate the fluorescence intensity of a pixel when all the sites in that area are occupied by proteins. We used the maximum intensity observed at a microtubule tip as an estimate of the pixel fluorescence at full occupation. Pinning this value for the profiles at different concentrations, lead to kinetic rates differing by an order of magnitude. This could be explained by different samples exhibiting different fluorescence values at full occupancy, suggesting that different samples displayed a different stoichiometry of proteins.

On the other hand, the only parameter we can obtain without any independent fluorescence calibration, measurement of particle velocity, or the on and off rates, is the wedge distance. Linear fitting of the *seed profile* yielded *wedge distances* of $1.67 \pm 0.35 \mu\text{m}$ for the sample at 100 nM Mal3 and $1.03 \pm 0.24 \mu\text{m}$ for the sample at 200 nM Mal3. Both values are in agreement, within the error, with the run lengths measured by direct tracing on kymographs ($1.51 \pm 0.44 \mu\text{m}$ for the 100 nM Mal3 sample and $1.78 \pm 0.79 \mu\text{m}$ for the 200 nM Mal3 sample).

Using equation 2.4, with the previously measured values of the run length, the dissociation constant and therefore the association rate can be calculated. However, the errors are too big to confidently extract these values.

We see that Tip1 qualitatively behaves like Parmeggiani particles as its average fluorescence intensity profiles exhibit an *antenna regime* and a *Langmuir regime* of expected values. Our measurements between different samples are inconsistent to one another. We believe that, with a larger set of data and a fluorescence calibration, one could use the analysis introduced to extract dynamic particle rates at high protein concentrations. This measurements are very valuable since protein-protein interactions may affect their dynamics. On the other hand, it could be possible to determine whether Tip1 forms different stoichiometric associations with Tea2 at different Mal3 concentrations.

2.7. DISCUSSION

The end tracking systems composed of Tea2, Tip1 and Mal3 is a complex system involving multiple low affinity bindings between each of the proteins and the microtubule. This leads to complex dynamics of the three proteins on the microtubule. In this chapter we studied the recruitment of Tip1 to the microtubule and its dynamics with different types of analyses. The raw data used was limited, therefore all results obtained are not conclusive. Nevertheless, we hope to have pointed out key elements on how the three proteins may act together and set bases for future research.

By direct observation, we found that recruitment to the microtubule plus end requires an interaction between Mal3 and Tip1, different than the interaction produced for recruitment to GDP lattices. It would be interesting to test if ATP is required for this tip specific binding to occur. On the other hand, crystallographic data would be very valuable to determine whether the proteins have different conformations on the microtubule depending on the tubulin conformation state.

Direct kymograph observations showed that Mal3 is required for recruitment and processive walking of Tea2-Tip1 particles in a non-linear concentration manner. Trace intensity measurements and analysis of transfer of Tea2-Tip1 particles from one microtubule to another seem to support the hypothesis that a fraction of Mal3, Tea2, and Tip1 form clusters that travel along microtubules. These clusters would contain a larger amount of Tip1 molecules than Tea2. The size of these clusters furthermore seems to depend on the available concentration of Mal3, suggesting that Mal3 proteins form an integral part of them.

We hypothesise that these clusters display higher processivity than stoichiometric Tea2-Tip1 particles in an analogous way as multiple motors sharing a cargo [Klumpp and Lipowsky 2005]. Given that Mal3, Tea2, and Tip1 contain multiple weak bindings to each other and the microtubule such clusters could behave as little phase separated domains [Li et al. 2012].

In this chapter we have furthermore introduced a method to characterize motor dynamics by their distributions on microtubule lattices comparing theoretical results for TASEP particles. With proper fluorophore calibrations it can give an unbiased way to measure run length of motors as well as binding and unbinding rates to the microtubule in samples at high density of motors on the microtubule. We extended the model for the case of a growing microtubule. Since microtubule growth speed can affect considerably the extent of motor accumulation at microtubule plus ends, we think that such extension of the model is essential for future descriptions of motor distributions. It would be very useful to compare the model to simpler motors which do not require auxiliary proteins for processive walks.

2.8. METHODS

Some of the methods of this chapter will be used during the whole thesis.

PROTEIN PURIFICATION

- Kinesin Tea2 was expressed in *E. coli* and purified as in Bieling et al. 2007.

The following proteins were purified as in Maurer et al. 2011:

- 6H::TEV::Mal3::mCherry sequence was obtained by deleting the GFP sequence in 6his::Mal3::GFP (generous gift by Thomas Surrey, [Maurer et al. 2011]) and inserting the mCherry sequence (generous gift from Milena Lanzova and Tom Shimizu) between the *PacI* and *NotI* restrictions sites. In order to select for correct ligations, we further digested the final constructs with *NdeI* before transformation.
- 6H::TEV::eGFP::Tip1 was obtained as in Bieling et al. 2007 and the oligo duplex 5'-tccgcgggtgagaatcttcagggcgcc-3' containing a TEV recognition site was added between the his-tag and the eGFP (recognition sites *SapI* and *NcoI*).

SAMPLE PREPARATION

Standard flow cell preparation: Glass slides were cleaned by sonication of 10 min in water, Hellmanex[®], water, 70% ethanol sequentially. They were stored in 70% ethanol and sonicated for 10 minutes in water before use. Coverslips (Menzel Gläser, No.1 24x24 mm 170 μ m) were cleaned by base piranha (NH₄OH:H₂O₂ in 3:1 at 75°C) for 10 min and sonicated for 10 min in water. Flow cells were made by placing two cut 5 mm wide stripes of parafilm on the glass slides separated 5 mm and placing on top the glass slides. Then the parafilm was melted by placing the sample several seconds on a 100°C hot plate and gently pressing a bit on it with tweezers.

Microtubule buffer: The standard buffer used for microtubule growth is MRB80: 80 mM KPipes, 4 mM MgCl₂, 1 mM ethylene glycol tetraacetic acid (EGTA), pH 6.8. We used it for all the flow cell incubations, except when stated otherwise.

GMPCPP-stabilized microtubule seeds:

Spontaneous microtubule nucleation requires a minimum critical tubulin concentration. However, once a microtubule has nucleated, the critical concentration for elongation is lower. In *in vitro* assays it is common in the field to initiate nucleation from so called 'seeds' consisting of short microtubule pieces polymerized with the slowly hydrolysable GTP analogue GMPCPP. These seeds do not depolymerize at room temperature in the absence of tubulin in solution [Hyman et al. 1992].

In this thesis we used seeds containing 12% of fluorescently labelled tubulin while in a dynamic assay we normally use 4-5%. This allows to distinguish the seed from the rest of the microtubule. Moreover, the seeds can contain 18% of biotinylated tubulin. In this case, they can be attached to the bottom surface of the glass slide or the micro-well via biotin - streptavidin linkages.

Microtubule seeds are prepared by a polymerization - depolymerization - polymerization cycle with GMPCPP in MRB80 (this cycling is done to get rid of residual GTP).

The first polymerization step is performed by incubating a tubulin mix of biotinylated tubulin, fluorescently labeled and nonlabeled tubulin in a ratio 18:12:70 (total of 20 μM tubulin) with 1 mM GMPCPP at 37°C for 30 min. For non-biotinylated seeds the biotinylated tubulin is simply exchanged by non-labeled tubulin. The mix is then airfuged 5 min at 30 psi with a Airfugee[®] Air-driven ultracentrifuge (Beckman Coulter, USA) and the pellet is re-suspended in 80% of the initial volume and left on ice for 20 min to depolymerize the microtubules. Then, 1 mM GMPCPP is added to the mix and left for 30 min at 37°C to polymerize again. The seeds are then airfuged again, re-suspended in MRB80 with 10% glycerol and stored at 80°C. Thawed seeds can be kept at room temperature for a week.

Gliding assay: In a clean flow cell, 200 nM Tea2 in MRB80 was incubated for 10 min. Then passivated with 0.6 mg·ml⁻¹ κ -casein for 10 min, followed by Rhodamine labeled GMPCPP stabilized microtubule seeds. After 3-5 min, the gliding buffer containing 50 mM ATP, 0.4 mg·ml⁻¹ glucose oxidase, 50 mM glucose and 0.4 mg·ml⁻¹ κ -casein in MRB80 was added. Gliding was recorded with a IX81F-ZDC2 microscope (Olympus, Japan) with a **spinning disk confocal** head CSU-X1 (Yokogawa, Japan) using 60X and 100X oil immersion objectives and EmCCD camera iXon3 (Andor, UK). Excitation lasers 488 and 561 nm (Andor, UK) with 300 ms exposure of 561 nm laser at frame rate of 1.3 s where used.

Mal3-dependent recruitment of Tip1 and density profile assay: In a flow cell functionalized with 0.2 mg·ml⁻¹ PLL(20)-g[3.1]-PEG(2)/-PEG(3.4)-biotin(17.5%) (SUSOS AG), with a subsequent incubation of 0.1 mg·ml⁻¹ streptavidin, and further passivation with 1.2 mg·ml⁻¹ κ -casein, biotinylated GMPCPP *seeds* where incubated for 5 minutes. Then dynamic microtubules where grown from a mix containing 14.25 μM tubulin, 0.75 μM rhodamine tubulin, 50 mM KCl, 0.6 mg·ml⁻¹ κ -casein, 0.4 mg·ml⁻¹ glucose oxidase, 50 mM glucose, 0.1% methyl cellulose, 1 mM GTP, and 2 mM ATP in MRB80 and the variable stated concentrations of 6H::eGFP::Tip1, Mal3, and Tea2.

Fluorescence was recorded with a **TIRF microscope** (Nikon Eclipse Ti-E inverted microscope) equipped with an Apo TIRF 100x1.49 N.A. oil objective, a Perfect Focus System (PFS), a motorized TIRF illuminator (Roper Scientific, Tucson, AZ, USA) and a QuantEM:512SC EMCCD camera (Photometrics, Roper Scientific). Images were taken at 300 ms exposure for excitation lasers 491 nm (40 mW) Calypso (Cobolt) diode-pumped solid state laser, 561 nm (50 mW) Jive (Cobolt, Solna, Sweden), and 641 nm 28 mW Melles Griot laser (CVI Laser Optics & Melles Griot, Didam, Netherlands) every 2 to 5 s with the same power for all samples. The temperature was kept at 26°C with a house-made objective heater device.

Protein transfer assays were performed in microfabricated glass micro-wells (explained in detail in Chapter 3) with a 150 nM 6H::eGFP::Tip1, 10 nM Tea2 and 200 nM Mal3 and no imidazole. Transfers were recorded with spinning disk microscopy with 300 ms exposures of 561 nm and 488 nm lasers, at frame rate of every 2.0 s.

2.9. DATA ANALYSIS

GLIDING ASSAY:

Gliding speeds were calculated from kymographs following seed tracks with **ImageJ** (<https://fiji.sc/>). Speed counts were determined by the slope of relatively constant speed sections weighted over intervals of 5 frames (shortest event). Histogram binning was determined by Freedman-Diaconis rule ($2 \cdot \text{IQR} \cdot n^{-1/3}$ [Freedman and Diaconis 1981]). Mean and std values were obtained by fitting a Gaussian distribution with *scipy.stats.norm.fit* package of **Python 2.7** (<http://code.google.com/p/winpython/downloads/detail?name=WinPython-64bit-2.7.5.3.exe>). Dwell times were calculated from kymographs and fitted with *textitscipy.stats.expon.fit* package of **Python 2.7**.

DIRECT MEASUREMENT OF DYNAMIC PARAMETERS:

Microtubule velocities as well as 6H::eGFP::Tip1 velocities and run lengths were measured by manually tracing segmented lines on kymographs along the microtubules with **ImageJ** and later computation in a custom program in **Python 2.7** in the same way as for the gliding assay. Average intensities were measured on traces on the kymographs. The dissociation rate was measured as the inverse of the residence time.

PROTEIN TRANSFER ASSAY:

Kymographs were obtained by manually tracing a spline along the *acceptor* microtubule at each frame from a reference point at the non-moving seed. Splines were then straightened with the *Straighten* function of **Fiji** and concatenated with a custom **Python 2.7** program. Speeds were calculated as in *Mal3-dependent recruitment of Tip1 assay*. Domain currents were calculated by:

$$j_k(t) = \langle v(t) \rangle \sum_{\ell} I(t) \quad (2.5)$$

being ℓ the length of domain k . For domain ii , ℓ was taken not longer than a micron. Domains were defined manually, 2 pixels away from the its boundaries. Statistical parameters were obtained by least square minimization (package *scipy.optimize.leastsq* of **Python 2.7**) of the parameters A , x_0 , σ , and α from a *skew Gaussian distribution* at each time frame defined by:

$$f\left(\frac{x-x_0}{\sigma}\right) = 2A\phi\left(\frac{x-x_0}{\sigma}\right)\Phi\left(\alpha\frac{x-x_0}{\sigma}\right) \quad (2.6)$$

with

$$\phi(t) = \frac{1}{2\pi} e^{-\frac{t^2}{2}} \quad (2.7)$$

$$\Phi(t) = \int_{-\infty}^t \phi(t) dt = \frac{1}{2} \left[1 + \text{erf}\left(\frac{t}{\sqrt{2}}\right) \right] \quad (2.8)$$

where erf is the error function and A the amplitude. Standard deviation and skewness were also calculated directly from the cumulants of the data, however the result highly depended on definition of the length of domain i . Domain i width was estimated by a threshold of 0.1 on the *skew Gaussian distribution* fit and manually adjusted for high skewness frames to the biggest intensity drop position.

AVERAGE FLUORESCENCE INTENSITY PROFILES:

Calculation of the average intensity profile of 6H::eGFP-Tip1 was obtained by averaging intensity profiles within microtubules and between microtubules as a function of distance from either the GMPCPP seed of the growing tip. We obtained *maximum pixel intensity wide kymographs* as the kymograph along a microtubule, taking the maximum intensity pixel on the perpendicular axis to microtubule growth (functions *Straighten*, *Reslice* and *Z Project* from **ImageJ**) (kymograph of figure 2.12a). Background was measured by determining the average pixel intensity over a window time of 60 frames, i. e. morphological opening of a 60 pixels long line along the temporal axis of the kymograph (*mahotas.morph.open* and *pymorph.seline* packages of **Python 2.7**, figure 2.12b), and subtracted (figure 2.12c). The seed and tip positions were traced manually with **ImageJ** and saved as coordinates for latter use in **Python 2.7**. The density profile from the seed was calculated as the average intensity over time at each pixel as a function of distance from the seeds, up to 1.5 microns away from the plus end (figure 2.12d shows an example of a lattice signal). The tip density profile was calculated analogously, as a function of pixel distance from the tip. Obtained profiles were then averaged for several kymographs.

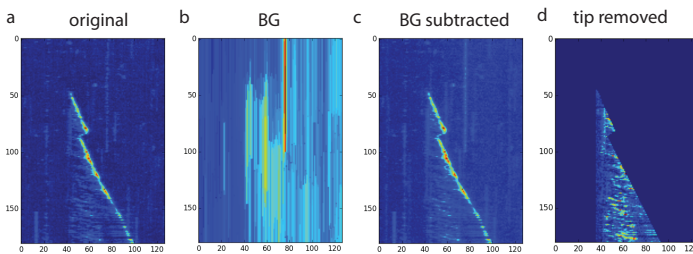


Figure 2.12: **Kymograph processing.** (a) Original maximum intensity wide kymograph. (b) Background (BG). (c) Background subtracted. (d) Masked lattice signal.

Linear fits of the density profiles were performed with the package *numpy.polyfit* and analytical density profile fits with *lmfit.minimize* of the *residual* function (*data - model*) by *least square* method (**Python 2.7**).

DERIVATION OF THE OCCUPATION DENSITY PROFILES

Here we derive the *occupation density profile* for the case of a growing microtubule. The method is an extension to the one of Parmeggiani et al. 2004 for a hopping rate u and with the addition of lattice growth with rate g . The non-growing case, can be obtained by setting $g = 0$.

We consider a 1-dimensional lattice with $i = 0, 1, \dots, N$ sites, where particles from a reservoir can bind to any empty site with rate ω_a , unbind from it with rate ω_d , and hop with rate u to the next site if unoccupied. The configuration of the lattice is described by the occupation numbers at each site, n_i , with value $n_i = 1$ when a particle occupies site i and $n_i = 0$ when the site is empty. The time evolution of the occupancy is given by the

following evolution probability

$$\frac{dn_i(t)}{dt} = un_{i-1}(t)(1 - n_i(t)) - un_i(t)(1 - n_{i+1}(t)) + \omega_a(1 - n_i(t)) - \omega_d n_i(t) \quad (2.9)$$

for $i = 1, 2, \dots, N-1$, while for the boundaries one obtains

$$\frac{dn_0(t)}{dt} = \omega_a(1 - n_1(t)) - un_1(t)(1 - n_2(t)), \quad (2.10)$$

$$\frac{dn_N(t)}{dt} = un_{N-1}(t)(1 - n_N(t)) - \beta n_N(t). \quad (2.11)$$

In the case of a growing microtubule, an empty site (a *hole*), is added at one extreme of the lattice with rate g . The equations of the movements of particles can be solved in the co-moving frame with the microtubules tip, as shown in Evans and Sugden 2007 (for expanding lattice TASEP) and Reese et al. 2011 (for a depolymerising microtubule). Then, the addition of a monomer supposes a hopping of all the particles and *holes* with rate g . Therefore, the occupation becomes

$$\frac{dn_i}{dt} = un_{i+1}(1 - n_i) - un_i(1 - n_{i-1}) + \omega_a(1 - n_i) - \omega_d n_i - g n_i(1 - n_{i-1}) + g(1 - n_i)n_{i-1} \quad (2.12)$$

for $i = 1, 2, \dots, N$, where now particle hop towards decreasing number lattice sites. The time dependence nomenclature was dropped for brevity. The occupancy at the tip is now

$$\frac{dn_0}{dt} = \frac{dn_{\text{tip}}}{dt} = un_1(1 - n_{\text{tip}}) + \omega_a(1 - n_{\text{tip}}) - \beta n_{\text{tip}} - g n_{\text{tip}}. \quad (2.13)$$

The average occupation density at site i is defined by $\rho_i(t) \equiv \langle n_i(t) \rangle$. By averaging the steady state probability equations and assuming the mean field approximation, $\langle n_i n_{i+1} \rangle \approx \langle n_i \rangle \langle n_{i+1} \rangle$, one obtains

$$\frac{d\rho_i}{dt} = u\rho_{i+1}(1 - \rho_i) - u\rho_i(1 - \rho_{i-1}) + \omega_a(1 - \rho_i) - \omega_d \rho_i - g\rho_i(1 - \rho_{i-1}) + g(1 - \rho_i)\rho_{i-1} \quad (2.14)$$

for $i = 1, 2, \dots, N-1$, and

$$\frac{d\rho_{\text{tip}}}{dt} = u\rho_1(1 - \rho_{\text{tip}}) + \omega_a(1 - \rho_{\text{tip}}) - \beta\rho_{\text{tip}} - g\rho_{\text{tip}} \quad (2.15)$$

at the tip.

Now, we can define the site size as $\varepsilon = \frac{L}{N}$ and take the *continuum limit* at $N \rightarrow \infty$. Then, taking $L = 1$, the rescaled position variable $x \equiv \frac{i}{N}$ with $0 \leq x \leq 1$ is quasi-continuous. Variable x corresponds to the distance from the growing tip. Expansion of the average density $\rho(x) \equiv \rho_i$ in powers of ε as $\rho(x \pm \varepsilon) = \rho(x) \pm \varepsilon \partial_x \rho(x) + O(\varepsilon^2)$ yields:

$$(u\varepsilon - g\varepsilon - 2u\varepsilon\rho(x))\partial_x \rho(x) + \omega_a(1 - \rho(x)) - \omega_d \rho(x) = 0 \quad (2.16)$$

Note that $v \equiv u\varepsilon$ is the average velocity of particles in units of x per unit of time, and $v_{\text{MT}} \equiv g\varepsilon$, the microtubule growth velocity. This equation can now be solved for the different boundary conditions.

AT THE BULK OF THE MICROTUBULE:

Away from the boundaries effects, the density profile does not depend on x , i.e. $\partial_x \rho(x) = 0$, and equation 2.16 gives the *Langmuir isotherm*

$$\rho_{La} = \frac{\omega_a}{\omega_a + \omega_d} = \frac{K}{1 + K} \quad (2.17)$$

where $K \equiv \omega_a/\omega_d$ is the *association constant*.

LINEARIZED DENSITY PROFILE FROM THE GMPCPP SEED:

We observe no particles at the GMPCPP seed, therefore the density from the left side tends to zero and expression 2.16 reduces to $v\partial_x \rho = \omega_a$. An *antenna* profile is thus obtained by direct integration:

$$\rho_-(x) \approx \frac{\omega_a}{v} x. \quad (2.18)$$

Further away from the seed, the density should tend to the *Langmuir isotherm*. The transition between those two domains can be estimated as in Reese et al. 2011 concatenating both domains and imposing local continuity of the current in the system. However, there are two qualitatively distinct scenarios:

- **For** $K < 1$, the *antenna* profile intersects the *Langmuir isotherm* resulting in a wedge-like profile at wedge distance from the seed determined by $\rho_-(d_{wedge}^-) = \rho_{La}$:

$$d_{wedge}^- \approx \frac{v}{\omega_a + \omega_d} = \frac{v}{\omega_d} \frac{1}{K + 1} = \frac{\ell_r}{K + 1} \text{ for } K < 1, \quad (2.19)$$

where $\ell_r \equiv v/\omega_d$ is the mean run length of the particles. Reformulating, one obtains

$$K = \frac{\ell_r - d_{wedge}^-}{d_{wedge}^-}, \quad (2.20)$$

which implies that, since K is always positive, $d_{wedge}^- < \ell_r$.

- **For** $K > 1$, the two profiles can no longer be matched continuously and there is a local discontinuity termed *domain wall* [Parmeggiani et al. 2003 and Reese et al. 2011]. Its position is determined by the local continuity condition $\rho_-(d_{dw}^-) = 1 - \rho_{La}$:

$$d_{dw}^- \approx \frac{v}{\omega_a} \frac{\omega_d}{\omega_a + \omega_d} = \frac{v}{\omega_a} \frac{1}{1 + K}. \quad (2.21)$$

ANALYTICAL SOLUTIONS

By introducing the rescaled density

$$\sigma(x) \equiv \frac{2(\rho(x) - \rho_{La})}{2\rho_{La} + \frac{c\bar{g}}{c\bar{u}} - 1}, \quad (2.22)$$

equation 2.16 simplifies to

$$\partial_x \sigma(x) + \partial_x \ln(|\sigma(x)|) = -\frac{\omega_d(K+1)}{\epsilon u(2\rho_{La} + \frac{\epsilon g}{\epsilon u} - 1)}. \quad (2.23)$$

2

Direct integration gives

$$|\sigma(x)| \exp[\sigma(x)] = Y(x) \quad (2.24)$$

where

$$Y(x) = |\sigma_{\text{boundary}}| \exp \left\{ -\frac{\omega_d(K+1)}{\epsilon u(2\rho_{La} + \frac{\epsilon g}{\epsilon u} - 1)} x + \sigma_{\text{boundary}} \right\}. \quad (2.25)$$

σ_{boundary} corresponds to the rescaled density given by the value of the density at the boundary considered, i.e. ρ_{seed} , ρ_{tip} or $\rho_{\text{growing tip}}$. We will discuss the boundary conditions later.

Equations of the form of 2.24 have an explicit solution in terms of the real part of the *Lambert W function* (figure 2.13) [Corless et al. 1996]:

$$\sigma(x) = \begin{cases} W_{-1}(-Y(x)), & \sigma(x) < -1 \\ W_0(-Y(x)), & \sigma(x) \in [-1, 0] \\ W_0(Y(x)), & \sigma(x) > 0, \end{cases} \quad (2.26)$$

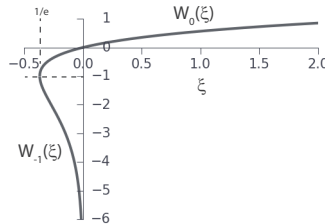


Figure 2.13: **Lambert W function.** Real branches of $W_0(\xi)$ and $W_{-1}(\xi)$. Dotted lines show the change of branch.

Therefore, the mean occupation density is described by

$$\rho(x) = \rho_{La} + \frac{2\rho_{La} + \frac{\epsilon g}{\epsilon u} - 1}{2} \sigma(x). \quad (2.27)$$

Notice that the branch changes are determined by σ , which itself is a function of K , g , u , and β . For growing lattices, the branch change occurs at the critical rates that satisfy $2\beta_c + g_c = u$. However, for the seed profile the branch change is simply determined by K , i.e. the *Langmuir kinetics* [Parmeggiani et al. 2003].

BOUNDARY CONDITIONS

- **Seed profile:** The density profile from the *seed* is obtained by setting the boundary condition $\rho(x=0) = 0$, therefore, $\sigma_{\text{seed}} = -\frac{2K}{K-1}$ and

$$\rho_{\text{seed}}(x) = \rho_{La} - \frac{1}{2} \frac{1-K}{K+1} \begin{cases} W_0 \left(\left| \frac{2K}{K-1} \right| \exp \left\{ \frac{\omega_d}{v} \frac{(K+1)^2}{K-1} x - 2\rho_{La} \right\} \right), & K < 1 \\ W_{-1} \left(- \left| \frac{2K}{K-1} \right| \exp \left\{ \frac{\omega_d}{v} \frac{(K+1)^2}{K-1} x - 2\rho_{La} \right\} \right), & K > 1, x < d_{\text{DW}} \end{cases} \quad (2.28)$$

The exact *domain wall* position for $K > 1$ is then given by the current continuity relation $\rho(d_{\text{DW}}) = 1 - \rho_{La}$, which corresponds to $\sigma(d_{\text{DW}}) = -2$. Substituting in equation 2.24 one obtains

$$d_{\text{DW}}(\omega_d, K) = \frac{2 + (K-1) \ln(|1 - \frac{1}{K}|)}{\frac{\omega_d}{v} (K+1)^2}. \quad (2.29)$$

- **Tip profile:** To determine the density at the tip, let us consider the current of particles arriving to the tip from the lattice and exiting from it. Given that the bulk density is $\rho_{\text{bulk}} = \rho_{La}$, the arriving current corresponds to

$$J_{\text{IN}} = u\rho_{La}(1 - \rho_{La}) - g\rho_{La}. \quad (2.30)$$

The exiting current is

$$J_{\text{EX}} = \beta\rho_{\text{tip}}. \quad (2.31)$$

In the steady state, the current in the system is conserved and therefore the two currents should be equal. Therefore the tip density is

$$\rho_{\text{tip}}^{\text{IN}} = \frac{1}{\beta} [u\rho_{La}(1 - \rho_{La}) - g\rho_{La}]. \quad (2.32)$$

However, this only happens when the exiting current is high enough that the last site does not become a bottleneck. In that case, a traffic jam appears, and the bulk site closest to the tip tends to the same occupation density than the tip. In that case, the tip occupation density is given by setting $\rho_{\text{bulk}} = \rho_{\text{tip}}$, therefore

$$\rho_{\text{tip}}^{\text{EX}} = 1 - \frac{\beta + g}{u}. \quad (2.33)$$

The critical unbinding rate at the tip at which the current becomes a bottleneck (β_c) corresponds to $\rho_{\text{tip}}^{\text{IN}} = \rho_{\text{tip}}^{\text{EX}}$. This can be arranged as

$$(\beta_c - u\rho_{La})(\beta_c - u\rho_{La} - u + g) = 0. \quad (2.34)$$

For particle hopping rate larger than the growth rate of the lattice, the solution that makes sense is $\beta_c = u\rho_{La}$.

ACKNOWLEDGEMENTS

The theoretical analysis of this chapter was performed in collaboration with Louis Resse. We thank Pauline van Nies for developing the protocol for the gliding assay. We thank

Liedewij Laan, Laura Munteanu, and Svenja-Marei Khalish for their previous experiments with Tea2, Tip1 and Mal3 proteins on whose shoulders this study stand. We thank Vanda Sunderlikova, Cristina Manatchal, Michel Steinmetz and Magdalena Preciado for help in protein purification. Thomas Surrey for kindly providing the 6H::Mal3::GFP plasmid. Roland Dries, Simona Botskam, and Pierre Recouvreux for help with cloning Mal3::mCherry and 6H::TEV::eGFP::Tip1. Milena Lanzova and Tom Shimizu for kindly providing an mCherry plasmid. Pierre Recoubreux, Roland Dries, and Magdalena Preciado for maintaining the Spinning disk and TIRF microscopes in Amolf. We thank Liedewij Laan for discussion and reading the manuscript.

3

DESIGNING AND BUILDING A MINIMAL POLARIZED CELL

*If you weren't an optimist,
it would be impossible to be an architect.*

Norman Foster

In vitro reconstitution experiments give us the possibility to study cellular components in controllable environments. Yet taking those components cut out of the cellular environment and their binding partners may inevitably change their behaviour. Minimal in vitro reconstitutions seek to find the essential components and mechanisms for a cellular process to occur, yet maintaining protein activities as native as possible. For this, we have to build them a simple controllable environment.

In this chapter we show how to build a cell-like environment where proteins can be deposited by microtubule tips to a biomimetic cortex. This cortex is formed by a glass barrier specifically coated with a receptor with tunable affinity for tagged proteins.

Parts of this chapter have been published in *Methods in Cell Biology* **120**, 69 (2014) Taberner et al..

3.1. INTRODUCTION AND RATIONALE

In this thesis we took the challenge to reconstitute *in vitro* microtubule-based establishment of cell polarity by deposition of polarity markers to a biomimetic cortex. In the first place we had to design and build this cell-like confinement with a biomimetic cortex. We used *Saccharomyces pombe* (*S. pombe*) as a model organism. This is a rod shaped unicellular eukaryote of 7-14 μm long where microtubule bundles deposit polarity factors to the poles of the cell by tip contacts with the cell cortex (figure 3.1).

We started with the premise of forming a *S. pombe*-like confinement where microtubules can self organize. The boundaries of such confinement should contain a protein receptor which can be tuned to meet the right affinity which allows protein deposition by microtubules.

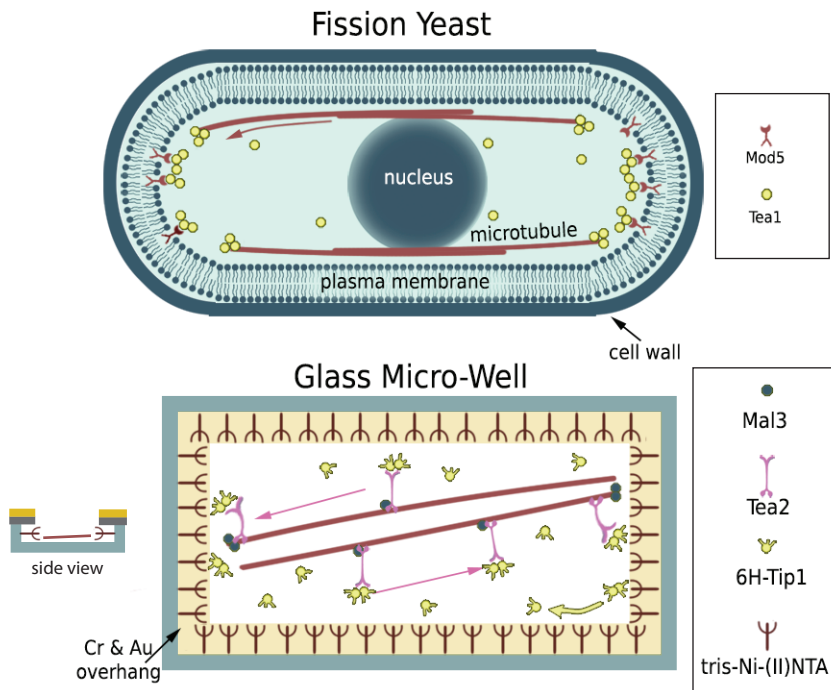


Figure 3.1: **From yeast to glass micro-wells.** Schematic representation of the microtubule-based polarity machinery in fission yeast (**top**) and the bio-mimetic micro-fabricated system (**bottom**). Note that although Tea2, Mal3 and Tip1 are not represented in the yeast scheme, they are involved in the microtubule-based transport of Tea1 (see chapter 1, figure 1.8).

Saccharomyces pombe has a hard cell wall formed of polysaccharides including glucans and galactomannan [Bush et al. 1974, Manners and Meyer 1977, Kopecka et al. 1995], with an elastic bending modulus of around $20\text{N}\cdot\text{m}^{-1}$ [Minc et al. 2009]. Individual microtubules can generate pushing forces of up to 10 pN by polymerization [Dogterom

and Yurke 1997, Janson et al. 2003, Laan et al. 2008]. Therefore, they do not produce any deformation of the cell wall by force. Types of compartments that meet this specification are micro-fabricated chambers or water in oil emulsion droplets. We used both. In this chapter we will explain how we build the microfabricated environment, while in chapter 6 we explain the water-in-oil emulsion droplets system.

In the past, micro-chambers have been used to study microtubule organization in rigid confinements [Holy et al. 1997, Nedelec et al., 1997, Cosentino Lagomarsino et al. 2007]. In addition, fabrication of micro-chambers with glass bottom surfaces and gold walls allowed immobilization of microtubule associated proteins only at the walls, which act as a biomimetic cortex [Romet-Lemone et al. 2005]. This setup allowed the *in vitro* reconstitution of microtubule aster positioning by microtubule pulling mediated by cortical dynein [Laan et al. 2012a].

The distinction between the bottom surface, as imaging substrate, and the walls, as bio-mimetic cortex gives a good *in vitro* model of a cell. Our *in vitro* setup built up on these previous experiments (figure 3.1).

Glass surfaces have been commonly used for *in vitro* microscopy assays, therefore glass passivation against unspecific protein absorption has been extensively assayed. Along the whole thesis we coated glass surfaces with poly(ethylene glycol)-grafted (PEG-g) with the brush copolymer poly(L-lysine) (PLL-g-PEG). PLL-g-PEG has a positively charged backbone at neutral pH that is absorbed spontaneously onto negatively charged metal-oxide surfaces, such as SiO₂. Certain PEG lengths and grafting ratios reduce considerably unspecific protein absorption [Kenausis et al. 2000]. Addition of PEG layers with a functional group like biotin, to which biotinylated proteins bind strongly by adding streptavidin or neutravidin as intermediates, have given a simple way to functionalize glass surfaces [Huang et al. 2002]. For instance, PLL-g-PEG/Biotin is commonly used to absorb biotinylated microtubule stabilized GMPCPP seeds to surfaces via biotin-streptavidin linkages.

On the other hand, thiol specific absorbency onto gold layers have been used to passivate and functionalize gold surfaces [see Love et al. 2005 and Frasconi et al. 2010 for review]. Combination of glass surfaces and gold barriers as in Romet-Lemone et al. 2005 and Laan et al. 2012a gives a way to distinctly functionalize both surfaces and that way distinguish the cell substrate from the cell cortex.

In our design phase, we considered what can be a suitable cortical receptor for proteins. Due to *S. pombe*'s size, the polarity factor Tea1 can both reach the cell boundaries directly from the reservoir and by microtubule-based depositions [Mata and Nurse 1997, Behrens and Nurse 2002, Feierbach et al. 2004, Bicho et al. 2010, Dodgson et al. 2013]. In the current thinking, Tea1 is always able to bind to its cortical receptor Mod5, meaning it does not have an inactive state. In order to obtain microtubule-based deposition of Tea1 to the cortical receptor Mod5, Tea1 affinity for the microtubule needs to be higher than for Mod5. Therefore, our *in vitro* assay requires an engineered binding between +TIPs and the wall with an affinity slightly lower than that of those proteins for the microtubule. Enzyme affinity to a receptor ligand is characterized by the equilibrium dissociation constant (K_D). This parameter corresponds to the protein concentration at which

half of the receptor molecules are occupied by proteins. A suitable receptor consists of nickel ions chelated by nitrilotriacetic acid (Ni(II)-NTA). Histidines can reversibly bind to Ni(II)-NTA and their affinity can be tuned by competition with imidazole [Hochuli et al. 1987]. This mechanism is commonly used in protein purification, since proteins with a his-tag, containing 6 histidines fused to one of the termini, can reversibly bind. This, allows us to fuse a his-tag to any protein and use it as putative polarity marker.

Commercial nitrilotriacetic acid contains a single NTA which chelates one nickel ion (Mono-NTA, figure 3.2). This, provides two weak binding sites for two histidines. The most stable immobilization of a his-tagged protein (6 histidines) occurs via binding to three Mono-Ni(II)-NTA [Zhen et al. 2006]. Alternatively, multivalent chelator head-groups containing more than one nickel ion can increase his-tag affinity [Lata and Piehler 2005, Lata et al. 2005]. Here, we used Tris-Ni(II)-NTA, which can bind stoichiometrically to his-tagged proteins in a stable manner. In the next chapter, we further tuned protein affinity by addition of controlled amounts of imidazole (figure 3.2).

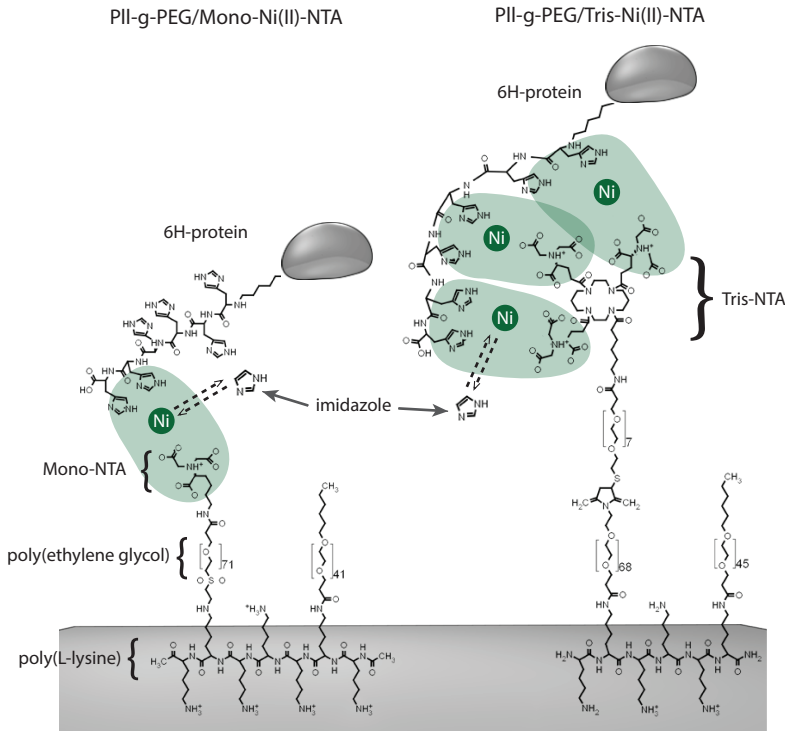


Figure 3.2: **Protein immobilization to glass via nitrilotriacetic acid.** Chemical structures of the root repetitions of PII-g-PEG/Ni(II)-Mono/Tris NTA and their binding to his-tagged proteins. The diagram shows only a minimal block of the molecules.

Following up from the Romet-Lemone and Laan method, we first tried to functional-

ize gold walls with Ni(II)-NTA. This, was done by forming a mixed self assembled monolayer (SAM) of mercapto undecanoic acid and mercapto undecanol (1:9 in ethanol) overnight. The mercaptoundecanol was then activated by pentafluorophenol catalysed by EDAC and finally bound to NTA-amino [Laan 2009]. This method showed several inconveniences. The homogeneity of Thiol-based SAMs is highly dependent on the purity of the gold layer, the presence of several contaminants, the length of the molecule, and the nature of the head group [Bain et al. 1989]. In our hands, specific binding of his-tagged proteins to NTA-coated gold walls was possible (tests with 6H::eGFP::Tip1), but the gold walls could not be totally passivated against some non-his-tagged proteins that we often use in our assays as well (in particular Mal3::mCherry). Moreover, thiols easily absorbed to the bottom glass surface from where they were difficult to remove (data not shown). For methodologies with gold, we refer the reader to Laan 2009, Laan and Dogterom 2010, Taberner et al. 2014.

For these reasons, we developed a new way to selectively functionalize the wall of micro-wells completely made of glass. In our hands, selective glass functionalization via Pll-g-PEGs gave a better specificity for his-tagged proteins versus unspecific absorption. Moreover, Pll-g-PEG coating of negatively charged surfaces occurs in time scales of minutes. Therefore, sample preparation is much shorter than in the case of thiols [Kenausis et al. 2000, Zhen et al. 2006].

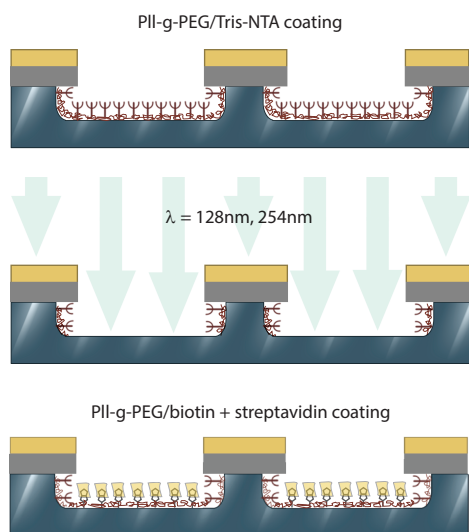


Figure 3.3: **Selective functionalization of glass micro-wells with a chromium/gold overhang.** **(Top)** Coating of all glass surfaces with Pll-g-PEG/Tris-NTA. **(Middle)** Photo-cleavage of compounds at the bottom surface. **(Bottom)** Coating of the bottom surface with Pll-g-PEG/Biotin for future absorption of streptavidin, followed by biotinylated microtubule seeds.

In order to achieve selective functionalization of the walls versus the bottom surface, we adapted micropatterning techniques used for flat surfaces to 3D structures. In particular, we microfabricate the glass wells with two additional thin layers of chromium and gold on top producing an overhang at the walls (figure 3.1). This layer has two functions, to prevent microtubules from growing over the walls, and to function as a photo-mask that shelters the walls. Selectivity is then achieved in a three-step process (figure 3.3). First, all glass surfaces are coated with the Pll-g-PEG desired to remain at the wall.

Then, the sample is dried and irradiated with deep UV. This, photo-cleaves the PLL-g-PEG coating [Azioune et al. 2009] everywhere, except at the walls, which are sheltered by the chromium and gold layers. Finally, a second functionalization or passivation can be applied to the bottom surface.

In this chapter we will describe in detail the production of the sheltered micro-wells and the subsequent selective functionalization of the walls. We also show how to prepare a microtubule-based protein delivery assay as used in chapter 4 (figure 3.1). The proteins that we use for this experiment are the fission yeast polarity factors: Mal3 (EB1 analogue), Tea2 (kinesin-like), and Tip1 (CLIP-170 family) described in chapter 3.

3.2. MATERIALS

MICROFABRICATION

SPECIAL EQUIPMENT

All the microfabrication steps except evaporation were performed inside a clean room (class ISO 6).

- Coverslips No. 1 24x24 mm 170 mm (Menzel Gläser, Germany).
- Delta 80 GYSET[®] Spin coater with a closed lid (Süss MicroTec, Germany).
- Hot plates.
- N₂ gas (hand gun).
- Homemade turbo pumped vacuum system with base pressure 10⁷ mbar equipped with a resistance heating evaporation system for tungsten boats loaded with chromium or gold.
- 2510 Ultrasonic Cleaner (Branson, USA).
- MJB3 mask aligner for UV exposure (Süss MicroTec).
- Binary chromium/soda lime mask (Delta Mask, The Netherlands).

REAGENTS

- Hexamethyldisilazane (HMDS) primer (Sigma-Aldrich, USA).
- Shipley Microposit[®] S1805 G2 positive UV-resist (Microresist, Germany).
- Microposit[®] MF[®]-319 developer (Microresist).
- Standard gold etchant (Sigma-Aldrich).
- Standard chromium etchant (Sigma-Aldrich).

SURFACE FUNCTIONALIZATION AND PASSIVATION

SPECIAL EQUIPMENT

- Compact UV-Ozone cleaner (Uvotech, USA).

REAGENTS

All reagents are dissolved in MRB80 buffer (80 mM KPipes, 4 mM MgCl₂, 1 mM ethylene glycol tetraacetic acid (EGTA), pH 6.8) at the stated stock concentration and stored at -80°C unless stated otherwise.

- **PLL-g-PEG:** PLL(20)-g[3.5]-PEG(2) (SUSOS AG, Switzerland); 2 mg·ml⁻¹ solution.
- **PLL-g-PEG/Biotin:** PLL(20)-g[3.1]-PEG(2)/PEG(3.4)-biotin(17.5%) (SUSOS AG); 2 mg·ml⁻¹ solution.
- **PLL-g-PEG/MonoNTA:** PLL(20)-g[3.5]-PEG(3.5)-(-3,4)NTA (SUSOS AG); 2 mg·ml⁻¹ solution.
- **PLL-g-PEG/Tris-NTA:** PLL-g3-PEG2k/PEG3.4K-Tris-NTA made by a two-step coupling process, as described in Bhagawati et al. 2013.
- **10mM NISO₄ solution** in MRB80 pH 7.5 stored at room temperature from Nickel(II) sulfate (Sigma-Aldrich).
- **Biotinylated BSA** Albumin, biotin labeled bovine (Sigma-Aldrich); 20 mg·ml⁻¹ solution.
- **Streptavidin:** (Invitrogen, USA); 1 mg·ml⁻¹ solution.
- **Alexa Fluor[®] 488 streptavidin** (Invitrogen); 1 mg·ml⁻¹ solution.
- **κ-casein** from bovine milk (Sigma-Aldrich); 5 mg·ml⁻¹ solution.

PROTEIN PURIFICATION

Protein biochemistry can be found in section 2.8.

3.3. MICRO-FABRICATION OF GLASS MICRO-WELLS WITH CHROMIUM OVERHANG

Micro-fabrication of the micro-wells consists of conventional photolithography and wet etching techniques. Figure 3.4 shows an overview of the steps. First, the metal layers are deposited by evaporation. Then a photoresist is spin-coated and a pattern is made by UV exposure through a binary mask. After development of the photoresist, the gold, the chromium and the glass are etched sequentially. The following subsections give a detailed protocol.

EVAPORATION

Start by cleaning the coverslips (Menzel Gläser, No.1 24x24 mm 170 μm) with base piranha (NH₄OH:H₂O₂ in 3:1 at 75°C) for 15 min and rinse them in ddH₂O and isopropanol. Evaporate a 50nm layer of chromium and 50nm of gold (both at rates 0.06 nm·s⁻¹) in an evaporation chamber at pressure below 10⁶ mbar. The gold layer protects the chromium from being attacked by KOH, used later in the glass etching step, and also prevents the chromium from peeling off due to mechanical strain. Figure 3.7 shows examples of prototypes of chamber without gold on top.

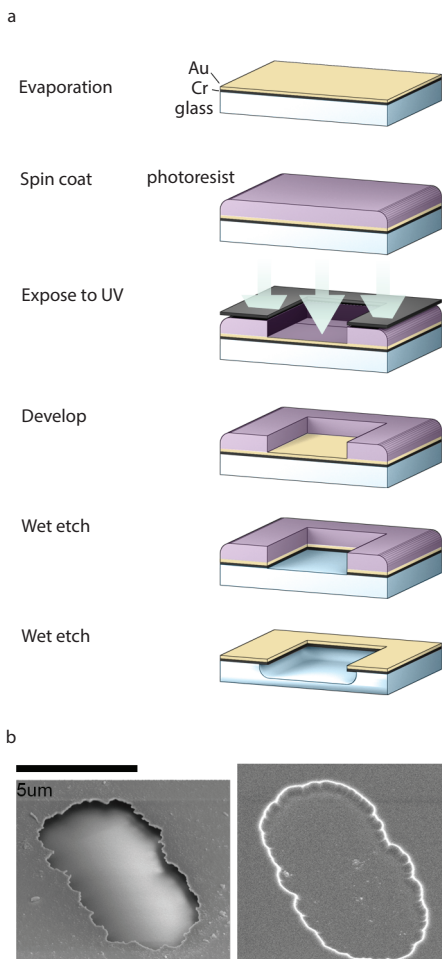


Figure 3.4: **Micro-well fabrication.** (a) Micro-fabrication steps from top to bottom. (b) Scanning electron microscopy on a finished microwell (left), and a well were the chromium has been removed (right).

PHOTOLITHOGRAPHY

Dry the samples 5 min at 150°C, cool them down with N₂ flow, spin-coat a thin layer of HMDS primer (Sigma-Aldrich, USA) at 4000 rpm for 32 s, and bake 1 min at 150°C. Spin-coat a thin layer (around 300 nm) of Shipley Microposit[®] S1805 G2 positive UV-resist (Microresist, Germany) at 500 rpm for 8 s followed by 4000 rpm for 32 s. Let dry 10 s, and soft bake at 115°C for 60 s. Expose to a dose of 25 mJ·cm² of 365 nm UV light using a Süss MJB3 mask aligner with a binary chromium/soda lime mask on top (Delta Mask, The Netherlands). For structures that do not require sharp corners (like straight lines), the sample can be postbaked 30 min at 130°C, which melts a little photoresist providing smoother structures. Immerse the sample in Microposit[®] MF[®]-319 developer (Microresist) for 1 min. The UV-exposed pattern will be developed (dissolved) while leaving the rest of the photoresist.

WET ETCHING

Immerse the sample in standard gold etchant (Sigma-Aldrich) the necessary time (etch rate around $2.8 \text{ nm}\cdot\text{s}^{-1}$) and rinse thoroughly in water. Check carefully with the microscope that the gold is properly etched. Proceed the same way with the standard chromium etchant (Sigma-Aldrich, etch rate around $4 \text{ nm}\cdot\text{s}^{-1}$). It is convenient to over etch a bit the chromium and gold, as remaining particles will lead to a non flat final glass bottom surface. Wet etching of gold, however, produces a non smooth profile which is transferred to the following steps, giving wavy walls with rough edges ($\sim 500 \text{ nm}$ wave length). Alternatively the gold layer can be etched by reactive ion plasma etching (RIE). Remove the photoresist by sonicating the samples 20 min in a big beaker with acetone. If needed, further removal can be achieved by base piranha. Isotropically etch the glass by immersing it in a 40% KOH solution at 80°C (etch rate around $5 \text{ nm}\cdot\text{min}^{-1}$, ¹). We found that for Menzel Gläser coverslips, KOH produced a smoother final surface than RIE etching or HF (not shown). A depth of 300 nm is convenient for later imaging of microtubules with confocal microscopy since it requires few focal z-planes.

Clean again the sample with base piranha to prepare it for functionalization steps and optionally cut each sample in four long pieces with a diamond cutter.

3.4. SELECTIVE SURFACE FUNCTIONALIZATION

The walls are functionalized with Tris-Ni(II)-NTA. The bottom surface in chapter 4 is functionalized with PLL-g-PEG/biotin and streptavidin, for later immobilization of biotinylated seeds. In chapter 5, where microtubules are not attached to the bottom surface, this surface is passivated with PLL-g-PEG. Note that alternatively, one could coat the walls with PLL-g-PEG/biotin, and passivate the bottom surface with PLL-g-PEG. In that case, biotinylated proteins can be immobilized nearly permanently at the wall via biotin-streptavidin linkages.

Drop 20 ml solution of 0.2-0.4 mM PLL-g-PEG/Tris-NTA on top of a microfabricated coverslip². Put the sample in a sealable plastic bag and immerse it in an ultrasonication bath for some seconds. This helps removing air bubbles in the micro-wells, resulting in a more homogeneous coating of the walls. Incubate for 30 min, wash with MRB80, and dry with N_2 flow. Expose to deep UV (185 and 254 nm) with an Ozone Cleaner for 10 min (the time depends on the power of the lamp and the distance to the sample).

FLOW CELL PREPARATION

Prepare a flow cell on a Hellmanex[®] cleaned glass slide by attaching two parallel strips of double-sided TESA[®] tape separated by 5 mm. Place the coverslip on top with the microfabricated wells facing the glass slide (10–20 μl flow cell volume). Now you can flow in the subsequent solutions by putting absorbent paper on the other side of the cell. Avoid the dry out of the flow cell.

¹<http://www.cleanroom.byu.edu/KOH.phtml>, as well as our own experience

²For the preliminary assays of this chapter, 0.1 mM PLL-g-PEG/Tris-NTA was used, which produced high heterogeneity in the coated walls

NICKEL LOADING AND PASSIVATION

Load the NTA with nickel ions by incubating a 10 mM NiSO₄ solution in MRB80 for 30 min. Clean thoroughly the flow cell with MRB80 buffer and incubate 15min with either 0.2 mg·ml⁻¹ PLL-g-PEG/biotin or 0.2 mg·ml⁻¹ PLL-g-PEG.

For immobilization of GMPCPP stabilized seeds, incubate 1 mg·ml⁻¹ streptavidin, and passivate with 1.2 mg·ml⁻¹ κ-casein (10min incubation each, rinsed in between with MRB80).

For a control experiment to visualize the selective coatings, omit the incubation of nonlabeled streptavidin and incubate a mix containing 500 nM 6H::Mal3::mCherry, 0.1 mg·ml⁻¹ Alexa Fluor[®] 488 streptavidin, 50 nM KCl, 0.6 mg·ml⁻¹ κ-casein, 0.4 mg·ml⁻¹ glucose oxidase, and 50 mM glucose in MRB80. This should lead to a bottom surface coated with streptavidin and only the walls coated with 6H::Mal3::mCherry (figure 3.5). When washing with 1M imidazole, 6H::Mal3::mCherry detaches from the walls while fluorescent streptavidin remains at the bottom surface.

3

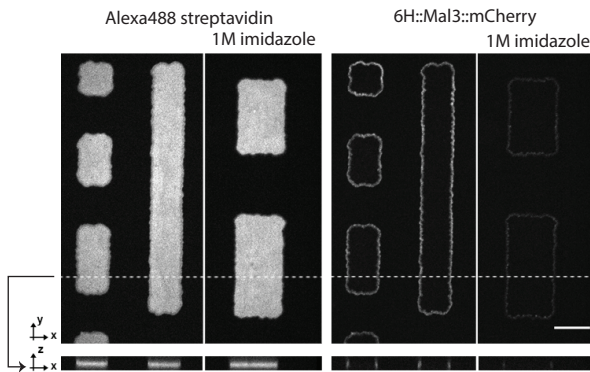


Figure 3.5: Selective surface functionalization Fluorescent microscopy images of micro-wells coated at the bottom surface with Alexa Fluor[®] 488 streptavidin and at the walls with 6H::Mal3::mCherry. Upon incubation of 1M imidazole, only Mal3 unbinds from the surface. Scale bar 10 μm.

3.5. MICROTUBULE ASSAYS

+TIP DELIVERY ASSAY

Take the flow cell from section 3.4 prepared with Tris-Ni(II)-NTA. Incubate for 5min with the biotinylated microtubule seeds 10 times diluted in MRB80 with 0.1% methyl cellulose so that they bind to the surface coated with PLL-PEG-biotin-streptavidin.

Prepare on ice a tubulin mix with end-binding proteins in MRB80 containing 14.25 mM tubulin, 0.75 mM rhodamine tubulin, 100 nM his-tagged eGFP::Tip1, 8 nM Tea2, 200 nM Mal3, 50 nM KCl, 0.6 mg·ml⁻¹ κ-casein, 0.4 mg·ml⁻¹ glucose oxidase, 50 mM glucose, 0.1% methyl cellulose, 1 mM GTP, and 2 mM ATP. For assays of delivery of Mal3, use his-tagged Mal3::mCherry and HiLyte[®] 488 labeled tubulin without Tea2 or Tip1. Airfuge 9min at 30 psi, introduce in the flow cell, and seal it with valap³ or vacuum grease.

The sample is warmed up to 26°C by an objective heater or a chamber surrounding the hole microscope. We take spinning disk confocal z-stacks every 5s of 300 ms expo-

³vaseline, lanolin, paraffin wax melted at equal concentrations

sure. We typically take 2 z positions: at the best focus for microtubules (bottom surface), and at the brightest focal plane of protein signal at the wall. Since those two signals correspond to different excitation and emission wavelengths, they might correspond to an objective z-distance similar to the actual height of the walls. Each image of the z-stack is later background corrected and projected by maximum intensity (see Image treatment section).

When using walls functionalized with Tris-Ni(II)-NTA, his-tagged proteins in solution have a relatively high affinity for the walls, leading to spontaneous coverage of the walls (figure 3.5). Additionally, end-binding proteins have a high affinity for growing microtubule ends.

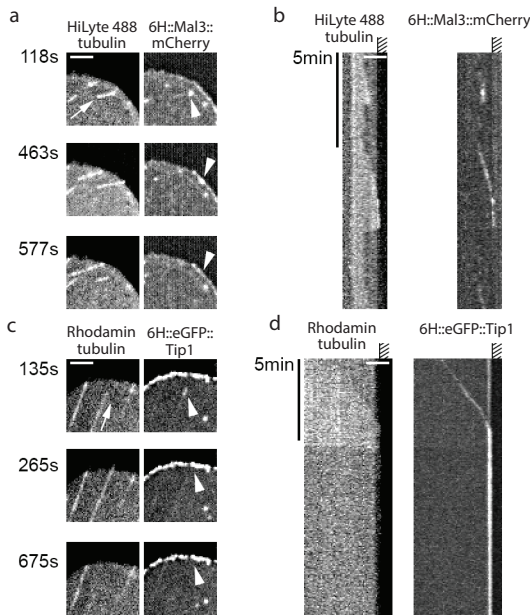


Figure 3.6: **Deliveries of +TIPs (a) and (c)** Spinning disk fluorescent microscopy images of microtubule plus end contacts with the functionalized wall carrying 6H::Mal3::mCherry (a) or 6H::eGFP::Tip1 in the presence of untagged Mal3 and Tea2. The different figures show states before, during and after microtubule tip contact with the wall. Since the microscopy snapshots had high background, the shown images correspond to the average of five snapshots. **(b) and (d)** Respective kymographs for the microtubules with the arrows. Scale bars $2\ \mu\text{m}$.

His-tagged Mal3 binds to microtubule ends with a dwell time of about 0.3s, leading to the appearance of Mal3 comets at growing microtubule ends (Bieling et al. 2007). When these comets reach a barrier, they do not leave “extra” Mal3 at the wall receptor upon microtubule de-polymerization (figure 3.6a and b).

By contrast, figure 3.6c and d shows a microtubule in the presence of his-tagged Tip1 reaching a wall functionalized with Tris-Ni(II)-NTA. When the microtubule reaches the wall an apparent cluster of tip1 proteins remains attached to the wall, even after the microtubule de-polymerizes. This preliminary observation suggests that effective clustering of proteins such as observed for Tip1, but not for Mal3, may be important for cortical deposition of proteins by microtubules.

This preliminary results were obtained without imidazole and lower Pll-g-PEG/Tris-Ni(II)-NTA incubation. Under this conditions 6H::eGFP::Tip1 depositions occurred in anecdotal cases, presumably in walls with a low coating of Tris-Ni(II)-NTA, or when equi-

librium with the reservoir had not been reached yet. In chapter 4 walls are better homogeneously coated and imidazole was required to adjust the K_D for his-tagged proteins. Characterization of the walls and quantitative results will be presented in that chapter.

3.6. DISCUSSION

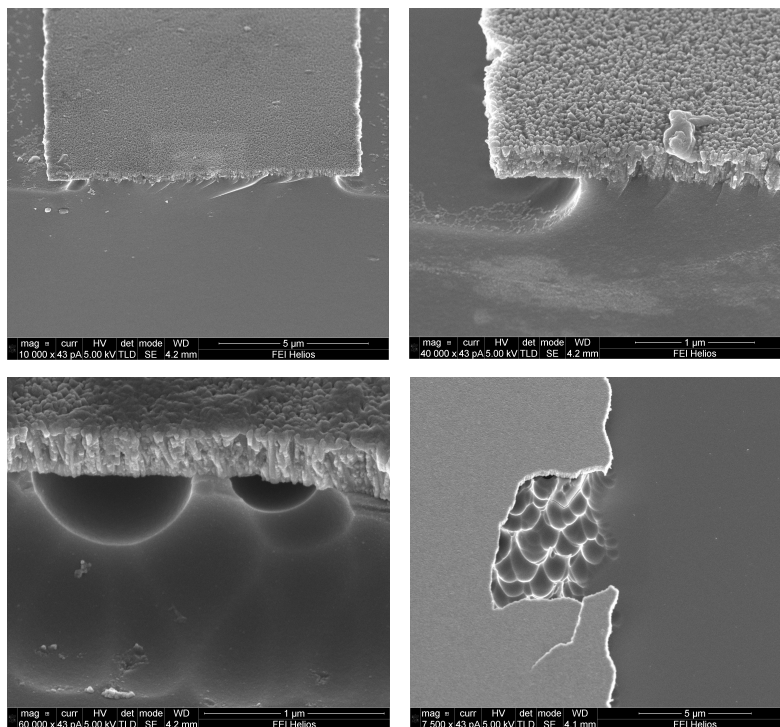
In this chapter, we presented a method to selectively functionalize glass surfaces in microchambers. Selective functionalization had been previously reported with the use of glass and gold surfaces [Romet-Lemone et al. 2005]. However, here, the combination of UV molecule photocleavage and a mask embed in the 3D structure makes the same task possible with only glass. The gain is robustness, shortened time of sample preparation, and more effective passivation against unspecific protein sticking.

The chromium overhang, moreover prevents microtubules from growing over the walls as in previous experiments [Dogterom and Yurke 1997, Janson and Dogterom 2004]. However, the chromium locally amplifies the detected fluorescence intensity of proteins by up to a factor of 2 (data not shown). This is likely due to reflections of the excitation and emission light at the chromium layer. To avoid this effect, we developed an alternative setup where the chromium and gold overhang is replaced by 80 nm of TiO₂. This layer is opaque to deep UV but 70–80% transparent to the emission and excitation range of wavelengths used in our experiments (480–620 nm) (see Taberner et al. 2015). An alternative way to selectively expose regions of the sample with deep UV is by employing an external binary chromium/quartz mask complementary to the 3D structures. In this case a proper alignment and close contact between the mask and the sample needs to be achieved. This method offers the additional possibility to selectively irradiate a subset of walls or wells in the sample. This would allow to compare in the same sample barriers with different functionalizations.

The techniques shown in this chapter can be used for microtubule-based deposition of proteins as well as for immobilization of proteins. In the later case, immobilized proteins can be used to reconstitute cytoskeleton interactions with the cell cortex mediated by cortical proteins like dynein or CLASP. Chapter 7 shows how CLASP proteins immobilized at walls can prevent microtubules from undergoing catastrophe upon contact with the wall. Other "end-on" interactions occurring in cells like microtubule attachment to kinetochores, can also be tested with this method. Alternatively, "end-on" interactions have recently been achieved using beads with the addition of a long tether [Volkov et al. 2013]. Potentially, functionalized microwells could furthermore provide a framework to study controlled lateral interactions; for example, by placing cells inside wells where the walls mimic lateral cellular adhesion conditions.

Ni(II)-NTA based immobilization does not require protein biotinylation and suffers little from protein inactivation (Bieling et al. 2010, Mukai and Travis 2012). Since it is reversible and tunable by imidazole addition, it is suited to study cellular processes that involve transient bindings.

SUPPLEMENTARY MATERIAL



3

Figure 3.7: **Microfabrication without a gold layer on top** SEM images of different microfabricated prototypes. Although some structures look good (**top**), in several occasions cracks in the chromium caused isotropic etching in the glass causing semi-spherical holes (**bottom**).

ACKNOWLEDGEMENTS

We thank Jacob Piehler and Changjiang You for development and synthesis of PLL-g-PEG/Tris-NTA. We thank Gijs Vollenbroek, Dimmitry Lamers, Andries Lof, and Hans Zeijlemaker for advice and help with microfabrication. Roland Dries for help with UV irradiation and developing a mask aligner (not shown). Liedewij Laan for initiating this project and advice. Finally, we thank David Minde for careful reading of the paper manuscript in which this chapter is based.

—

—

4

MICROTUBULE-BASED DEPOSITION OF +TIPS TO A BIO-MIMETIC CORTEX

*I prefer transporting people than goods;
people unload themselves.*

Ernest Carretero Serra (My uncle and a driver)

In this chapter we study the process of how microtubule plus ends can deposit +TIP proteins to a cellular cortex. We use the bio-mimetic cortex developed in the previous chapter and quantify his-tagged +TIP depositions to the wall. We show that 6H::eGFP::Tip1 can be deposited to the bio-mimetic wall upon microtubule catastrophe in the presence of Tea2 and Mal3. Microtubule catastrophe is not required for delivery, but it enhances its efficiency. Our data suggest that 6H::eGFP::Tip1 can connect microtubule plus ends to deposition sites. However, 6H::Mal3::mCherry alone, which is not deposited at the wall cannot form those bridges.

4.1. INTRODUCTION

From fungi, to neurons, to motile fibroblasts and epithelial cells, microtubules contribute to cell polarity [Siegrist and Doe 2007]. They distribute proteins and organelles to certain sides of the cell in an asymmetric fashion [Hirokawa 1998, Rodriguez-Boulan et al. 2005, van Beuningen and Hoogenraad 2016]. In addition, they orchestrate actin assembly and disassembly in not yet well understood ways, which often require multiple tip contacts with the cortex [Waterman-Storer et al. 1999].

In the unicellular fungi *Schizosaccharomyces pombe* (*S. pombe*), microtubules deposit polarity factors to specific sites of the cell cortex in a kinesin-mediated way (see section 1.1 in chapter 1). Analogous depositions have been observed in the filamentous fungus *Aspergillus nidulans* [Ishitsuka et al. 2015]. Those polarity factors, activate at the cortex other proteins that lead to cell growth. Similar depositions might also occur in *Drosophila* S2 cells [Rogers et al. 2004].

To help understand how microtubules can deposit proteins at cortical receptors, we reconstituted *in vitro* microtubule-based deposition of polarity factors to engineered bio-mimetic cortices. We provided microtubule tip tracking proteins (+TIPs) with a tag of tunable affinity for the walls of glass micro-wells functionalized with a receptor. We show that a tagged kinesin cargo protein Tip1 from the *S. pombe* polarity machinery can be deposited to a wall upon microtubule tip contact. In our system, microtubule catastrophe is not necessary for Tip1 deposition to the wall, however it enhanced its efficiency. In addition, there are indications that a fraction of Tip1 molecules from the microtubule form a bridge between the microtubule and the wall that promotes microtubule plus end capturing at sites of deposition. This capturing can promote multiple deliveries at the same wall spot. However, in our system repeated deliveries do not lead in general to increased amounts of protein at the wall spot, as its receptors get often saturated with a single microtubule-based deposition.

By contrast, tagged Mal3, from the EB family, could not be deposited to the wall upon microtubule contact under conditions analogous to the ones in which tagged Tip1 did. The different outcomes between the two proteins remains unclear. The two proteins locate at microtubule tips by two qualitatively and quantitatively different ways as several factors may play a role. Mal3 is an autonomous tip tracker with a sub-second microtubule dwell time [Bieling et al. 2007]. Tip1 can reach the microtubule plus end by interaction with Mal3 and the kinesin Tea2, directly from the reservoir, or by Tea2 walking along the microtubule lattice [Bieling et al. 2007, chapter 3]. Its residence time can be of several tens seconds. We hypothesize that the previously observed cluster formation of Tip1 on microtubule tips facilitates its deposition to the wall.

4.2. DESIGN AND OPTIMIZATION OF THE BIO-MIMETIC CORTEX

We fabricated glass micro-wells 300-400 nm deep containing a double layer of 50 nm chromium and 50 nm gold on top, which creates an overhang (figure 4.1 a). The walls of the wells are coated with poly(ethylene glycol)-grafted with copolymer poly(L-lysine)

and derivatives of copolymer poly(L-lysine) with a functional three-head nitrilotriacetic acid that chelates three nickel ions (Pll-g-PEG/Tris-Ni(II)-NTA) [Bhagawati et al. 2013]. The bottom layer of the micro-wells is coated with either Pll-g-PEG/biotin for subsequent immobilization of biotinylated microtubule stable seeds or Pll-g-PEG for passivation against unspecific absorption of proteins. The method to fabricate and functionalize this chamber can be found in chapter 3 or Taberner et al. 2014.

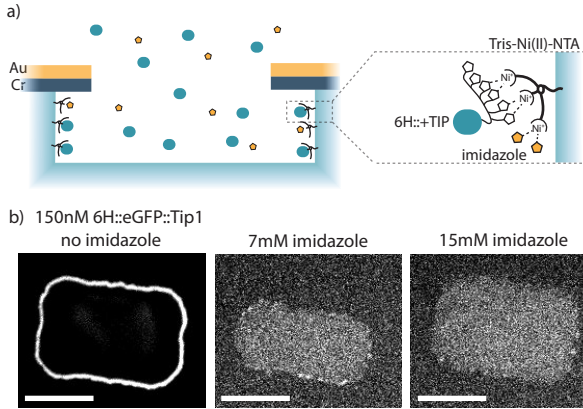


Figure 4.1: Tuning 6H::+TIP affinity to Tris-Ni(II)-NTA coated walls. (a) Scheme of a micro-well and free 6H::+TIP binding to the Tris-Ni(II)-NTA functionalized walls in competition with imidazole. Imaging is performed with an inverted microscope. (b) Spinning disk confocal images of 150 nM 6H::eGFP::Tip1 at different imidazole concentrations. Scale bars 10 μ m.

Each Tris-Ni(II)-NTA unit contains three chelated nickel(II) ions. To each of these ions two histidines can reversibly bind via their imidazole functional group. A his-tagged (6H) protein, containing six consecutive histidines, can thus bind stoichiometric to a Tris-Ni(II)-NTA unit [Lata and Piehler 2005].

In order to obtain microtubule-based deposition of his-tagged proteins to a Tris-Ni(II)-NTA coated wall, it is needed that the protein has higher affinity for the microtubule than for the wall. This condition is fulfilled at protein concentrations in which the amount of proteins tip tracking is high, and the walls appear practically exempt of bound protein. After exploratory experiments, we chose to work at 150 nM concentrations of 6H::eGFP::Tip1 and 6H::Mal3::mCherry, since both proteins display large accumulations at microtubule plus ends (chapter 2). At this concentration, Pll-g-PEG/Tris-Ni(II)-NTA coated walls appeared completely covered by 6H::eGFP::Tip1 once equilibrium was reached (20-30 min after protein incubation, figure 4.1 b). Analogous incubations with 7-15 mM imidazole added in solution highly reduced protein immobilization at the wall yielding isolated spots of 6H::eGFP::Tip1 fluorescence at the wall (figure 4.1 b). Given sample variability, we found convenient to assess protein depositions at 10 mM imidazole concentrations.

CHARACTERIZATION OF THE BIO-MIMETIC CORTEX

Ligand receptor affinity is normally characterized by the dissociation constant, defined as $K_D = \frac{k_d}{k_a}$, where k_a and k_d are the association and dissociation rates. The K_D corresponds to the protein concentration at which half of the receptors are occupied. Imidazole competes with the his-tagged protein for nickel ion binding sites and effectively increases the K_D . In the presence of imidazole, a 6H::protein needs more than one Tris-

Ni(II)-NTA to bind with maximum stability, therefore its avidity (immobilization via multiple low affinity bonds) depends on the density of Tris-Ni(II)-NTA at the wall.

To estimate the effective dissociation constant of 6H::+TIPs at 10 mM imidazole, we incubated different concentrations of 6H::Mal3::mCherry and measured the average amount of protein bound at the wall (fluorescence intensity) at equilibrium (30 min after incubation). To account for pipetting errors and inhomogeneities in sample illumination, we used the bulk fluorescence intensity (protein in solution in the middle of a well) as a proxy for protein concentration. As observed in figure 4.2 a, solution intensity increases linearly with protein concentration. Figure 4.2 b shows the average amount of protein bound to the wall as a function of protein in solution (in fluorescence intensity units). This graph shows a large spread in the data points (reddish colours) which can be fitted by a Michaelis-Menten relation (light blue line), as confirmed for the binned mean values (black dots). This gives a $K_D = 230 \pm 20$ nM. Therefore, at 150 nM his-tagged protein concentrations with 10 mM imidazole at which we perform microtubule end-binding assays it is expected to obtain very little binding to the walls.

4

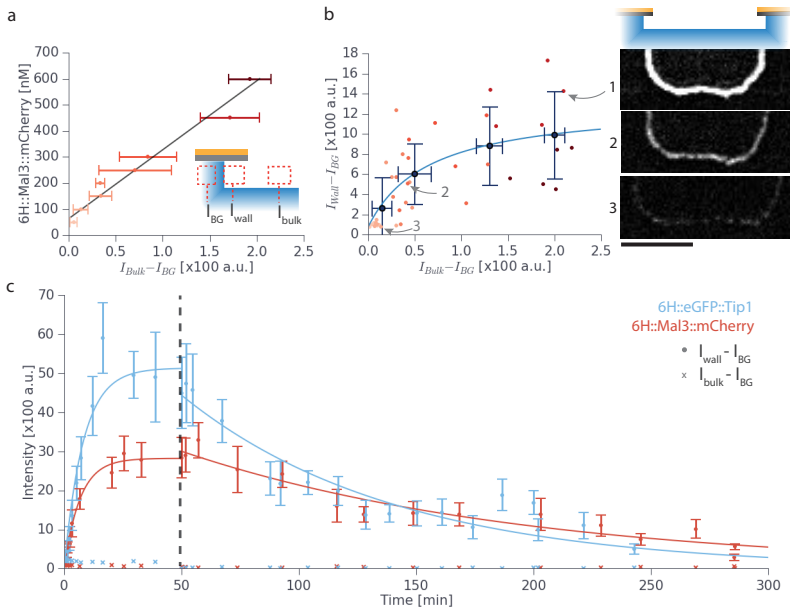


Figure 4.2: Protein immobilization to the bio-mimetic cortex from solution in competition with 10mM imidazole. (a) Look up plot of 6H::Mal3::mCherry protein concentration as a function of bulk fluorescence signal. Each data point correspond to the average of 5 wells measured in different positions in the sample. (b) Wall fluorescence signal as a function of bulk signal. Yellow-to-red dots correspond to individual measurements colour coded by protein incubation concentrations as in a. Black dots corresponds to the binned data by the Freedman-Diaconis rule (67 a.u.) [Freedman and Diaconis 1981], except for the first bin which was taken smaller (35 a.u.). Blue line corresponds to a Michaelis-Menten law fitting. Right side: examples of background subtracted images for different wall intensities. Scale bar $5 \mu\text{m}$. (c) Binding kinetics of $1.5 \mu\text{M}$ 6H::eGFP::Tip1, cyan, and 6H::Mal3::mCherry, red, to Tris-Ni(II)-NTA coated walls at 10 mM imidazole. From time 50 min onwards, unbound protein is removed by flushing 10 mM imidazole every 5 min. Wall and bulk intensities are measured in the same way as in a and b. Fitted association and dissociation rates can be found in table 4.1.

	k_a [$10^{-3}\mu\text{M}\cdot\text{s}^{-1}$]	k_d [10^{-3}s^{-1}]	K_D [nM]
6H::Mal3::mCherry	1.6 [1.3 - 1.9]	0.11 [0.09 - 0.13]	72 [48 - 110]
6H::eGFP::Tip1	1.2 [0.6 - 1.8]	0.183 [0.14 - 0.22]	148 [78 - 350]

Table 4.1: **His-tagged protein binding to Tris-Ni(II)-NTA.** Kinetic parameters are obtained by least-square fitting of the binding curve $\Gamma(t) = \Gamma_{\text{eq}}(1 - e^{-(k_a c + k_d)t})$ and unbinding curve $\Gamma(t) = \Gamma_{\text{eq}}e^{-k_d t}$. Values in brackets indicate the 95% confidence intervals.

We observe a high variability between samples. This, may come from uncontrolled variations in the density of Tris-Ni(II)-NTA at the wall surfaces. Since this coating is PEG based, it depends on the electrostatic properties of the glass [Kenausis et al. 2000]. In this assay the glass walls consist of common etched glass slides of amorphous SiO_x with impurities. All the slides were base piranha cleaned right before surface functionalization, which had been observed to reduce sample variability. Nevertheless, the specific functionalization of the walls involves a step of drying the sample, which may induce inhomogeneities between samples and within the sample due to sedimented salts.

We performed an alternative experiment to estimate the association and dissociation rates in a particular sample. In this case, we incubated $1.5\mu\text{M}$ 6H::protein (6H::eGFP::Tip1 or 6H::Mal3::mCherry) at 10mM imidazole and monitored the fluorescence intensity signal at the walls over time. As seen in figure 4.2 c, 50 minutes after incubation, protein immobilization has reached equilibrium. We then wash unbound protein out with 10mM imidazole and monitor protein unbinding from the wall receptors.

Table 4.1 shows the fitted association and dissociation rates, and the K_D for each sample. In this case the K_D of the Mal3 experiment was around 70 nM and the one of Tip1 around 150 nM. These values are slightly lower than the ones obtained from the binding curve using multiple samples (230nM). Differences could be due to sample variability. In our imaging conditions, $1.5\mu\text{M}$ of 6H::eGFP::Tip1 is 2.6 ± 0.2 times brighter in the bulk than the same concentration of 6H::Mal3::mCherry. In agreement, fluorescence intensity at the wall is higher for Tip1 than Mal3 (figure 4.2 c). Assuming that fluorescence intensity scales linearly with protein concentration for the case of 6H::eGFP::Tip1 as we have seen for 6H::Mal3::mCherry, we can correct for the different intensity read-out. This correction yields higher coating of Mal3 than Tip1, as expected for the fitted binding and unbinding rates.

4.3. MICROTUBULE-BASED DELIVERY OF +TIPS TO THE BIO-MIMETIC CORTEX.

In the previous section we measured the concentration dependency of free binding of his-tagged +TIP proteins to the functionalized walls. Microtubules produce a local increase in +TIP concentration at their plus end that can be brought to the wall. However, is this higher concentration of protein sufficient to enhance local deposition to the wall?

We expect two possible ways of microtubule-based +TIP deposition: either the protein transiently binds to both the microtubule and the wall receptor, thereby tethering the microtubule to the wall, or the protein unbinds first from the microtubule and

reaches the wall receptor after 3D diffusion. In the later case, protein binding to the wall follows the same kinetics as measured for free binding in the previous section.

In both cases, when a microtubule undergoes catastrophe, it acts as an instant source of proteins close or pre-bound to the wall which may promote binding to the receptors.

In the tethering case, simultaneous binding of +TIPs at the microtubule might cause two opposing effects. On the one hand, the microtubule can catalyse +TIP binding to the wall as it produces a multivalent protein scaffold; i.e. several proteins with a low affinity for the wall receptor are bound together by the microtubule. This increases the avidity of the whole system, acting as an oligovalent ligand [Kitov and Bundle 2003, Krishnamurthy and Estrofi 2006]. However, by staying attached to the microtubule, proteins have reduced degrees of freedom. The kinetics of a single binding to the wall receptor may then be slowed down by the entropic cost for the protein link and the wall receptor to change conformation and produce the binding [Martinez-Veracoechea and Leunissen 2013]. If the entropic cost of translation and rotation of the links is small, then the microtubule can speed up protein deposition via the scaffolding property mentioned before.

4

+TIP DELIVERY ASSAY

To test microtubule-based deposition of +TIPs to the bio-mimetic cortex we let microtubules grow towards the walls in the presence of 6H::Mal3::mCherry or 6H::eGFP::Tip1, Tea2 and Mal3. Figure 4.3 a shows a scheme of the assay used. Dynamic microtubules grow from GMPCPP stabilized microtubule seeds immobilized on the surface via biotin-streptavidin linkages. When a microtubule tip encountered the Tris-Ni(II)-NTA functionalised wall at a certain spot, its tip could remain in contact with the wall spot by either stalling or maintaining growth and buckling. After some contact time, the microtubule tip would leave the spot by undergoing catastrophe or sliding with the tip along the wall (figures 4.3 b, 4.5 a and b, and 4.6 a and b).

The probability of a tip leaving the first wall contact spot by catastrophe as opposed to sliding along the wall differed between samples with 6H::Mal3::mCherry and samples with 6H::eGFP::Tip1 in the presence of Tea2 and Mal3 (figure 4.4 a). In samples with only 6H::Mal3::mCherry, 70% of the microtubules left the spot by catastrophe, while only 44% did so in the 6H::eGFP::Tip1, Tea2 and Mal3 samples. Moreover, in the 6H::eGFP::Tip1 samples, half of the sliding microtubules would also buckle.

Stalling and buckling microtubules had been already observed before with bare micro-fabricated barriers. Stalling occurs because the polymerization rate decreases under load [Dogterom and Yurke 1997]. Stalled microtubules are more prone to undergo catastrophe [Janson et al. 2003, Janson and Dogterom 2004]. This process can be modulated by +TIPs. In the absence of +TIPs, *in vitro studies* showed that microtubule stalling times follow a gamma distribution with half time of ~ 90 s and the shortest contact time of ~ 40 s [Kalisch 2013]. However, in the presence of Mal3 as only +TIP, the distribution of contact times is exponential with a half time of 20 s. In the presence of Tea2, Tip1, and Mal3, microtubule stalling times also showed an exponential distribution with a half time of 35 s. It was therefore concluded that Tea2-Tip2 do not significantly stabilize microtubules under load [Kalisch 2013].

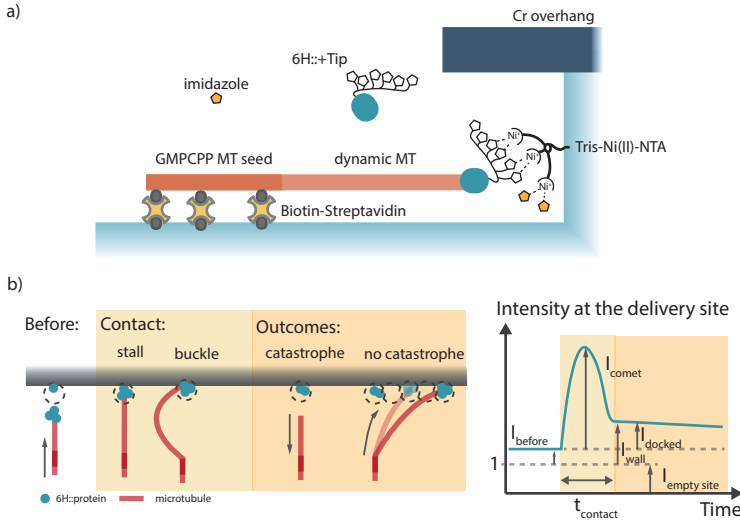


Figure 4.3: **Schematic of a delivery experiment.** (a) Experimental setup. Observation is done with spinning disk microscope at 2 or 3 z planes separated $0.3 \mu\text{m}$ and collapsed in one image by maximum pixel projection. (b) Possible outcomes upon microtubule contact with the wall in 'end-on' configuration. For the cases when the microtubule does not undergo catastrophe, we segment the microtubule path into contact sites and perform the same analysis at each site. The last site will correspond to the *catastrophe* site. The path segmentation is optimized to minimize splitting of the point spread signal of docked protein.

In our hands the average microtubule-barrier contact time at a fixed spot was 40 s for 6H::Mal3::mCherry and 130 s for 6H::eGFP::Tip1, Tea2 and Mal3 (see figure 4.4 b for the distributions). Note that in Kalisch 2013, only stalling events were considered, while in figure 4.4 b also buckling events are counted.

In our assay, the presence of 6H::eGFP::Tip1, Tea2, and Mal3, stabilizes microtubules upon barrier contact with respect to the presence of Mal3 alone. The reason why this was not found in Kalisch 2013 may be due to different protein concentrations used (50 nM Tip1 in Kalisch 2013 versus 150 nM Tip1 in our assays). In addition, there might be a stabilizing effect due to the engineered affinity between 6H::eGFP::Tip1 and the functionalized walls.

MEASUREMENT OF PROTEIN DEPOSITED

In order to quantify the amount of protein deposited from the microtubule to the wall, we defined wall contact spots (dotted circles in figure 4.3 b) where we monitored the fluorescence intensity over time (4.3 right). When a microtubule tip enters the spot, the fluorescence signal increases, and upon microtubule departure, it decreases. We defined the deposited intensity, $I_{deposited}$, as the difference in intensity between after and before the microtubule contact. To account for non-uniform illumination in the field of view, the images were background subtracted and the intensity in the contact spot was normalized by the average intensity of empty sites in that well, i.e. sites unvisited by a microtubule and where there is not protein immobilized. Therefore, a spot intensity be-

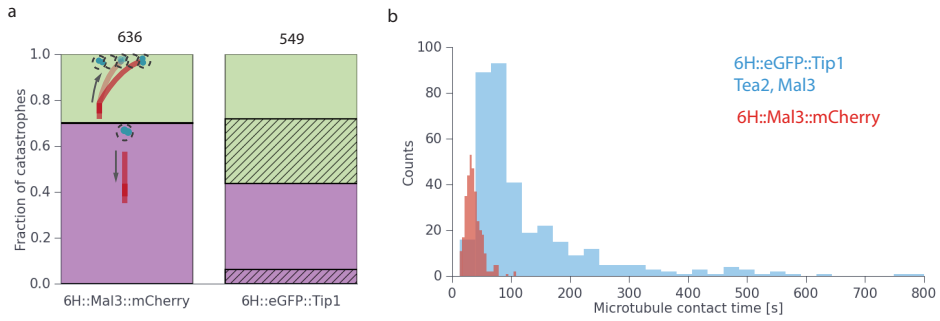


Figure 4.4: **Dynamics of microtubule wall contact.** (a) Fraction of microtubules leaving the first wall contact spot by catastrophes, **purple**, and sliding along the wall **green**. Hatched area corresponds to microtubule buckling, prior to catastrophe, or during gliding. Numbers on top are the number of events observed. (b) Histogram of the microtubule residence time at the wall spot of measurement.

4

fore contact of 1 a.u. corresponds to no protein pre-bound on the wall spot. The amount of protein brought by a microtubule tip was obtained by the amplitude of a Gaussian fit to the intensity at the spot during microtubule contact. Since long microtubule tip contacts displayed high spot intensity oscillations over time, the Gaussian fitting was limited to the times of highest intensity. This comet intensity is referred as I_{comet} . Alternatively, we measured the average intensity during the whole contact with the wall, $I_{contact}$.

The defined contact spot corresponds to the same volume of a cylinder of radius 225 nm and height 300 nm, which is $9.5 \cdot 10^7 \text{ nm}^3$. This measurement expands along a wall surface of $\sim 0.14 \mu\text{m}^2$. Due to the normalization performed, when there are no proteins bound to the wall spot its intensity is 1 a.u independently of the fluorophore used. For a bulk protein concentration of 150 nM, the defined spot contains on average approximately 8.6 his-tagged fluorescent molecules. Assuming some protein loses in sample incubation due to protein sticking in surfaces, the real amount of protein observed is expectedly less than the theoretically incubated. Due to a lack of better calibration of the fluorescence intensity for tagged proteins, we estimate to have 8 fluorescent molecules per spot volume, which corresponds to a 8% of protein loss. Then, the average intensity measured per protein would be around 0.125 a.u.

In order to obtain a better estimate of the intensity value of a fluorescent molecule, one could do the calibration by plotting the histogram of all the intensities of proteins bound to the wall. This should give periodic peaks indicating the average measured fluorescence intensity signal of integer number of fluorophores. However, since our assay has a high background number of proteins in solution, such analysis is not possible.

To determine that fluorescence intensity scales linearly with the spot fluorescence intensity, even after background subtraction, one should measure bulk fluorescence intensities at the wall spots at different protein concentrations. Unfortunately we have not performed this measurement for this thesis, therefore we will assumed linearity between fluorescence intensity and amount of protein.

MICROTUBULES CAN DEPOSIT 6H::EGFP::TIP1 TO THE BIOMIMETIC CORTEX, BUT NOT 6H::MAL3::MCHERRY.

Figure 4.5 shows two examples of microtubule-based delivery of 6H::Mal3::mCherry. In both cases Mal3 delivered to the wall did not remain attached to it after microtubule catastrophe. This can be clearly seen in the kymographs along the microtubules and the intensity at the spot (4.5 b and c). Although the 6H::Mal3::mCherry fluorescence signal at the wall spot increased upon microtubules contact, it returned to pre-contact values, after microtubule catastrophe. In example 1, the wall already contained some protein bound ($I_{before} > 1$ a.u.), while in example 2, the site was empty ($I_{before} \sim 1$ a.u.).

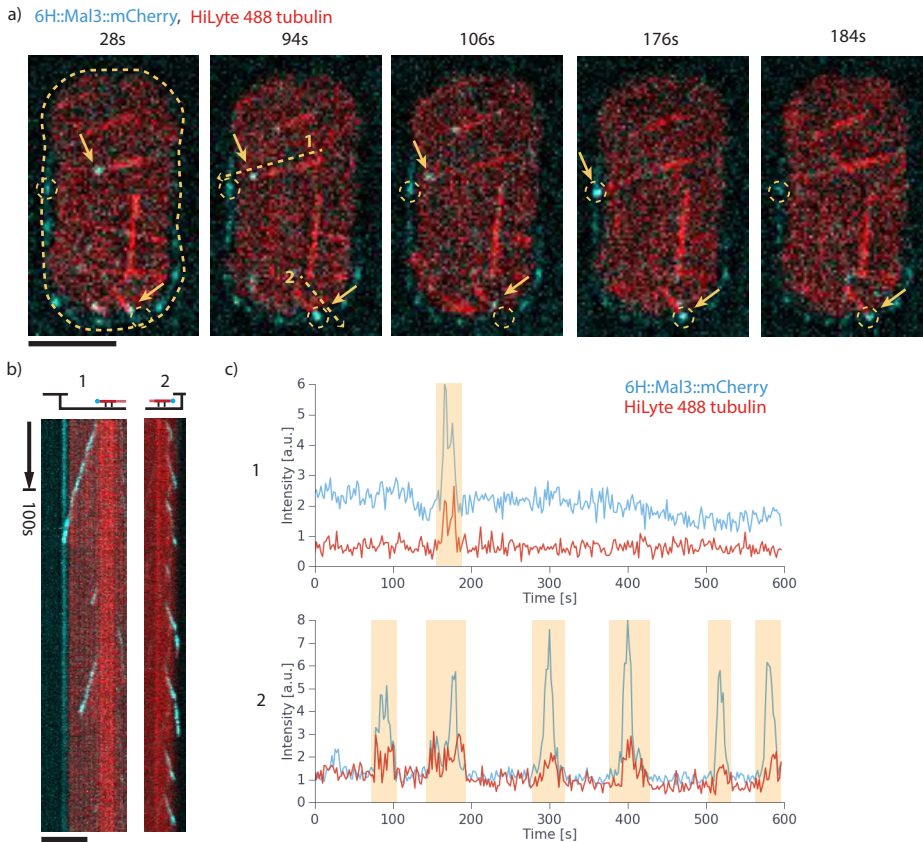


Figure 4.5: **Delivery of 6H::Mal3::mCherry.** (a) Spinning disk confocal images of selected times of two deliveries of 6H::Mal3::mCherry. Yellow dashed lines indicate the wall position and the delivering microtubules. Arrows indicate the locations of delivery. Scale bars $5 \mu\text{m}$. (b) Kymographs of the two microtubules with the arrows in (a). Scale bars $5 \mu\text{m}$. (c) Fluorescence intensity over time at the spot of delivery (dotted circles on (a)) in arbitrary units normalized at bulk intensity at the wall when there is not protein immobilized). Orange bars indicate the contact times between the microtubule and the wall spot.

In the case of delivery of 6H::eGFP::Tip1 in the presence of Tea2 and Mal3, clear depositions could be observed. Figure 4.6 shows two examples. In example 1, the microtubule did not undergo catastrophe and kept sliding along the wall after 6H::eGFP::Tip1 deposition. This indicates that microtubule catastrophe is not required for microtubule-based docking of proteins to a cortical receptor. In example 2, the microtubule tip stopped at the docking spot while maintaining growth and buckling. After microtubule catastrophe it can be seen that some amount of protein was left behind. During the de-polymerizing phase, the microtubule slid back along the wall, and passed again through the spot of example 1. This contact did not leave extra protein behind at the wall (figure 4.6c at ~110s). None of the two examples contained protein at the docking site before the microtubule contact ($I_{before} \sim 1$ a.u.).

4

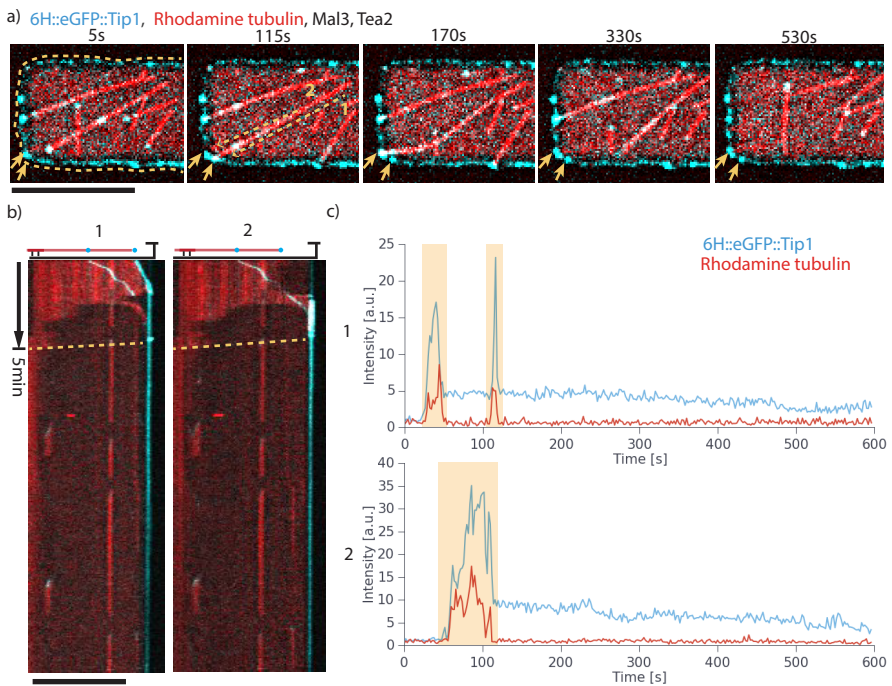


Figure 4.6: **Delivery of 6H::eGFP::Tip1.** (a) Spinning disk confocal images of delivery 6H::eGFP::Tip1 to functionalized walls at selected times. Yellow dashed lines indicate the wall position and the delivering microtubules. Scale bar $10 \mu\text{m}$. (b) Kymographs of the microtubule with the arrows in (a). After the first delivery of protein, the microtubule kept sliding at the wall until a second spot (second kymograph) where it delivered more protein and underwent a catastrophe. Since the microtubule kept growing under load, it buckled, and no tubulin signal is observed in the kymograph along a straight line. The dotted yellow line indicates the time of catastrophe. Scale bar $10 \mu\text{m}$. (c) Fluorescence intensity over time at the spot of delivery (dotted circles on (a)) in arbitrary units normalized at bulk intensity (Intensity at the wall when there is not protein immobilized). Orange bars show the contact times between the microtubule and the wall.

EFFICIENCY OF PROTEIN DEPOSITION UPON CATASTROPHE

We defined the efficiency of protein docking at the wall by the ratio between the amount of protein deposited at a contact spot and the amount brought by the microtubule comet. Note that this value may depend on many factors like microtubule contact time at the spot, accessibility of the his-tagged proteins to the wall receptor and local density of Tris-Ni(II)-NTA molecules. Here, we arbitrarily decided to consider only the events in which a microtubule underwent a catastrophe while in contact with the wall in an angle with the wall bigger than $\sim 15^\circ$. Depositions from the microtubule lattice or while sliding along the wall will be discussed later.

Figure 4.7 a shows the comparison between 6H::eGFP::Tip1 and 6H::Mal3::mCherry depositions. Delivery events were binned by comet intensity. Histograms on the sides illustrate the event count. 6H::eGFP::Tip1 deposition exhibited an average $20 \pm 1\%$ docking efficiency, i.e. $20 \pm 1\%$ of the comet protein docked on average to the wall spot upon microtubule tip contact. However, for 6H::Mal3::mCherry, there is virtually no transfer of protein, as the average amount of intensity transferred is ~ 0.03 a.u., regardless of the amount of protein delivered by the microtubule. With our resolution it is not possible to discard that no 6H::Mal3::mCherry is deposited at all.

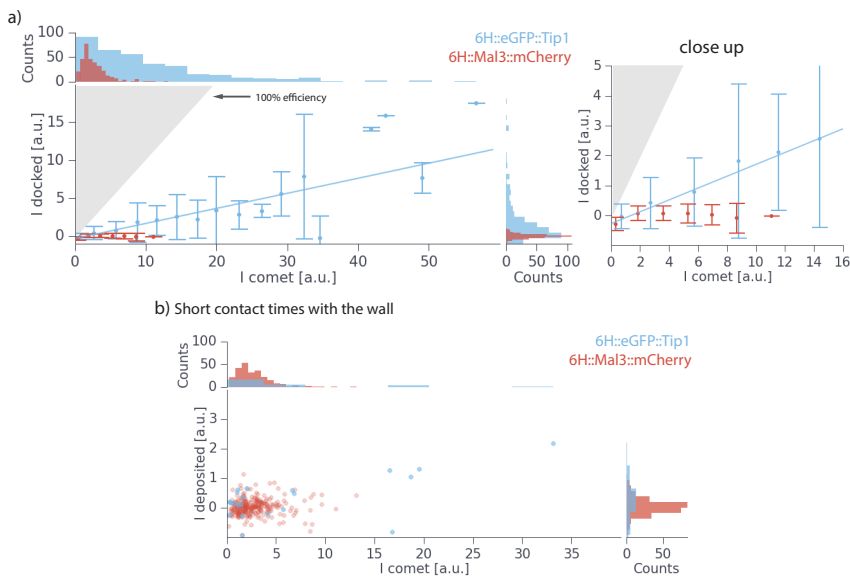


Figure 4.7: **+TIP deposition efficiency upon microtubule catastrophe.** (a) Amount of protein deposited at the wall spot (fluorescence intensity units) versus protein delivered by the microtubule for all the cases a microtubule tip encountered the wall in less than 15° and underwent catastrophe. The data is shown binned by comet intensity according to the Friedrich-Diaconis rule [Freedman and Diaconis 1981]. For all the data points, see figure 4.15. (b) Scatter plot of the amount of protein deposited in microtubule wall contacts shorter than 40 second (time between the microtubule enters and leaves the measurement area).

Given our estimate of the average fluorescence of one molecule around 0.125 a.u.

(section 4.2), in our conditions, a microtubule tip brings on average 22 6H::Mal3::mCherry molecules and can easily bring up to 70. Analogously, a 6H::eGFP::Tip1 comet consists on average of 80 Tip1 molecules, and can easily contain up to 280. The average microtubule tip, therefore, deposits 16 Tip1 molecules and no Mal3 upon catastrophe. Those values are slightly lower than the amounts of +TIPs estimated in cells. For instance, in epithelial cells, microtubule tips have been estimated to contain ~ 270 EB1 molecules [Seetapun et al. 2012]. Tea1 deposition efficiency in *S. pombe* cells has not been measured. Qualitative analysis suggest it is much higher than in our *in vitro* assay [Dodgson et al. 2013].

Since microtubules in the presence of 6H::eGFP::Tip1, Tea2 and Mal3 exhibit longer residence time in contact with a wall spot (figure 4.4 b), we also plotted the deposition efficiency for the subset of microtubules which had short wall contact times (figure 4.7 b). These were very few cases, which only lead to clear 6H::eGFP::Tip1 depositions when higher amounts of 6H::eGFP::Tip1 than 6H::Mal3::mCherry were brought on the microtubule tip.

4

6H::EGFP::TIP1 DEPOSITION WITHOUT CATASTROPHE

The example of figure 4.6 showed that microtubules do not need to undergo catastrophe to deposit 6H::eGFP::Tip1 at the wall. We looked at the efficiency of delivery to a spot when the microtubule leaves that spot without undergoing a catastrophe (figure 4.6 b). We observed that in several occasions, microtubule-based deposition while sliding occurred in discrete spots.

We looked at the docking efficiency as a function of microtubule contact time with the wall spot. Figure 4.8 shows the same efficiency plots as before for each microtubule contact event for the cases in which the microtubule exited the spot by catastrophe and the cases in which it slid (no catastrophe). Those events have been colour coded by the time the microtubule remained in contact with the wall spot. Blue data points correspond to contacts shorter than the average contact time, ~ 100 s; while red data points correspond to longer contacts.

For the catastrophe cases, long contacts were equally efficient at depositing 6H::eGFP::Tip1 than short contacts (18% versus 23% respectively, figure 4.8a). However, microtubules with very low comet intensities exhibited a short contact with the wall (as observed by the prevalent display of blue data points for $I_{\text{comet}} < 4$ a.u.). This is in agreement with Tea2-Tip1 stabilizing the microtubule upon barrier contact in a concentration dependent manner, i.e. microtubules with little amount of Tea2-Tip at the tip are more prone to undergo catastrophe upon wall contact.

For the no catastrophe cases, deposition efficiency was on average lower than the catastrophe cases. Moreover, short contacts lead, on average, to much less deposition of 6H::eGFP::Tip1 (figure 4.8 b). This, indicates that microtubule catastrophe facilitates protein deposition.

This result is quite intuitive. His-tagged eGFP::Tip1 binding to the wall receptor may occur simultaneous to binding to the microtubule tip, or after 3D diffusion upon unbinding from the microtubule. In both cases, complete deposition of the protein (off-loading to the wall) requires unbinding from the microtubule. Microtubule catastrophes causes

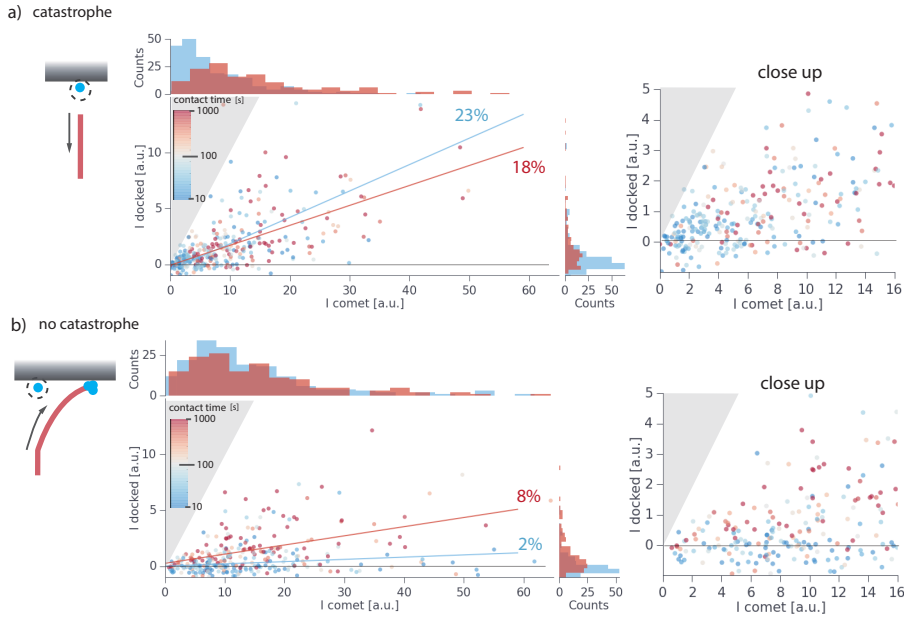


Figure 4.8: **Dependency of 6H::eGFP::Tip1 deposition efficiency.** Amount of protein deposited at the wall spot (fluorescence intensity units) vs protein delivered by the microtubule after (a) catastrophe or (b) microtubule leaving the spot without catastrophe. Data points are colour coded by microtubule residence time at the spot.

protein unbinding from the tip, therefore it can facilitate protein deposition. It is therefore not surprising that the efficiency of protein deposition does not depend on the time the microtubule remained in contact with the wall prior to catastrophe. This pulse release of protein does not occur when there is no catastrophe. In this case, microtubule sliding away from the spot may force the rupture of a pre-established bond with the wall. Since the walls are prepared so that the $K_D^{\text{wall}} > K_D^{\text{microtubule}}$, it is less probable that binding to the wall triggers unbinding from the microtubule than the opposite. Then, protein unbinding from the microtubule is approximately described by its dissociation rate, independently of any effect from the wall receptors.

The dissociation rate of a +TIP from the microtubule tip can be measured by fluorescence intensity recovery after photobleaching (FRAP). Those measurements were presented in chapter 2 (table ??). The data showed that 6H::eGFP::Tip1 displays two distinct dynamics on the microtubule tips. One type has half time of 5-20 s, while the other type does not exchange on the tip in at least 40 s. We hypothesized that the slowly exchangeable fraction of Tip1 may be associated in clusters held by Mal3 and carried by more than one Tea2. Then, even though these particles detach less easily from the microtubule (as seen from their high dissociation rate), they would have a higher avidity for the wall receptor due to containing multiple Tip1 molecules.

In chapter 2 we showed that high densities of Tip1 in the presence of Tea2 and Mal3

can steer a microtubule tip along another microtubule. Analogously, microtubule tips could be captured by Tip1-mediated binding at the wall. We investigated this effect in the next section.

MICROTUBULE TIP CAPTURING AT THE WALL

We observed that microtubule tips sliding along the wall would often stop at spots (figure 4.9 a). The question is, what makes the microtubule tip stop at those places? There are three non-excluding factors that can cause the stopping: 1) a bump on the wall surface, 2) 6H::eGFP::Tip1 protein at the wall spot binding to the microtubule, and 3) Tip1 protein from the microtubule tip docking to the wall.

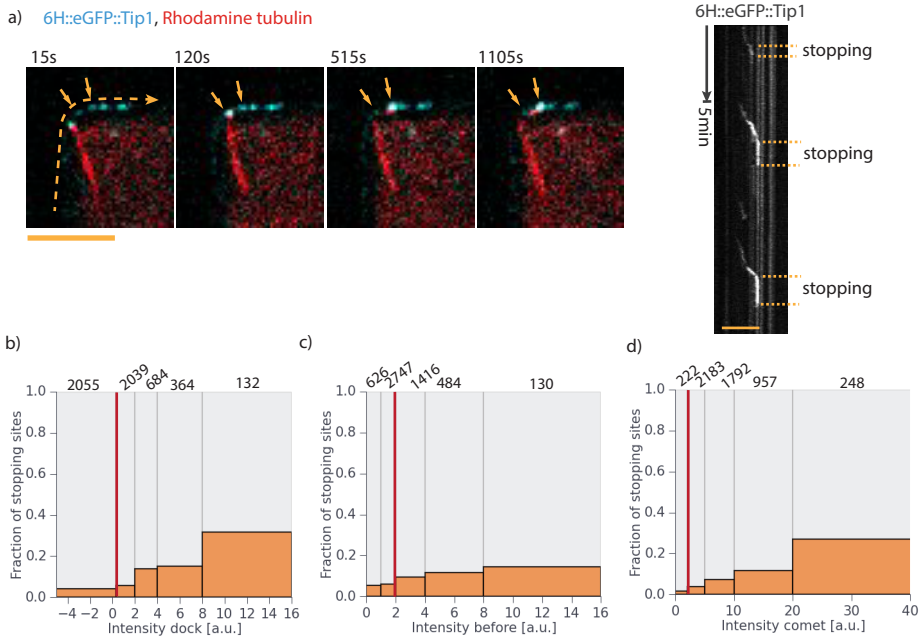


Figure 4.9: **Feedback with pre-docked protein.** (a) Example of microtubule gliding along the wall with multiple stops. Arrows point at stopping locations. Image on the right shows the kymograph along the wall (dashed line). Scale bars 5 μm . (b) Fraction of sites along the wall (pixels, 0.156 μm) where a microtubule stopped as a function of protein docked ($I_{\text{docked}} = I_{\text{after}} - I_{\text{before}}$), (c) protein pre-docked (I_{before}), and (d) protein at the microtubule tip (I_{contact}). Numbers on top are the total amount of counts per bin. Intensities have been normalized to the average intensity of no protein docked. The red line indicates the separation between a non-successful docking and a successful one. A stop is defined by a sliding speed slower than $0.2 \mu\text{m}^{-1}$. The red line indicates the separation between no protein pre-docked before the microtubule arrived, and protein pre-docked.

To determine the contribution of the last two factors, we performed kymographs of splines along the perimeter of the walls where microtubule tips slid (figure 4.9 a right). For each pixel position along the wall, we measured the fluorescence intensity before,

after, and while the microtubule tip was in contact, as well as the time the microtubule plus end remained at that pixel location.

Figures 4.9 b, c and d show the fractions of pixel locations where a microtubule tip stopped as a function of the amount of protein docked, the amount of protein found in that location before microtubule arrival, and the amount of protein brought by the microtubule respectively. Docking intensities below 0.3 a.u. were considered as non successful docking events. Figure 4.9 b shows that the sites where a microtubule stopped correlate positively with the sites where protein was deposited. On the other hand, stopping showed nearly no correlation with the amount of protein previously bound at the wall but a slightly stronger correlation with the amount of protein brought by the microtubule tip. This data suggests that 6H::eGFP::Tip1 in the presence of Tea2 and Mal3 can form a bridge between the microtubule and the wall that captures microtubules. Moreover, this bridge is easier to form from protein that pre-bound to the microtubule tip reaching the wall than from protein pre-bound at the wall. This, could be because all the sites at the microtubule tip are already occupied once the microtubule reaches the wall site.

The observed microtubule tip capturing by 6H::eGFP::Tip depositions to the wall are very reminiscent to *in vivo* observations. In *S. pombe* cells microtubule capturing has been suggested to occur via interaction between Tea1 and its cortical receptor since deletion of Tea1 lead to microtubule curling around the poles [Mata and Nurse 1997].

FEEDBACK WITH PRE-DOCKED PROTEIN

Saccharomyces pombe cells have a positive feedback between the receptor Mod5 and the polarity factor Tea1. Mod5 localization at the cell poles is enforced by Tea1 depositions there (see chapter 1). In our case, the engineered receptor is not mobile. However, other types of feedbacks could occur. For instance if a microtubule tip remained longer in spots of previous Tip1 depositions, more protein could be deposited there. On the other hand, cooperative docking, obtained when previously docked protein enhances the binding affinity for new protein, would also act as a feedback. In the previous section we saw that pre-docked protein has little, if no, effect on stopping the microtubules. Here we ask whether it can facilitate docking of new Tip1 molecules.

Figures 4.10 a and b shows an example of a microtubule that stopped two times at the same wall spot. The first time, a high number of 6H::eGFP::Tip1 was deposited, however the second time no protein was deposited. In both cases, the microtubule buckled maintaining a plus end contact with the deposition spot at the wall while growing.

Quantification of all the sliding events (figure 4.10 c) shows that the percentage of events with a docking success decreased with the amount of protein pre-docked at the wall. This data indicates that microtubule can deliver up to a maximum amount of protein to a wall spot, once this is filled, multiple contacts do not lead to more protein deposition. Therefore, in our assay, protein binding to the wall is not cooperative.

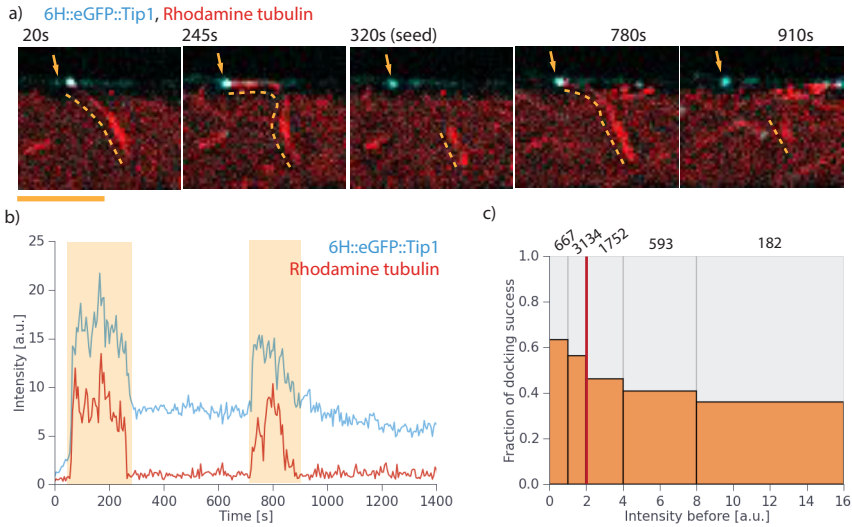


Figure 4.10: **Feedback with pre-docked protein.** (a) Example of microtubule gliding along the wall with two stops at the same wall spot. The arrow indicates the stopping location. Scale bar $5\ \mu\text{m}$. (b) Fluorescence in intensity overtime at the stopping spot. Orange bars indicate the contact times between the microtubule and the wall. (c) Fraction of successful docking events (at a pixel length along the wall) of 6H::eGFP::Tip1 as a function of pre-docked protein (I_{before}). Numbers on top indicate the total amount of counts per bin. Intensities have been normalized to the average intensity of an empty site. A successful docking was defined as $I_{\text{dock}} > 0.3$ a.u., where only cases with $I_{\text{comet}} > 1.5$ were considered. The red line indicates the separation between no protein pre-docked before the microtubule arrived, and protein pre-docked.

6H::eGFP::TIP1 DOCKING FROM LATERAL CONTACTS WITH THE WALL

Often, microtubules would contact the wall laterally from the GDP lattice. Occasionally, docking of 6H::eGFP::Tip1 would occur in those circumstances. See an example in figure 4.11. In those cases, microtubules exhibited gliding along the lateral wall contacts towards the minus end. This gliding must be mediated by Tea2, either deposited to the wall together with Tip1, or interacting with Tip1 at the wall. From our data, it is not possible to distinguish between the two cases. However, since Tip1 and Tea2 form a stable complex [Bieling et al. 2007], it is quite probable that both proteins are deposited.

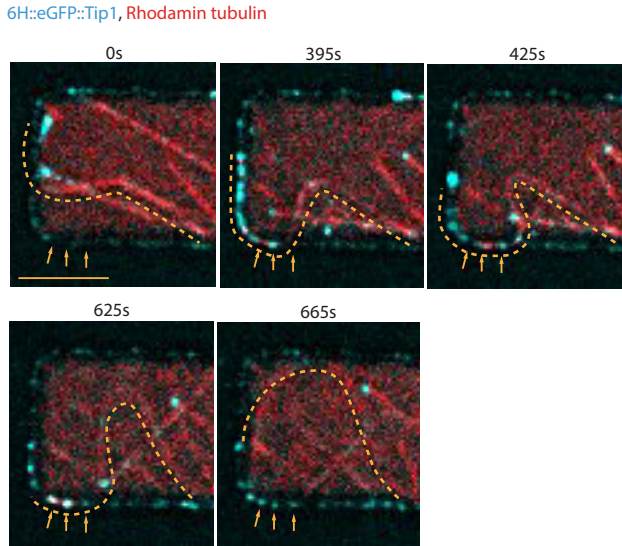


Figure 4.11: **6H::eGFP::Tip1 docking to the wall from the microtubule GDP lattice.** Example fo GDP lattice docking events. Yellow dotted lines indicate the shape of the microtubule of interest, and arrows indicate the docking sites. The shape of the microtubules is caused by the seed attachment to the surface, interactions with other microtubules and sliding mediated by Tea2-6H::eGFP::Tip1 molecules at the walls. Scale bar $5\ \mu\text{m}$.

4.4. DISCUSSION

In this chapter we reconstituted microtubule-based deposition of 6H::eGFP::Tip1 to a bio-mimetic cortex on glass micro-wells. The K_D of the synthetic cortical receptor used, Tris-NI(II)-NTA, could be tuned to the range of cytoplasmic protein concentrations needed for microtubule tip tracking. This allowed +TIPs to bind first to the microtubule tip, and later be delivered to the bio-mimetic cortex by the microtubule.

We found that 6H::eGFP::Tip1 in the presence of Mal3 and Tea2 could be efficiently deposited to the bio-mimetic cortex while 6H::Mal3::mCherry alone could not. In particular, a microtubule tip contact with the wall deposited on average 20% of 6Hs::eGFP::Tip1 from the microtubule tip to the wall upon catastrophe.

His-tagged eGFP::Tip1 deposition did not require microtubule catastrophe. However, microtubule catastrophe enhanced deposition efficiency. Efficient deliveries without microtubule catastrophe correlated with long contacts of the microtubule tip with the wall spot. Further analysis suggests that 6H::eGFP::Tip1 in the presence of Tea2 and Mal3 can tether microtubules by their tip at the wall. This state can be maintained for some seconds and the microtubule can still grow and buckle. Such long tethering events may be analogous to previously observed Tip1, Tea2 and Mal3-based steering of a microtubule tip on another microtubule GDP lattice (chapter 2).

The reason why depositions without microtubule catastrophe are on average less efficient than upon catastrophe may have several factors. A 6H::eGFP::Tip comet ex-

tends a few hundreds of nanometres (see chapter 2). Due to geometry reasons, not all 6H::eGFP::Tip1 may have access to binding at the wall receptor while bound to the microtubule tip. Therefore, microtubule tethering to the wall is held by a subset of 6H::eGFP::Tip1s from the tip. Microtubule sliding away from the wall may be due to stochastic unbinding of the tethering molecules from the microtubule, or release of bending energy from the buckled microtubule (i.e. the microtubule suddenly straightens and snaps away). In both cases, the non tethering molecules are more probable to remain bound to the microtubule than to suddenly unbind. Therefore, only the tethering molecules may contribute to deposition.

His tagged eGFP::Tip1 stabilizes the microtubule against catastrophes upon contact with the wall in a dose dependent manner. This allows microtubule tips to slide along the wall before 6H::eGFP::Tip1 deposition. In the rod-shaped *S. pombe*, this effect may prevent deposition at the sites of the cell by reducing the probability of catastrophes there. We have further seen that 6H::eGFP::Tip1 allows microtubules in the presence of Mal3 to grow while buckling for several seconds. In cells, this ability is necessary for proper nucleus centring [Tran et al. 2001, Daga et al. 2006b].

High amounts of pre-docked protein at the wall reduce the percentage of successful posterior docking, indicating a saturation on the amount a microtubule can deposit. This effect, may impede high accumulation of protein at specific spots, therefore, it is expected to reduce the robustness of a cortical pattern.

There are several differences between the 6H::Mal3::mCherry delivery assay and the 6H::eGFP::Tip1 in the presence of Tea2 and Mal3 one including protein residence times and organizations of proteins at the microtubule tip, and microtubule dynamics. Therefore, several factors may play a role on the reason why we only observe clear depositions for the 6H::eGFP::Tip1 case. The biggest difference consists on the amount of protein. A microtubule tip brings less amount of 6H::Mal3::mCherry than 6H::eGFP::Tip1. Since Mal3 recruits Tea2-Tip1 complexes to the microtubule, the 'additional' amount of Tip1 found at microtubule tips comes from a non-stoichiometric interaction between the proteins. Several experiments in chapter 2 pointed out the existence of clusters of Tip1, Tea2, and Mal3 containing a high amount of Tip1 accumulating at microtubule tips. These clusters, would have a higher affinity for the wall receptor than single his-tagged particles, causing the observed difference between Tip1 and Mal3 depositions.

The data indicates that 6H::eGFP::Tip1 docking is not cooperative; i.e. protein binding to the wall does not facilitate the binding of new protein. This argues against the existence of Tip1 clusters, since, they cannot be formed at the wall. Nevertheless, the microtubule may serve as a better template for cluster formation since all the three proteins have a binding affinity for it, whereas only 6H::eGFP::Tip1 has an affinity for the wall. Therefore, cluster formation could happen only at the microtubule. This specific microtubule-based cluster formation would act as a switch to facilitate protein binding at the wall. In *S. pombe* cells, Tea1 accumulation at the poles depends on its trimerizing region [Bicho et al. 2010]. Furthermore, its appearance in the plasma membrane takes the form of clusters [Dodgson et al. 2013]. Together, our findings suggest that Tea1 clustering may occur on the microtubule to facilitate its deposition to the plasma membrane.

Cluster formation may have an implication in microtubule stability. One could wonder if 6H::eGFP::Tip1 docking to the wall and unbinding from the microtubule, promotes catastrophe since the Tip1-Tea2 stabilization has disappeared. If 6H::eGFP::Tip1 unbinds from the microtubule in a discrete manner, the new empty spot could also be replenished by new protein coming from the cytoplasm or the microtubule lattice. Therefore, microtubule destabilization upon discrete protein docking would be unexpected. On the other hand, if 6H::eGFP::Tip1 unbinds from the microtubule in clusters, replenishment might take longer, and a microtubule catastrophe could be promoted.

Another factor that may play a role in 6H::Mal3::mCherry unsuccessful docking may be its inability to tether the microtubule to the wall receptor. This can be because the protein is too small as compared to Tip1 or clusters of Tip1, therefore the his-tag is not accessible to the wall receptor, or because of Mal3 not sitting at the very tip of a growing microtubule [Maurer et al. 2012] which may be accessible by Tea2-Tip1 clusters.

Regarding the differences in Mal3 and Tip1 sizes, indeed Tip1 is a longer protein that could facilitate a flexible tethering of the microtubule to the wall. Moreover, members of the same family, CLIP-170, have been shown to mediate microtubule capturing at the cell cortex [Fukata et al. 2002b]. For the case of Mal3, a previous study in *S. pombe* cells showed that a chimera protein consisting of Mal3 fused to a membrane binding domain (Mal3::GFP::Pom1[305-510]) could interact with microtubule tips while bound to the plasma membrane [Recouvreux et al. 2016]. Similarly, other engineered chimeras of EB1 with motor proteins could produce steering of a microtubule tip on another microtubule *in vitro* [Doodhi et al. 2014, Chen et al. 2014]. It would be interesting to test if other constructs of Mal3 with a long linker for the his-tag, or chimeric proteins, would be able to be deposited and or tether microtubules to the bio-mimetic wall.

Regarding to the different protein distributions at microtubule tips, Mal3's inability to reach the very tip of the microtubule should only be relevant in 'end-on' microtubule-wall configurations. Analysis of depositions when the microtubule touches the wall in a parallel configuration, where Mal3 is presumably closer to the wall, showed no protein depositions (figure 4.15). Therefore, Mal3 distribution on microtubule tips is not a reason for its unsuccessful deposition to the wall.

Another factor that may play a role in protein deposition is microtubule contact time with the wall. Typical microtubule-wall contact times in 6H::Mal3::mCherry deliveries are 20-30 seconds, which is shorter than for samples in the presence of 6H::eGFP::Tip1, but arguably long enough for a binding reaction to occur. In addition, the short residence time of Mal3 at the microtubule tip would facilitate protein orientation and 3D diffusion towards the wall receptor. Therefore, we do not expect that binding to the wall receptor would take longer than the microtubule-wall contact time observed. As a comparison, similar short events in the assay of 6H::eGFP::Tip1 delivery were rare and only exhibited clear depositions in cases in which the microtubules contained a high number of 6H::eGFP::Tip1 molecules, possibly clustered, not observed in 6H::Mal3::mCherry comets.

In sum, 6H::eGFP::Tip1 deposition to the wall may be self-favoured by the way this protein accumulates at the microtubule tip and its effect on microtubule dynamics. Since

these factors are difficult to decouple, it is not possible to assess the importance of each by comparing the different results between the Tip1 and Mal3 depositions. To dig further, one could produce chimeric proteins with known modular functions, such as protein oligomerization, microtubule stabilization, etc.

In *S. pombe*, the receptor for polarity factors, protein Mod5, changes its distribution along the plasma membrane in accordance with to Tea1 deposition. In *Tea1* Δ cells, Mod5 is homogeneously distributed along the cell cortex. However, in wild type, Mod5 is enriched at the cell poles [Snaith and Sawin 2003]. This positive 'feedback' helps focussing the Tea1 cortical pattern. A mobile receptor could increase protein affinity at places of microtubule contact by increasing its density there. Nevertheless, deposited protein could diffuse away with the receptor, after microtubule release. It would be very interesting to test in the future the process of microtubule-based deposition to mobile receptors. This could be achieved by forming lipid by-layers on the micro-wells with functionalized lipids or in water in oil emulsion droplets. In chapter 6 we show a methodology developed to test deposition in emulsion droplets.

4

4.5. SAMPLE PREPARATION AND DATA ACQUISITION

Micro-well fabrication and wall functionalization

See chapter 3.

Protein purification and biochemistry

Proteins were purified as in section 2.8.

Data acquisition

All data shown in this chapter was obtained by spinning disk fluoresce microscopy using a IX81F-ZDC2 microscope (Olympus, Japan) with a spinning disk confocal head CSU-X1 (Yokogawa, Japan), 100X oil immersion objectives, and EmCCD camera iXon3 (Andor, UK). Excitation lasers 488 and 561 nm (Andor, UK) were used.

Unless stated otherwise, we used the following condition: AOTF laser intensity 22, exposure 300 ms, and EM Gain 115.

Free binding assay

After functionalization of the walls with Pll-g-PEG/Tris-Ni(II)-NTA ($0.2 \text{ mg}\cdot\text{ml}^{-1}$), with a bottom surface passivated with Pll-g-PEG ($0.2 \text{ mg}\cdot\text{ml}^{-1}$), surfaces were further passivated with κ -casein ($1.2 \text{ mg}\cdot\text{ml}^{-1}$ for 10 min). Right after, the stated protein concentration of either 6H::Mal3::mCherry or 6H::eGFP::Tip1 was incubated for 50 min in a MRB80 solution containing 0.1 % methyl cellulose, $0.4 \text{ mg}\cdot\text{ml}^{-1}$ glucose oxidase, 50 mM glucose, $0.6 \text{ mg}\cdot\text{ml}^{-1}$ κ -casein, 50 mM KCl and 10 nM imidazole. For the equilibrium binding curve fluorescence microscopy images were taken 50 minutes after protein incubation. For the unbinding measurement, the flow cell was flashed with MRB80 buffer with 50 mM KCl and 10 mM imidazole every 5 minutes. For all measurements fluorescence microscopy snapshots were taken at different locations along the sample at the z position of highest protein fluorescence intensity at the wall.

Microtubule-based +TIP deposition

Due to the big variability of the Tris-Ni(II)-NTA wall densities obtained from one sample to another, we typically pre-coated the walls of a whole cover-slip with Pll-g-PEG/Tris-NTA, and cut it to make three flow cells. The first flow cell would contain 10 mM imidazole in the final incubation. If the walls would get completely covered by 6H::eGFP::Tip1, the next flow cell would be incubated with a slightly lower concentration of imidazole, and vice-versa. That way, the K_D could be adjusted. After functionalization of the walls with Pll-g-PEG/Tris-Ni(II)-NTA ($0.2 \text{ mg}\cdot\text{ml}^{-1}$). The bottom surface was functionalized with Pll-g-PEG/biotin ($0.2 \text{ mg}\cdot\text{ml}^{-1}$ for 15 min), followed by streptavidin ($1 \text{ mg}\cdot\text{ml}^{-1}$ for 10 min), and then further passivated with κ -casein ($1.2 \text{ mg}\cdot\text{ml}^{-1}$ for 10 min).

The 6H::Mal3mCherry deposition assay was prepared by incubating 150 nM 6H::Mal3::mCherry in a MRB80 solution containing $14.25 \mu\text{M}$ tubulin, $0.75 \mu\text{M}$ Rhodamine tubulin, 1 mM GTP, 0.1% methyl cellulose, $0.4 \text{ mg}\cdot\text{ml}^{-1}$ glucose oxidase, 50 mM glucose, $0.6 \text{ mg}\cdot\text{ml}^{-1}$ κ -casein, 50 mM KCl and 10 mM imidazole. Z-stacks of 2-3 focal planes separated 300 nm were taken every 2 s for 10 min.

The 6H::eGFP::Tip1 deposition assay was prepared by incubating 150 nM 6H::eGFP::Tip1, 100 nM Mal3 and 10 nM Tea2 in a MRB80 solution containing $14.25 \mu\text{M}$ tubulin, $0.75 \mu\text{M}$ Rhodamine tubulin, 1 mM GTP, and 2 mM ATP, 0.1% methyl cellulose, $0.4 \text{ mg}\cdot\text{ml}^{-1}$ glucose oxidase, 50 mM glucose, $0.6 \text{ mg}\cdot\text{ml}^{-1}$ κ -casein, 50 mM KCl and 10 mM imidazole. Z-stacks of 2-3 focal planes separated 300 nm were taken every 5 s for 25 min.

4.6. DATA ANALYSIS

FFT IMAGE CORRECTION

Due to some unfixed problem in the spinning disk used, the signal from the 561 nm emission laser would contain extra intensity speckles (figure 4.12 top left). Since those speckles were periodically spaced (most probably coming from the pinholes of the spinning disk), they could be reduced by erasing periodic signals in the Fourier transform of each image. All this treatment was done with a custom **ImageJ** macro (functions *FFT*, *make rectangle*, *cut*, and *Inverse FFT*).

BACKGROUND SUBTRACTION AND MAXIMUM PIXEL INTENSITY PROJECTION

To account for inhomogeneous illumination along the field of view and at each plane of the z-stack, we determined the background by morphological opening of each picture with a 2D disk structuring element of radius 3 (*mahotas.morph.open* and *pymorph.sedisk* packages in **Python 2.7**). The obtained background was subtracted (figure 4.13). Figure 4.14 shows the intensity profile along a horizontal line along the image for the raw image, the calculated background and the final image after background subtraction.

The sample shown consists of 6H::GFP::CLASP2 α (chapter 7) bound to Pll-g-PEG/Tris-Ni(II)-NTA coated walls and in solution. It can be observed that this method gives a unfair ratio between the signal in the middle of a well and under the overhang. Independently, the chromium overhang produces an amplification of the fluorescence signal (not shown), therefore, it is not suitable to compare signals under the overhang and away from it. This method of background subtraction may cause a sharpening effect at the edge of the overhang.

After background subtraction, the different focal planes where projected into one

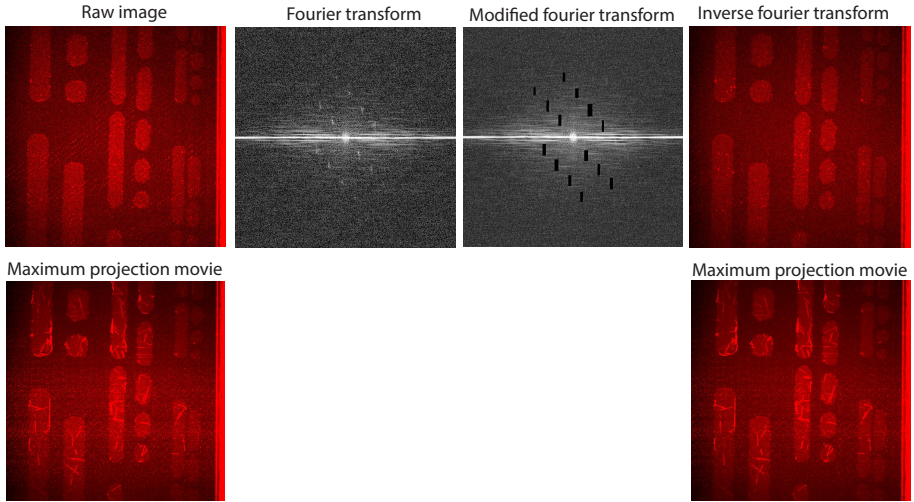


Figure 4.12: **Fourier transform image correction of periodic speckles.** Bottom images show the pixel maximum projection on all the focal planes and along a time lapse movie of 300 frames (25 min).

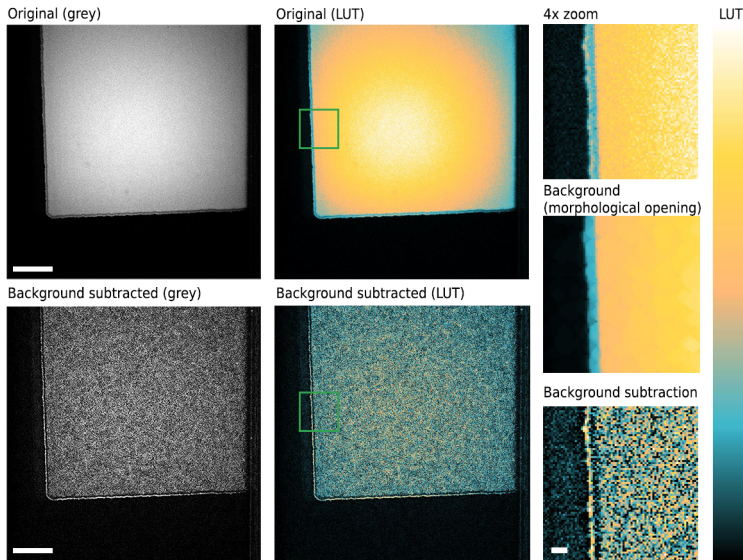


Figure 4.13: **Background subtraction.** The left and bottom dark sides of the image correspond to the chromium-gold layer overhang. The right dark side, corresponds to the extreme of the field of view. Scale bars $5\ \mu\text{m}$.

image by maximum pixel intensity. That way the final image corresponds to a selection

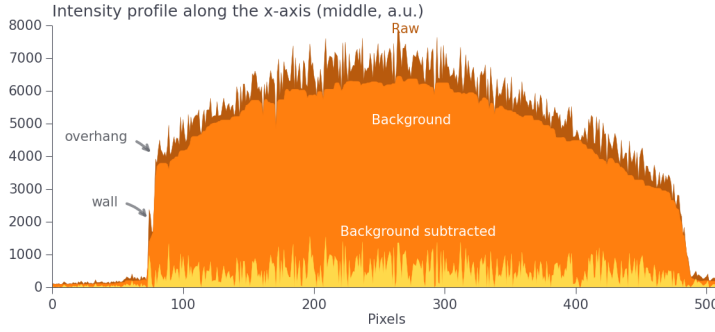


Figure 4.14: **Background subtraction profile.** Intensity profile along a horizontal line on the image of figure 4.13 and the corresponding background detection and subtraction. Note that on the left the image contains a wall, while on the right the profile is darker due to the end of the field of view.

of the best focal place where the fluorophore is found.

6H::+TIP FREE BINDING CURVES

Surface coverage of a ligand binding to an immobilized receptor in a 1:1 stoichiometry follows the following relation:

$$\frac{d\Gamma}{dt} = k_a \Gamma_{\max} c - (k_a c + k_d) \Gamma(t) \quad (4.1)$$

Therefore, integrating

$$\Gamma(t) = \Gamma_{\text{eq}} \left(1 - e^{-(k_a c + k_d)t} \right) \quad (4.2)$$

Dissociation after wash-out of the protein is given by

$$\Gamma(t) = \Gamma_{\text{eq}} e^{-k_d t} \quad (4.3)$$

The equilibrium coverage is given by the Michaelis-Menten relation

$$\Gamma_{\text{eq}} = \Gamma_{\max} \frac{c}{K_D + c} \quad (4.4)$$

where

$$K_d = \frac{c(\Gamma_{\max} - \Gamma_{\text{eq}})}{\Gamma_{\text{eq}}} \quad (4.5)$$

6H::Mal3::mCherry binding curve to the wall

Bulk and background intensities (I_{Bulk} and I_{BG}) were measured from an area of $1\text{-}2 \mu\text{m}^2$ on the middle of the wells and on the chromium covered regions respectively using **ImageJ**. For this measurement we used raw images, without the disk background subtraction described in the previous section. That way, we avoided biasing the ratio between

the bulk signal and the wall signal. Since then, laser illumination is not homogeneous in the field of view (figures 4.13 and 4.14), we performed all the measurements within the brightest area on the field of view.

$I_{\text{Bulk}} - I_{\text{BG}}$ was then fitted by a linear relation to the protein incubation concentration with the package *numpy.polyfit* of **Python2.7**. Standard deviation errors were obtained as the square root of the diagonal of the covariance matrix obtain from the fitting.

Wall intensities were measured on disk background subtracted images to reduce the effect of non-uniform illumination. Measurements were obtained as the average and std values on $\sim 1 \mu\text{m}$ ROI distance along the brightest wall of the fluorescence image (using **ImageJ**). Background intensities were measured again in this disk background subtracted images.

The dissociation constant was obtained by fitting

$$I_{\text{Wall}}^* - I_{\text{BG}}^* = \frac{I_{\text{Bulk}} - I_{\text{BG}}}{I_{\text{Bulk}} - I_{\text{BG}} + K_D} \quad (4.6)$$

with the package *scipy.optimize.curve_fit* of **Python2.7**. The symbol * denotes that those measurements were performed in disk background subtracted images. Standard deviation errors were obtained by the square root of the diagonal of the covariance matrix obtain from the fitting.

6H::+TIP binding kinetics to the wall

Wall intensities were measured as above in disk subtracted images. Dissociation rates were obtained by fitting 4.3 by linear square fitting with the function *lsqcurvefit* of **Matlab R2013b**. The obtained values were used in the fit of 4.2 to obtain the association rate. Confidence intervals were obtained with the function *nlparci* of **Matlab R2013b**.

MICROTUBULE-BASED DELIVERY OF 6H::+TIPS

Docking efficiency plots:

All the following image analysis was perform in custom programs on **Python 2.7** in a semi-automated way aided by *PyQt4* graphical user interfaces (GUI).

Spots on the wall with protein docked where semi-automatically detected by thresholding of the chromium sheltered region of each micro-well. The regions of the wall that were not identified as spots with protein were used to determine the average fluorescence of a site without immobilized protein, which was used for normalization.

Spots were automatically distinguished by the contact or not of a microtubule tip at any time during the time lapse movie. Note that if a microtubule contacted an empty spot while gliding and no protein was deposited, this spot would not have been detected by the analysis. For this reason, in order to obtain probabilities of delivery, we did an alternative analysis on kymographs along the wall that will be discussed in the next subsection.

Spots with a clear microtubule arrival and departure were selected for measurement of the fluorescence intensity over time. To correct for possible drifting, the intensity was measured in a disk area of 6 pixels radius (package *pymorph.sedisk*) centred by a 2D Gaussian fitting of the signal at each frame (package *scipy.optimize.curve_fit*) on a 4x interpolated image (package *scipy.ndimage.interpolation.zoom*). The exact instants of

microtubule arrival and departure were determined manually by looking at the movies. The information of each microtubule contact was stored as a *Python dictionary*. This included the date and movie recording, spot location over time, the times of arrival and departure of a microtubule, the protein fluorescence signal over time, and the conditions in which the microtubule contacted the wall; i.e. whether it was a lateral or a tip contact, if the microtubule underwent catastrophe or not, and the count of times a microtubule had visited that same spot before in the movie.

The information of all the microtubule contact events was then organized in *Panda's DataFrame* structures and plot selectively according to its specifications.

Average fluorescence before and after microtubule contact were calculated from the 4 and 2 time measurements right before or after microtubule contact (20 s and 10 s for 6H::eGFP::Tip1 deposition experiments and 8 s and 4 s for the 6H::Mal3::mCherry experiments). The comet intensity was measured by Gaussian fitting of the fluorescence signal during microtubule contact (package *scipy.optimize.curve_fit*).

Linear fitting to obtain the deposition efficiency was obtained by using the package *scipy.stats.linregress*.

Kymograph analysis:

Kymographs of a spline along the walls at regions of microtubule tip sliding were obtained by manual tracing with **ImageJ** on a wide area of 3 pixels by using the functions *Straighten*, *Reslice* and *Z Project*. Microtubule tip position at the kymographs was then traced manually. Intensities before, during and after microtubule contact were determined automatically with a custom **Python2.7** program. Intensity of microtubule contact corresponded to the average of 5 time frames on the kymographs centred on the manually traced line. Intensities before and after corresponded to the previous and posterior 4 time frames. The background was obtained from a close-by region without pre-docked protein.

SUPPLEMENTARY MATERIAL

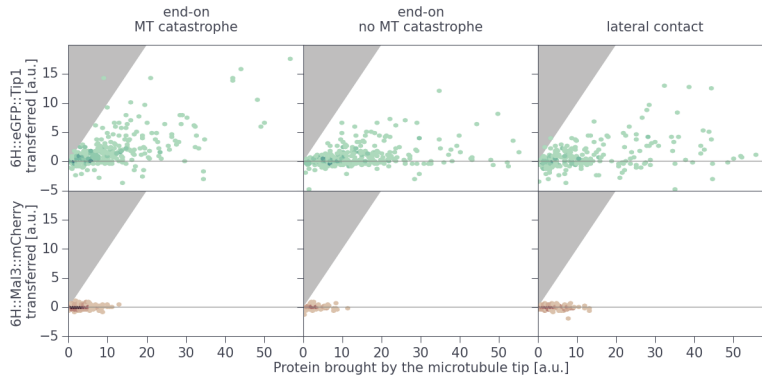


Figure 4.15: **Microtubule-based deposition of +TIPs efficiency.** Hexagon binning plot of the amount of protein deposited at the wall spot (fluorescence intensity units) versus protein delivered by the microtubule for all the cases a microtubule tip encountered the wall in different configurations: ‘end-on’ contact with the wall, or ‘lateral’ contact.

ACKNOWLEDGEMENTS

We thank Jacob Piehler and Changjiang You for development and synthesis of Pll-g-PEG/Tris-NTA. We thank Gijs Vollenbroek, Dimmitry Lamers, Andries Lof, and Hans Zeijlemaker for advice and help with microfabrication. Roland Dries for help with UV irradiation and developing a mask aligner (not shown). Liedewij Laan for initiating this project and advice. We also thank Vladimir Volkov for careful reading of the manuscript and Sophie Roth, Maurits Kok, Louis Reese, Pierre Recubreaux, Pieter-Rein ten Wolde and Thomas Sokolowski for discussions.

5

MICROTUBULE-BASED ESTABLISHMENT OF POLARIZED PATTERNS *in vitro*

Every battle is won before it is fought.

Sun Tzu

In this chapter we assess the emergence of polarized patterns inside bio-mimetic cells aided by microtubules. We use the obtained phenomenon of 6H::eGFP::Tip1 deposition by microtubules to functionalized walls described in the previous chapter, and let now microtubules self-organize in elongated micro-wells. We quantify microtubule organization as a function of micro-well size and shape, as well as the obtained cortical pattern of 6H::eGFP::Tip1. We obtained 6H::eGFP::Tip1 polarized patterns in wells of aspect ratio between 1.3 and 3 of size smaller than the average microtubule length without confinement. Nevertheless, those conditions also lead to non-polarized 6H::eGFP::Tip1 patterns. We found that bumping and sliding between microtubules affects microtubule organization and hinders the establishment of a polarized pattern. To reduce this factor, we promoted microtubule organization by adding Ase1 and Dynein to the system. This produced anti-parallel bundles of microtubules able to deliver 6H::eGFP::Tip1 to the polar walls of the wells.

5.1. INTRODUCTION

Microtubule-based establishment of polarity is an interplay between the microtubule organization and the ability of those microtubules to deposit polarity factors.

In *Saccharomyces pombe* (*S. pombe*), microtubules are organized in 3-4 anti-parallel bundles connected to the nucleus with the plus ends facing towards the poles of the cell [Hagan and Hyams 1988, Tran et al. 2001]. This ensures that polarity factors, carried by microtubule plus ends, are brought preferentially to the poles. In this chapter we wondered what the minimal set of components is to obtain microtubules deliveries with bias towards the poles of an elongated cell. Moreover, given these conditions, we assessed whether polarized delivery of polarity factors to the cell cortex is sufficient to produce a polarized pattern.

Although nearly all microtubule bundles in *S. pombe* are associated with the nuclear envelope [Tran et al. 2001] and enforce its centring [Daga et al. 2006b, Carazo-Salas and Nurse 2006], the nucleus itself is not required for proper microtubule organization [Daga et al. 2006a]. Anti-parallel bundles are organised by the combined effect of the anti-parallel bundler Ase1 (PRC1 homologue) [Loiodice et al. 2005, Yamashita et al. 2005] and the minus end directed motor and bundler Klp2 (kinesin-14 class, Kar3-like). Klp2 slides microtubules from the plus end towards the minus end of the other microtubule [Carazo-Salas et al. 2005, Carazo-Salas and Nurse 2006, Daga et al. 2006a, Janson et al. 2007]. Then, Ase1 acts as a length-dependent brake that prevents complete separation of the microtubules by slowing down the sliding to a complete stop [Braun et al. 2011]. This, leaves a stable overlapping mid-zone, exposing the growing plus ends outside of the bundle [Janson et al. 2005, Janson et al. 2007]. This is possible since Klp2 does not slide apart parallel microtubules [Janson et al. 2007]. On the other hand, Tip1 is required to ensure microtubule are long enough to orient preferentially along the longest axis of the cell [Brunner and Nurse 2000, Daga et al. 2006a].

In this chapter we assess how the interplay between cell shape, size, and microtubule associated proteins acts to produce a biased polarized protein depositions. In the previous chapter, we showed that a system composed of the yeast proteins, EB homologue Mal3, kinesin like Tea2, and Tip1, can suffice to deposit his-tagged Tip1 (6H::eGFP::Tip1) to micro-fabricated walls coated with tris-Ni(II)-NTA. This system is now used for microtubule growth from unbound seeds to allow microtubules to dynamically self-organize inside the micro-wells. We observed that this system could produce a minimum degree of cortical polarity in short cells. However, in cells longer than 20 μm , microtubules failed to reach the poles of the cell and arranged in smectic layers with the plus ends facing towards the middle of the cell.

In addition, to produce longer microtubule structures and enforce that the plus ends grow towards the poles of the micro-wells, we added Ase1 and the minus end directed motor protein dynein. This combination produced dynamic anti-parallel bundles centred on the minus ends allowing the plus ends to grow towards the poles of the cell and produce polarized Tip1 deliveries.

5.2. POLARITY IN THE ABSENCE OF MICROTUBULE ORGANIZING PROTEINS

Microtubules have shown to tend to align with the walls of micro-wells in the absence of +TIPs [Cosentino Lagomarsino et al. 2007]. At the same time steric interactions between microtubules also affect their organization. Recent Monte-Carlo simulations of rigid rods inside squared quasi-2D chambers showed a stable rod configuration depends on the volume fraction occupied by the rods, i.e. the density of rods [Gârlea and Mulder 2015]. For low volume fractions, close to the cavity boundaries, the rods align to the boundaries (wall induced ordering). However, far from the boundaries the order degree, a measure of how probable is the preferred orientation of the rods, drops rapidly. In this region, all rod orientations are equally probable. This regime is called *isotropic*. For intermediate volume fractions, rods in the centre of the cavity orient along one diagonal with high order degree, as being this the longest distance on the cavity. This causes a discontinuity in the orientation of the rods, termed *disclination* [de Gennes and Prost 1995] in the corners of the other diagonal. This regime is termed *nematic*. Finally, for high volume fractions, the rods show a *smectic regime*, characterized by a high order degree. In this case, the rods form rows, smectic layers, parallel to one of the boundaries and no disclinations appear. The amount of smectic layers depended on the ratio between the rod length and the cavity size.

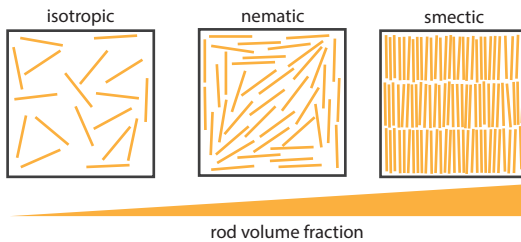


Figure 5.1: **Rigid rod organization in semi-2D confinement due to body exclusion** Different possible rod configurations as a function of rod volume fraction as observed in Gârlea and Mulder 2015.

Microtubules are flexible and have an intrinsically dynamic length. In addition to tubulin concentration and temperature, microtubule length is affected by rigid structures like the boundaries of the cell. +TIPs tips affect microtubules' dynamics and therefore their organization in confinement. In the previous chapter, we saw that microtubules with the plus ends decorated with 6H::eGFP::Tip1, Tea2 and Mal3 were less prone to undergo catastrophe upon contact with the tris-Ni(II)-NTA functionalized walls than microtubules grown in the presence of 6H::Mal3::mCherry alone. Moreover, those microtubules could sustain growth against the wall while buckling.

MICROTUBULE ORGANIZATION IN QUASI-2D ELONGATED MICRO-WELLS FOR 6H::EGFP::TIP1 DEPOSITION TO THE WALLS

We grew dynamic microtubules from GMPCPP stabilized seeds inside rectangular micro-wells of different aspect ratios and sizes ranging from 7 to 50 μm . 6H::eGFP::Tip1, Tea2 and Mal3 were added to the system in order to promote microtubule-based deposi-

tion of 6H::eGFP::Tip1 to the walls. Although the microtubule seeds were free to diffuse out of the wells, the addition of methyl cellulose keeps them close to the bottom surface. This happens because of depletion attraction forces, occurring in crowded environments [Asakura and Oosawa 1954, Yodh et al. 2001] as it is entropically favourable to deplete the space between the microtubule and the surface from crowding agents [see Marenduzzo et al. 2006 for review]. The wells are 300 nm deep and contain a chromium overhang that prevents growing microtubules to go over the walls. This depth allows microtubule to cross-over each other. These conditions therefore permit microtubule growth in quasi-2D cavities in the presence of a reservoir of components (GTP, tubulin, +TIP proteins, etc.). We observed that short microtubules often entered and left the micro-wells. However, pieces longer than 5 μm rarely exited a well.

In order to quantify how microtubules organize inside the micro-wells, we performed z-stacks over the wells for 10-20 min with a time lapse of 5 s. We treated the wells as 2D spaces by projecting the images in z. Figure 5.2 a shows examples of microtubule configurations (snapshots) in micro-wells of different aspect ratios. We determined the preferred microtubule orientation and order parameter at each pixel location over the movie (see methods, figure 5.2 b and c). The order parameter is a measure of how probable is the calculated preferred orientation.

In the examples shown, microtubules in micro-wells with an aspect ratio bigger than 1, show shallow angles with respect the long axis and their tips reach the the boundaries at the most distant sides (poles). For aspect ratio 1, microtubule alignment is along the diagonal. Most of the wells show a high order parameter through the whole space, indicating that microtubule orientations changed little during the time-lapse movie. This value is lower at regions with less microtubules and at the poles. This indicates that microtubules reach the poles with variable angles.

To compare multiple wells, we computed the preferred orientation angle of the ensemble of microtubules in each well. Figure 5.3 shows that the preferred angle fell always between zero (long axis) and the angle of the diagonal for all wells of aspect ratio higher than 1.6. For wells of aspect ratio 1 (square wells), microtubules could align in any angle, with average centred on the diagonal. In these wells, microtubules tended to co-align in a dynamic angle instead of forming isotropic aster-like configurations. This can be observed in the histograms of all pixel orientations in figure 5.11 as most of the distributions show a peak at an arbitrary angle, instead of being flat. The reader can find all histogram distributions in that figure. Preferred alignment along the long axis was obtained precisely in the range of the aspect ratios of *S. pombe*, which typically evolves from 1.75 to 3.5 [Mitchison and Nurse 1985].

As observed in the longest well of figure 5.2 b, which holds for long wells in general, microtubules failed to extend as long as the long axis. Figure 5.3 b shows the average microtubule length as a function of the diagonal length of the micro-well. For wells with diagonal shorter than 15 μm , the average microtubule length was nearly equal to the diagonal. A percentage of the microtubules in those wells would actually be longer than the diagonal and buckle. For bigger wells, microtubule average length was shorter than the diagonal and no buckle was observed. In cells bigger than 30 μm , the average micro-

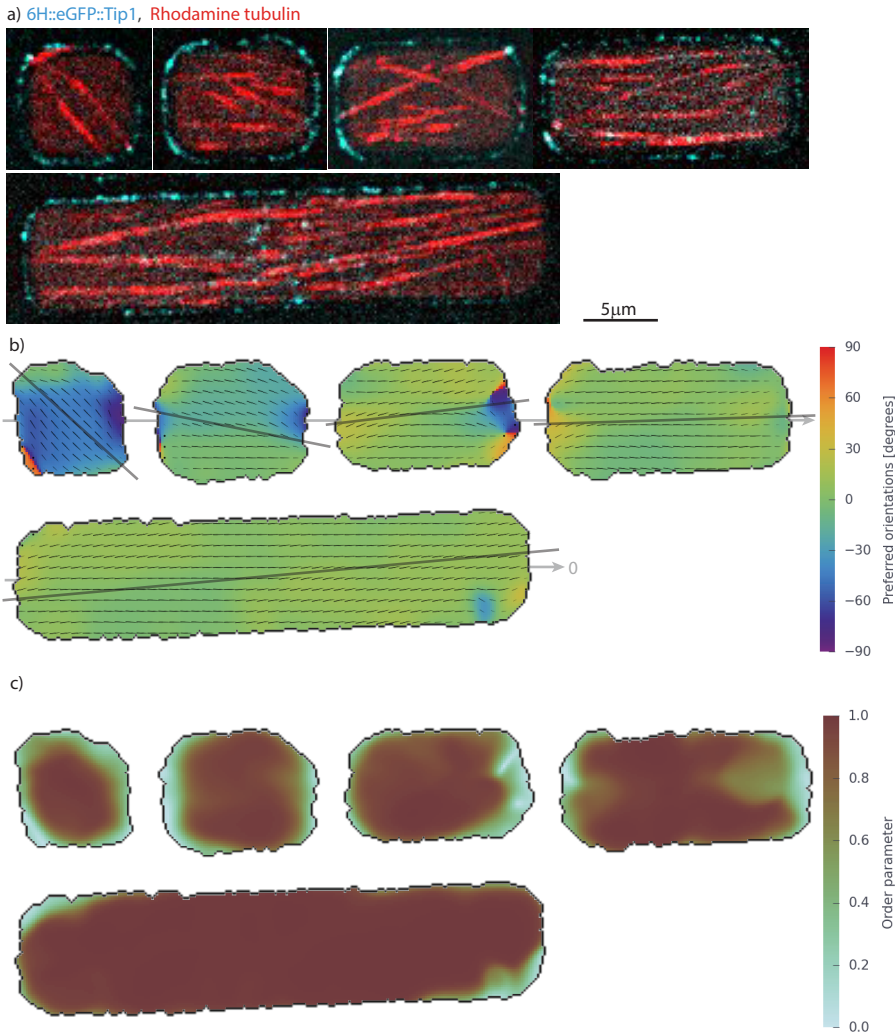


Figure 5.2: **Microtubule organization inside elongated micro-wells.** (a) Fluorescence microscopy images dynamic microtubules in micro-wells in the presence of 150 nM 6H::eGFP::Tip1, 100 nM Mal3 and 10 nM Tea2. The two laser channels were imaged sequentially, resulting in a delay of 400ms between the two images, which often leads to positional mismatch between the observed microtubule tip and the comet position. (b) Microtubule preferred microtubule orientations over the whole 5-10 min movie at each pixel position (equation 5.4) relative to the long axis of the well. The length of the lines proportional to the order parameter. Grey lines indicate the overall preferred orientation of the ensemble of microtubule in each well. (c) Order parameter at each pixel position as calculated from 5.3 indicating how probable the preferred angle is.

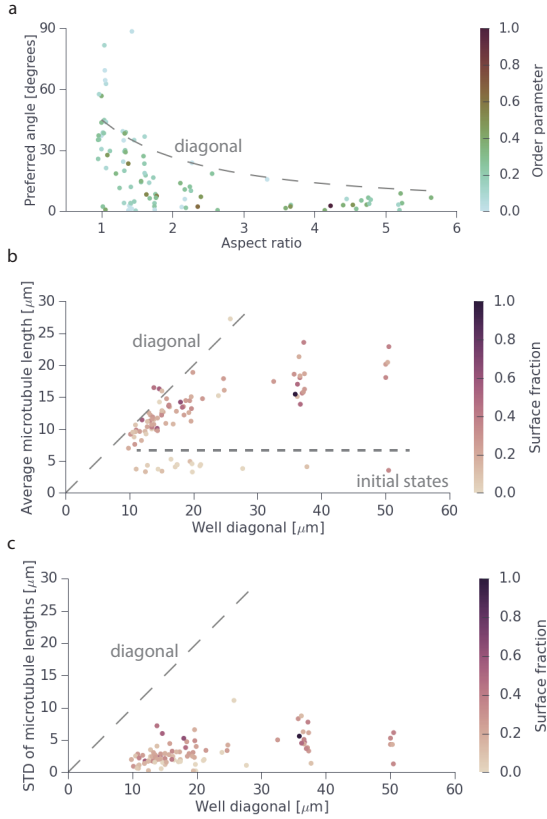


Figure 5.3: Microtubule distribution inside elongated micro-wells. (a) Preferred angle of the ensemble of microtubules in each well as a function of the aspect ratio of the well. Slashed lines shows the corresponding angle to the diagonal. (b) and (c) Mean and standard deviation of the microtubule length per each well as a function of the diagonal distance of the well. Colour coding shows the estimated measurement of the fraction of the surface of the well occupied by microtubules. Slashed line shows the length of the diagonal. This plot includes the very initial states after sample preparation when the microtubules are very short or simply seeds (annotated by a slashed line). Those data points show clear independence on the size of the well where they were found. This correlates with a low surface fraction.

5

tubule length was $\sim 20 \mu\text{m}$, independently on well size.

The standard deviations of the microtubule length in each well scale little with the average microtubule length (figure 5.3). This, indicates that the microtubule distribution is not exponential. Since the micro-wells are open, short microtubule pieces could easily exit the wells, leaving inside only long pieces.

Microtubule catastrophes may be induced by microtubule tip bumping into other microtubules. Therefore, average microtubule lengths may be longer for sparsely packed wells. To account for this factor, data points of figures 5.3 b and c are colour coded by the surface fraction of the well occupied by microtubules. This parameter consists on the space occupied by microtubules in the 2D z-projection of the wells. Most of the studied wells had similar surface fractions. It would be interesting to test whether lesser dense wells (achieved by adding less seeds) exhibit longer microtubules.

A closer look at the long wells shows that microtubules formed quasi smectic layers with the plus ends (detected by 6H::eGFP::Tip1 signal) facing towards the middle of the well. While smectic layers preferentially align with the long axis of the cavities, in our case, the alignment was found to be between the well's long axis and the diagonal (figure 5.3). This can also be observed by a decrease of the order parameter at two opposite

corners of the well (figure 5.2 c), which at the same time shows a lower fraction of microtubules there. The obtained microtubule organization resembles a mitotic spindle, where the minus ends are focussed at the poles and the plus ends form a wider overlap region in the middle.

Given a certain microtubule length and surface fraction, it is not surprising to find a quasi smectic arrangement. However, why would the plus ends face towards the centre of the cell? To answer this question, we looked at 6H::eGFP::Tip1 dynamics inside the wells.

POSITIONING OF TIP1

Figure 5.4 a shows an example of a short well where the microtubule plus ends reach the poles. However, longer wells, or wells with densely packed areas appearing at locations such as the diagonal, microtubule plus ends rarely reached the poles (5.4 b, and c). In those cases, the microtubule tips exhibited phases of backwards movement, i.e. the whole microtubule moved in the direction of the minus end. This can be due to a combination of an exclusion effect occurring between different smectic layers and anti-parallel sliding between microtubules mediated by Tea2, Tip1 and Mal3. In the first place, volume exclusion makes different layers to sense each other as soft walls difficult to penetrate by single microtubules. This enforces the layered configuration. Secondly, microtubules meeting in anti-parallel configuration may slide apart via interactions with Tea2 and Tip1. Since Tea2 is a plus end directed motor, sliding will bring the plus ends together. On the other hand, microtubules meeting in a parallel configuration will not exhibit any sliding effect. This may explain why different layers point with the plus ends to the same inter-layer space.

Collisions and sliding between microtubules cause an extra negative effect on polarity: microtubules deviating from the most probable alignment find less microtubules on the way therefore have higher chances to reach the wall at the sides of the well and deposit there polarity factors. The bottom arrow in the snapshot of figure 5.4b shows an example of such microtubules.

Another observation that may render difficult the emergence of polarity, was microtubule gliding along the walls when the microtubule lattices entered in contact with the wall. This, happened mostly in short wells after buckling mediated by contact of the two poles with the microtubule tips. Similar gliding was observed in chapter 4 and was attributed to Tea2 molecules connecting the wall and the microtubule via 6H::eGFP::Tip1.

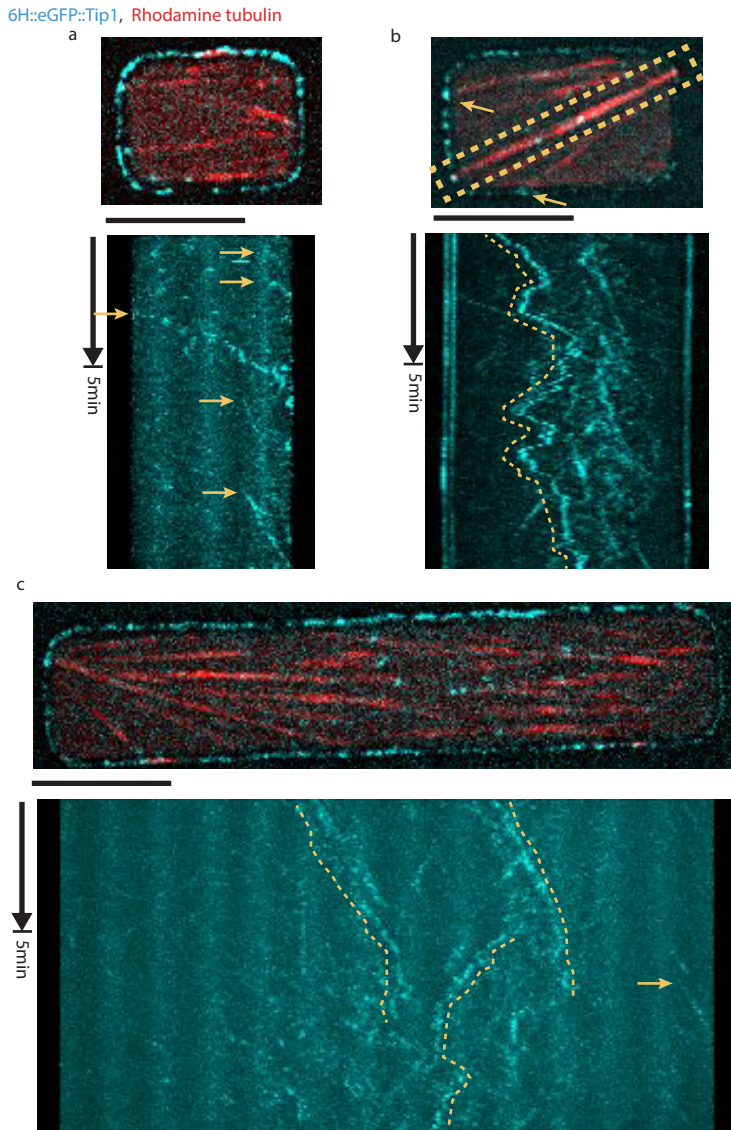


Figure 5.4: **Location of the plus ends.** (a, b, and c top) Fluorescence microscopy images of wells with different long axis. (a) and (c) **bottom** kymograph of the Tip1 signal inside the well, 1 μm away from the walls. (b) **bottom** kymograph along the diagonal of the well. Arrows show the start of microtubule tips that reach the well poles. Dotted lines show the path of a microtubule tip. Scale bars 10 μm .

CORTICAL POLARITY

Given the studied microtubule organizations, we now look at how polarized the 6H::eGFP::Tip1 distribution at the walls is. In order to quantify the degree of cortical polarization of the micro-wells we computed the polarity score introduced in Sokolowski 2013. It consists on the ratio between the amount of protein bound at the poles and at the sides of the wells. In our fluorescence intensity units

$$\text{Polarity score} = \frac{I_{\text{poles}} - I_{\text{background}}}{I_{\text{sides}} - I_{\text{background}}} \quad (5.1)$$

where $I_{\text{background}}$ corresponds to the fluorescence intensity when there is no 6H::eGFP::Tip1 bound to the wall. As observed in figure 5.5, the polarity score ranged from 1 to 4 in our wells. Values above 2 (at least two times more protein at the poles than at the sides) occur nearly exclusively for wells shorter than $20 \mu\text{m}$ and aspect ratios between 1.3 and 3. Microtubules in these wells were long enough to touch both poles simultaneously ($\bar{L}_{\text{microtubules}} - \text{diagonal} < 10 \mu\text{m}$). The plot of figure 5.5 suggests that the larger the well, the bigger has to be the aspect ratio to obtain polarity. Although the data suggests that this system can attain some degree of cortical polarity, this is much less than what a normal fission yeast cell displays.

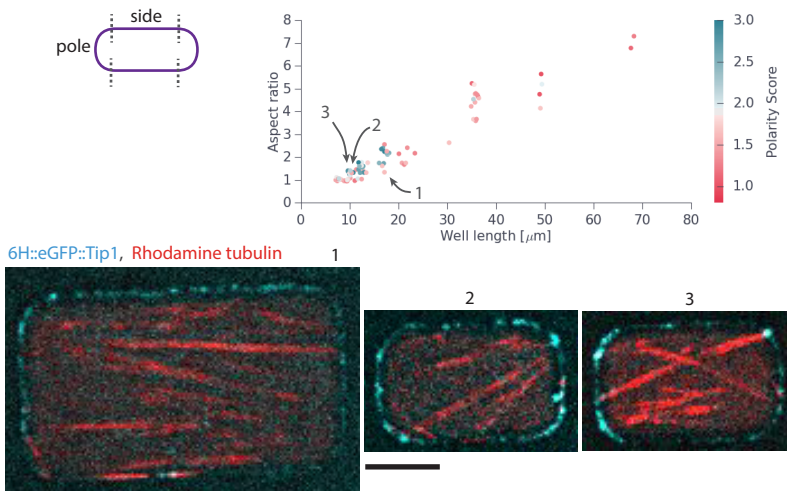


Figure 5.5: **6H::eGFP::Tip1 distribution at the walls.** (Top) Polarity score as a function of the aspect ratio and length of the well. Note that not all wells on a sample were imaged, therefore we might have had a bias for imaging polarized wells. (Bottom) Examples of wells with the same aspect ratio displaying different polarity scores. Scale bar $5 \mu\text{m}$

5.3. POLARITY IN THE PRESENCE OF MICROTUBULE ORGANIZING PROTEINS

As seen in the previous section, microtubules-microtubule interactions can interfere in the formation of polarized cortical patterns. To have better control of microtubule organization, cells use a number of proteins which mediate microtubule-microtubule interactions. In the case of fission yeast, microtubules are arranged in anti-parallel bundles with the plus ends facing towards the poles by the action of Ase1 and Klp2. From what we learned in the previous section, this bundle formation has at least four beneficial effects to the establishment of cortical polarity: 1) doubling the extent of microtubules, 2) ensuring that the plus ends grow towards the poles of the cell, 3) reducing the volume fraction occupied by microtubules, and 4) using the long microtubule as guides for short microtubule to reach the poles.

In this section, we seek to prevent the appearance of smectic layers and enforce microtubule configurations with the plus ends facing towards the poles by forming *S. pombe*-like anti-parallel bundles. With this aim, we added Ase1 and the minus end directed motor Dynein to the system. Ase1 promotes anti-parallel microtubule bundle formation [Daga et al. 2006a, Carazo-Salas and Nurse 2006]. Dynein has been shown to produce microtubule-microtubule gliding, which should bring the minus ends together [Tanenbaum et al. 2013].

First, we determine the conditions under which Ase1 and Dynein can form stable anti-parallel bundles with plus-end facing outside of the bundle. Then we show preliminary results of polarized delivery and docking of 6H::eGFP::Tip1 in *S. pombe* sized and shaped wells. Experiments in bigger wells faced surface passivation issues and microtubules growing from the top of the wells entering inside (data not shown).

ANTI-PARALLEL BUNDLE FORMATION BY ASE1 AND DYNEIN

We sought under which conditions Ase1 could slow down dynein-based sliding between microtubules and form stable bundles. We used 6H::Ase1::GFP and an artificially dimerized Dynein fragment from Reck-Peterson et al. 2006 containing a GFP that we will refer as GFP::Dynein.

We performed experiments with different ratios of 6H::Ase1::GFP and GFP::Dynein where a fraction of free seeds could slide along surface bound seeds. Figure 5.6 shows examples of how 6H::Ase1::GFP concentrations affected the stability of bundles. A ratio Ase1:Dynein of 100:1 led mainly to unstable bundles (left). For 200:1 most of the bundles were stable with a complete overlap (right). A 150:1 ratio produced stable bundles with a partial overlap (presumably at the minus ends).

Then, we tested whether the addition of Tea2-Tip1 and Mal3 would interfere in the formation of Ase1-Dynein bundles. Previous *tug-of-war in vitro* experiments with cytoplasmic Dynein and Kinesin1 bound to a DNA origami scaffold showed that 1 Dynein molecule over-competes up to 5 or 6 Kinesin1 molecules [Derr et al. 2012] even though its stall force is lower (5 pN versus 7 pN) [Constantinou and Doiehl 2010]. In our experiment, Tea2-Tip1 complexes do not bind to the GMPCPP seed [chapter 2]. Therefore, a tug-of-war is only expected on the dynamic part of microtubules (assuming microtubule

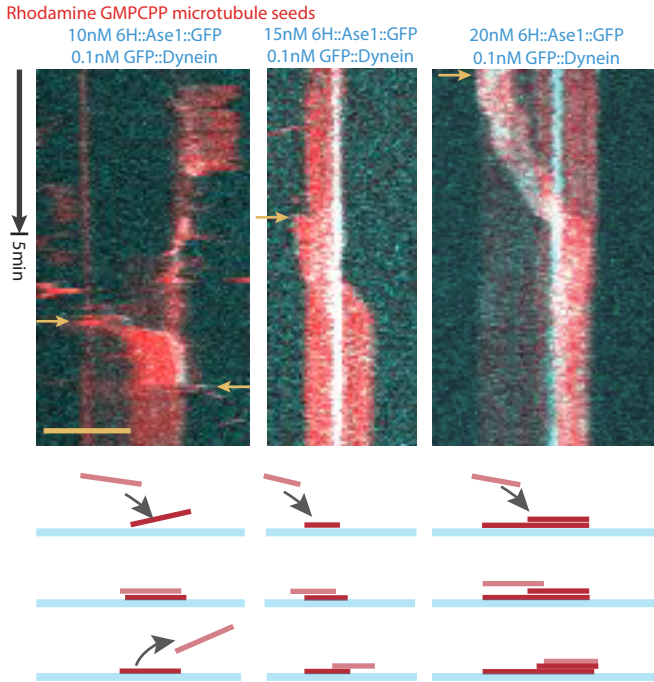


Figure 5.6: **Titration of Ase1 Dynein stoichiometry.** Fluorescent microscopy kymographs of free microtubule seeds gliding on a specifically bound seeds due to the effect of 6H::Ase1::GFP and GFP::dynein. In the left kymograph the template seed was only partially attached to the glass surface as it pivoted during the first minutes. Scale bar 5 μm .

bundling does not affect Tea2-Tip1-Mal3 microtubule binding rates).

In samples containing 6H::eGFP::Tip1, Tea2 and Mal3, all bundles displayed the plus ends facing outwards (see example in figure 5.7). Since both the Dynein and the Tip1 constructs contain a GFP, identification of the plus ends could be done microtubule growth speed.

The overlap region did not necessarily occur at the GMPCPP seed. This is because *in vitro* microtubules exhibit minus end growth. We often observed relatively fast movements between the microtubules (faster than Dynein or Tea2 velocities, not shown). We attribute those movements to catastrophes of the minus end of one microtubule, followed by subsequent fast movement of the other microtubule towards the plus ends.

Bundles were usually composed of several microtubules. Parallel microtubules kept bundled with the short microtubule following the longest microtubule. In figure 5.7, the right side of the bundle contains at least two microtubule plus ends. We interpret that this parallel bundling is maintained by a collective effect between 6H::eGFP::Tip1, Tea2 and Mal3.

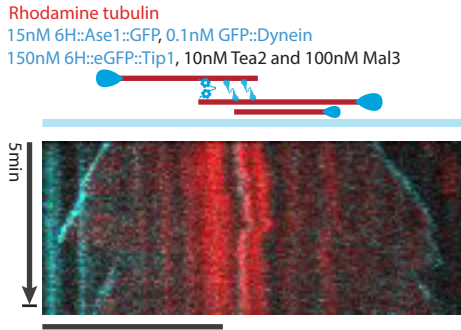


Figure 5.7: **Stable anti-parallel bundle with partial overlap.** Kymograph of self-assembled microtubule overlaps in the presence of 6H::Ase1::GFP, GFP::Dynein, Mal3, Tea2 and 6H::eGFP::Tip1. Scale bar 10 μm .

POLARIZED DELIVERY OF 6H::eGFP::TIP1

We performed the previous assay of microtubule organization in micro-wells and deposition of 6H::eGFP::Tip1 to the walls with the addition of 6H::Ase1::GFP and GFP::Dynein. Under these conditions, the microtubule *surface fraction* was substantially lower than in the previous assay without bundling proteins for a similar amount of microtubule seeds. However, bundles appeared to be slightly a-specifically bound to both the bottom surface of the micro-wells. This hindered free movement and free orientations of the bundles. Moreover, several microtubules landed inside the wells from the top in random orientations (data not shown).

We could observe some bundles moving relatively free in small fission-yeast size wells (figure 5.8). In those cases, wells contained one or two bundles with dynamic orientations deviating little from the longest distance of the well (not quantified). Figure 5.8 shows that bundles delivered 6H::eGFP::Tip1 at both extremes. Deliveries at the sides of the wells (away from the poles) were not observed since bundle length always kept longer than the short axis of the well ($\sim 5 \mu\text{m}$). This prevented bundles orientation to deviate substantially from the long axis.

In the assays performed we obtained in general little efficiency of deposition of 6H::eGFP::Tip1 to the walls. This can simply be because the K_D for the prepared walls was too high. Nevertheless, correlating with the observed microtubule organization, 6H::eGFP::Tip1 signal was found nearly exclusively at the cell poles.

We also observed that prolonged microtubule plus end contact with the wall caused pushing of the bundle towards the opposite side (figure 5.8 c).

Bundles were dynamic and thus occasionally assembled and disassembled (figure 5.8 b). In experiments with low Ase1 concentration, pushing of growing microtubules at the walls could cause bundle disassembly when the other, non-mobile extreme of the bundle, found the opposite wall (data not shown).

Rhodamine tubulin

15nM 6H::Ase1::GFP, 0.1nM GFP::Dynein, 150nM 6H::eGFP::Tip1, 10nM Tea2 and 100nM Mal3

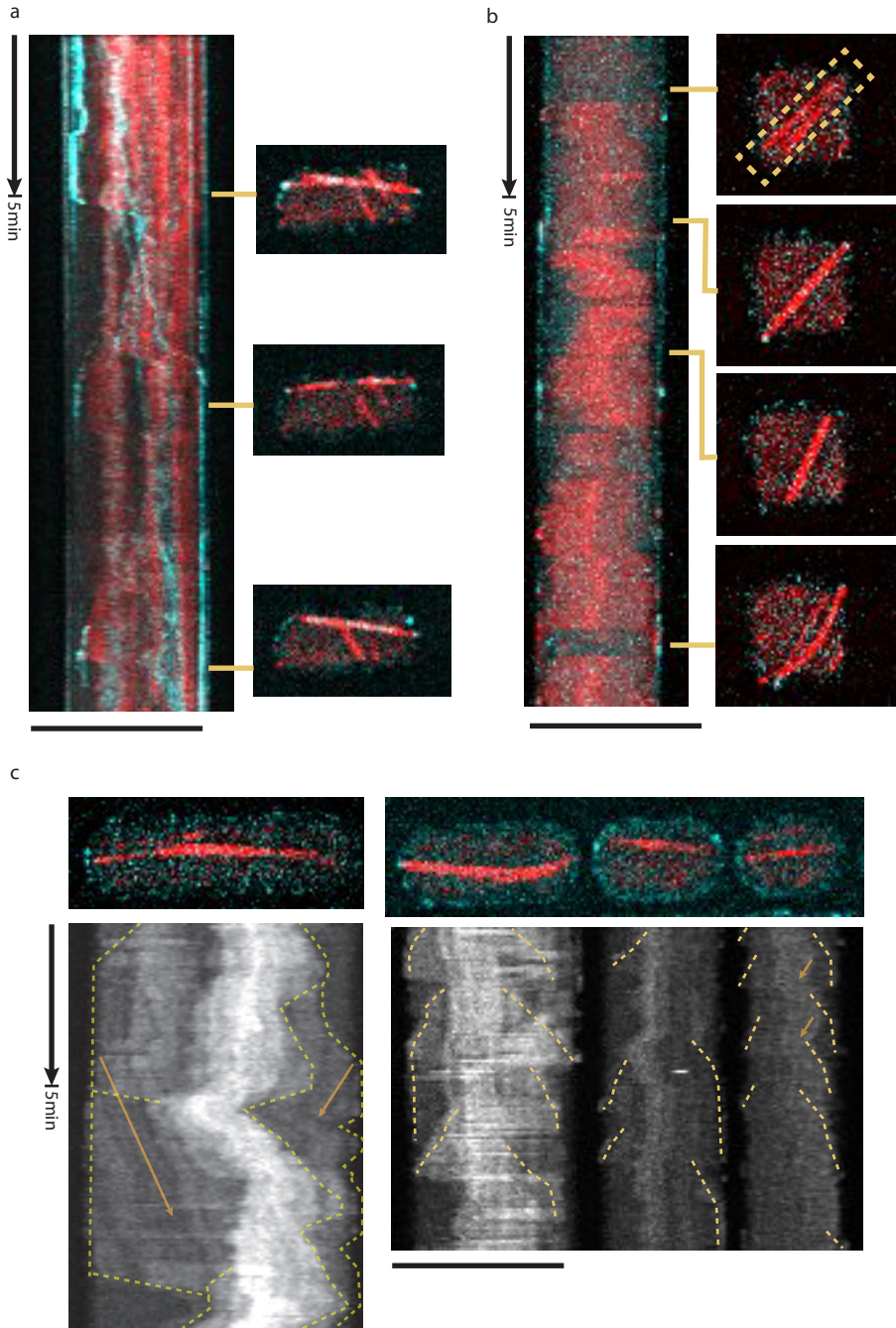


Figure 5.8: **Polarized delivery of 6H::eGFP::Tip1.** Kymographs of the complete well, or the diagonal, of different wells. Scale bars 10 μm . Dotted lines in the kymographs of **c**, indicate the location of the plus ends. Arrows indicate clear pushing events by plus end growing at the walls.

5.4. DISCUSSION

In this chapter we showed that for certain occupation surface fractions microtubules self-organized inside quasi 2D micro-wells at angles between the diagonal and the long axis. Data on lower occupation fractions was not shown since those assays contained little amount of 6H::eGFP::Tip1 at microtubule plus ends and no docking at the walls. This was because, as mentioned in the previous chapter, uncontrolled variability on the wall functionalization caused that not all samples prepared equally displayed the exact same protein affinity. In those cases, microtubules oriented more isotropically, diffused more readily and often exited the well. In order to prevent seeds leaving the wells, two methods were tried to seal the wells: PDMS sealing by pressure [Laan and Dogterom 2010] and flowing oil on top. Both methods led to sealing of the wells. However, it was not possible to find good conditions for dynamic microtubule growth in such small quasi 2D volumes. In the future, deeper chambers, as reported in Laan et al. 2012a could be employed to procure enough amount of reagents per chamber.

5

Small micro-wells strongly reduced microtubule length, while wells longer than 15 μm reduced it mildly. This caused small wells of aspect ratio bigger than 1.3 to contain buckled microtubules that reached the poles of the well and deposited 6H::eGFP::Tip1. A few of those wells showed weak cortical polarity (more than 2 times more protein at the poles than at the sides). However, for bigger wells, microtubules assembled in quasi smectic layers with the plus ends facing towards the centre of the cell. We did not investigate further the reason as to why the plus ends preferentially faced the inner side of the cell. Nevertheless, observations of microtubule-microtubule anti-parallel sliding mediated by Tip1, Tea2 and Mal3 oligomers suggest that they contribute to this asymmetric configuration. A negative control without Tea2-Tip1 and Mal3 would require a marker for the microtubule plus, or minus, ends which does not affect microtubule dynamics. To our knowledge, this has not been found yet. Therefore, it is difficult to determine the cause behind the preferential orientation observed of microtubules.

It is important to note that, although sporadic Tip1 depositions to the walls were observed, their frequency was very low (around 1-5 per 20 minutes). Therefore, the observed cortical patterns correspond, in a big extend, to the whole history of the well previous to the recorded time-lapse. Moreover, this time scale is insufficient in the life-span of fission yeast (2-3 h [Fantès 1977]).

Most of the wells seemed to have higher amounts of 6H::eGFP::Tip1 at the corners. It would be interesting to verify this observation with a quantified analysis since those places might facilitate the highest percentage of microtubule catastrophes at the walls.

In order to enforce microtubule organization we produced self-assembled anti-parallel microtubule bundles with partial overlaps at the minus ends by the addition of Ase1 and Dynein. These bundles were able to deliver 6H::eGFP::Tip1 in a polarized manner to *S. pombe* sized micro-wells. This was partly because bundles contained multiple microtubules, which caused that the average bundle length was in general longer than two thirds of the long axis of the wells (from qualitative observations of kymographs such as the ones of figure 5.8). Therefore, bundle alignment was improved versus single mi-

cro-tubules, while reducing the microtubule occupation surface fraction. In addition, experiments with bundled microtubules lead to a higher frequency of microtubule tip encounters with the pole walls (see figures 5.4 and 5.8 for comparison).

Long microtubule plus end contacts with the wall produced pushing backwards of the bundle as a whole. This is associated in cells with nucleus centring [Tran et al. 2001]. In our experiments, bundle overlaps were not necessarily placed in the centre of the wells. See figures 5.8a and c left for examples. This could be due to growth from the minus ends, which does not occur in cells. To elucidate the effect of minus end growth in bundle organization, minus end dynamics could be inhibited in future experiments by addition of Camsap2 protein [Jiang et al. 2014].

In *S. pombe*, Klp2 contributes to bundle formation by sliding microtubule from the plus ends towards the minus end of the template microtubule [Carazo-Salas et al. 2005, Janson et al. 2007]. In contrast, Dynein seems to accumulate at microtubule minus ends (figure 5.6). We did not explore here if this causes any substantial difference in the formed bundles.

The experiments on self-assembled bundled microtubules, need further improvement. Principally by reducing bundle sticking at the micro-fabricated surfaces. Preliminary experiments with Pluronic F-127 passivation [Preciado Lopez et al. 2014] have shown to be successful (data not shown).

Microtubule-based establishment of polarity in *S. pombe* involves a feedback with the formed cortical pattern and the microtubules based on mobile receptors [Snaith and Sawin 2003]. Future directions should involve experiments with mobile receptors to test if this new property helps focussing cortical patterns. In the following chapter we expose a method we have been developing to test the emergence of cortical polarity in elongated water-in-oil emulsion droplets.

5.5. SAMPLE PREPARATION AND DATA ACQUISITION

Micro-well fabrication and wall functionalization

See chapter 3.

Protein purification

- The Dynein construct consisted of an artificial dimerization of truncated 331 kDa version of *S. cerevisiae* Dynein containing the motor domains as in Reck-Peterson et al. 2006. Dimerization is obtained by a GST-tag of the N-terminus. This terminus contains in addition a SNAP-tag, later functionalized with a Biotin (SNAP biotin[®], New England Biolabs), and a GFP. The C-terminus contains a Halotag, which was labelled with TMR (Halotag[®] TMR, Promega). Therefore, the construct consists of GFP::SNAP-tag/biotin::GST::[331kD Dynein]::Halo-tag/TMR. Purification and labelling was done as in Reck-Peterson et al. 2006.
- 6H::eGFP::Ase1 was obtained and purified as in Braun et al. 2011.

- The other plus tips were purified as in section 2.8

Data acquisition

All data shown in this chapter was obtained by spinning disk fluoresce microscopy using a IX81F-ZDC2 microscope (Olympus, Japan) with a spinning disk confocal head CSU-X1 (Yokogawa, Japan). 100X oil immersion objectives and EmCCD camera iXon3 (Andor, UK). Excitation lasers 488 and 561 nm (Andor, UK).

Unless stated otherwise, we used the following condition: AOTF laser intensity 22, exposure 300 ms, and EM Gain 115.

Polarity in the absence of microtubule organizing proteins

After functionalization of the walls with PLL-g-PEG/Tris-Ni(II)-NTA (0.2 mg·ml⁻¹). The bottom surface was passivated with PLL-g-PEG (0.2 mg·ml⁻¹ for 15 min), and κ -casein (1.2 mg·ml⁻¹ for 10 min). Then, microtubule seeds were incubated in an MRB80 solution containing 0.1% methyl cellulose and let sediment for 5 min. The 6H::eGFP::Tip1 deposition assay was prepared by incubating 150 nM 6H::eGFP::Tip1, 100 nM Mal3 and 10 nM Tea2 in a MRB80 solution containing 14.25 μ M tubulin, 0.75 μ M Rhodamine tubulin, 1 mM GTP, 2 mM ATP, 0.1% methyl cellulose, 0.4 mg·ml⁻¹ glucose oxidase, 50 mM glucose, 0.6 mg·ml⁻¹ κ -casein, 50 mM KCl and ~10 mM imidazole.

Z-stacks of 2-3 focal planes separated 300 nm were taken every 5 s.

Anti-parallel seed bundle formation by Ase1 and Dynein

On a flow cell formed by base piranha cleaned coverslips and Helmanex cleaned glass slides, fluorescently labelled seeds were incubated for 10 min. Then, the surface was passivated with PLL-g-PEG (0.2 mg·ml⁻¹ for 15 min), and κ -casein (4.8 mg·ml⁻¹ or 10 min). This was followed by a second incubation of seeds in a MRB80 solution containing the stated concentrations of 6H::Ase1::GFP, and GFP::Dynein, and 0.1% methyl cellulose, 0.4 mg·ml⁻¹ glucose oxidase, 50 mM glucose, 2.4 mg·ml⁻¹ κ -casein, and 50 mM KCl.

Confocal images were taken at a single focal plane with a time-lapse of 5 s.

Polarity in the presence of Ase1 and Dynein

The samples were prepared as the ones in the absence of Ase1 and Dynein, but with the addition of those two proteins and 4 times more κ -casein.

Z-stacks of 2-3 focal planes separated 300 nm were taken every 5 s.

5.6. DATA ANALYSIS

Obtained z-stacks were background subtracted and 2D projected by maximum pixel intensity as in 4.6 and 4.6. Part of the image analysis performed was based on a previous method from Alvarado 2013 and Alvarado et al. 2014.

Microtubule orientations were obtained by employing the plugin *OrientationJ* of **ImageJ** (<http://bigwww.epfl.ch/demo/orientation/#analysis>, [Fonck et al. 2009, Rezakhanliha et al. 2011]). To avoid including the wall orientation in the measurement, complete wells were segmented and the background outside signal was replaced by a Gaussian noise with the same mean and std than the signal inside of the wells (figure 5.9). Well segmentation was performed by semi-automated threshold using the packages *mahotas* and

`scipy.ndimage.label` in **Python2.7**. The orientation of the long axis of the wells was obtained by the function `orientation` of the package `skimage.measure` on the labelled longest well of the field of view and assumed parallel for all the other wells.

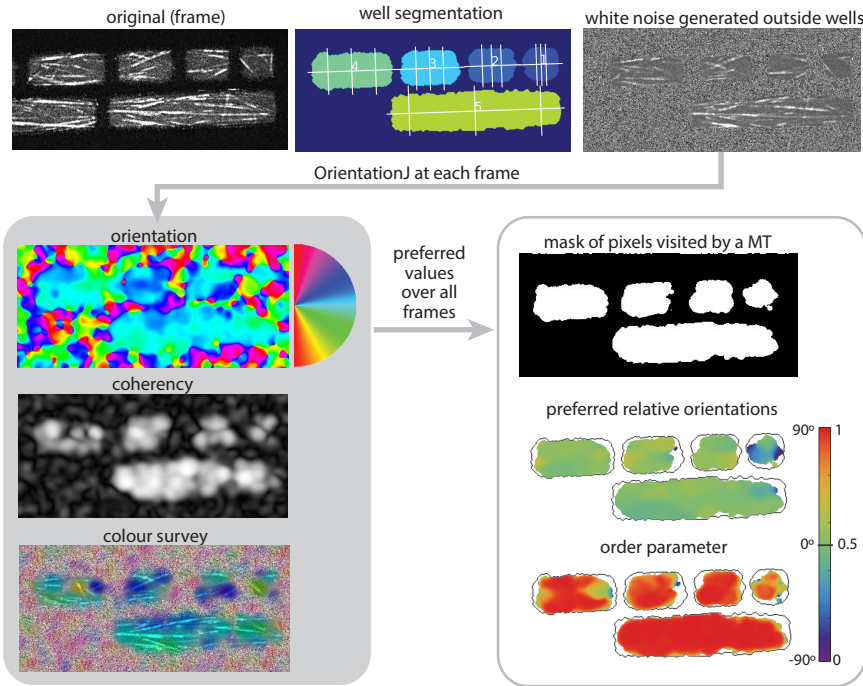


Figure 5.9: **Histograms of pixel preferred orientations.** Count of the preferred orientations of each pixel inside the well over movies of 10-20 minutes. Only pixels with *coherciness* higher than 0.4, corresponding to places visited by microtubules are plotted. Dashed lines represent the angle of the diagonal of the well. Histograms are packed vertically by increasing short axis width, dy .

Then, local anisotropies were measured with *OrientationJ* using a Gaussian window with radius $\sigma = 3$ px for each frame. The program gives a matrix with the orientations at each pixel position and the coherency matrix, a measure of the degree of co-alignment with the neighbouring pixels.

The preferred orientation of microtubules at each pixel position over a whole movie was obtained by building the weighted second-order tensor order parameter S_2 [Hess and Kohler 1980] per each pixel location (px)

$$S_{2,px} = \begin{pmatrix} \frac{\sum_{i=1}^n \omega_{i,px} \cos 2\theta_{i,px}}{\sum_{i=1}^n \omega_{i,px}} & \frac{\sum_{i=1}^n \omega_{i,px} \sin 2\theta_{i,px}}{\sum_{i=1}^n \omega_{i,px}} \\ \frac{\sum_{i=1}^n \omega_{i,px} \sin 2\theta_{i,px}}{\sum_{i=1}^n \omega_{i,px}} & -\frac{\sum_{i=1}^n \omega_{i,px} \cos 2\theta_{i,px}}{\sum_{i=1}^n \omega_{i,px}} \end{pmatrix} \quad (5.2)$$

where $\theta_{i,px}$ denotes the orientation at that pixel at time frame i , and $\omega_{i,px}$ denotes the

respective coherency. The eigenvalues of the this tensor give the order parameter

$$\lambda_{\pm} = \pm OP_{px} = \pm \sqrt{\left(\frac{\sum_{i=1}^n \omega_{i,px} \cos 2\theta_{i,px}}{\sum_{i=1}^n \omega_{i,px}}\right)^2 + \left(\frac{\sum_{i=1}^n \omega_{i,px} \sin 2\theta_{i,px}}{\sum_{i=1}^n \omega_{i,px}}\right)^2}. \quad (5.3)$$

The preferred orientation is pointed by the eigenvector $\vec{\lambda}_+ = \lambda_{+,x} \vec{x} + \lambda_{+,y} \vec{y}$ corresponding to the eigenvalue λ_+ . The preferred angle, $\langle \theta \rangle_{px}$, is obtained by

$$\langle \theta \rangle_{px} = \arctan \left(\frac{\lambda_{+,x}}{\lambda_{+,y}} \right)_{px}. \quad (5.4)$$

The eigenvalues and eigenvectors of $S_{2,px}$ were obtained using the function `linalg.eig` of the package `numpy` from **Python2.7**. The relative preferred angles of the microtubules at each pixel location was obtained by subtracting the previously obtained orientation of the long axis to $\langle \theta \rangle_{px}$.

The preferred orientation of the ensemble of microtubules inside each well was determined by calculating now the following tensor

$$S_{2,well} = \begin{pmatrix} \frac{\sum_{j=1}^m OP_j \cos 2\langle \theta \rangle_j}{\sum_{j=1}^m OP_j} & \frac{\sum_{j=1}^m OP_j \sin 2\langle \theta \rangle_j}{\sum_{j=1}^m OP_j} \\ \frac{\sum_{j=1}^m OP_j \sin 2\langle \theta \rangle_j}{\sum_{j=1}^m OP_j} & -\frac{\sum_{j=1}^m OP_j \cos 2\langle \theta \rangle_j}{\sum_{j=1}^m OP_j} \end{pmatrix} \quad (5.5)$$

where j corresponds to each pixel location of a well composed of m pixels. The preferred orientation of the well is obtained from linearisation of the matrix as before.

Microtubule lengths were measured by direct tracing with `ImageJ` in some frames.

Microtubule surface fraction was obtained by computing

$$\text{Surface fraction} = \frac{\langle I \rangle - \langle I_{BG} \rangle}{\langle I_{MT} \rangle - \langle I_{BG} \rangle} \quad (5.6)$$

where $\langle I \rangle$ and $\langle I_{MT} \rangle$ correspond to the average intensity of a pixel in the well and of a microtubule, and $\langle I_{BG} \rangle$ to the average intensity outside of the well. Those intensities were measured manually with `ImageJ`. We note that there could be better ways to obtain this parameter which should be considered for more thorough analysis.

Kymographs of the width of a well were obtained using the functions `Straighten`, `Reslice` and `Z Project` of `ImageJ`.

The polarity score was obtained by first computing the fluorescence intensity profile of protein at the wall as a function of distance along the from one pole along the long axis. For this, the signal $1 \mu\text{m}$ away from the walls was masked using a threshold detection (figure 5.10 top). Then, we obtained kymographs at each y position parallel to the long

axis (arrow in figure 5.10 top) using the functions *Straighten* and *Reslice* from **ImageJ**. We computed the average intensity (figure 5.10 bottom) at each x position over time. We defined the background as 40 a.u., slightly lower than any measured intensity value, and computed the average intensity at the poles and the sides, delimited by the first and last 10 pixels. The polarity score was calculated by applying equation 5.1.

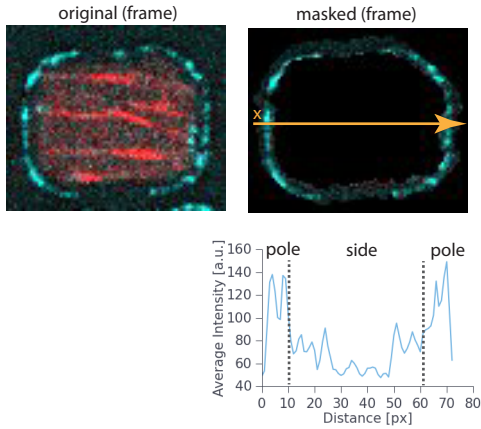


Figure 5.10: **Calculation of the polarity score.** Example of polarity score measurement. In this case $PS = 3.7$.

We note that other quantification methods might give better measurements, as for example plotting histograms of the pixel intensities and distinguish the microtubule contribution from the bulk contribution.

SUPPLEMENTARY MATERIAL

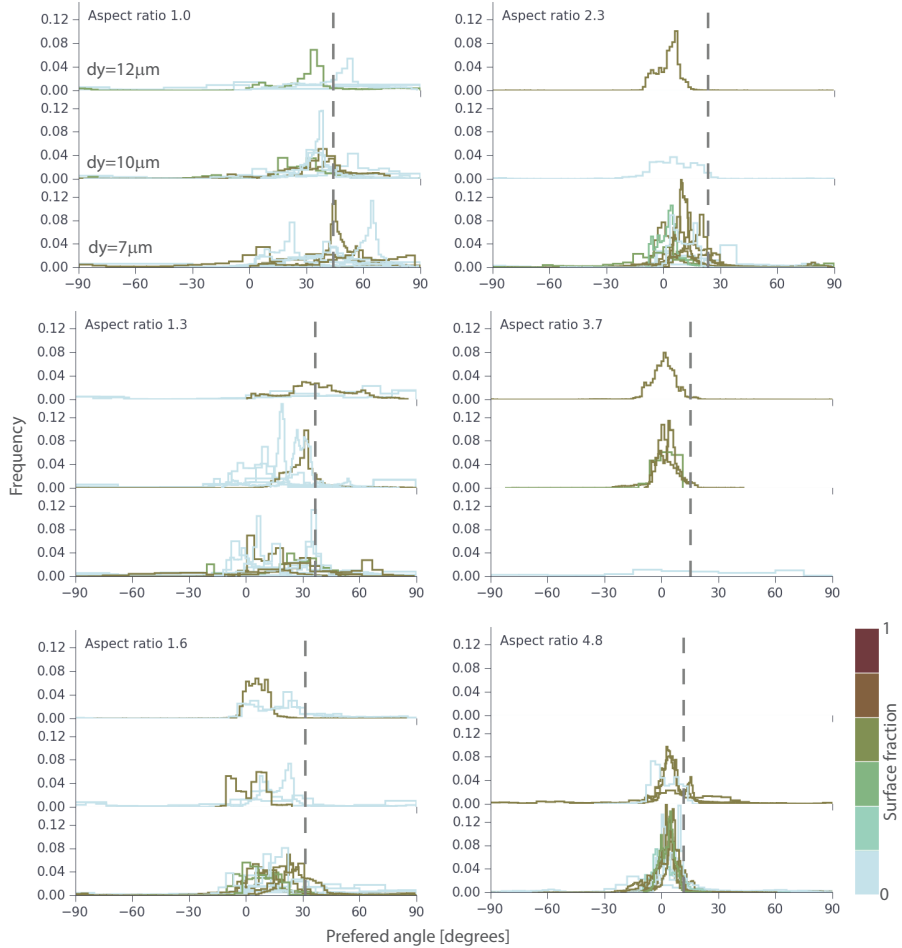


Figure 5.11: **Histograms of pixel preferred orientations.** Count of the preferred orientations of each pixel inside the well over movies of 10-20 minutes. Only pixels with *coherency* higher than 0.4, corresponding to places visited by microtubules are plotted. Dashed lines represent the angle of the diagonal of the well. Histograms are packed vertically by increasing short axis width, dy .

ACKNOWLEDGEMENTS

We thank Samara-Reck Peterson for providing the dynein construct and Sophie Roth for dynein purification and discussion. We thank Aniek Jongerius and Marcel Janson for purification of 6H::Ase1::GFP. We thank Maurits Kok and Louis Reese for discussions and José Alvarado for advice. We thank Maurits Kok for reading the manuscript.

6

TOWARDS THE ESTABLISHMENT OF POLARITY WITH A DIFFUSING RECEPTOR

It is not enough that we build products that function, that are understandable and usable, we also need to build products that bring joy and excitement, pleasure and fun, and, yes, beauty to people's lives.

Donald Norman

In the previous chapters we showed that tagged Tip1 could be deposited by microtubules to bio-mimetic cortices in the presence of Tea2 and Mal3. That assay differed in two key ways from real cells. In the first place, proteins were found as a reservoir, thus in non-limiting conditions. On the other hand, the cortical receptor was not mobile.

In this chapter, we developed a new bio-mimetic systems which address those two aspects. We form water-in-oil emulsion droplets where microtubules can grow inside and position +TIPs. The water-oil interphase contains absorbed functionalized lipids to which tagged +TIPs can reversibly bind in an analogous way as in the wall surfaces.

Parts of this chapter have been published in *Methods in Cell Biology* **128**, 1-22 (2015) Taberner et al..

6.1. INTRODUCTION AND RATIONALE

In the previous chapter we have seen how microtubules can establish a certain degree of cortical polarity in elongated micro-fabricated wells. However, this phenomenon is not robust. In that case, the cortical pattern displayed by the wells, is presumably composed by all the spots where a microtubule has successfully deposited protein plus a little amount of protein bound isotropically from the bulk. As we learned in chapter 4, 6H::eGFP::Tip1 deposition to the walls is not cooperative. Although microtubules tend to stay longer at places where they have already delivered protein, they do not leave an increased amount of protein there. Therefore, the pattern corresponds to nearly all the places a microtubule tip has visited, instead of the places most probable to visit. This lack of a positive feedback or regulatory mechanisms, reduces the robustness of polarity. In systems without a preferential site of delivery of polarity markers, computational simulations have shown that polarity requires positive feedback, mutual inhibition between two species of markers or inhibition with positive feedback [Chau et al. 2012].

In fission yeast, the cortical receptor for polarity factors is the membrane-associated prenylated anchor protein Mod5p [Snaith and Sawin 2003, Snaith et al. 2005]. In the absence of its ligand Tea1, Mod5 can freely diffuse along the whole plasma membrane [Snaith and Sawin 2003]. However, upon Tea1 tethering, occurring mostly at the poles of the cells, the two proteins form "nodes" of up to 100 nm diameter which nearly do not diffuse [Dodgson et al. 2013]. A possible excess of "free" Mod5 proteins may explain higher diffusivity observed in Mod5 [Bicho et al. 2010]. However, the increased concentration of Mod5 to the poles of the cell, caused by Tea1 deposition, may increase Tea1 affinity there.

The immobility of Tea1 nodes is not yet well understood as it does not seem to correspond to any lipid compartmentalization [Dodgson et al. 2013] or actin architecture. It depends on Tea1 trimerization and separate formation of nodes of the ERM (Ezrin-Radixin-Moesin) family protein Tea3 [Snaith et al. 2005, Bicho et al. 2010, Dodgson et al. 2013]. In forced co-localization of Tea1 and Tea3, a hypothesized network that keeps the clusters immobile is disrupted and the clusters diffuse away of the poles, but with slow diffusivity [Dodgson et al. 2013].

Stochastic simulation showed that diffusive cortical proteins can exhibit a polarized pattern if the rate of protein arrival to the poles by microtubule tips is high enough as compared to the rate at which proteins leave the poles by unbinding from the cortical receptor or diffusing away from the pole [Sokolowski 2013]. Protein clustering may reduce diffusivity at the membrane, thus facilitate polarity.

Interestingly, fission yeast displays another polarized pattern which does function with diffusion in the plasma membrane. It is the dual-specificity tyrosine phosphorylation-regulated kinase (DYRK) family Pom1 gradient [Bahler and Pringle 1998]. Pom1 forms a concentration gradient from the poles to the middle of the cell acting as a ruler for cell length [Martin 2009, Moseley et al. 2009]. It inhibits actomyosin ring formation. Only when the cell has grown $\sim 14 \mu\text{m}$, Pom1 concentration at the centre of the cell is low enough to allow the actomyosin ring formation [Rinc et al. 2014, Deng et al. 2014, Bhatia et al. 2014, Kettenbach et al. 2015, Ullal et al. 2015]. Pom1 is recruited to the

cell poles by Tea1-Tea4 in its unphosphorylated state [Martin et al. 2005, Tatebe et al. 2005, Celton-Morizur et al., 2006, Padte et al. 2006, Hachet et al. 2011]. Then, clusters of Pom1 diffuse at the membrane independently from Tea1-Tea4 [Dodgson et al. 2013], auto-phosphorylate, dissociate, and return to the cytoplasmic pool in its phosphorylated state [Saunders et al. 2013].

In order to study in a controlled manner the effects of membrane protein diffusion in the formation and establishment of polarized patterns, we have developed a method based on water in oil emulsion droplets (figure 6.1). We form droplets containing all the proteins and reagents needed to nucleate microtubules [Laan et al. 2012b, Roth et al. 2014] with a +TIP protein tracking system. The interphase with the oil contains a mix of lipids which prevents proteins from sticking to the oil phase and includes lipids functionalized with Ni(II)-NTA moieties to where his-tagged +TIPs can reversibly bind [Hochuli et al. 1987]. Moreover, the droplets are formed and compressed in PDMS (Poly (dimethylsiloxane)) elongated storage cavities so that they have a predetermined elongated shape [Boukellal et al. 2008] (figure 6.2).

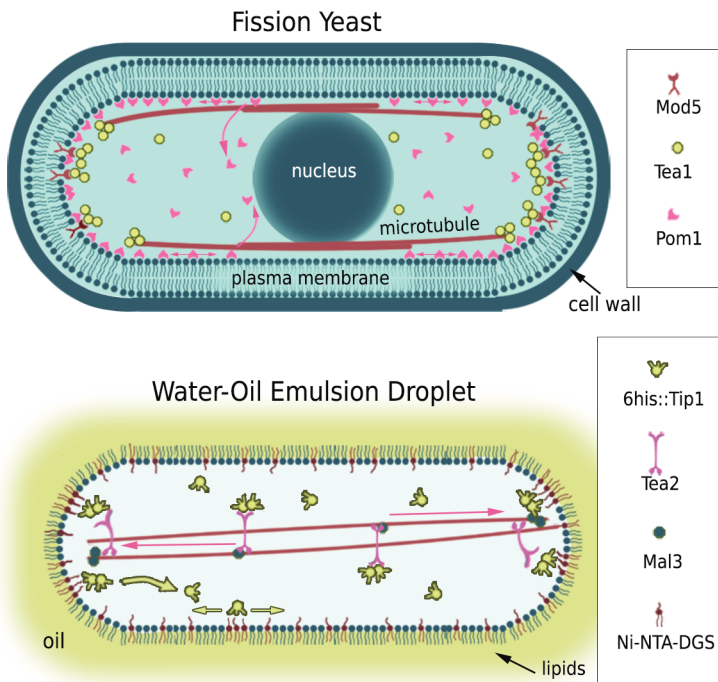


Figure 6.1: **From yeast to water-in-oil droplets.** Schematic representation of the microtubule-based polarity machinery in fission yeast (**top**) and the biomimetic droplet-based system (**bottom**). Note that although Tea2, Mal3 and Tip1 are not represented in the yeast scheme, they are involved in the microtubule-based transport of Tea1 (see chapter 1, figure 1.8).

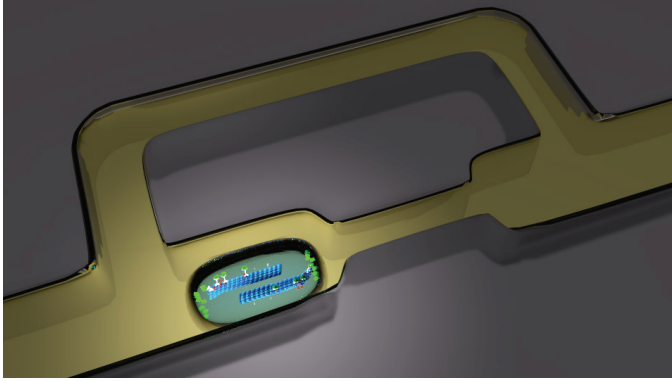


Figure 6.2: **Compressed droplets.** 3D cartoon render of a water droplet (blue) formed in the microfluidic chip (grey). The microfluidic channels are filled with an oil phase of continuous flow from left to right (yellow).

As in previous chapters, we use his-tagged constructs of *S. pombe* polarity proteins as polarity markers. These are the EB1 homologue, Mal3 (6H::Mal3::mCherry), and the kinesin-cargo system composed of Tea2, Tip1 and Mal3 with a hist-tag on Tip1 (6H::eGFP::Tip1) [Busch and Brunner 2004, Bieling et al. 2007].

We first explain in detail the setup preparation to obtain elongated droplets. It involves the microfabrication of two negative moulds later used for casting the PDMS. Then, we explain how to fabricate the PDMS chip and elongated droplets formation. Finally, we show preliminary results on his-tagged proteins selective binding to the Ni(II)-NTA lipids and microtubule essays.

6

6.2. MATERIALS

All reagents are dissolved in MRB80 buffer (80 mM KPipes, 4mM MgCl₂, 1mM ethylene glycol tetraacetic acid (EGTA), pH 6.8) at the stated stock concentration and stored at -80°C unless stated otherwise.

MASTER MICRO-FABRICATION

SPECIAL EQUIPMENT

- 4 in silicon wafer P/BOR <1-0-0> 10-20Ω-cm 500-550mm prime, single side polish w/2 flats (WRS Materials, USA)
- Delta 80 GYSET Spin coater with a close lid (Süss MicroTec, Germany)
- MJB3 mask aligner for UV exposure (Süss MicroTec)
- Surface profiler, Alpha step 500 (KLA-Tencor Corporation, USA)
- Binary chromium/soda lime mask (Delta Mask, The Netherlands) for the droplet channels
- Photomask on film substrate (Selba S.A, Switzerland) for the buffer reservoir

REAGENTS

- Different SU-8 Permanent Epoxy Negative Photoresist (MicroChem, USA) depending on the desired height: 2005 for 5 μm , 2010 for 10 μm and 15 μm , and 3025 for 40 μm . Even though the 2000 series were used, it is advisable to use the 3000 ones since they produce better adhesion to the silicon wafer
- Developer mr-Dev 600 (Micro Resist Technology GmbH, Germany)

PDMS CHIP FABRICATION**SPECIAL EQUIPMENT**

- Spin coater SPIN150i Table-Top (SPS-Europe, The Netherlands)
- Microscope coverslips 24 x 60 x 0.170 mm (Menzel Gläser)
- Eppendorf Centrifuge (VWR International B.V., The Netherlands)
- Vacuum desiccator
- Corona treater, model BD-20AC (Electro-Technic Products INC, USA).
- Oven, E28 (Binder, Germany).
- Razor blades
- Harris Uni-CoreTM cutting tip of 2 \emptyset mm (Ted Pella, Inc., USA)

REAGENTS

- Poly(dimethylsiloxane) (PDMS), Momentive RTV615A + B (Lubribond Benelux, The Netherlands)

MICROFLUIDICS SETUP AND DROPLET PREPARATION**SPECIAL EQUIPMENT**

- MFCSTM-EZ system 0-7000 mbar (Fluigent, France)
- Fluiwell-4C device (Fluigent)
- Microwlock tubes: T341-2TTP of 2 and 0.5 ml (Simport, Canada)
- Tube PEEK 510 mm OD x 125 mm ID Naturel (Cluzeau Info. Labo, France)
- Hamilton syringe (Hamilton-Bonaduz, Schweiz) 1 ml Syringe
- 23G Tygon tubing (Elvesys, France)

REAGENTS**Oil phase**

- Mineral oil (Sigma-Aldrich)
- Span[®] 80 (Sigma-Aldrich)
- 1,2-dioleoyl-sn-glycero-3-phospho-L-serine (sodium salt) (Avanti Polar Lipids Alabaster, AL, USA) (DOPS)
- 1,2-dioleoyl-sn-glycero-3-[(N-(5-amino-1-carboxypentyl)iminodiacetic acid)succinyl] (nickel salt) (Avanti Polar Lipids Alabaster, AL, USA) (Ni(II)-NTA-DGS)

Water phase (protein mix)

- Dextran, Alexa Fluor[®] 647, 10,000 MW, Anionic, Fixable (Life technologies, The Netherlands): 25 mg·ml⁻¹
- Tween[®] 20 (Sigma Aldrich)

6.3. METHODS**MICROFLUIDIC DESIGN**

PDMS is a widely used material to produce microfluidic chips [McDonald et al. 2000]. It is easy to handle, reliable, and low cost. However, it is also highly permeable to oxygen and slightly to water (Watson and Baron 1995). In our case, evaporation is critical, because we store droplets with a *S. pombe* size (0.2-0.4 pL) and observe them for hours. Evaporation of the small water droplets can be avoided by adding an extra water phase channel on top (with the same salt concentration) separated by a thin PDMS membrane, which allows water diffusion to and from the droplets, keeping their volume constant (Shim et al. 2007).

The microfluidic chip we use consists of two PDMS layers (figure 6.3a): A thin layer (~30 μm high) on top of a PDMS coated glass slide where droplets are formed and stored, and an additional thick layer (~0.5 cm) with a buffer channel reservoir on top. Buffer can be inserted in the upper channel reservoir with a syringe (no flow needed during the experiment), while the flow in the lower channels is controlled with a MFCSTM-EZ system.

The droplet formation and storage design is an adaptation of the one from Boukellal et al. 2008. It consists of several modules placed in serial with an inlet and outlet reservoirs. Each module creates and stores droplets (figure 6.3b). The inlet reservoir contains a filter to retain possible PDMS broken pieces produced when connecting the tubes. The resistivity of the filter should preferably not be higher than the sum of the droplet modules one.

Each droplet module has a storage, a bypass, and a restriction channels of widths “s,” “w,” and “r,” respectively (figure 6.3 b zoom). As detailed in Boukellal et al. 2008, the device is first filled with oil. A plug of water phase is then introduced, followed again by the oil phase. The widths are such that the water phase is first pushed to the storage,

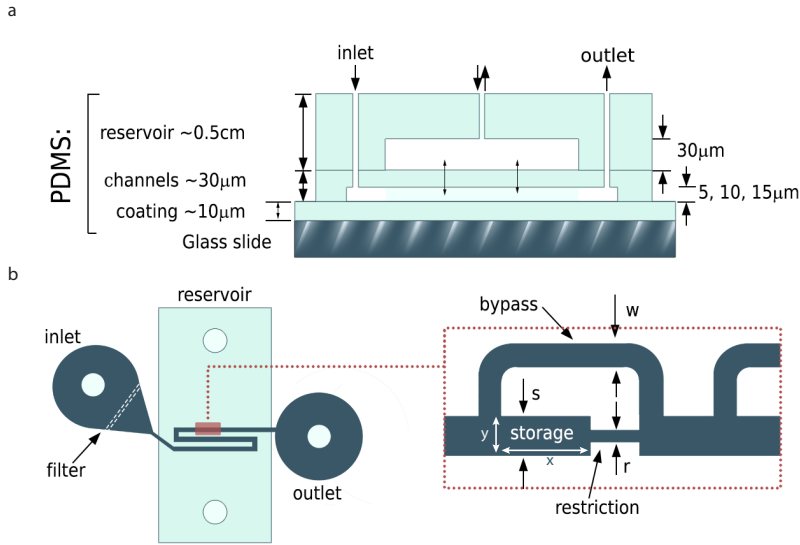


Figure 6.3: **Chip design and PDMS layout.** (a) Cross-section of the double-layered microfluidic chip for creation of elongated water-in-oil emulsion droplets. (b) Front view of the reservoir and droplet channel design. Zoom shows one module for creation and storage of an elongated droplet.

blocked at the oil filled restriction, and once the storage is filled, proceeds through the bypass ($s > w > r$). This is because, when the water plug arrives at the intersection with the bypass, it should deform to enter to the narrower bypass channel. Therefore, it proceeds towards the storage. In this case the bypass acts as a capillary valve [Eijkel and van den Berg 2006]. However, once the water phase reaches the even narrower restriction, the water flows through the bypass, where less deformation is needed ($w > r$) (figure 6.4 left). Once oil is flown again, it pushes the water phase, both towards the restriction and the bypass, leaving a droplet in the storage (figure 6.4 middle and right).



Figure 6.4: **Droplet formation.** Bright field view of droplet formation in $10 \cdot 15 \cdot 10 \mu\text{m}$ ($x \cdot y \cdot z$) storage. The water phase appears darker than the oil. Scale bar $5 \mu\text{m}$.

We want to keep close to a *S. pombe* size: $\sim 3 \mu\text{m}$ diameter. However, optical lithography limits our resolution to channels of $1.5 \mu\text{m}$. We decided to use height = $s = 5 \mu\text{m}$, $w = 3 \mu\text{m}$, and $r = 1.5 \mu\text{m}$. Wider or higher designs were also made for testing purposes.

MASKS FOR MICROFLUIDIC CHIP FABRICATION

To produce the two-layered PDMS chip, a negative mould for each of the layers needs to be made. Since the reservoir design does not need micrometer precision, it can be made with a low cost flexible photomask by Selba S.A. However, the formation-storage chip should be made in a soda-lime chromium mask with micrometer precision (Delta mask). These masks are then used to transfer the pattern to an SU-8-coated silicon wafer by photolithography, which will serve as negative mould for PDMS.

SU-8 NEGATIVE MOULD

Photolithography of SU-8 is a standard process. The steps are: spin coat the SU-8, bake at 95°C, expose to UV light through the photomask, bake at 95°C, develop with MicroChem's SU-8 developer, and bake at 150°C. MicroChem provides different SU-8 suitable for each thickness. We produced three masters for the formation - storage with 5 μm (with SU-8 2005, spin coated at 3800 rpms for 30 s), 10 μm , and 15 μm (with SU-8 2010, spin coated at 4000 and 1700 rpms, respectively for 32 s); and one master for the reservoir of 40 μm (SU-8 3025, spin coated at 1800 rpms for 45 s). However, since SU-8 ages, the spinning speeds given are indicative and might have to be adjusted in later productions. The samples were exposed to 195, 185, 195, and 250 $\text{mJ}\cdot\text{cm}^{-2}$ 365 nm UV light for the respective 5, 10, 15, and 40 μm thicknesses.

6

PDMS CHIP

Figure 6.5 shows a schematic cartoon of all the steps in the fabrication of the PDMS chips.

All parts of the PDMS chip are made with 10 weights of PDMS pre-polymer RTV615 and 1 weight of the curing agent. The two components are mixed in a plastic weighting boat, placed in a 50 mL falcon tube (BD Falcon), and centrifuged at 300 rcf for 5 min to remove air bubbles.

Start with the reservoir channel making a pot-like structure with aluminium foil around the silicon master and pour on it around 40 mL of premixed PDMS. Put it in a vacuum desiccator until all the air bubbles are gone (around 1.5 h). Then, bake it at 100°C for 1 h to cure it. Remove the aluminium foil with the help of a razor blade and peel the PDMS off by gently pulling it from one side. Cut with a razor the non-flat edges of the piece and punch 0.5 mm holes at the extremes of each reservoir channel with a Harris Unicore cutting tip. To avoid dust in the channels, one can put some MagicTM tape (Scotch) on it. Before sticking two PDMS, one can also remove possible dust from the surfaces by putting some tape on it and removing it.

For the droplet channel, a thin layer of PDMS (around 30 μm) is spin coated at 1000 rpm for 20 s with an initial step of 800 rpm for 5 s. After spinning, bake it at 100°C for at least 15 min.

Bind the reservoir channel on top of the droplet one by applying for a few seconds O_3 plasma on both pieces with the corona treater and quickly placing the reservoir channel on top of the other one, properly aligned. The PDMS layers should stick without need of extra pressure. Bake it at 100°C for at least 1 h. Cut with a razor blade the extra PDMS

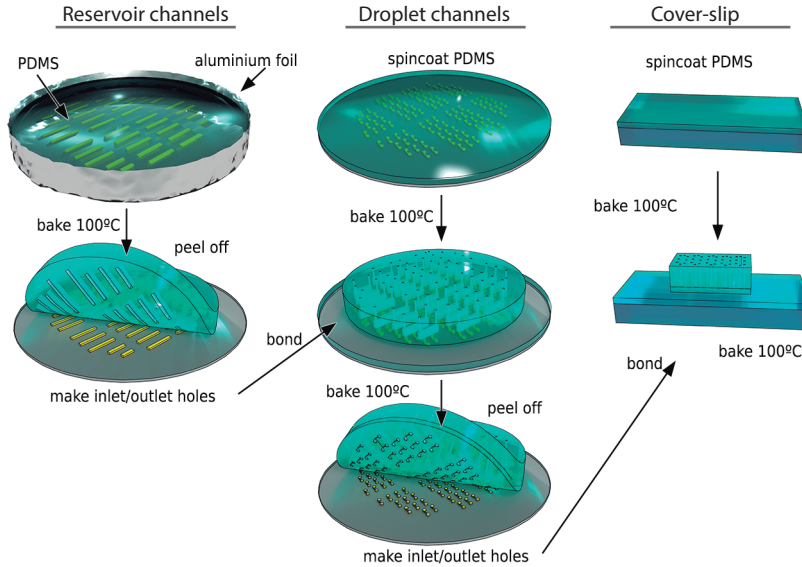


Figure 6.5: **Chip design and PDMS layout.** (a) Cross-section of the double-layered microfluidic chip for creation of elongated water-in-oil emulsion droplets. (b) Front view of the reservoir and droplet channel design. Zoom shows one module for creation and storage of an elongated droplet.

part of the droplet channel that has no reservoir piece on top and peel it off. Peel off the rest of the chip with both layers by carefully pulling it from one side. Protect the side with the channels with tape and cut each modular chip with the razor. Punch the inlet and outlet holes as before.

For the cover-slip support, spin PDMS at 4000 rpm for 30 s with a previous step at 200 rpm for 100 s. Bake it for at least 15 min at 100°C.

Finish the chip by binding the two-layer formed before with the PDMS coated cover-slip. This is done by applying for a few seconds O_3 plasma on both pieces with the corona treater and quickly placing the two-layer chip on top of the cover-slip. Bake it at 100°C overnight to obtain very hydrophobic PDMS channels.

MICROFLUIDIC SETUP AND DROPLET FORMATION

Start by inserting buffer with the same osmotic pressure as the droplets inside the reservoir channels with a syringe and 23G Tygon tubes connected to the channels via a cut piece of a 1.20 mm needle.

The flow for the droplet channels is controlled by a pressure controller MFCSTM-EZ system connected to a Fluiwell accessory with Microwlock tubes. PEEK 1250 mm tubes directly connect the Microwlock tubes in the Fluiwell to the inlets of the microfluidic chip.

Both, the droplet formation and observation of the fluorescent microtubule assay,

are done with a spinning disk confocal microscope.

Droplets are formed by flowing first a mix of oil with lipids, followed by the water phase containing the protein mix and, again, the oil phase. Since there is only one inlet, each phase is added by exchanging the PEEK tubes. For 5 μm high channels, the initial oil phase flows easily with 1-2 bars. The protein mix needs up to 4 bars to reach the filter of the inlet. We found important to push the water phase till the filter of the inlet before exchanging the tube back to the oil one. Otherwise, we experienced the water phase to be pushed back to the PEEK tube when releasing the pressure of the water phase prior to tube exchange.

For the final oil flow, the pressure can be kept low (a few hundreds millibars). Once the droplets are formed, lower the flow of oil to keep the droplets close to the restriction without deforming them.

Pressures have to be tested for each design and chip since the resistance of the channels might vary from one chip to another.

Alternatively to the presented procedure, one could preform droplets in a T-shape microfluidic chip as in Roth et al. 2014 and insert them instead of the water phase in the previous steps. In this case, the percentage of Span[®]80 has to be such that droplets are stable enough for a T-shape channel formation (which requires high amount of Span[®]80), and unstable enough to re-adapt their size to the storage one (low amount of Span[®]80). If the conditions can be met, this way of producing droplets would reduce the amount of pressure needed to push the water phase.

6

LIPIDS COMPOSITION

For the proper functioning of the microfluidic chip, it is essential that the PDMS is very hydrophobic. The water phase must not wet the surfaces. Protein sticking to PDMS will make water wet the surface. The use of surfactants such as Span[®]80 helps preventing protein interaction with the PDMS and the oil because it is absorbed at the water-oil interface much faster than lipids. Indeed surfactant absorption is diffusion limited, while lipid absorption appears to be more complex and can take up to several minutes for full coverage [Pautot et al. 2003]. The amount of Span[®]80 needed depends on the lipid composition and the use of Tween[®]20 in the water phase. An excessive amount of surfactant leads to very stable droplets and the undesired accumulation of several small droplets not coalescing in the storage channel. In our hands, for 0.03 % Tween[®]20 in the water phase, a molar ratio of Span[®]80, DOPS and Ni(II)-NTA-DGS of 90:4:1 with 0.5 mg·mL⁻¹ of lipids in oil (without counting Span[®]80) was used for his-tagged protein binding experiments and a 96:3.6:0.4 for the microtubule assay.

Prepare the oil phase by first mixing DOPS and Ni(II)-NTA-DGS in chloroform in a glass vial (use glass syringes). Dry it in nitrogen flow. Add the Span[®]80 and mineral oil. Mix by pipetting several times. Sonicate for 30 min to dissolve the lipids in oil.

ASSAYS

Here we first present the control experiment testing the specific binding of his-tagged proteins to Ni(II)-NTA-DGS lipids. We then describe a protocol to grow dynamic microtubules from seeds.

Assay on His-tagged protein specific binding to Ni(II)-NTA lipids:

The binding assay mix contains 500 nM 6H::Mal3::mCherry or Mal3::Cherry (for a negative test), with 0.03 % Tween[®]20, 2 mg·mL⁻¹ BSA, 2 mg·mL⁻¹ κ -casein, 0.4 mg·mL⁻¹ glucose oxidase, 50 mM glucose, in MRB80 with 50 mM KCl and 0.7 mM dextran 467. Centrifuge 8 min at 30 psi to sediment possible protein aggregates and transfer the supernatant to a 0.5 mL Microwlock tube to prepare the droplets as explained above.

Figure 6.6a shows examples of droplets with either Mal3::mCherry or 6H::Mal3::mCherry. No unspecific binding of Mal3::mCherry to the water-oil interface is observed (figure 6.6a, left). By contrast, 6H::Mal3::mCherry is visible both inside the droplet and at the lipid covered interface, confirming the specific interaction with Ni(II)-NTA lipids.

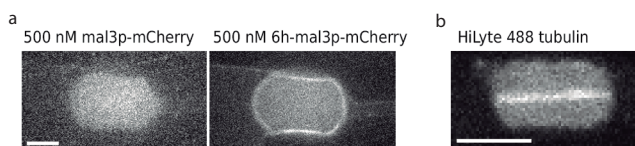


Figure 6.6: **Droplet formation.** (a) Confocal fluorescent microscopy images on the equator of droplets formed in 10·15·10 μm ($x \cdot y \cdot z$) storage with Mal3::mCherry (left) and 6H::Mal3::mCherry (right). (b) Confocal fluorescent microscopy images of tubulin on the equator of a droplet formed in 5·11·5 μm storage. Microtubules can be seen aligned along the long axis of the droplet. Scale bars 5 μm .

Assay on microtubule organization in elongated droplets:

Mix on ice the following 10 mL MRB80 solution reserving 1 mL (seeds will be added later): 26 mM unlabelled tubulin, 1.75 mM HiLyte 488 tubulin, 5 mM GTP, 0.03 % Tween-20, 5 mg·mL⁻¹ BSA, 5 mg·mL⁻¹ κ -casein, 50 mM KCl, 0.4 mg·mL⁻¹ glucose oxidase, 50 mM glucose, and 0.6 mM Dextran 647. Centrifuge 8 min at 30 psi to sediment possible protein aggregates. Transfer the supernatant to a 0.5 mL Microwlock tube and add 1 mL of seeds. Prepare the droplets as explained above. Once the droplets are formed, set the temperature controlled chamber of the microscope to 26-30°C to trigger polymerization. Figure 6.6 b shows an example of a droplet with dynamic microtubules inside. They align in the longest direction.

6.4. DISCUSSION AND PERSPECTIVES

We developed a method to produce elongated cavities where microtubules can dynamically grow and proteins can reversibly bind to the boundaries of the cavity. The protein

receptors are mobile. This may allow for a redistribution upon local binding of proteins at a certain spot of the cavity.

This method still requires optimization in order to find the proper conditions for microtubule-based deposition of polarity markers. With the current lipid mixture, 500 nM of 6H::Mal3::mCherry only binds partially to the Ni(II)-NTA lipids. In typical microtubule end binding assays 50-150 nM protein is used. At this concentration, no protein was found binding to the lipids. Therefore, the protein affinity for the lipids might need to be increased in order to obtain microtubule-based depositions. In previous experiments in microfabricated wells, this was obtained by employing tris-Ni(II)-NTA instead of mono-Ni(II)-NTA [see chapter 3]. This is technologically possible for lipids [Beutel et al. 2014] and should be tried in the future.

On the other hand, the proportion of functionalized lipids could be increased. In this case, the addition of negatively charged Ni(II)-NTA lipids tends to destabilize the droplets. This, could be compensated by exchanging the DOPS lipids (negatively charged) by DOPE (neutral).

The setup presented potentially offers a simplified framework to study both the Tea1 and the Pom1 polarity patterns with a reliable control on droplet size and shape. Moreover, the continuous flow of oil in principle opens the possibility to introduce (oil-soluble) drugs to the system to, for example, trigger microtubule polymerization.

The microfluidic chip can also be designed to produce elongated droplets in a vertical position, such that the poles of the droplets can be imaged at higher resolution.

This setup, moreover, opens the possibility to study cytoskeleton organization in predetermined confinements. This includes assessing spindle positioning due to cell shape or microtubule reorganization due to cell shape changes occurring for example in platelets.

ACKNOWLEDGEMENTS

The design of this setup was done in collaboration with Sophie Roth. We further thank her for advice in microfluidics.

7

CONTROL OF MICROTUBULE DYNAMICS BY CORTICAL PROTEINS

Microtubule dynamics are affected by the cell boundaries. In some cases cells need to tune those dynamics by for instance keeping microtubules longer in contact with the cell wall. In this chapter we asses whether the microtubule stabilizing protein CLASP, can exert microtubule stabilization while being bound to a barrier mimicking a cell wall. The results presented are exploratory, and suggest that indeed CLASP can produce such stabilization.

7.1. INTRODUCTION

In the previous chapters we explored conditions to produce a cortical protein pattern. In this chapter we are interested in how a pre-established cortical pattern can affect microtubule dynamics. Several studies identified two main proteins as key regulators of microtubule dynamics from the cortex: the Cytoplasmic Linker Associated Proteins (CLASP), and the adenomatous polyposis coli protein (APC) [Gundersen et al. 2004, Mimori-Kiyosue 2011].

In migrating fibroblasts, CLASP have shown to participate in the polarized organization of microtubule networks by specifically stabilizing microtubules at the leading edge [Akhmanova et al. 2001]. In mammalian cells, CLASP binds to the cell cortex via $LL5\alpha/\beta$ in non focal adhesions regions and stabilizes microtubules from there via interaction with other proteins, including EB1 and integrins [Mimori-Kiyosue et al. 2005, Lansbergen and Akhmanova 2006, Hotta et al. 2010]. In epithelial cells CLASP- $LL5\alpha/\beta$ contribute to microtubule stabilization and organization in the basal side [Hotta et al. 2010]. In *S. pombe*, the CLASP homologue, Cls1, produces rescues in microtubules promoting multiple encounters with the cell cortex [Al-Bassam et al. 2010, Kelkar and Martin 2015].

Another protein that anchors microtubule tips to the cortex is the adenomatous polyposis coli protein APC [Reilein and Nelson 2005, Wen et al. 2004, Mimori-Kiyosue et al. 2007]. It is transported to microtubule tips by kinesin and tethers the microtubules through EB1 and actin-binding proteins including mDia (a Rho effector) and IQGAP1 (a Rec1/Cdc42 effector) at the leading edge in migrating Vero cells [Watanabe et al. 2004]. APC also arranges polarized microtubule arrays, directed towards the leading edge of migrating cells [Etienne-Manneville et al. 2005] or the basal side of epithelial cells [Reilein and Nelson 2005].

Interestingly, the proteins mentioned above, CLASP and APC, have interaction with EB [Lansbergen and Akhmanova 2006], which by itself alone, is a microtubule destabilizer. Precisely, this association of EB with stabilizing proteins has often hidden its destabilizing effect (as in yeast [Tirnauer and Bierer 2000, Busch and Brunner 2004]). Recent studies showed XMAP215, a protein containing TOG domains similar to the ones of CLASP, act in synergy with EB1 to increase microtubule growth speed [Zanic et al. 2013].

In this chapter we explore in a minimal *in vitro* system how CLASP can stabilize microtubules only by "end-on" interaction from a cortex. We functionalized micro-fabricated glass barriers with CLASP molecules and let dynamic microtubules grow towards the walls in the presence of EB3 in solution. Similar experiments performed with microtubules alone, showed that a barrier causes a microtubule destabilization that reduces its polymerization speed, causes stalling, and therefore triggers microtubule catastrophe [Dogterom and Yurke 1997, Janson et al. 2003-2004]. The presence of EB proteins, further destabilizes the microtubule as catastrophes occur shortly after barrier contact (20-40 seconds for Mal3 [Kalisch, chapter 4]). In this chapter we show that the presence of CLASP at the walls stabilizes microtubules by extending the time they can sustain stalled contact with the wall for several seconds, up to a few minutes. The results obtained, we will see, require further validations by repeated experiments since we observed intrinsic variations between the samples with and without CLASP at the walls.

7.2. MICROTUBULE DYNAMICS REGULATION BY CLASP

Recent *in vitro* experiments with purified human CLASP2 α (with a GFP fused) in the lab of Anna Akhmanova showed that in the presence of mCherry::EB3, GFP::CLASP2 α stabilizes microtubules. Figure 7.1 shows kymographs of dynamic microtubules grown in the absence of +TIPs, in the presence of mCherry::EB3 and in the presence of EB3 and GFP::CLASP2 α . While catastrophes are frequent in bare microtubule and its frequency increased in the presence of EB3, addition of GFP::CLASP2 α shows microtubules without catastrophes. GFP::CLASP2 α fluorescent signal appears along the microtubule lattice and with higher intensity at the growing microtubule ends.

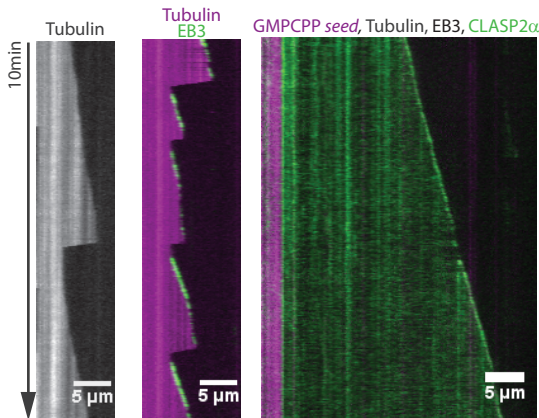


Figure 7.1: **Microtubule growth with +TIPs in solution.** Kymographs of dynamic microtubules grown in the absence and presence of +TIPs. 15 μ M tubulin, 20 nM mCherry::EB3 and 30 nM GFP::Clasp2 α . The mCherry::EB3 signal shows much lower intensity than the GMPCPP seed, therefore it is not appreciable with the brightness contrast displayed in the picture. TIRF microscopy images, courtesy of Maurits Kok.

The way in which CLASP2 α stabilizes microtubules is not yet clear. Does it suppress catastrophes or promote rescues? How relevant is the lattice binding as opposed to the tip binding? Is CLASP2 α also able to stabilize microtubule against force-induced catastrophe?

In this chapter we address those questions by locating CLASP2 α at barriers so that it might affect microtubule dynamics only when a microtubule tip gets in contact with the barrier.

7.3. MICROTUBULE 'END-ON' INTERACTION WITH CLASP

EXPERIMENT OVERVIEW

We functionalized 300 nm high glass barriers with two different concentrations of 6H::GFP::CLASP2 α immobilized. Dynamic microtubules were grown from GMPCPP stabilized seeds bound to the bottom surface of the glass slide by biotin-streptavidin linkages as shown in figure 7.2. Microtubule growth was observed in the presence of mCherry::EB3 or unlabelled EB3. Growing microtubule tips, decorated with an EB3 comet, often encountered the barriers, where they could potentially interact with 6H::GFP::CLASP2 α . The barriers contained $\sim 1 \mu$ m long overhang layers of chromium and gold, ~ 50 nm thick each, on top which prevents microtubule from growing over (see chapter 3 for micro-fabrication details).

We measured the time that the microtubule plus end kept in contact with a spot at the barrier prior to undergoing catastrophe (barrier contact time) and compared it for the two cases of different densities of 6H::GFP::CLASP2 α at the barriers. In this assay, CLASP interaction with the microtubule could occur only at the tip.

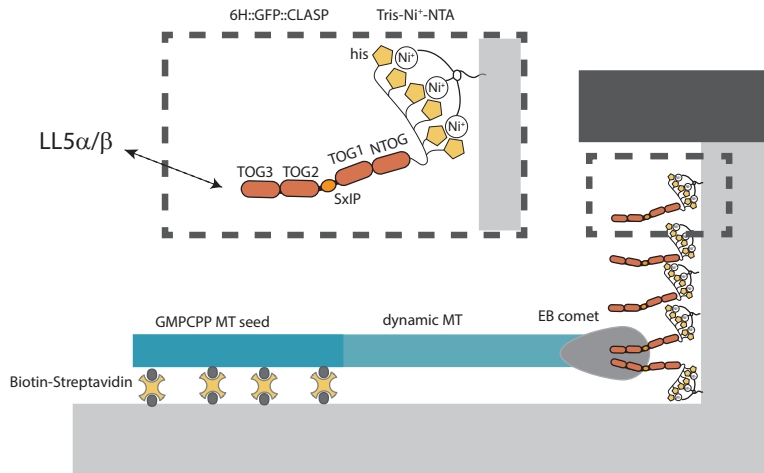


Figure 7.2: **Diagram of cortical CLASP assay.** We use micro-fabricated barriers functionalized with PLL-g-PEG/tris-Ni(II)-NTA to which his-tagged proteins can be immobilized. The basement surface is coated with PLL-g-PEG/biotin to which biotinylated microtubule seeds bind by a sandwiched streptavidin complex.

7

COATING OF THE WALLS WITH CLASP

His-tagged GFP::CLASP2 α was immobilized at the barriers by spontaneous binding of the his-tag to a pre-coating of PLL-g-PEG/tris-Ni(II)-NTA bound specifically to that glass surface [Taberner et al. 2014, chapter 3]. Although this binding is reversible [Hochuli et al. 1987], proteins bound via a his-tag have more degrees of freedom than in other stronger immobilizations [Tinazli et al. 2005], as for instance biotin-streptavidin, therefore it is less susceptible to impede protein binding to the microtubule and exertion of its function (as in Bieling et al. 2008b).

The sample of low density of CLASP at the barrier (low cortical CLASP) was obtained by incubating 0.6 μM of 6h::GFP::CLASP2 α for 20 min, while the high density CLASP sample (high cortical CLASP) was obtained by incubating 1.2 μM 6H::GFP::CLASP2 α . After incubation, the unbound protein was thoroughly washed out with abundant MRB80 buffer. Then, GMPCPP biotinylated seeds were incubated for 5 min, followed by the tubulin mix with 50 nm EB3.

Since his-tag binding to tris-Ni(II)-NTA is reversible, protein might unbind during the microtubule assay. We monitored the amount of bound CLASP at the barrier over

	k_a [$10^{-3}\mu\text{M}\cdot\text{s}^{-1}$]	k_d [10^{-3}s^{-1}]	K_D [nM]
High cortical CLASP	1.3 [- 2.7]	0.13 [0.11 - 0.16]	105 [40 -]

Table 7.1: **6H::protein binding to tris-Ni(II)-NTA**. Kinetic parameters are obtained by least-square fitting of the binding curve $\Gamma(t) = \Gamma_{\text{eq}}(1 - e^{-(k_a c + k_d)t})$ and unbinding curve $\Gamma(t) = \Gamma_{\text{eq}}e^{-k_d t}$. Values in brackets indicate the 95% confidence intervals. The lowest interval value for the association rate could not be calculated.

time by measuring its fluorescence intensity there. As expected, this intensity increased during the incubation time, and decreased after unbound protein washout and during the dynamic microtubule assay (figure 7.3).

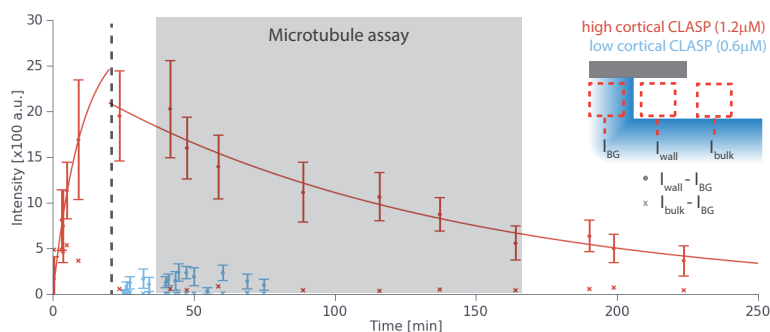


Figure 7.3: **6H::GFP::CLASP2 α immobilization to the barriers**. Binding kinetics of Clasp to the barriers in terms of barrier fluorescence intensity at the wall. The unbinding kinetics correspond to the evolution observed during the microtubule assay (next section). The dashed line shows the end of the incubation step and wash out of the non-immobilized protein. Continuous lines show fits to obtain the association and dissociation rate (see table 7.1).

The low cortical CLASP sample showed much lower intensity values than the high cortical CLASP one. We only measured the binding kinetics for the high cortical CLASP sample. Fitting by a simple exponentials of the binding and unbinding yielded a dissociation constant of $K_D = 105\text{nM}$ (table 4.1). This value is similar than the ones obtained for 6H::eGFP::Tip1 and 6H::Mal3::mCherry in chapter 4 (72 nM and 148 nM respectively, table 4.1). However, in the 6H::eGFP::Tip1 and 6H::Mal3::mCherry cases, incubations included 10 mM imidazole, which competes for nickel binding, and effectively increases the his-tagged protein K_D . We note here that 6H::CLASP2 α incubation was limited to 20 minutes to minimize protein denaturation prior to the microtubule assay. This was not enough time to reach equilibrium, therefore we do not dispose of the whole binding curve to determine the dissociation constant. This reduces the accuracy of the fitting.

Given the dissociation constant obtained for the high cortical CLASP sample, a 6H::CLASP2 α incubation of $0.6\mu\text{M}$ should produce a higher protein binding to the barriers than observed. We hypothesized that the low cortical CLASP sample experienced some un-noticed mistake during sample preparation. In this screening study we will consider this sample as a sample containing practically no CLASP2 α at the barriers.

THE EFFECT OF CORTICAL CLASP ON MICROTUBULE DYNAMICS

Microtubules in the low cortical CLASP sample exhibited catastrophes shortly after plus end contact with the wall (see figure 7.4 a for examples); often with no clear stalling. However, in the high cortical CLASP sample, microtubules often stalled at the barrier for several seconds up to a few minutes (figure 7.4 b). Although the apparent microtubule stabilization at the wall, all the microtubule contacts eventually lead to catastrophe.

Rhodamin tubulin, 6H::GFP::CLASP2 α

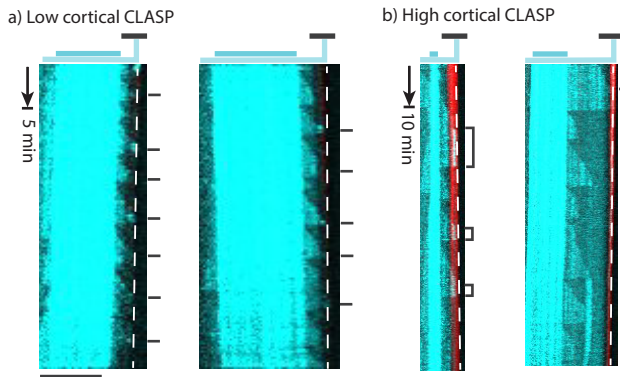


Figure 7.4: Barrier contact times. Examples of representative kymographs along microtubules encountering the barrier with (a) low cortical CLASP and (b) high cortical CLASP. The CLASP signal in a is not appreciable for the same brightness contrast and in b. The cartoons on top show the positions of the seeds with respect to the wall, also marked with a white dashed line in the kymographs. Barrier contact events are indicated at the right. Scale bars 5 μ m.

Deep observation of microtubule-barrier contacts showed that microtubule stability evolved over time. Microtubules appeared more stable (less prone to undergo catastrophe) some minutes after tubulin incubation than in the first time-lapses taken. This evolution could be intrinsic to the experimental setup since 6H::GFP::CLASP2 α release over time from the barriers. Released CLASP2 α could stabilize the microtubules. Whether this is the case is not clear since we did not observe any 6H::GFP::CLASP2 α signal at the tips of microtubules (not shown). On the other hand, protein denaturation during the experiment, or acidification of buffer by the oxygen scavenger system used (glucose oxydase, Shi et al. 2010]), could cause *in vitro* artefacts.

Due to the observed evolution in our samples, we decided to report microtubule dynamics in solution and against the coated barriers over experimental time: starting at 6H::CLASP2 α incubation, 20 minutes before addition of the tubulin and EB3 mix.

OUTCOMES UPON MICROTUBULE-BARRIER CONTACT

In the low cortical CLASP sample between 60 and 80 % of the microtubule barrier contacts lead to stalling of microtubule growth, followed by a catastrophe (figure 7.5). This percentage increased over experiment time. The remaining percentage corresponded to microtubules sliding at the wall for a short distance (1-2 μ m), followed also by catastrophe. In anecdotal cases, the microtubule tip remained at a spot on the barrier and slowed growth producing buckling. These results are in agreement with the outcomes of microtubule-barrier contact in the presence of the *S. pombe* EB1 homologue, protein Mal3, found in chapter 4, which yielded 70% stalling.

Buckling occurrence is dependent on morphology of the barriers. Microtubules may be more prone to get stopped at rougher surfaces or at the edge of the overhang. How-

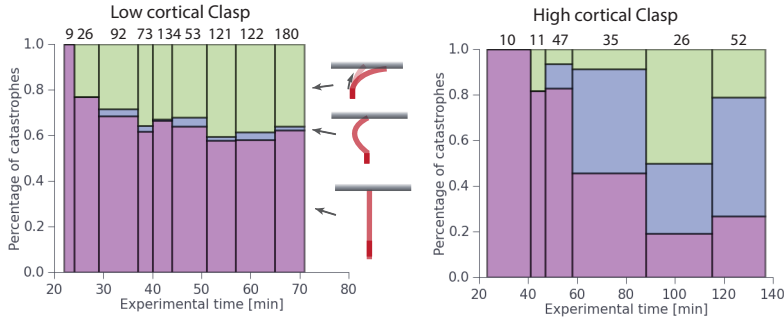


Figure 7.5: **Microtubule-barrier interactions.** Evolution of the frequency of stalling (purple), buckling at one spot (blue), and sliding (green) upon microtubule tip contact with the barrier during the time of the experiment after 6H::GFP::CLASP2 α incubation. Number on top show the total amount of events computed.

ever, in the presence of EB3 or Mal3, microtubules are rarely able to buckle and undergo catastrophe.

In the high cortical CLASP sample, up to 50 % of the microtubule-barrier contacts displayed buckling before catastrophe (figure 7.5). This percentage, and the percentage of sliding events increased during experiment time. Stalling events were reduced to up to 20 % of the cases.

The appearance of buckling upon barrier contact had already been observed in bare microtubule assays [Janson et al. 2003]. Moreover, we observed buckling in the presence of the *S. pombe* kinesin-cargo system Tea2-Tip1 employing the same barriers and with the added ability of Tip1 ability to bind to the barrier via his-tag interactions (figure 4.4). In that case, we argued that Tip1 stabilizes microtubules, allowing them to sustain growth under load; an effect that is reduced in the presence of only EB proteins [Kalisch 2013, chapter 4]. Microtubules in the high cortical CLASP assay also display the capacity to sustain growth under load. However, here, the frequency of sliding is lower than for the Tip1 case. The addition of 6H::GFP::CLASP2 α may contribute to stopping to microtubule tips at barrier spots that otherwise would have slid. This is supported by the appearance of less sliding, in general, in the high cortical CLASP sample than in the low cortical CLASP.

MICROTUBULE DYNAMICS

In order to determine whether cortical CLASP is affecting microtubule dynamics, it is needed to first set as control that microtubule dynamics are not modified away from the cortex. For this reason, we measured the microtubule catastrophe times, defined as the time between start of growth from the seed until the first catastrophe. This time, has been shown in the past to follow a non-exponential distribution [Odde et al. 1995, Gardner et al. 2011]. In the presence of Mal3, the distribution typically peaks around 100 seconds, shorter than for bare microtubules, around 200 seconds [Kalisch 2013].

Figure 7.6 a shows the evolution of the catastrophe times of microtubules not en-

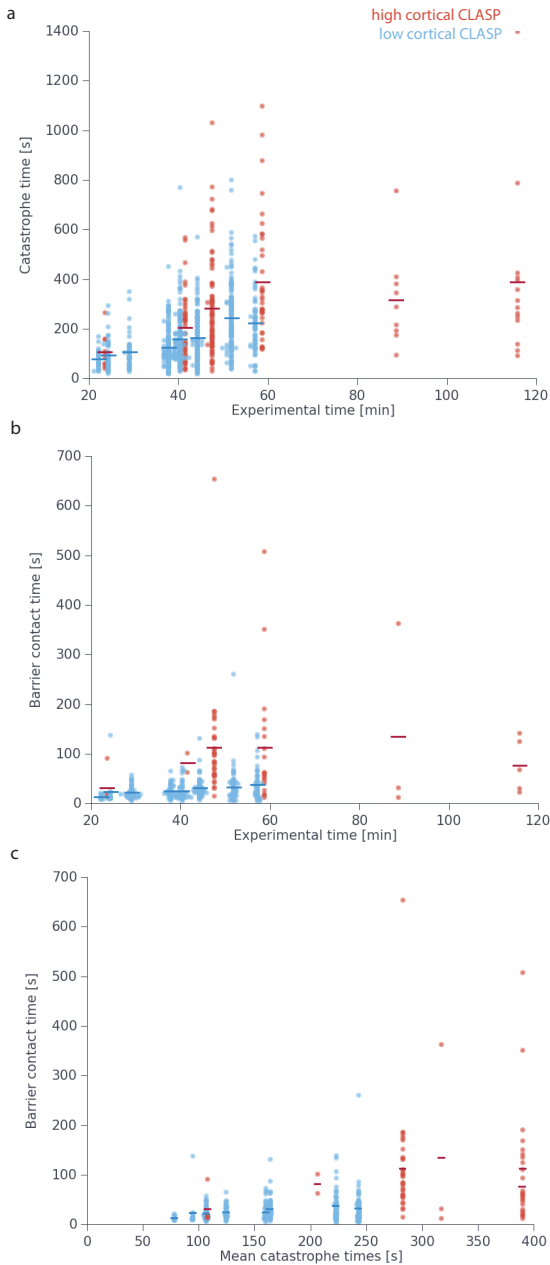


Figure 7.6: Microtubule dynamics. (a) Evolution of the catastrophe time distribution for microtubules not encountering the barriers and their mean value (hyphen) over time after CLASP2 α incubation. (b) Same evolution of the barrier contact times for stalling microtubules without clear sliding or buckling. (c) Same barrier contact times distribution as a function of the mean catastrophe time of the set of microtubules not encountering the barriers in the same field of view.

countering the barriers over the experiment time. It should be noted that this assays had a high density of microtubules. This caused microtubules to often bump into each other. Therefore, the obtained distribution is not completely free of any physical contact with obstacles.

Both samples showed a clear increase on the catastrophe times during the first 50 minutes of experiment. Mean values ranged between 50 and 140 seconds for the low cortical CLASP and between 110 and 400 seconds for the high cortical CLASP. The higher catastrophe times for the high cortical CLASP are unexpected for microtubule growth in the presence of EB3. They could be due to 6H::GFP::CLASP2 α in solution released from the walls. Experiments should be repeated to determine the cause of the differences between the two samples.

We defined the barrier contact times as the time the microtubule tip remains in contact with a barrier site without clear buckling or sliding before undergoing catastrophe. The two samples showed a big difference in this barrier contact time (figure 7.6). Mean barrier contact times in the low cortical CLASP sample were relatively constant around 30 seconds, while for high cortical CLASP, they increased to up to around 100 seconds. Since the two samples displayed different catastrophe times, it is not possible to solely attribute the higher barrier contact times in the high cortical CLASP sample solely to 6H::GFP::CLASP2 α in the barrier.

In order to better compare both samples, we plotted again the same barrier contact times, as a function of the mean catastrophe times obtained in the same time lapse movie (figure 7.6 c). It is important to note that the catastrophe times exhibit a a distribution skewed towards long times (or a Gamma distribution with a non-integer shape parameter). Therefore, microtubules in each movie showed high variations from the mean catastrophe times.

The high cortical CLASP sample exhibited a positive correlation between the barrier contact times and the catastrophe times. On the other hand, the low cortical CLASP kept short mean barrier contact times for any mean catastrophe time. Nevertheless, all barrier contact times distributions became wider with higher catastrophe times. These observations suggests that cortical 6H::GFP::CLASP produced an extra stabilization of microtubules upon barrier contact only in the high cortical CLASP sample.

7.4. DISCUSSION

In this chapter we showed a different application of the system developed in chapter 3. Here, we reconstituted a bio-mimetic cortex, where cortical proteins can affect microtubule dynamics. In particular, we showed how cortical CLASP may stabilize microtubules upon plus end contact with a cortex. The presented results are exploratory and require replication. Nevertheless, they suggest that CLASP is able to stabilize microtubules upon barrier induced catastrophes by interactions occurring only from the barrier. This results further suggest that CLASP can stabilize microtubules from interactions occurring only at the tip of the microtubule.

Experiments in our group of microtubule encountering barriers in the presence of EB3 and CLASP2 α in solution showed no catastrophes at all (data not shown). In the cortical CLASP case, microtubule do undergo catastrophes. Therefore, the obtained stabilization is less effective than when CLASP is present in solution. It would be interesting to study in the future the cause behind this observation. We hypothesize three possible explanations. Firstly, microtubule stabilization by CLASP might be concentrations dependent. In this scenario, our cortical CLASP experiments might not render enough amount of CLASP at a barrier spot to fully immobilize a microtubule. Secondly, 6H::GFP::CLASP2 α at the wall might have a disadvantageous orientation to properly interact with microtubules. It is known from XMAP215 that TOG domains bind to tubulin dimers in a specific orientation [Ayaz et al. 2012]. In our assay, 6H::GFP::CLASP2 α is anchored to the barrier from the C-terminal, while in cells, CLASP2 α interacts with LL5 α/β , its cortical binding partner, from the N-terminal (figure 7.2). It would be interesting to test in the future constructs with the his-tag in the N-terminal. Thirdly, CLASP binding at the microtubule lattice, in addition to the tip, might be crucial for a full microtubule stabilization.

The results shown have difficult interpretation due to the observed evolution on microtubule dynamics over the experimental time. This effect should be studied further. Since part of this effect might be due to 6H::GFP::CLASP2 α unbinding from the tris-Ni(II)-NTA in the barrier, stronger binding tags should be tried.

The microtubule barrier interactions reconstituted in this chapter can be used to study other cortical protein effects, as for example APC. In addition, these assays produce an 'end-on' interaction between the barrier-attached protein and the microtubule. Therefore, the same methodology may be used for other 'end-on' interactions as for instance kinetochore attachments.

7.5. METHODS

Protein purification: 6H::GFP::CLASP2 α and EB3 were a gift from Anna Akhmanova and its purifications will be published elsewhere.

Barrier fabrication and surface functionalization was done as explained in chapter 3 with 0.5 mM Pll-g-PEG/Tris-NTA (instead of 0.1 mM) for the wall incubation and 0.2 mg·ml⁻¹ of Pll-g-PEG/Biotin for the bottom surface incubation. Next, 1 mg·ml⁻¹ of streptavidin was incubated for 10 min followed by passivation with 1.2 mg·ml⁻¹ κ -casein.

Sample preparation. Following from the functionalization and passivation steps, the

stated concentrations of 6H::GFP::CLASP2 α were incubated for 20 min in a MRB80 solution containing 0.4 mg·ml⁻¹ κ -casein. Next, the flow cells was thoroughly flashed with buffer until no unbound protein was observed under spinning disk observation. A solution containing GMPCPP microtubule seeds in 0.1% methyl cellulose was incubated for 5 min. In cases where some CLASP remained in solution, the seeds bundled. This was used as an criteria to discard the sample. Then we incubated the tubulin mix containing 14.25 μ M tubulin, 0.75 μ M Rhodamine tubulin, 20 nM EB3, 1 mM GTP, 0.1% methyl cellulose, 0.4 mg·ml⁻¹ glucose oxidase, 50 mM glucose, 9.6 mg·ml⁻¹ κ -casein and 50 mM KCl. The sample of low cortical CLASP contained mCherry::EB3, while the sample of high cortical CLASP contained unlabelled EB3. Flow cells were sealed with valap (vaseline, lanolin, paraffin wax melted at equal concentrations) and maintained at 26°C during imaging via a temperature controlled box surrounding the microscope.

Data acquisition

All data shown in this chapter was obtained by spinning disk fluoresce microscopy using a IX81F-ZDC2 microscope (Olympus, Japan) with a spinning disk confocal head CSU-X1 (Yokogawa, Japan). 100X oil immersion objectives and EmCCD camera iXon3 (Andor, UK). Excitation lasers 488 and 561 nm (Andor, UK).

Z-stacks of 2-3 focal planes separated 300 nm were taken every 2-5 s for 10-25 min using a exposure of 300 ms and a EM Gain 115.

7.6. DATA ANALYSIS

Obtained z-stacks were background subtracted and 2D projected by maximum pixel intensity as in 4.6 and 4.6. Free binding curves were measured and fitted as in section 4.6. Microtubule catastrophe times and barrier contact times were manually from kymographs performed with **ImageJ**.

ACKNOWLEDGEMENTS

We thank Amol Aher and Anna Akhmanova for proposing this line of research, providing the CLASP and EB3 purified proteins and discussion. We thank Maurits Kok for alternative experiments with CLASP and EB3 and discussions.

—

—

BIBLIOGRAPHY

- [1] Akhmanova, A., Hoogenraad, C. C., Drabek, K., Stepanova, T., Dortland, B., Verkerk, T., Vermeulen, W., Burgering, B. M., de Zeeuw, C. I., Grosveld, F., and Galjart, N. (2001). CLASP Are CLIP-115 and -170 Associating Protein involved in the Regional Regulation of Microtubule Dynamic in Motile Fibroblasts. *Cell*, 104:923–235.
- [2] Akhmanova, A. and Steinmetz, M. O. (2008). Tracking the ends: a dynamic protein network control the fate of microtubule tips. *Nature Reviews Molecular Cell Biology*, 9:309–322.
- [3] Akhmanova, A. and Steinmetz, M. O. (2010). Microtubule +TIPs at a glance. *Journal of Cell Science*, 123:3415–3419.
- [4] Akiyoshi, B., Sarangapani, K. K., Powers, A. E, Nelson, C. R., Reichow, S. L., Arellano-Santoyo, H., Gonen, T., Ranish, J. A., Asbury, C. L., and Biggins, S. (2010). Tension directly stabilizes reconstituted kinetochore-microtubule attachments. *Nature*, 468:576–579.
- [5] Al-Bassam, J., Kim, H., Brouhard, G., van Oijen, Antoine Harrison, S. C., and Chang, F. (2010). Clasp promote microtubule rescue by recruiting tubulin dimers to the microtubule. *Developmental Cell*, 19(2):245–258.
- [6] Al-Bassam, J., van Breugel, M., Harrison, S. C., and Hyman, A. (2006). Stup2p binds tubulin and undergoes an open-to-closed conformational change. *Journal of Cell Biology*, 172(7):1009–1022.
- [7] Alushin, G. M., Lander, G. C., Kellog, E. H., Zhang, R., Baker, D., and Nogales, E. (2014). High-Resolution Microtubule Structures Reveal the Structural Transitions in α -Tubulin upon GTP Hydrolysis. *Cell*, 157:1117–1129.
- [8] Alvarado, J. (2013). *Biological Polymers. Confined Bent & Driven*. PhD thesis, Vrije Universiteit Amsterdam.
- [9] Alvarado, J., Mulder, B. M., and Koenderink, G. (2014). Alignment of nematic and bundled semiflexible polymers in cell-sized confinement. *Soft Matter*, 10(14):2354–2364.
- [10] Arai, T. and Kaziro, Y. (1976). Effect of guanine nucleotides on the assembly of brain microtubules. ability of 5'-guanylyl imidodiphosphate to replace gtp in promoting the polymerization of microtubules in vitro. *Biochemical and Biophysical Research Communications*, 69(2):369–376.
- [11] Asakura, S. and Oosawa, F. (1954). On Interaction between Two Bodies Immersed in a Solution of Macromolecules. *The Journal of Chemical Physics*, 22:1255–1256.

- [12] Asenjo, A. B., Chatterjee, C., Tan, D., DePaoli, V., Rice, W. J., Diaz-Avalos, R., Silvestry, M., and Sosa, H. (2013). Structural Model for Tubulin Recognition and Deformation by Kinesin-13 Microtubule Depolymerases. *Cell Reports*, 3:759–768.
- [13] Ayaz, P., Munyoki, S., Geyer, E. A., Piedra, F.-A., Vu, E. S., Bromberg, R., Otwinowski, Z., Grishin, N. V., A., B. C., and Rice, M. (2014). A tethered delivery mechanism explains the catalytic action of a microtubule polymerase. *eLife*, 3(e03069).
- [14] Ayaz, P., Ye, X., Huddleston, P., Brautigam, C. A., and Rice, L. M. (2012). A TOG: $\alpha\beta$ -tubulin Complex Structure Reveals Conformation-Based Mechanism for a Microtubule Polymerase. *Science*, 337:857–337.
- [15] Azioune, A., Storch, M., Bornens, M., They, M., and Piel, M. (2009). Simple and rapid process for single cell micro-patterning. *Lab on Chip*, 9:1640–1642.
- [16] Bahler, J. and Pringle, J. R. (1998). Pom1p, a fission yeast protein kinase that provides positional information for both polarized growth and cytokinesis. *Genes & Development*, 12:1356–1370.
- [17] Bain, C. D., Trogton, E. B., Tao, Y.-T., Evall, J., Whitesides, G. M., and Nuzzo, R. G. (1989). Formation of Monolayer Films by the Spontaneous Assembly of Organic Thiols from Solution onto Gold. *American Chemical Society*, 111(1):321–335.
- [18] Barnes, A. P. and Polleux, F. (2009). Establishment of Axon-Dendrite Polarity in Developing Neurons. *Annual Review in Neuroscience*, 32:347–381.
- [19] Bearce, E. A., Erdogan, B., and Lowery, L. A. (2015). TIPsy tour guides: how microtubule plus-end tracking proteins (+TIPs) facilitate axon guidance. *Frontiers in Cellular Neuroscience*, 9(241):1–12.
- [20] Bechstedt, S. and Brouhard, G. J. (2012). Doublecortin Recognizes the 13-Protofilament Microtubule Cooperative and Tracks Microtubule Ends. *Developmental Cell*, 23(1):181–192.
- [21] Bechstedt, S., Lu, K., and Brouhard, G. J. (2014). Doublecortin Recognizes the Longitudinal Curvature of the Microtubule End and Lattice. *Current Biology*, 24:2366–2375.
- [22] Behrens, R. and Nurse, P. (2002). Roles of fission yeast teal in the localization of polarity factors and in organizing the microtubular cytoskeleton. *Journal of Cell Biology*, 157(5):783–793.
- [23] Bendezú, F. O. and Martin, S. G. (2011). Actin cable and the exocyst form two independent morphogenesis pathways in the fission yeast. *Molecular Biology of the Cell*, 22:44–53.
- [24] Bershafsky, A. D., Vaisberg, E. A., and Vasilev, J. M. (1991). Pseudopodial activity at the active edge of migrating fibroblast is decreased after drug-induced microtubule depolymerization. *Cell Motility and the Cytoskeleton*, 19(3):152–8.

- [25] Beutel, O., Nikolaus, J., Birkholz, O., You, C., Schmidt, T., Hermann, A., and Piehler, J. (2014). High-fidelity protein targeting into membrane lipid microdomains in living cells. *Angew Chem Int Ed Engl*, 53(5):1311–5.
- [26] Bhagawati, M., You, C., and Piehler, J. (2013). Quantitative Real-Time Imaging of Protein-Protein Interactions by LSRP Detection with Micropatterned Gold Nanoparticles. *Analytical Chemistry*, 85:9564–9571.
- [27] Bhatia, P., Hachet, O., Micha, H., Rincon, S., Berchelot-Grosjean, M., Dalessi, S., Basterra, L., Bergmann, S., Paoletti, A., and Martin, S. G. (2014). Distinct levels in Pom1 gradient limit Cdr2 activity and localization to time and position division. *Cell Cycle*, 13(4):538–552.
- [28] Bi, E. and Park, H.-O. (2012). Cell Polarization and Cytokinesis in Budding Yeast. *Genetics*, 191(2):347–87.
- [29] Bicho, C. C., Kelly, D. A., Snaith, Hilary A. and Goryachev, A. B., and Sawin, K. E. (2010). A Catalytic Role for Mod5 in the Formation of the Tea1 Cell Polarity Landmark. *Current Biology*, 20:1752–1757.
- [30] Bieling, P., Kandels-Lewis, S., Telley, I. A., van Dijk, J., Janke, C., and Surrey, T. (2008a). CLIP-170 tracks growing microtubule ends by dynamic recognizing composite eb1/tubulin binding sites. *Journal Cell Biology*, 183(7):1223–1233.
- [31] Bieling, P., Laan, L., Schek, H., Munteanu, E. L., Sandblad, L., Dogterom, M., Brunner, D., and Surrey, T. (2007). Reconstitution of a microtubule plus-end tracking system in vitro. *Nature*, 450(7172):1100–1105.
- [32] Bieling, P., Telley, I. A., Hentrich, C., Piehler, J., and Surrey, T. (2010). Fluorescence Microscopy Assays on Chemically Functionalized Surfaces for Quantitative Imaging of Microtubule, Motor, and +TIP Dynamics. *Methods in Cell Biology*, 95:555–80.
- [33] Bieling, P., Telley, I. A., Piehler, J., and Surrey, T. (2008b). Processive kinesin require loose mechanical coupling for efficient collective motility. *EMBO Journal*, 9(11):1121–1127.
- [34] Bormuth, V., Nitsche, B., Ruhnnow, F. A., Stork, M., Rammner, Burkhard, H. J., and Diez, S. (2012). The Highly Processive Kinesin-8, Kip3, Switches Microtubule Protofilaments with a Bias towards the Left. *Biophysical Journal*, 103(1):L4–L6.
- [35] Boukellal, H., Selimovic, v. S., Jia, Y., Cristobal, a., and Fraden, S. (2008). Simple, robust storage of drops and fluids in microfluidic device. *Lab on Chip*, 9:331–338.
- [36] Bowen, J. R., Hwang, D., Bai, X., Roy, D., and Spiliotis, E. T. (2011). Septin GTPases spatially guide microtubule organization and plus end dynamics in polarizing epithelia. *Journal of Cell Biology*, 194(2):187–197.
- [37] Bratman, S. V. and Chang, F. (2007). Stabilization of overlapping microtubules by fission yeast CLASP. *Developmental Cell*, 13(6):812–827.

- [38] Braun, M., Lansky, Z., Fink, G., Ruhnnow, F., Diez, S., and Janson, M. E. (2011). Adaptive braking by Ase1 prevents overlapping microtubules from sliding completely apart. *Nature Cell Biology*, 13(10):1259–1264.
- [39] Bretschneider, T., Anderson, K., Echke, M., Muller-Taubenberger, A., Schroth-Diez, B., Ichikawa-Ankerhold, H. C., and Gerish, G. (2009). The Three-Dimensional Dynamic of Actin Waves, a Model of Cytoskeletal Self-Organization. *Biophysical Journal*, 96(7):2888–2900.
- [40] Bretschneider, T., Diez, S., Anderson, K., Heuser, J., Clarke, M., Muller-Taubenberger, A., Jana, K., and Gerisch, G. (2004). Dynamic Actin Patterns and Arp2/3 Assembly at the Substrate-Attached Surface of Motile Cells. *Current Biology*, 14(1):1–10.
- [41] Briggs, M. W. and Sacks, D. B. (2003). IQGAP proteins are integral components of cytoskeletal regulation. *EMBO Journal*, 4(6):571–574.
- [42] Briscoe, J., Lawrence, P., and Vincent, J. (2010). *Generation and Interpretation of Morphogen Gradients*. Cold Spring Harbour.
- [43] Brouhard, G. J. (2015). Dynamic instability 30 years later: complex in microtubule growth and catastrophe. *Molecular Biology of the Cell*, 26:1207–1210.
- [44] Brouhard, G. J. and Rice, L. M. (2014). The contribution of $\alpha\beta$ -tubulin curvature to microtubule dynamics. *Journal Cell Biology*, 207(3):323–334.
- [45] Brouhard, G. J., Stear, J. H., Noetzel, T. L., Al-Bassam, J., Kinoshita, K., Harrison, S. C., Howard, J., and Hyman, A. A. (2008). XMAP215 Is a Processive Microtubule Polymerase. *Cell*, 132:79–88.
- [46] Browning, H. and Hackney, D. D. (2005). The EB1 Homolog Mal3 Stimulates the ATPase of the Kinesin Tea2 by Recruiting it to the Microtubule. *Journal of Biological Chemistry*, 280(13):12299–12304.
- [47] Browning, H., Hackney, D. D., and Nurse, P. (2003). Targeted movement of cell end factors in fission yeast. *Nature Cell Biology*, 5(9):812–818.
- [48] Browning, H., Hayles, J., Mata, J., Aveline, L., and Nurse, P. (2000). Tea2p Is a Kinesin-like Protein Required to Generate Polarized Growth in Fission Yeast. *Journal Cell Biology*, 151(1):15–28.
- [49] Brunner, D. and Nurse, P. (2000). CLIP170-like tip1p Spatially Organizes Microtubular Dynamics in Fission Yeast. *Cell*, 102:695–704.
- [50] Bruns, K. M., Wagenbach, M., Wordeman, L., and Schriemer, D. C. (2014). Nucleotide exchange in dimeric MCAK induces longitudinal and lateral stress at microtubule ends to support depolymerization. *Structure*, 22(8):1173–1183.
- [51] Bryant, D. M. and Mostov, K. E. (2008). From cells to organs: building polarized tissue. *Nature Reviews*, 9:887–901.

- [52] Buhiel, M., Bohl, E., and Schaffer, E. (2015). The Kinesin-8 Kip3 Switches Protofilaments in a Sideward Random Walk Asymmetric Biased by Force. *Biophysical Journal*, 108(8):2019–2027.
- [53] Burack, M. A., Silverman, M. A., and Banker, G. (2000). The Role of Selective Transport in Neuronal Protein Sorting. *Neuron*, 26(2):465–472.
- [54] Busch, K. E. and Brunner, D. (2004). The Microtubule Plus End-Tracking Proteins mal3p and tip1p Cooperate for Cell-End Targeting of Interphase Microtubules. *Current Biology*, 14:548–559.
- [55] Busch, K. E., Gayles, J., Nurse, P., and Brunner, D. (2004). Tea2p Kinesin Is Involved in Spatial Microtubule Organization by Transporting Tip1p on Microtubules. *Developmental Cell*, 6:831–843.
- [56] Bush, D., Horisberger, M., Horman, I., and Wursch, P. (1974). The wall structure of *Schizosaccharomyces pombe*. *J Gen Microbiol.*, 81(1):199–206. Yeast cell wall.
- [57] Cao, D., Su, Z., Wang, W., Wu, H., Akram, S., Qin, B., Zhou, J., Zhuang, X., Adams, G., Jin, C., Wang, X., Liu, L., Hill, D., Wang, D., Ding, X., and Yao, X. (2015). Signaling Scaffold Protein IQGAP1 Interacts with Microtubule Plus-end Tracking Protein SKAP and Links Dynamic Microtubule Plus-end to Steer Cell Migration. *Journal Biological Chemistry*, 290(39):23766–80.
- [58] Caplow, M., Ruhlen, R. L., and Shanks, J. (1994). The free energy for hydrolysis of a microtubule-bound nucleotide triphosphate is near zero: All of the free energy for hydrolysis is stored in the microtubule lattice. *Journal of Cell Biology*, 127(3):779–788.
- [59] Carazo-Salas, R. E., Antony, C., and Nurse, P. (2005). The Kinesin Klp2 Mediates Polarization of Interphase Microtubule in Fission Yeast. *Science*, 309:297–300.
- [60] Carazo-Salas, R. E. and Nurse, P. (2006). Self-organization of interphase microtubule arrays in fission yeast. *Nature Cell Biology*, 8(10):1102–1107.
- [61] Carrier, M.-F., Didry, D., and Pantaloni, D. (1987). Microtubule Elongation and Guanosine 5'-Triphosphate Hydrolysis. Role of Guanine Nucleotides in Microtubule Dynamics. *Biochemistry*, 26:4428–4437.
- [62] Carrier, M.-F., Didry, D., Simon, C., and Pantaloni, D. (1989). Mechanism of GTP Hydrolysis in Tubulin Polymerization: Characterization of the Kinetic Intermediate Microtubule-GDP-Pi Using Phosphate Analogues. *American Chemical Society*, 28(4):1783–1791.
- [63] Celton-Morizur, S., Racine, V., Sibarita, J.-B., and Paoletti, A. (2006). Pom1 kinase links division plane position to cell polarity by regulating Mid1p cortical distribution. *Journal Cell Science*, 119:4710–4718.
- [64] Chang, F. and Martin, S. G. (2009). Shaping Fission Yeast with Microtubules. *Cold Spring Harbor Perspectives in Biology*, 1(1):a001347.

- [65] Chau, A. H., Walter, J. M., Gerardin, J., Tang, C., and Lim, W. A. (2012). Designing Synthetic Regularity Networks Capable of Self-Organizing Cell Polarization. *Cell*, 151:320–332.
- [66] Cheeseman, I. M., Chappie, J. S., Wilson-Kubalek, E. M., and Desai, A. (2006). The Conserved KMN Network Constitutes the Core Microtubule-Binding Site of the Kinetochore. *Cell*, 127:983–997.
- [67] Chen, Y., Rolls, M. M., and Hancock, W. O. (2014). An EB1-Kinesin Complex Is Sufficient to Steer Microtubule Growth In Vitro. *Current Biology*, 24:1–6.
- [68] Chretien, D., Kenney, J. M., Fuller, S. D., and Wade, R. H. (1996). Determination of microtubule polarity by cryo-electron microscopy. *Structure*, 4(9):1031–1040.
- [69] Cingolani, L. A. and Goda, Y. (2008). Actin in action: the interplay between the actin cytoskeleton and synaptic efficacy. *Nature Reviews Neuroscience*, 9:344–356.
- [70] Constantinou, P. E. and Doehhl, M. R. (2010). The mechanochemistry of integrated motor protein complexes. *Journal of Biomechanics*, 43:31–37.
- [71] Corless, R. M., Gonnet, G. H., Hare, D. E. G., Jeffrey, D. J., and Knuth, D. E. (1996). On the Lambert W Function. *Advances in Computational Mathematics*, 5:329–359.
- [72] Cosentino Lagomarsino, M., Tanase, C., Vos, J. W., Emons, A. M. C., Mulder, B. M., and Dogterom, M. (2007). Microtubule Organization in Three-Dimensional Confined Geometries: Evaluating the Role of Elasticity Through a Combined in Vitro and Modeling Approach. *Biophysical Journal*, 92:1046–1057.
- [73] Crick, F. (1970). Diffusion in Embryogenesis. *Nature*, 225:420–422.
- [74] Cullen, C. E., Deak, P., Glover, D. M., and Ohkura, H. (1999). mini spindles: A Gene Encoding a Conserved Microtubule-associated Protein Required for the Integrity of the Mitotic Spindle in *Drosophila*. *Journal of Cell Biology*, 146:1005–1018.
- [75] Daga, R. R., Lee, K.-G., Bratman, S., Salas-Pino, S., and Chang, F. (2006a). Self-organization of microtubule bundles in anucleate fission yeast cells. *Nature cell biology*, 8(10):1108–1113.
- [76] Daga, R. R., Yonetani, A., and Chang, F. (2006b). Asymmetric Microtubule Pushing Force in Nuclear Centering. *Current Biology*, 16:1544–1550.
- [77] David-Pfeuty, T., Erickson, H. P., and Pantaloni, D. (1977). Guanosinetriphosphatase activity of tubulin associated with microtubule assembly. *PNAS*, 74(12):5372–5376.
- [78] de Gennes, P. G. and Prost, J. (1995). *The Physics of Liquid Crystals*. Oxford University Press.
- [79] DeLuca, J. G., Dong, Y., Herget, P., Strauss, J., Hickey, J. M., Salmon, E. D., and McEwen, B. F. (2005). Hec1 and Nuf2 Are Core Components of the Kinetochore Outer Plate Essential for Organizing Microtubule Attachment Sites. *Molecular Biology of the Cell*, 16(2):519–531.

- [80] Deng, L., Baldissard, S., Kettenbach, A. N., Gerber, S. A., and Mosseley, J. B. (2014). Dueling kkinase regulate cell size at disviision through the SAD kinase Cdr2. *Current Biology*, 24(4):428–433.
- [81] Derr, N. D., Goodman, B. S., Jungmann, R., Leschziner, A. E., Shih, W. M., and Reck-Peterson, S. L. (2012). Tug of War in Motor Protein Ensembles Revealed with a Programmable DNA Origami Scaffold. *Science*, 338(6107).
- [82] des Portes, V., Francis, F., Pinard, J.-M., Desguerre, I., Moutard, M.-L., Snoek, I., Meiners, L. C., Capron, F., Cusmai, R., Ricci, S., Motte, J., Echenne, B., Ponsot, G., Dulac, O., Chelly, J., and Beldjord, C. (1998). doubledouble is the major gene causing X-linked subcortical laminar heterotopia (SCLH). *Human Molecular Genetics*, 7(7):1063–1070.
- [83] Desai, A., Verma, S., Mitchison, T. J., and Walczak, C. E. (1999). Kin I Kinesins Are Microtubule-Destabilizing Enzymes. *Cell*, 96:69–78.
- [84] Devreotes, P. N. and Zigmond, S. H. (1988). CHEMOTAXIS IN EUKARYOTIC CELLS: A focus on leukocytes and dictyostelium. *Annural Review of Cell Biology*, 4:649–686.
- [85] Dixit, R., Levy, J. R., Tokito, M., Ligon, L. A., and Holzbaur, E. L. F. (2008). Regulation of Dynactin through the Differential Expression of p150^{glued} Isoforms. *Journal Biological Chemistry*, 283(48):33611–33619.
- [86] Dodgson, J., Chessel, A., Yamamoto, M., Vaggi, F., Cox, S., Rosten, E., Albrecht, D., Geymonat, M., Csikasz-Nagy, A., Sato, M., and Carazo-Salas, R. (2013). Spatial segregation of polarity factors into distinct cortical clusters is required for cell polarity control. *Nature Communications*, 4:1834.
- [87] Doe, C. Q. (2001). Cell polarity: the PARty expands. *Nature Cell Biology*, 3:E7–E9.
- [88] Dogterom, M., Kerssemakers, J. W. J., Romet-Lemone, G., and Janson, M. E. (2005). Force generation by dynamic microtubules. *Current Opinion in Cell Biology*, 17:67–74.
- [89] Dogterom, M. and Yurke, B. (1997). Measurement of the Force-Velocity Relation for Growing Microtubules. *Science*, 278(856).
- [90] Doodhi, H., Katrukha, E. A., Kapitein, L., and Akhmanova, A. (2014). Mechanical and Geometrical Constraints Control Kinesin-Based Microtubule Guidance. *Current Biology*, 24:1–7.
- [91] Dotti, C. G., Sullivan, C. A., and Banker, G. A. (1988). The Establishment of Polarity by Hyppocampal Neurons in Culture. *The Journal of Neuroscience*, 8(4):1454–1468.
- [92] Dragestein, K. A., van Cappellen, W. A., van Haren, J., Tsiibidis, G. D., Akhmanova, A., Knoch, T. A., Grosveld, E., and Galjart, N. (2008). Dynamic behavior of GFP-CLIP-170 reveals fast protein turnover on microtubule plus ends. *Journal of Cell Biology*, 180(4):729–737.

- [93] Drummond, D. R. and Cross, R. A. (2000). Dynamic of interphase microtubules in *Schizosaccharomyces pombe*. *Current Biology*, 10(13):766–75.
- [94] Duellberg, C., Cade, I. N., Holmes, D., and Surrey, T. (2016). The size of the EB cap determines instantaneous microtubule stability. *eLife*, 5(e13470):1–23.
- [95] Eijkel, J. C. T. and van den Berg, A. (2006). Young 4ever - the use of capillarity for passive flow handling in lab on a chip devices. *Lab on a Chip*, 6:1405–1408.
- [96] Erickson, H. P. and O'Brien, E. T. (1992). Microtubule dynamic instability and GTP hydrolysis. *Annu. Rev. Biophys. Biomol. Struct.*, 21:145–66.
- [97] Estravís, M., Rincón, S. A., Santos, B., and Pilar, P. (2011). Cdc42 Regulates Multiple Membrane Traffic Events in Fission Yeast. *Traffic*, 12:1744–1758.
- [98] Etienne-Manneville, S., Manneville, J.-B., Nicholls, S., Ferenczi, M., and Hall, A. (2005). Cdc42 and Par6-PKCxi regulate the spatially localized association of Dlg1 and APC to control cell polarization. *Journal Cell Biology*, 170(6):895–901.
- [99] Evans, N. R. and Sugden, K. E. P. (2007). An exclusion process for model fungal hyphal growth. *Physica A*, 384:53–58.
- [100] Ezratty, E. J., Partridge, M. A., and Gundersen, G. G. (2005). Microtubule-induced focal adhesion disassembly is mediated by dynamin and focal adhesion kinase. *Nature Cell Biology*, 7:581–590.
- [101] Fantes, P. A. (1977). Control of cell size and cycle time in *Schizosaccharomyces Pombe*. *Journal of Cell Science*, 24:51–67.
- [102] Feierbach, B. and Chang, F. (2001). Roles of the fission yeast formin for3p in cell polarity, actin cable formation and symmetric cell division. *Current Biology*, 11(21):1656–1665.
- [103] Feierbach, B., Verde, F., and Chang, F. (2004). Regulation of a formin complex by the microtubule plus end protein tea1p. *Journal of Cell Biology*, 165(5):697–707.
- [104] Flemming, W. (1882). *Zellsubstanz, Kern und Zelltheilung*. Verlag von E.C.W.Vogel, Leipzig.
- [105] Foethke, D., Makushok, T., Brunner, D., and Nedelec, F. J. (2009). Force- and length-dependent catastrophe activities explain interphase microtubule organization in fission yeast. *Molecular Systems Biology*, 5(241):1–6.
- [106] Fonck, E., Feigl, G. G., Fasel, J., Sage, D., Unser, M., Rufenacht, D. A., and Stergiopoulos, N. (2009). Effect of Aging on Elastin Functionality in Human Cerebral Arteries. *Stroke*, 40:2552–2556.
- [107] Footer, M. J., Kerssemakers, J. W. J., Theriot, J. A., and Dogterom, M. (2007). Direct measurement of force generation by actin filament polymerization using an optical trap. *PNAS*, 104:2181–2186.

- [108] Fowler, R. H. (1929). *Statistical Mechanics, the theory of the properties of matter in equilibrium*. Cambridge [Eng.] University Press.
- [109] Frasconi, M., Mazzei, F., and Ferri, T. (2010). Protein immobilization at gold-thiol surfaces and potential for biosensing. *Anal Bioanal Chem.*, 398:1545–1564.
- [110] Freedman, D. and Diaconis, P. (1981). On the Histogram as a Density Estimator: L2 Theory. *Z. Wahrscheinlichkeitstheorie*, 57:453–486.
- [111] Fujita, A., Vardy, L., Garcia, M. A., and Toda, T. (2002). A Fourth Component of the Fission Yeast gamma-Tubulin Complex, Alp16, Is Required for Cytoplasmic Microtubule Integrity and Becomes Indispensable when gamma-Tbulin Function Is Compromised. *Molecular Biology of the Cell*, 13(7):2360–2373.
- [112] Fukata, M., Watanabe, T., Noritake, J., Nakagawa, M., Yamaga, M., Kuroda, S., Matsuura, Y., Iwamatsu, A., Perez, F., and Kaibuchi, K. (2002a). Rac1 and Cdc42 Capture Microtubule through IQGAP1 and CLIP-170. *Cell*, 109:873–885.
- [113] Fukata, Y., Itoh, T. J., Kimura, T., Menager, C., Nishimura, T., Shiromizu, T., Watanabe, H., Inagaki, N., Iwamatsu, A., Hotani, H., and Kaibuchi, K. (2002b). CRMP-2 binds to tubulin heterodimers to promote microtubule assembly. *Nature Cell Biology*, 4:583–591.
- [114] Fygenson, D. K., Marko, J. E., and Libchaber, A. (1997). Mechanics of Microtubule-Based Membrane Extension. *Physical Review Letters*, 79(22):4497–4500.
- [115] Galjart, N. (2010). Plus-End-Tracking Protein and Their Interaction at Microtubule Ends. *Current Biology*, 20:R528–R537.
- [116] Ganem, N. J., Upton, K., and Compton, D. A. (2005). Efficient Mitosis in Human Cells Lacking Poleward Microtubule Flux. *Current Biology*, 15:1827–1832.
- [117] Gard, D. L. and Kirschner, M. (1987). A Microtubule-associated Protein from Xenopus Eggs That Specifically Promotes Assembly at the Plus-End. *Journal Cell Biology*, 105:2203–2215.
- [118] Gardner, M. K., Zanic, M., Gell, C., Bormuth, V., and Howard, J. (2011). Depolymerizing Kinesins Kip3 and MCAK Shape Cell Microtubule Architecture by Differential Control of Catastrophe. *Cell*, 147:1092–1103.
- [119] Gârlea, I. C. and Mulder, B. M. (2015). Defect structures mediate the isotropic-nematic transition in strongly confined liquid crystals. *Soft Matter*, 11(3):608–614.
- [120] Gerish, G., Bretschneider, T., Muller-Taubenberger, A., Simeth, E., Ecke, M., Diez, S., and Anderson, K. (2004). Mobile Actin Clusters and Traveling Waves in Cells Recovering from Actin Depolymerization. *Biophysical Journal*, 87(5):3493–3503.
- [121] Gigant, B., Curmi, P. A., Martin-Barbey, C., Charbeaut, E., Lachkar, S., Luc, L., Siavoshian, S., Sobel, A., and Knossow, M. (2000). The 4 Å X-Ray Structure of a Tubulin:Stathmin-like Domain Complex. *Cell*, 102(6):809–816.

- [122] Gleeson, J. G., Allen, K. M., Fox, J. W., Lamperti, E. D., Berkovic, S., Scheffer, I., Copper, E. C., Dobyns, W. B., Minnerath, S. R., Ross, M. E., and Walsh, C. A. (1998). doubledouble, a Brain-Specific Gene Mutated in Human X-Linked Lissencephaly and Double Cortex Syndrome, Encodes a Putative Signaling Protein. *Cell*, 92(1):63–72.
- [123] Glynn, J. M., Lustig, R. J., Belin, A., and Chang, F. (2001). Role of bud6p and teap in the interaction between actin and microtubules for the establishment of cell polarity in fission yeast. *Current Biology*, 11(11):836–845.
- [124] Goldman, R. D., Grin, B., Mendez, M. G., and Kuczmarski, E. R. (2008). Intermediate Filaments: Versatile Building Blocks of Cell Structure. *Current Opinion Cell Biology*, 20(1):28–34.
- [125] Goshima, G., Wollman, R., Stuurman, N., Scholey, J. M., and Vale, R. D. (2005). Length Control of the Metaphase Spindle. *Current Biology*, 15:1979–1988.
- [126] Grimaldi, A. D., Maki, T., Fitton, B. P., Roth, D., Yampolsky, D., Davidson, M. W., Svitkina, T., Straube, A., Hayashi, I., and Kaverina, I. (2014). Clasp are required for proper microtubule localization of End-binding proteins. *Developmental Cell*, 30(3):343–352.
- [127] Grishchuk, E. L., Molodtsov, M., Ataullakhanov, F. I., and McIntosh, J. R. (2005). Force production by disassembling microtubules. *Nature*, 438:384–388.
- [128] Gundersen, G. G., Gomes, E. R., and Wen, Y. (2004). Cortical control of microtubule stability and polarization. *Current Opinion Cell Biology*, 16:106–112.
- [129] Gupta, K. K., Li, C., Duan, A., Alberico, Emily O. ad Kim, O. V., Alber, M. S., and Goodson, H. V. (2013). Mechanism for the catastrophe-promoting activity of the microtubule destabilizer op18/stathmin. *PNAS*, 110(51):20449–20454.
- [130] Gupta, M. L., Carvalho, P., Roof, D. M., and Pellman, D. (2006). Plus end-specific depolymerase activity of kip3, a kinesin-8 protein, explains its role in positioning the yeast mitotic spindle. *Nature Cell Biology*, 8(9):913–923.
- [131] Hachet, O., Berthelo-Grosjean, M., Kokkoris, K., Vincenzetti, V., Moosbrugger, J., and Martin, S. G. (2011). A Phosphorylation Cycle Shapes Gradients of the DYRK Family Kinase Pom1 at the Plasma Membrane. *Cell*, 145(7):1116–28.
- [132] Hagan, I. M. and Hyams, Jeremy, S. (1988). The use of cell division cycle mutants to investigate the control of microtubule distribution in the fission yeast *Schizosaccharomyces pombe*. *Journal of Cell Science*, 89:343–357.
- [133] Hatanaka, Y., Yamauchi, K., and Murakami, F. (2012). Formation of axon-dendrite polarity in situ: Initiation of axons from polarized and non-polarized cells. *Development, Growth & Differentiation*, 54(3):398–407.
- [134] Hayashi, I. and Ikura, M. (2003). Crystal Structure of the Amino-terminal Microtubule-binding Domain of End-Binding Protein 1 (eb1). *Journal of Biological Chemistry*, 278(38):36430–36434.

- [135] Hess, S. and Kohler, W. (1980). *Formeln zur tensor-rechnung*. Erlangen: Palm & Enke.
- [136] Hirokawa, N. (1998). Kinesin and Dynein Superfamily Proteins and the Mechanism of Organelle Transport. *Science*, 279:519–526.
- [137] Hochuli, E., Dobeli, H., and Schacher, A. (1987). Nea metal chelate adsorbent selective for pprotein and peptides containing neighbouring histidine residues. *Journal of Chromatography*, 411:177–184.
- [138] Hoepflich, G. J., Thompson, A. R., McVicker, D. P., Hancock, W. O., and Berger, C. L. (2014). Kinesin's Neck-Linker Determines its Ability to Navigate Obstacles on the Microtubule Surface. *Biophysical Journal*, 106(8):1691–1700.
- [139] Holy, T. E., Dogterom, M., Yurke, B., and Leibler, S. (1997). Assembly and positioning of microtubule asters in microfabricated chambers. *Proc. Natl. Acad. Sci. USA*, 94:6228–6231.
- [140] Honnappa, S., John, C. M., Kostrewa, D., Winkler, F. K., and Steinmetz, M. O. (2005). Structural insights into the EB1-APC interaction. *EMBO Journal*, 24:261–269.
- [141] Honnappa, S., Montenegro Gouveia, S., Weisbrich, A., Damberger, F. F., Bhavesh, N. S., Jawhari, H., Grigoriev, I., van Rijssel, F. J. A., Buey, R. M., Lawera, A., Jelesarov, I., Winkler, F. K., Wuthrich, K., Akhmanova, A., and Steinmetz, M. O. (2009). An EB1-Binding Motif Acts as a Microtubule Tip Localization Signal. *Cell*, 138(2):366–376.
- [142] Horiguchi, K., Hanada, T., Fukui, Y., and Chishti, A. H. (2006). Transport of PIP3 by GAKIN, a kinesin-3 family protein, regulates neuronal cell polarity. *Journal Cell Biology*, 174(3):425–436.
- [143] Hotta, A., Kawakatsu, T., Nakatani, T., Sato, T., Matsui, C., Sukezane, T., Akagi, T., Hamaji, T., Grigoriev, I., Akhmanova, A., Takai, Y., and Mimori-Kiyosue, Y. (2010). Laminin-based cell adhesion anchors microtubule plus ends to the epithelial cell cortex through ll5/. *Journal Cell Biology*, 189(5):901–17.
- [144] Howard, J. (2001). *Mechanics of motor proteins and the cytoskeleton*. Sinauer Associates, Sunderland.
- [145] Hu, Z., Gogol, E. P., and Lutkenhaus, J. (2002). Dynamic assembly of MinD on phospholipid vesicles regulated by ATP and MinE. *PNAS*, 99(10):6761–6766.
- [146] Hu, Z. and Lutkenhaus, J. (1999). Topological regulation of cell division in *Escherichia coli* involves rapid pole to pole oscillation of the division inhibitor Minc under the control of Mind and Mine. *Molecular Microbiology*, 34(1):82–90.
- [147] Hu, Z. and Lutkenhaus, J. (2001). Topological Regulation of Cell Division in *E. coli*: Spatiotemporal Oscillation of MinD Requires Stimulation of Its ATPase by MinE and Phospholipid. *Molecular Cell*, 7(6):1337–1343.

- [148] Hu, Z., Saez, C., and Lutkenhaus, J. (2003). Recruitment of MinC, and Inhibitor of Z-Ring Formation, to the Membrane in *Escherichia coli*: Role of MinD and MinE. *Journal of Bacteriology*, 185(1):196–203.
- [149] Huang, N.-P., Voros, Janos and De paul, S. M., Textor, M., and Spencer, N. D. (2002). Biotin-Derivatized Poly(L-lysine)-g-poly(ethylene glycol): A Novel Polymeric Interface for Bioaffinity Sensing. *Langmuir*, 18:220–230.
- [150] Hunter, A. W., Caplow, M., Coy, D. L., Hancock, W. O., Diez, S., Wordeman, L., and Howard, J. (2003). The Kinesin-Related Protein MCAK Is a Microtubule Depolymerase that Forms an ATP-Hydrolyzing Complex at Microtubule Ends. *Molecular Cell*, 11(2):445–457.
- [151] Hyman, A. A., Chren, D., Arnal, I., and Wade, R. (1995). Structural Changes Accompanying gtp Hydrolysis in Microtubules: Information from a Slowly Hydrolyzable Analogue Guanylyl-(α, β)-Methylene-Diphosphonate. *Journal of Cell Biology*, 128(1):117–125. GMPCPP.
- [152] Hyman, A. A., Salser, S., Dreschsel, D., Unwin, N., and Mitchison, T. (1992). Role of gtp Hydrolysis in Microtubule Dynamics: Information from a Slowly Hydrolyzable Analogue, gmpcpp. *Molecular Biology of the Cell*, 3(10):1155–1167. GMPCPP.
- [153] Iglesias, P. A. and Devreotes, P. N. (2008). Navigating through mmodel of chemotaxis. *Current Opinion in Cell Biology*, 20:35–40.
- [154] Iglesias, P. A. and Devreotes, P. N. (2012). Biased axcitable networks: How cells direct motien in response to gradients. *Current Opinion Cell Biology*, 24(2):245–253.
- [155] Inagaki, N., Toriyama, M., and Sakamura, Y. (2011). Systems Biology of Symmetry Breaking During Neuronal Polarity Formation. *Dev. Neurobiol.*, 71(6):584–93.
- [156] Inoue, S. and Salmon, E. (1995). Force Generation by Microtubule Assembly/Disassembly in Mitosis and Related Movements. *Molecular Biology of the Cell*, 6:1619–1640.
- [157] Inouè, Shinya, S. (1953). Polarization optical studies of the mitotic spindle. I. the demonstration of spindle fibers in living cells. *Chromosoma*, 5:487–500.
- [158] Irazoqui, J. E., Howell, A. S., Theesfeld, C. L., and Lew, D. J. (2005). Opposing Roles for Actin in Cdc42 Polarization. *Molecular Biology of the Cell*, 16(3):1296–1304.
- [159] Ishitsuka, Y., Savage, N., Li, Y., Bergs, A., Grun, N., Kohler, D., Donnelly, R., Nienhaus, G. U., Fischer, R., and Takeshita, N. (2015). Superresolution microscopy reveals a dynamic picture of cell polarity maintenance during directional growth. *Science Advances*, 1:e1500947.
- [160] Jacobs, M., Smith, H., and Taylor, E. W. (1974). Tubulin: Nucleotide bbindi and enzymic activity. *Journal of Molecular Biology*, 89(3):455–468.

- [161] Jacobson, C., Schnapp, B., and Banker, G. A. (2006). A Change in the Selective Translocation of the Kinesin-1 Motor Domain Marks the Initial Specification of the Axon. *Neuron*, 49(6):797–804.
- [162] Janson, M. E., de Dood, M. E., and Dogterom, M. (2003). Dynamic instability of microtubules is regulated by force. *Journal of Cell Biology*, 161(6):1029–1034.
- [163] Janson, M. E. and Dogterom, M. (2004). Scaling of Microtubule Force-Velocity Curves Obtained at Different Tubulin Concentrations. *Physical Review Letters*, 92(24):248101.
- [164] Janson, M. E., Loughlin, R., Loiodice, I., Fu, C., Brunner, D., Nedelec, F. J., and Tran, P. T. (2007). Crosslinkers and Motors Organize Dynamic Microtubule to Form Stable Bipolar Arrays in Fission Yeast. *Cell*, 128:357–368.
- [165] Janson, M. E., Setty, T. G., Paoletti, A., and Tran, P. T. (2005). Efficient formation of bipolar microtubule bundles requires microtubule-bound gamma-tubulin complexes. *Journal Cell Biology*, 169(2):297–308.
- [166] Jiang, K., Hua, S., Mohan, R., Grigoriev, I., Yau, K. W., Liu, Q., Katrukha, E. A., Altelaar, A. F. M., Heck, A. J. R., Hoogenraad, C. C., and Akhmanova, A. (2014). Microtubule Minus-End Stabilization by Polymerization-Driven CAMSAP Deposition. *Developmental Cell*, 28:295–309.
- [167] Kalisch, S.-M. J. (2013). *Insights into microtubule catastrophes. The effects of end-binding pprotein and force*. PhD thesis, Universiteit Leiden.
- [168] Kapitein, L. and Hoogenraad, C. C. (2011). Which way to go? Cytoskeletal organization and polarized transport in neurons. *Molecular and Cellular Neuroscience*, 46:9–20.
- [169] Katsuki, M., Drummond, D. R., Osei, M., and Cross, R. A. (2009). Mal3 Masks Catastrophe Events in *Schizosaccharomyces pombe* Microtubules by Inhibiting Shrinkage and Promoting Rescue. *The Journal of Biological Chemistry*, 284(43):29246–29250.
- [170] Kaverina, I., Krylyshkina, O., and Small, J. V. (1999). Microtubule Targeting of Substrate Contacts Promotes Their Relaxation and Dissociation. *Journal Cell Biology*, 146(5):1033–1044.
- [171] Kelkar, M. and Martin, S. G. (2015). PKA antagonizes CLASP-dependent microtubule stabilization to re-localize Pom1 and buffer cell size upon glucose limitation. *Nature Communications*, 6(8445).
- [172] Kempthues, K. (2000). PARsing Embryonic Polarity. *Cell*, 101(4):345–348.
- [173] Kenausis, G. L., Voros, J., Elbert, D. L., Huang, N., Hofer, R., Ruiz-Taylor, L., Textor, M., Hubbell, J. A., and Spencer, N. D. (2000). Poly(L-lysine)-g-Poly(ethylene glycol) Layers on Metal Oxide Surfaces: Attachment Mechanism and Effects of Polymer Architecture on Resistance to Protein Adsorption. *Journal of Physical Chemistry*, 104:3298–3309.

- [174] Kettenbach, A., Deng, L., Wu, Y., Baldissard, S., Adamo, M., Gerber, S., and Moseley, J. (2015). Quantitative phosphoproteomics reveals pathways for coordination of cell growth and division by the conserved fission yeast kinase pom1. *Mol Cell Proteomics*, 14(5):1275–87.
- [175] Kimura, T., Arimura, N., Fukata, Y., Watanabe, H., Iwamatsu, A., and Kaibuchi, K. (2005). Tubulin and CRMP-2 complex is transported via Kinesin-1. *Journal of Neurochemistry*, 93:1371–1382.
- [176] Kirschner, M., Williams, R. C., Weingarten, M., and Gerhart, J. C. (1974). Microtubule from Mammalian Brain: Some Properties of Their Depolymerization Products and a Proposed Mechanism of Assembly and Disassembly. *PNAS*, 71(4):1159–1163.
- [177] Kitov, P. I. and Bundle, D. R. (2003). On the Nature of the Multivalency Effect: A Thermodynamic Model. *JACS*, 125:1627–16284.
- [178] Klumpp, S. and Lipowsky, R. (2005). Cooperative cargo transport by several molecular motors. *PNAS*, 102(48):17284–17289.
- [179] Kokkoris, K., Gallo Castro, D., and Martin, S. G. (2014). The Tea4-PP1 landmark promotes local growth by dual Cdc42 GEF recruitment and GAP exclusion. *Journal of Cell Science*, 127:2005–2016.
- [180] Kolomeisky, A. B., Schutz, G. M., Kolomeisky, E. B., and Straley, J. P. (1998). Phase diagram of one-dimensional driven lattice gases with open boundaries. *J. Phys. A: Math*, 31:6911–6919.
- [181] Kopecka, M., Fleet, G. H., and Phaff, H. J. (1995). Ultrastructure of the Cell Wall of *Schizosaccharomyces pombe* Following Treatment with Various Glucanases. *Journal of Structural Biology*, 114:140–152. Pombe cell wall.
- [182] Krishnamurthy, V. M. and Estrofi, Lara A. and Whitesides, G. M. (2006). *Multivalency in Ligand Design Introduction and Overview*. WILEY-VCH Verlag GmbH & Co.
- [183] Kumar, P. and Wittmann, T. (2012). +Tips: SxIPping along microtubule ends. *Trends in Cell Biology*, 22(8):418–428.
- [184] Kutejova, E., Briscoe, J., and Kicheva, A. (2009). Temporal dynamics of patterning by morphogen gradients. *Current Opinion in Genetics & Development*, 19(4):315–322.
- [185] Laan, L. (2009). *Force generation at microtubule ends: An in vitro approach to cortical interactions*. PhD thesis, Universiteit Leiden.
- [186] Laan, L. and Dogterom, M. (2010). In Vitro Assays to Study Force Generation at Dynamic Microtubule Ends. *Methods in Cell Biology*, 95:617–639.
- [187] Laan, L., Husson, J., Munteanu, E. L., Kerssemakers, J. W. J., and Dogterom, M. (2008). Force-generation and dynamic instability of microtubule bundles. *PNAS*, 105(26):8920–8925.

- [188] Laan, L., Pavin, N., Husson, J., Romet-Lemone, G., van Duijn, M., Preciado Lopez, M., Vale, R. D., Julicher, F., Reck-Peterson, S. L., and Dogterom, M. (2012a). Cortical Dynein Controls Microtubule Dynamic to Generate Pulling Force that Position Microtubule Asters. *Cell*, 148:502–514.
- [189] Laan, L., Roth, S., and Dogterom, M. (2012b). End-on microtubule-dynein interactions and pulling-based positioning of microtubule organizing centers. *Cell Cycle*, 11(20):3750–3757.
- [190] Lackner, L. L., Raskin, D. M., and de Boer, P. A. J. (2003). ATP-Dependent Interaction between Escherichia coli Min Proteins and the Phospholipid Membrane in Vitro. *Journal of Bacteriology*, 185(3):735–749.
- [191] Laloux, G. and Jacobs-Wagner, C. (2014). How do bacteria localize proteins to the cell poles? *Journal of Cell Science*, 127(1):11–9.
- [192] Lander, A. D., Lo, W.-C., Nie, Q., and Wan, F. Y. M. (2009). The Measure of Success: Constraints, Objectives, and Tradeoffs in Morphogen-mediated Patterning. *Cold Spring Harbor Perspectives in Biology*, 1(1):a002022.
- [193] Lansbergen, G. and Akhmanova, A. (2006). Microtubule Plus End: A Hub of Cellular Activities. *Traffic*, 7:499–507.
- [194] Lata, S. and Piehler, J. (2005). Stable and Functional Immobilization of Histidine-Tagged Proteins via Multivalent Chelator Headgroups on a Molecular Poly(ethylene glycol) Brush. *Anal. Chem.*, 77:1096–1105.
- [195] Lata, S., Reichel, A., Brock, R., Tampe, and Piehler, J. (2005). High-Affinity Adaptors for Switchable Recognition of Histidine-Tagged Proteins. *JACS*, 127:10205–10215.
- [196] Leano, J. B., Rogers, S. L., and Slep, Kevin, C. (2013). A Cryptic TOG Domain with a Distinct Architecture Underlies CLASP-Dependent Bipolar Spindle Formation. *Structure*, 21(6):939–950.
- [197] Leduc, Cecile and Padberg-Gehle, K., Varga, V., Lebing, D., Diez, S., and Howard, J. (2012). Molecular crowding creates jams of kinesin motors on microtubules. *PNAS*, 109(16):6100–6105.
- [198] Li, P., Banjade, S., Cheng, H.-C., Kim, S., Chen, B., Guo, L., Llaguno, M., Hollingsworth, J. V., King, D. S., Banani, S. F., Russo, P. S., Jiang, Q.-X., Nixon, B. T., and Rosen, M. K. (2012). Phase transition in the assembly of multivalent signaling proteins. *Nature*, 483(336).
- [199] Lighthill, M. J. and Whitham, G. B. (1955). On kinematic waves. ii. a theory of traffic flow on long crowded roads. *Proceedings of the Royal Society of London*, 229(1178):317–345.
- [200] Lo Presti, L., Chang, F., and Martin, S. G. (2012). Myosin Vs organize actin cables in fission yeast. *Molecular Biology of the Cell*, 23:4579–4591.

- [201] Lo Presti, L. and Martin, S. G. (2011). Shaping Fission Yeast Cell by Recruiting Actin-Based Transport on Microtubules. *Current Biology*, 21(24):1–6.
- [202] Loiodice, I., Staub, J., Setty, T. G., Nguyen, N.-P. T., Paoletti, A., and Tran, P. T. (2005). Ase1p Organizes Antiparallel Microtubule Arrays during Interphase and Mitosis in Fission Yeast. *Molecular Biology of the Cell*, 16:1756–1768.
- [203] Love, J. C., Estroff, L. A., Kriebel, J. K., Nuzzo, R. G., and Whitesides, G. M. (2005). Self-Assembled Monolayers of Thiolates on Metals as a Form of Nanotechnology. *Chem Rev.*, 105:1103–1169.
- [204] Macara, I. G. and Mili, S. (2010). Polarity and Differential Inheritance - Universal Attributes of Life? *Cell*, 135:801–812.
- [205] MacDonald, C. T., Gibbs, J. H., and Pipkin, A. C. (1968). Kinetics of Biopolymerization on Nucleic Acid Templates. *Biopolymers*.
- [206] Macnab, R. M. and Koshland, D. E. J. (1972). The Gradient-Sensing Mechanism in Bacterial Chemotaxis. *PNAS*, 69(9):2509–2512.
- [207] Mandelkow, E.-M., Mandelkow, E., and Milligan, R. A. (1991). Microtubule Dynamic and Microtubule Caps: A Time-resolved Cryo-Electron Microscopy Study. *Journal of Cell Biology*, 114(5):977–991.
- [208] Maney, T., Hunter, A. W., Wagenbach, M., and Wordeman, L. (1998). Mitotic Centromere-associated Kinesin Is Important for Anaphase Chromosome Segregation. *Journal of Cell Biology*, 142(3):787–801.
- [209] Manners, D. J. and Meyer, M. T. (1977). The molecular structures of some glucans from the cell wall of *Schizosaccharomyces pombe*. *Carbohydrate Research*, 57:189–203. Pombe cell wall.
- [210] Marenduzzo, D., Finan, K., and Cook, P. R. (2006). The depletion attraction: an underappreciated force driving cellular organization. *Journal of Cell Biology*, 175(5):681–686.
- [211] Martin, S. G. (2009). Microtubule-dependent cell morphogenesis in the fission yeast. *Trends in Cell Biology*, 19(9):447–54.
- [212] Martin, S. G., McDonald, W. H., Yates III, J. R., and Chang, F. (2005). Tea4p Links Microtubule Plus Ends with the Formin For3p in the Establishment of Cell Polarity. *Developmental Cell*, 8:479–491.
- [213] Martin, S. G., Rincón, S. A., Basu, Roshni, P. P., and Chang, F. (2007). Regulation of the formin for3p by cdc42 and bud6p. *Molecular Biology of the Cell*, 18:4155–4167.
- [214] Martinez-Veracoechea, F. J. and Leunissen, M. (2013). The entropic impact on ethering, multivalency and dynamic recruitment in a system with specific binding groups. *Soft Matter*, 9:3213.

- [215] Mata, J. and Nurse, P. (1997). *tea1* and the Microtubular Cytoskeleton Are Important for Generating Global Spatial Order within the Fission Yeast Cell. *Cell*, 89:939–949.
- [216] Mattila, P. K. and Lappalainen, P. (2008). Filopodia: molecular architecture and cellular functions. *Nature Reviews Molecular Cell Biology*, 9:446–454.
- [217] Maurer, S. P., Bieling, P., Cope, J., Hoenger, A., and Surrey, T. (2011). GTPs microtubules mimic the growing microtubule end structure recognized by end-binding protein (EBs). *PNAS*, 108(10):3988–3993.
- [218] Maurer, S. P., Cade, N. I., Bohner, G., Gustafsson, N., Boutant, E., and Surrey, T. (2014). EB1 Accelerates Two Conformational Transitions Important for Microtubule Maturation and Dynamics. *Current Biology*, 24(4):372–84.
- [219] Maurer, S. P., Fourniol, F. J., Bohner, G., Bohner, G. C. A., and Surrey, T. (2012). EBs Recognize a Nucleotide-Dependent Structural Cap at Growing Microtubule Ends. *Cell*, 149:371–382.
- [220] McCaffrey, L. M. and Macara, I. G. (2011). Epithelial organization, cell polarity and tumorigenesis. *Trends in Cell Biology*, 21(12):727–735.
- [221] McClelland, M. L., Kallio, M. J., Barrett-Wilt, G. A., Kestner, C. A., Shabanowitz, J., Hunt, D. F., Gorbsky, G. J., and Stukenberg, P. T. (2004). The Vertebrate Ndc80 Complex Contains Spc24 and Spc25 Homologs, which Are Required to Establish and Maintain Kinetochores-Microtubule Attachment. *Current Biology*, 14(2):131–137.
- [222] McDonald, J. C., Duffy, D. C., Anderson, J. R., Chiu, D. T., Wu, H., A., S. O. J., and Whitesides, G. M. (2000). Fabrication of microfluidic system in poly(dimethylsiloxane). *Electrophoresis*, 21:27–40.
- [223] Melki, R., Carlier, M. F., Pantaloni, D., and Timasheff, S. N. (1989). Cold depolymerization of microtubules to double rings: geometric stabilization of assemblies. *Biochemistry*, 28(23):9143–9152.
- [224] Mimori-Kiyosue, Y. (2011). Shaping Microtubules Into Diverse Patterns: Molecular Connections for Setting Up Both Ends. *Cytoskeleton*, 68:603–618.
- [225] Mimori-Kiyosue, Y., Grigoriev, I., Lansbergen, G., Sasaki, H., Matsui, C., Severin, F., Galjart, N., Grosveld, F., Vorobjev, I., Tsukita, S., and Akhmanova, A. (2005). CLASP1 and cLASP2 bind to EB1 and regulate microtubule plus-end dynamic at the cell cortex. *Journal Cell Biology*, 168:141–153.
- [226] Mimori-Kiyosue, Y., Grigoriev, I., Sasaki, H., Matsui, C., Akhmanova, A., Tsukita, S., and Vorobjev, I. (2006). Mammalian CLASP are required for mitotic spindle organization and kinetochore alignment. *Genes Cells*, 11:845–857.
- [227] Mimori-Kiyosue, Y., Matsui, C., Sasaki, H., and Tsukita, S. (2007). Adenomatous polyposis coli (APC) protein regulated epithelial cell migration and morphogenesis via PDZ domain-based interactions with plasma membranes. *Molecular Biology Society of Japan*, 12:219–233.

- [228] Minc, N., Boudaoud, A., and Chang, F. (2009). Mechanical Forces of Fission Yeast Growth. *Curr. Biol.*, 19(13):1096–1101.
- [229] Mitchison, J. M. and Nurse, P. (1985). Growth in cell length in the fission yeast *Schizosaccharomyces pombe*. *Journal Cell Science*, 75:357–376.
- [230] Mitchison, T. and Kirschner, M. (1984). Dynamic instability of microtubule growth. *Nature*, 312:237–242.
- [231] Mitchison, T. J. (1993). Localization of an Exchangeable GTP Binding Site at the Plus End of Microtubules. *Science*, 261:1044–1047.
- [232] Miyamoto, H. and Hotani, H. (1988). Polymerization of microtubules in liposomes produces morphological changes of shape. *Proc. Tanaguichi Int. Symp.*, 14:220–242.
- [233] Moores, C. A., Perderiset, M., Francis, F., Chelly, J., Houdusse, A., and Milligan, R. A. (2004). Mechanism of Microtubule Stabilization by Doublecortin. *Molecular Cell*, 14:833–839.
- [234] Moores, C. A., Yu, M., Guo, J., Beraud, C., Sakowicz, R., and Milligan, R. A. (2002). A Mechanism for Microtubule Depolymerization by Kinl Kinesins. *Molecular Cell*, 9(4):903–909.
- [235] Moseley, J. B., Mayeux, A., Paoletti, A., and Nurse, P. (2009). A spatial gradient coordinates cell size and mitotic entry in fission yeast. *Nature*, 459(7248):857–60.
- [236] Mostowy, S. and Corrat, P. (2012). Septins: the fourth component of the cytoskeleton. *Nature Reviews Molecular Cell Biology*, 13:183–194.
- [237] Motegi, F., Arai, R., and Mabuchi, I. (2001). Identification of Two Type V Myosins in Fission Yeast, One of Which Functions in Polarized Cell Growth and Moves Rapidly in the Cell. *Molecular Biology of the Cell*, 12(5):1367–1380.
- [238] Mukai, C. and Travis, A. J. (2012). What Sperm Can Teach us About Energy Production. *Reproduction in Domestic Animals*, 74(4):164–169.
- [239] Munro, E., Nance, J., and Priess, J. R. (2004). Cortical Flows Powered by Asymmetric Contraction Transport PAR Protein to Establish and Maintain Anterior-Posterior Polarity in the Early *C. elegans* Embryo. *Developmental Cell*, 7(3):413–424.
- [240] Munteanu, L. (2008). *Dynamics and regulation at the tip. A high resolution view on microtubule assembly*. PhD thesis, Universiteit Leiden.
- [241] Nakamura, S., Grigoriev, I., Nogi, T., Hamaji, T., Cassimeris, L., and Mimori-Kiyosue, Y. (2012). Dissecting the Nanoscale Distributions and Functions of Microtubule-End-Binding Protein EB1 and ch-TOG in Interphase HeLa Cells. *PlosOne*, 7(12):e51442.
- [242] Nakano, K., Imai, J., Arai, R., Toh-e, A., Matsui, Y., and Mabuchi, I. (2002). The small GTPase Rho3 and the diaphanous/formin For3 function in polarized cell growth in fission yeast. *Journal of Cell Science*, 115:4629–4639.

- [243] Nakata, T. and Hirokawa, N. (2003). Microtubule provide direct cues for polarized axonal transport interaction with kinesin motor head. *Journal Cell Biology*, 162(6):1045–1055.
- [244] Nance, J. and Zallen, J. A. (2011). Elaborating polarity: PAR proteins and the cytoskeleton. *Development*, 138(5):799–809.
- [245] Nariko, T., Arimura, N., Fukata, Y., Watanabe, H., Iwamatsu, A., and Kaibuchi, K. (2005). Tubulin and CRMP-2 complex is transported via Kinesin-1. *Journal of Neurochemistry*, 93:1371–1382.
- [246] Nedelec, F., Surrey, T., Maggs, A. C., and Leibler, S. (1997). Self-organization of microtubules and motors. *Nature*, 389(6648):305–308.
- [247] Nelson, W. J. (2003). Adaptation of core mechanism to generate cell polarity. *Nature*, 422:766–774.
- [248] Niethammer, P., Bastiaens, P., and Karsenti, E. (2004). Stathmin-Tubulin Interaction Gradients in Motile and Mitotic Cells. *Science*, 303:1862–1866.
- [249] Nogales, E. (2000). Structural Insights into Microtubule Function. *Annual Review Biochemistry*, 69:277–302.
- [250] Nogales, E., Whittaker, M., Milligan, R. A., and Downing, K. H. (1999). High-Resolution Model of the Microtubule. *Cell*, 96:79–88.
- [251] Nurnberg, A., Kitzing, T., and Grosse, R. (2011). Nucleating actin for invasion. *Nature Reviews Cancer*, 11:177–187.
- [252] Odde, D. J., Cassimeris, L., and Buettner, H. M. (1995). Kinetics of Microtubule Catastrophe Assessed by Probabilistic Analysis. *Biophysical Journal*, 69:796–802.
- [253] Oriola, D., Roth, S., Dogterom, M., and Casademunt, J. (2015). Formation of helical membrane tubes around microtubules by single-headed kinesin KIF1A. *Nature Communications*, 6:8025.
- [254] Padte, N. N., Martin, S. G., Howard, M., and Chang, F. (2006). The Cell-End Factor Pom1p Inhibits Mid1p in Specification of the Cell Division Plane in Fission Yeast. *Current Biology*, 16(24):2480–2487.
- [255] Panda, D., Daijo, J. E., Jordan, M. A., and Wilson, L. (1995). Kinetic Stabilization of Microtubule Dynamic at Steady State in Vitro by Substoichiometric Concentrations of Tubulin-Colchicine Complex. *Biochemistry*, 34:9921–9929.
- [256] Parmeggiani, A., Franosch, T., and Frey, D. (2004). Totally asymmetric simple exclusion process with Langmuir kinetics. *Physical Review E*, 70(4):046101.
- [257] Parmeggiani, A., Franosch, T., and Frey, E. (2003). Phase Coexistence in Driven One-Dimensional Transport. *Physical Review Letters*, 90(8):086601.

- [258] Pasqualone, D. and Huffaker, T. C. (1994). TSU1, a Suppressor of a β -Tubulin Mutation, Encodes a Novel and Essential Component of the Yeast Mitotic Spindle. *Journal of Cell Biology*, 127(6):1973–1984.
- [259] Pautot, S., Frisken, B. J., and Weitz, D. A. (2003). Production of unilamellar vesicles using an inverted emulsion. *Langmuir*, 19:270–2879.
- [260] Perez, P. and Rincon, S. A. (2010). Rho GTPases: regulation of cell polarity and growth in yeasts. *Biochemical Journal*, 426(3):243–253.
- [261] Peskin, C. S., Odell, Garrett, M., and Oster, G. F. (1993). Cell Motions and Thermal Fluctuations: The Brownian Ratchet. *Biophysical Journal*, 65:316–324.
- [262] Postma, M., Roelofs, J., Goedhart, J., Gadella, T. W. J., Visser, A. J. W. G., and Van Haastert, P. J. M. (2003). Uniform caMP Stimulation of Dictyostelium Cells Induces Localized Patches of Signal Transduction and Pseudopodia. *Molecular Biology of the Cell*, 14(12):5019–5027.
- [263] Preciado Lopez, M., Huber, E., Grigoriev, I., Steinmetz, M. O., Akhmanova, A., Dogterom, M., and Koenderink, G. (2014). In Vitro Reconstitution of Dynamic Microtubules Interacting with Actin Filament Networks. *Methods in Enzymology*, 540:301–320.
- [264] Ramon y Cajal, S. (1890). A quelle époque apparaissent les expansions des cellules nerveuses de la moelle épinière du poulet. *Anat. Anzeiger*, 5:609–613.
- [265] Raskin, D. M. and de Boer, P. A. J. (1999). Rapid pole-to-pole oscillation of a protein required for directing division to the middle of Escherichia coli. *PNAS*, 96(9):4971–4976.
- [266] Ravelli, R. B. G., Gigant, B., Curmi, P. A., HJourdain, I., Lanchkar, S., Sobel, A., and Knossow, M. (2004). Insights into tubulin regulation from a complex with colchicine and a stathmin-like domain. *Nature*, 428:198–202.
- [267] Ray, Sanghamitra, M. E., Milligan, R. A., and Howard, J. (1993). Kinesin Follows the Microtubule's Protofilament Axis. *Journal Cell Biology*, 121(5):1083–1093.
- [268] Reck-Peterson, S. L., Yildiz, A., Carter, A. P., Gennerich, A., Zhang, N., and Vale, R. D. (2006). Single-Molecule Analysis of Dynein Processivity and Stepping Behaviour. *Cell*, 126:335–348.
- [269] Recouvreux, P., Sokolowski, T. R., Gramoustianou, A., ten Wolde, P. R., and Dogterom, M. (2016). Chimera proteins with affinity for membrane and microtubule tips polarize in the membrane of fission yeast cells. *PNAS*, 113(7):1811–1816.
- [270] Reese, L., Melbinger, A., and Frey, E. (2011). Crowding of Molecular Motors Determines Microtubule Depolymerization. *Biophysical Journal*, 101:2190–2200.
- [271] Reilein, A. and Nelson, W. J. (2005). APC is a component of an organizing template for cortical microtubule networks. *Nature Cell Biology*, 7(5):463–473.

- [272] Rezakhanliha, R., Agianniotis, A., Schrauwen, J. T. C., Gridda, A., Sage, D., Bouten, C. V. C., van de Vosse, F. N., Unser, M., and Stergiopoulos, N. (2011). Experimental investigation of collagen waviness and orientation in the arterial adventitia using confocal laser scanning microscopy. *Biomechanics and Modeling in Mechanobiology*, 11(3-4):461–73.
- [273] Ridley, A. J., Peterson, H. F., Johnston, C. J., Diekmann, D., and Hall, A. (1992). The small GTP-binding protein rac regulates growth factor-induced membrane ruffling. *Cell*, 70(3):401–410.
- [274] Rinc. A., Bhatia, P., Bicho, C., Guzman-Vendrell, M., Fraissier, V., Borek, W. E., de Lima Alves, F., Dingli, F., Loew, D., Rappsilber, J., Sawin, K. E., Martin, S. G., and Paoletti, A. (2014). Pom1 regulated the assembly of cdr2-mid1 cortical nodes for robust spatial control of cytokinesis. *Journal Cell Biology*, 206(1):61–77.
- [275] Rincón, S. A., Yanfang, Y., Villar-Tajadura, M. A., Santos, B., Martin, S. G., and Pérez, P. (2009). Pob1 Participates in the Cdc42 Regulation of Fission Yeast Actin Cytoskeleton. *Molecular Biology of the Cell*, 20:4390–4399.
- [276] Rizk, R. S., DiScipio, K. A., Proudfoot, K. G., and Gupta Jr, M. L. (2014). The kinesin-8 kip3 scales anaphase spindle length by suppression of midzone microtubule polymerization. *Journal of Cell Biology*, 204(6):966–975.
- [277] Rodriguez-Boulan, E., Kreitzer, G., and Musch, A. (2005). Organization of vesicular trafficking in epithelia. *Nature Reviews*, 6:233–247.
- [278] Rogers, K. W. and Schier, A. F. (2011). Morphogen Gradients: From Generation to Interpretation. *Annual Review Cell and Developmental Biology*, 27:377–407.
- [279] Rogers, S. L., Wiedemann, U., Udo, H., Turck, C., and Vale, R. D. (2004). Drosophila RhoGEF2 Associates with Microtubule Plus Ends in an EB1-Dependent Manner. *Current Biology*, 14:1827–1833.
- [280] Roll-Mecak, A. and McNally, F. J. (2010). Microtubule severing enzymes. *Current Opinion Cell Biology*, 22(1).
- [281] Romet-Lemone, G., VanDuijn, M., and Dogterom, M. (2005). Three-dimensional control of protein patterning in microfabricated devices. *Nano Letters*, 5(12):2350–2354.
- [282] Rossman, K. L., Der, C. J., and Sondek, J. (2005). GEF means go: Turning on RHO GTPases with guanine nucleotide-exchange factors. *Nature Reviews Molecular Cell Biology*, 6:167–180.
- [283] Roth, S., Laan, L., and Dogterom, M. (2014). Reconstitution of cortical dynein function. *Methods in Enzymology*, 540:205–230.
- [284] Sagolla, M. J., Uzawa, S., and Cande, Z. (2003). Individual microtubule dynamics contribute to the function of mitotic and cytoplasmic arrays in fission yeast. *Journal Cell Science*, 116:4891–4903.

- [285] Sakakibara, A. and Hatanaka, Y. (2015). Neural polarization in the developing cerebral cortex. *Frontiers in Neuroscience*, 9(116).
- [286] Samejima, I., Louren P. C. C., Snaith, H. A., and Sawin, K. E. (2005). Fission Yeast *mto2p* Regulates Microtubule Nucleation by the Centrosomin-related Protein *mto1p*. *Molecular Biology of the Cell*, 16(6):3040–3051.
- [287] Saunders, T. E., Pan, K. Z., Angel, A., Guan, Y., Shah, J. V., Howard, M., and Chang, F. (2013). Noise Reduction in the Intracellular *Pom1p* Gradient by a Dynamic Clustering Mechanism. *Developmental Cell*, 22(3):558–72.
- [288] Sawin, K. E., Louren P. C. C., and Snaith, H. A. (2004). Microtubule Nucleation at Non-Spindle Pole Body Microtubule-Organizing Centers Requires Fission Yeast Centrosomin-Related Protein *mod20p*. *Current Biology*, 14(9):763–775.
- [289] Sawin, K. E. and Snaith, H. A. (2004). Role of microtubules and *tealp* in establishment and maintenance of fission yeast cell polarity. *Journal of Cell Science*, 117(5):689–700.
- [290] Schaap, I. A. T., Carrasco, C., de Pablo, P. J., and Schmidt, C. F. (2011). Kinesin Walks the Line: Single Motors Observed by Atomic Force Microscopy. *Biophysical Journal*, 100(10):2450–2456.
- [291] Schott, D., Ho, Jackson, P. D., and Bretscher, A. (1999). The COOH-Terminal Domain of *Myo2p*, a Yeast Myosin V, Has a Direct Role in Secretory Vesicle Targeting. *Journal Cell Biology*, 147(4):791–808.
- [292] Seetapun, D., Castle, B. T., McIntyre, A. J., Tran, P. T., and Odde, D. J. (2012). Estimating the Microtubule GTP Cap Size In Vivo. *Current Biology*, 22(18):1681–1687.
- [293] Shi, X., Lim, J., and Ha, T. (2010). Acidification of the Oxygen Scavenging System in Single-Molecule Fluorescence Studies: In Situ Sensing with a Ratiometric Dual-Emission Probe. *Analytical Chemistry*, 82:6132–6138.
- [294] Shibata, K., Miura, M., Watanabe, Y., Saito, K., Nishimura, A., Furuta, K., and Toyoshima, Y. Y. (2012). A Single Protofilament is Sufficient to Support Unidirectional Walking of Dynein and Kinesin. *PLoS One*, 7(8):e42990.
- [295] Shim, J.-u., Cristobal, G., Link, D. R., Thorsen, T., Katie Piattelli, Y. J., and Fraden, S. (2007). Control and measurement of the phase behaviour of aqueous solutions using microfluidics. *J Am Chem Soc*.
- [296] Siegrist, S. E. and Doe, C. Q. (2007). Microtubule-induced cortical cell polarity. *Genes & Development*, 21:483–496.
- [297] Slep, Kevin, C. and Vale, R. D. (2007). Structural Basis of Microtubule Plus End Tracking by XMAP215, CLIP-170, and EB1. *Molecular Cell*, 27:946–991.
- [298] Small, J. V. and Kaverina, I. (2003). Microtubules meet substrate adhesions to arrange cell polarity. *Current Opinion Cell Biology*, 15(1):40–47.

- [299] Snaith, H. A., Samejima, I., and Sawin, K. E. (2005). Multistep and multimode cortical anchoring of tea1p at cell tips in fission yeast. *The EMBO Journal*, 24:3690–3699.
- [300] Snaith, H. A. and Sawin, K. E. (2003). Fission yeast mod5p regulates polarized growth through anchoring of tea1p at cell tips. *Nature*, 423:647–651.
- [301] Sokolowski, T. R. (2013). *A Computational Study of Robust Formation of Spatial Protein Patterns*. PhD thesis, Vrije Universiteit Amsterdam.
- [302] Sourjik, V. and Wingreen, N. S. (2012). Responding to Chemical Gradients: Bacterial Chemotaxis. *Current Opinion Cell Biology*, 24(2):262–268.
- [303] Spiliotis, E. T. and Gladfelter, A. S. (2012). Spatial Guidance of Cell Asymmetry: Septin GTPases Show the Way. *Traffic*, 13(2):195–203.
- [304] St Johnston, D. and Ahringer, J. (2010). Cell Polarity in Eggs and Epithelia: Parallels and Diversity. *Cell*, 141:757–774.
- [305] Stearns, T., Evans, L., and Kirschner, M. (1991). γ -Tubulin is a highly conserved component of the centrosome. *Cell*, 65(5):825–836.
- [306] Steinmetz, M. O., Kammerer, R. A., Jahnke, W., Goldie, K. N., Lustig, A., and Oostrom, J. v. (2000). Op18/stathmin caps a kinked protofilament-like tubulin tetramer. *The EMBO Journal*, 19(4):572–580.
- [307] Stiess, M. and Bradke, F. (2011). Neuronal Polarization: The Cytoskeleton Leads the Way. *Neuronal Polarization*, 71(6):430–444.
- [308] Sui, Haixin, D. K. H. (2010). Structural basis of inter-protofilament interaction and lateral deformation of microtubules. *Structure*, 18(8):1022–1031.
- [309] Swaney, K. E., Huang, C.-H., and Devreotes, P. N. (2010). Eukaryotic Chemotaxis: A Network of Signaling Pathways Control Motility, Directional Sensing, and Polarity. *Annu. Rev. Biophys.*, 39:265–289.
- [310] Tabata, T. and Takei, Y. (2004). Morphogens, their identification and regulation. *Development*, 131:703–712.
- [311] Taberner, N., Lof, A., Roth, S., Lamers, D., Zeijlemaker, H., and Dogterom, M. (2015). In vitro system for the study of microtubule-based cell polarity in fission yeast. *Methods in Cell Biology*, 128:1–22.
- [312] Taberner, N., Weber, G., You, C., Dries, R., Piehler, J., and Dogterom, M. (2014). Reconstituting Functional Microtubule-Barrier Interactions. *Methods in Cell Biology*, 120:69–90.
- [313] Tanenbaum, M. E., Vale, R. D., and McKenney, R. J. (2013). Cytoplasmic dynein crosslinks and slides anti-parallel microtubules using its two motor domains. *eLIFE*, 2(e00943):1–20.

- [314] Tatebe, H., Shimada, K., Uzawa, S., Morigasaki, S., and Shiozaki, K. (2005). Wsh3/Tea4 Is a Novel Cell-End Factor Essential for Bipolar Distribution of Tea1 and Protects Cell Polarity under Environmental Stress in *S. pombe*. *Cell*, 15:1006–1015.
- [315] Taylor, K. R., Holzer, A. K., Bazan, J. F., Walsh, C. A., and Gleeson, J. G. (2000). Patient Mutations in Doublecortin Define a Repeated Tubulin-binding Domain. *The Journal of Biological Chemistry*, 3:34442–34450.
- [316] Terenna, C. R., Makushok, T., Velve-Casquillas, G., Baigl, D., Chen, Y., Bornens, M., Paoletti, A., Piel, M., and Tran, P. T. (2008). Physical Mechanism Redirecting Cell Polarity and Cell Shape in Fission Yeast. *Current Biology*, 18:1748–1753.
- [317] Tilney, L. G., Bryan, J., Buch, D. J., Fujiwara, K., Mooseker, M. S., Murphy, D. B., and Snyder, D. H. (1973). Microtubule: evidence for 13 protofilaments. *Journal of Cell Biology*, 59(1):267–275.
- [318] Tinazli, A., Tang, J., Valiokas, R., Picuric, S., Lata, S., Piehler, J., Liedberg, B., and Tampe, R. (2005). High-Affinity Chelator Thiols for Switchable and Oriented Immobilization of Histidine-Tagged Proteins: A Generic Platform for Protein Chip Technologies. *Chemistry*, 11(18):5249–59.
- [319] Tirnauer, J. S. and Bierer, B. E. (2000). EB1 Protein Regulate Microtubule Dynamic, Cell Polarity, and Chromosome Stability. *Journal Cell Biology*, 149(4):761–766.
- [320] Tischer, C., Brunner, D., and Dogterom, M. (2009). Force- and kinesin-8-dependent effects in the spatial regulation of fission yeast microtubule dynamics. *Molecular Systems Biology*, 5(250):1–10.
- [321] Tran, P. T., Marsh, L., Doye, V., Inoué, Shinya, S., and Chang, F. (2001). A Mechanism for Nuclear Positioning in Fission Yeast Based on Microtubule Pushing. *Journal of Cell Biology*, 153(2):397–411.
- [322] Turing, A. M. (1952). The Chemical Basis of Morphogenesis. *Philosophical Transactions of the Royal Society of London*, 237(641):37–72.
- [323] Ullal, P., McDonald, N. A., Chen, J.-S., Lo Presti, L., Roberts-Galbraith, R. H., Gould, K. L., and Martin, S. G. (2015). The DYRK-family kinase Pom1 phosphorylates the F-BAR protein Cdc15 to prevent division at cell poles. *Journal Cell Biology*, 211(3):653–668.
- [324] Valee, R. B. and Sheetz, M. P. (1996). Targeting of motor proteins. *Science*, 271:1539–1544.
- [325] van Beuningen, S. F. and Hoogenraad, C. C. (2016). Neuronal polarity: remodeling microtubule organization. *Current Opinion in Neurobiology*, 39:1–7.
- [326] van Doorn, G. S., Tånase, C., and Mulder, B. M. (2000). On the stall force for growing microtubules. *European Biophysics Journal*, 29:2–6.

- [327] Vardy, L. and Toda, T. (2000). The fission yeast gamma-tubulin complex is required in g1 phase and is a component of the psindle assembly checkpoint. *The EMBO Journal*, 19(22):6098–6111.
- [328] Varga, V., Helenius, J., Tanaka, K., Hyman, A. A., Tanaka, T. U., and Howard, J. (2006). Yeast kinesin-8 depolymerizes microtubules in a length-dependent manner. *Nature Cell Biology*, 8(9):957–962.
- [329] Varga, V., Leduc, C., Bormouth, V., Diez, S., and Howard, J. (2009). Kinesin-8 Motors Act Cooperative to Mediate length-dependent microtubule depolymerization. *Cell*, 138:1174–1183.
- [330] Vasilev, J., Gelfand, I. M., Domina, L. V., Ivanova, O. Y., Komm, S. G., and Olshetskaja, L. V. (1970). Effect of colcemid on the locomotory behaviour of fibroblasts. *Development*, 24:625–640.
- [331] Venkatram, S., Jennings, J., Links, A., and Gould, K. L. (2005). Mto2p, a Novel Fission Yeast Protein Required for Cytoplasmic Microtubule Organization and Anchoring of the Cytokinetic Actin Ring. *Molecular Biology of the Cell*, 16(6):3052–3063.
- [332] Venkatram, S., Tasto, J. J., Feoktistova, A., Jennings, J. L., Link, A. J., and Gould, K. L. (2004). Identification and Characterization of Two Novel Proteins Affecting Fission Yeast gamma-tubulin Complex Function. *Molecular Biology of the Cell*, 15(5):2287–2301.
- [333] Verde, F., Mata, J., and Nurse, P. (1995). Fission Yeast Cell Morphogenesis: Identification of New Genes and Analysis of Their Role during the Cell Cycle. *Journal Cell Biology*, 131(6):1529–1538.
- [334] Vicker, M. G. (2000). Reaction-diffusion waves of actin filament polymerization/depolymerization in dictyostelium pseudopodium extension and cell locomotion. *Biophysical Chemistry*, 84(2):87–98.
- [335] Vicker, M. G. (2002). Eukaryotic Cell Locomotion Depends on the Propagation of Self-Organized Reaction-Diffusion Waves and Oscillations of Actin Filament Assembly. *Experimental Cell Research*, 275(1):54–66.
- [336] Vicker, M. G., Xiang, W., Plath, P. J., and Wosnoik, W. (1997). Pseudopodium extension and amoeboid locomotion in Dictyostelium discoideum: Possible autowave behaviour of F-actin. *Physica D: Nonlinear Phenomena*, 101(3-4):317–332.
- [337] Vitre, B., Coquelle, F. M., Heichette, C., Garnier, C., Chretien, D., and Arnal, I. (2008). Eb1 regulated microtubule dynamics and tubulin sheet closure in vitro. *Nature Cell Biology*, 10(4):415–421.
- [338] Volkov, V. A., Zaytsev, A. V., Gudimchuk, N., Grissom, P. M., Gintsburg, A. L., Ataulkhanov, F. I., McIntosh, J. R., and Grishchuk, E. L. (2013). Long tethers provide high-force coupling of the dam1 ring to shortening microtubules. *PNAS*, 110(19):7708–7713.

- [339] Walker, R. A., O'Brien, E. T., Pryer, N. K., Soboeiro, M. F., Erickson, H. P., and Salmon, E. D. (1988). Dynamic Instability of Individual Microtubule Analyzed by Video Light Microscopy Rate Constants and Transition Frequencies. *Journal of Cell Biology*, 107:1437–1448.
- [340] Wang, F. (2009). The Signaling Mechanism Underlying Cell Polarity and Chemotaxis. *Cold Spring Harbor Perspectives in Biology*, 1(4):a002980.
- [341] Wang, H.-W. and Nogales, E. (2005). Nucleotide-dependent bending flexibility of tubulin regulates microtubule assembly. *Nature*, 435:911–915.
- [342] Wang, K., Herzmark, P., Weiner, O. D., Srinivasan, S., Servant, G., and RBoorne, H. R. (2002). Lipid products of Pi(3)Ks maintain persistent cell polarity and directed motility in neutrophils. *Nature Cell Biology*, 4:513–518.
- [343] Wang, P. J. and Huffaker, T. C. (1997). Stup2p: a Microtubule-Binding Protein that Is an Essential Component of the Yeast Spindle Pole Body. *Journal Cell Biology*, 105(5):2203–2215.
- [344] Wartlick, O., Kicheva, A., and Ginzalez-Gaitan, M. (2009). *Morphogen gradient formation*. *Perspect. Biol. Cold Spring Harbour*.
- [345] Watanabe, T., Wang, S., Noritake, J., Sato, K., KFukata, M., Takefuji, M., Nakagawa, M., Izumi, N., Akiyama, T., and Kaibuchi, K. (2004). Interaction with IQGAP1 Links APC to Rac1, Cdc42, and Actin Filaments during Cell Polarization and Migration. *Developmental Cell*, 7:871–883.
- [346] Waterman-Storer, C. M. and Salmon, E. D. (1998). Endoplasmic reticulum membrane tubules are distributed by microtubules in living cells using three distinct mechanisms. *Current Biology*, 8(14):798–807.
- [347] Waterman-Storer, C. M., WorthyLake, R. A., Liu, B. P., Burridge, K., and Salmon, E. D. (1999). Microtubule growth activates Rac1 to promote lamellipodial protrusion in fibroblasts. *Nature Cell Biology*, 1:45–50.
- [348] Watson, Peter and Stephens, D. J. (2006). Microtubule plus-end loading of p150^{glued} is immediate by eb1 and clip-170 but is not required for intracellular membrane traffic in mammalian cells. *Journal Cell Science*, 119(13):2758–2767.
- [349] Watson, J. and Baron, M. G. (1995). Precise static and dynamic permeation measurement using a continuous-flow vacuum cell. *Journal of Membrane Science*, 106:259–268.
- [350] Weiner, O. D., Marganski, W. A., Wu, L. E., Altschuler, S. J., and Kirschner, M. W. (2007). An Actin-Based Wave Generator Organizes Cell Motility. *PlosBiology*, 5(9):e221.
- [351] Weiner, O. D., Neilsen, P. O., Prestwich, G. D., KiKirschner, M., Cantley, L. C., and Bourne, H. R. (2002). A PtdinsP3- and Rho GTPase-mediated positive feedback loop regulates neutrophil polarity. *Nature Cell Biology*, 4(7):509–513.

- [352] Weisbrich, A., Honnappa, S., Jaussi, R., Okhrimenko, O., Frey, D., Jelesarov, I., Akhmanova, A., and Steinmetz, M. O. (2007). Structure-function relationship of CAP-Gly domains. *Nature Structural & Molecular Biology*, 14(10):959–67.
- [353] Weisenberg, R. C., Deery, W. J., and Dickington, P. J. (1976). Tubulin-Nucleotide Interaction during the Polymerization and Depolymerization of Microtubules. *Biochemistry*, 15(19).
- [354] Wen, Y., Eng, C. H., Schomoranzer, J., Cabrera-Poch, N., Morris, E. J. S., Chen, M., Wallar, B. J., Alberts, A. S., and Gundersen, G. G. (2004). EB1 and APC bind to mDia to stabilize microtubules downstream of Rho and promote cell migration. *Nature Cell Biology*, 6:820–830.
- [355] Widlund, P. O., Stear, J. H., Pozniakovsky, A., Zanic, M., Reber, S., and Brouhard, G. J. (2011). Xmap215 polymerase activity is built by combining multiple tubulin-binding tog domains and a basic lattice-binding region. *PNAS*, 108(7):2741–2746.
- [356] Wilson-Kubalek, E. M., Kubalek, E. M., Cheeseman, I. M., Yoshioka, C., Desai, A., and Milligan, R. A. (2008). Orientation and structure of the Ndc80 complex on the microtubule lattice. *Journal of Cell Biology*, 182(6):1055–1061.
- [357] Win, T. Z., DGachet, Y., Mulvihill, D. P., May, K. M., and Hyams, J. S. (2001). Two type V myosins with non-overlapping functions in the fission yeast *Schizosaccharomyces pombe*: Myo52 is concerned with growth polarity and cytokinesis, Myo51 is a component of the cytokinetic actin ring. *Journal Cell Science*, 114:69–79.
- [358] Witte, H., Neukirchen, D., and Bradke, F. (2008). Microtubule stabilization specifies initial neuronal polarization. *Journal Cell Biology*, 180(3):619–632.
- [359] Yajima, H., Ogura, T., Nitta, R., Okada, Y., Sato, C., and Hirokawa, N. (2012). Conformational changes in tubulin in gmpcpp and gdp-taxol microtubules observed by cryoelectron microscopy. *Journal of Cell Biology*, 198(3):315–322.
- [360] Yamashita, A., Sato, M., Fujita, A., Yamamoto, M., and Toda, T. (2005). The Roles of Fission Yeast Ase1 in Mitotic Cell Division, Meiotic Nuclear Oscillation, and Cytokinesis Checkpoint Signaling. *Molecular Biology of the Cell*, 16:1378–1395.
- [361] Yodh, A. G., Lin, L., Crocker, J. C., Dinsmore, A. D., Verma, R., and D., K. P. (2001). Entropically driven self-assembly and interaction in suspension. *Philosophical transactions of the royal society of London*, 359:921–937.
- [362] Zakharov, P., Gudimchuk, N., Voevodin, V., Tikhonravov, A., Ataulakhanov, F. I., and Grishchuk, E. L. (2015). Molecular and mechanical causes of microtubule catastrophe and aging. *Biophysical Journal*, 109:2574–2591.
- [363] Zanic, M., Widlund, P. O., Hyman, A. A., and Howard, J. (2013). Synergy between XMAP215 and EB1 increases microtubule growth rates to physiological levels. *Nature Cell Biology*, 15(6):688–693.

- [364] Zhang, R., Alushin, G. M., Brown, A., and Nogales, E. (2015). Mechanistic Origin of Microtubule Dynamic Instability and its Modulation by EB Proteins. *Cell*, 162(4):849–859.
- [365] Zhen, G., Falconnet, D., Kuennemann, E., Voros, J., Spencer, N. D., Textor, M., and Zurcher, S. (2006). Nitrilotriacetic Acid Functionalized Graft Copolymers: A Polymeric Interface for Selective and Reversible Binding of Histidine-Tagged Proteins. *Advanced Functional Materials*, 16:243–251.
- [366] Zimmerman, S. and Chang, F. (2005). Effects of gamma-Tubulin Complex Protein on Microtubule Nucleation and Catastrophe in Fission Yeast. *Molecular Biology of the Cell*, 16(6):2719–2733.
- [367] Zimmerman, S., Tran, P. T., Daga, R. R., Niwa, O., and Chang, F. (2004). Rsp1p, a Domain Protein Required for Dissassembly and Assembly of Microtubule Organizing Centers during Fission Yeast Cell Cycle. *Developmental Cell*, 6(4):497–509.

SUMMARY

*Al andar se hace el camino, y al volver la vista atrás
se ve la senda que nunca se ha de volver a pisar.*

Antonio Machado

*We make the way as we walk, and looking back
we see the trail that no foot shall tread again.*

In this thesis we took the challenge to *in vitro* reconstitute a minimal phenomenon essential for life: Cell polarity. This is an ubiquitous phenomenon that allows cells to define a direction for migration, growth or division. Our study focussed on microtubule-based establishment of polarity taking *S. pombe* as a model organism. In this rod-shaped unicellular organism, microtubules deposit polarity factor proteins to the poles of the cell, leaving only these cues for initiating the cascade for cellular growth. Such pattern formation is very robust and is believed to rely on feedback mechanisms. In our study, we hypothesized what would be the minimum components needed for the establishment of a polarized cortical pattern of proteins and developed an *in vitro* system that fulfils those requirements. Those where:

- Microtubule-based transport of polarity factors.
- Elongated cell shape.
- Cortical receptor for the polarity factors.

The microtubule-based transport of polarity factors used consisted on a reduced system of the proteins involved in transporting polarity factors in *S. Pombe*. This included the EB protein Mal3, the kinesin Tea2 and the CLIP-170 homologue Tip1 [Bieling et al. 2007]. We used fluorescently labelled Tip1 as a polarity marker. In chapter 2 we studied how this system localizes at microtubule tips. It had already been shown before that Tip1-Tea2 complexes bind directly to microtubule tips via interaction with Mal3 as well as to the microtubule lattice in lower amounts [Bieling et al. 2007]. We showed that Tea2-Tip1 coming from the lattice could form little traffic jams at the microtubule tips. Moreover, we showed indications that Tea2 and Tip1 in the presence of high concentrations of Mal3 probably form clusters of a non-fixed stoichiometry.

For the elongated cell shape and the cortical receptor we developed two systems: one consisting of glass micro-wells with a static cortical receptor (chapters 3-5), and another one consisting of emulsion droplets with a diffusive receptor (chapter 6).

In the first system we developed a protocol to easily form *S. pombe*-like glass micro-wells where the wall surfaces can be specifically functionalized, distinct from the the

bottom surfaces. This had been achieved before by employing different materials [Laan and Dogterom 2010]. Here, adapting 2D micro-patterning techniques to 3D structures, we could keep all the cavity surfaces of the same material (glass). This improved surface specificity (bottom surface versus walls), reduced unspecific protein sticking at the surfaces, and reduced sample preparation time. We used Tris-Ni(II)-NTA moieties bound to the walls as cortical receptor for his-tagged Tip1 or other proteins. The binding affinity between his-tagged Tip1 and Tris-Ni(II)-NTA was tuned by controlled addition of imidazole to the system. Proper tuning yielded samples in which microtubule tips carrying several his-tagged Tip1 molecules would deposit on average 20 % of those molecules to the wall upon contact. Our analysis suggests that his-tagged Tip1 in the presence of Tea2 and Mal3 is able to form a connection between the microtubule and the wall receptor. This produces capturing of the microtubule tips at locations where his-tagged Tip1 is deposited. Interestingly, analogous assays with his-tagged Mal3 alone, which is known to not form any type of clusters, would not lead to Mal3 depositions.

The reason why his-tagged Tip1 would be deposited to the walls in our assays while his-tagged Mal3 would not remains unclear. Being his-tagged Mal3 smaller than the his-tagged Tip1-Tea2-Mal3 complex, it could simply not be able to simultaneously connect the microtubule tip with the wall receptor due to steric reasons. However, *in vivo* experiments in our group showed that a chimera protein of Mal3 fused to a membrane binding domain, would localize to *S. pombe* poles in a microtubule-dependent manner, presumably by direct interaction with the microtubule tip [Recouvreux et al. 2016]. Therefore, the small size of his-tagged Mal3 may not be the reason why we do not observe clear depositions. It seems that the ability of Tip1 to form cluster may be decisive on its successful wall deposition. This is very interesting because polarity markers of *S. pombe* have been found to sit in clusters in the plasma membrane [Dodgson et al. 2013]. Our findings suggest that clustering occurring at a microtubule tip would enhance protein deposition to the plasma membrane, giving an added functionality to the clusters observed *in vivo*.

In this thesis, we further tested whether microtubules free to self-organize in the elongated micro-wells would preferentially deposit his-tagged Tip1 to the poles of the micro-wells and establish a polarized cortical pattern. Although microtubule alignment along the longest axis of the micro-wells was predominant, very few micro-wells exhibited a polarized pattern. The reason of polarity not being predominant may be the lack of a positive feedback in our system. It was surprising for us to see that in micro-wells where microtubules were highly packed, those microtubules would interfere to each other and have difficulties reaching the poles of the cell. Interestingly, the same Tea2-Tip1 packets that may facilitate his-tagged Tip1 depositions, would produce sliding between microtubules leading to a stable microtubule configuration of layers of microtubules with the plus ends facing towards the centre of the micro-well. This configuration is not desirable since it makes protein depositions to the poles of the cell very unprovable. To prevent this phenomenon, we added the microtubule bundler protein Ase1 and the minus end directed motor dynein, whose combined action would produce dynamic anti-parallel microtubule bundles with the plus ends facing the bundle extremes. This resulted in polarized deposition of his-tagged Tip1 in elongated micro-wells.

The micro-well method developed with selective functionalization of surfaces could also be applied to study microtubule-cortex interactions modulated by cortical proteins. As an example, we show exploratory experiments in which CLASP2 α bound to the walls seemed to stabilize microtubules upon plus end contact. The study performed is not conclusive and further conditions have to be tried.

The other setup developed goes two steps closer to the *in vivo* polarity case. It adds confinement and allows for diffusion of the cortical receptor. It consists of water-in-oil emulsion droplets where microtubules can grow inside and interact via his-tagged Tip1 with lipids functionalized with Tris-Ni(II)-NTA at the water-oil inter-phase. To obtain elongated droplets (*S. pombe*-like shapes), we adapted a microfluidics method consisting of microchambers where droplets are pushed to deform to the chamber shape [Boukellal et al. 2008] to small *S. pombe* sizes. We hope that the method developed will be very useful for studying the emergence of polarity and microtubule organization in non-spherical confinements.

—

—

SAMENVATTING

In dit proefschrift zijn we de uitdaging aangegaan om *in vitro* een minimaal fenomeen te reconstitueren dat essentieel is voor leven: Cel polariteit. Dit is een alomtegenwoordige fenomeen dat het mogelijk maakt voor cellen om een richting voor migratie, groei of deling te definiëren. Onze studie richtte zich op het ontstaan van polariteit gebaseerd op microtubuli met *S. pombe* als modelorganisme. In dit staaformige, eencellige organisme, microtubuli zetten eiwitten die de polariteit beïnvloeden af op de polen van de cel, waardoor er alleen daar indicators achterblijven voor het initiëren van cellulaire groei. Dergelijke patroonvorming is zeer robuust en wordt verondersteld afhankelijk te zijn van terugkoppelingsmechanismen. In onze studie hebben we een hypothese opgesteld over de minimale componenten die nodig zijn voor het ontstaan van een gepolariseerd patroon van eiwitten op de cel cortex, en een *in vitro* systeem ontwikkeld dat aan deze vereisten voldoet. Die vereisten waren:

- Transport van polariteitsfactoren gebaseerd op microtubuli.
- Langwerpige vorm van de cel.
- Receptor voor polariteitsfactoren op de cel cortex.

Het transport van polariteitsfactoren door microtubuli in onze experimenten bestond uit een gereduceerd systeem van de eiwitten betrokken bij dit transport in *S. pombe*. Dit systeem bevatte het EB eiwit Mal3, de kinesine Tea2 en de CLIP-170 homoloog Tip1 [Bieling et al. 2007]. We gebruikten fluorescent gelabeld Tip1 als polariteitsmarker. In hoofdstuk 2 bestudeerden we hoe dit systeem lokaliseert op het uiteinde van microtubuli. Het was al eerder aangetoond dat Tip1-Tea2 complexen rechtstreeks binden aan de tips via een interactie met Mal3, maar ook in kleine hoeveelheden aan het microtubule rooster [Bieling et al. 2007]. We hebben aangetoond dat Tea2-Tip1 afkomstig van het microtubule rooster kleine files op de microtubule tips kan vormen. Bovendien hebben we aanwijzingen laten zien dat Tea2 en Tip1 in de aanwezigheid van hoge concentraties Mal3 waarschijnlijk clusters vormen met variabele stoichiometrie.

Voor de langwerpige vorm van de cellen en de receptor op de cel cortex ontwikkelden we twee systemen: één bestaande uit micro-putjes van glas met een statische corticale receptor (hoofdstukken 3-5), en een andere bestaande uit emulsie druppels met een diffunderende receptor (hoofdstuk 6).

In het eerste systeem ontwikkelden we een protocol om gemakkelijk *S. pombe*-achtige glazen micro-putjes te vormen, waarvan het oppervlak van de wanden specifiek gefunctionaliseerd kan worden op een andere manier dan het grondvlak. Dit werd eerder bereikt door verschillende materialen gebruiken [Laan and Dogterom 2010]. Hier konden we alles van hetzelfde materiaal (glas) maken, door 2D micro-patterning technieken aan

te passen voor 3D structuren. Dit verbeterde de oppervlakte specificiteit (grondvlak versus oppervlak van de wanden), verminderde niet-specifieke binding van eiwitten aan de oppervlakken, en verminderde de voorbereidingstijd van de samples. We gebruikten Tris-Ni(II)-NTA fracties gebonden aan de wanden als corticale receptor voor Tip1 gelabeld met een his-tag of andere eiwitten. De bindingsaffiniteit tussen his-tagged Tip1 en Tris-Ni(II)-NTA werd afgesteld door gecontroleerde toevoeging van imidazol aan het systeem. Een goede afstelling leverde samples op waarin microtubule tips die verscheidene his-tagged Tip1 moleculen transporteren gemiddeld 20% van deze moleculen op de wand zou afzetten bij contact. Onze analyse suggereert dat his-tagged Tip1 in aanwezigheid van Tea2 en Mal3 een verbinding kan vormen tussen de microtubule en de receptor op de wand. Dit levert het vasthouden van microtubule tips op plaatsen waar his-tagged Tip1 is afgezet. Overeenkomstige experimenten met enkel his-tagged Mal3, waarvan bekend is dat het geen clusters vormt, leidden niet tot Mal3 afzettingen.

De reden dat his-tagged Tip1 wel zou worden afgezet op de wanden in onze experimenten en his-tagged Mal3 niet blijft onduidelijk. Aangezien his-tagged Mal3 kleiner is dan het his-tagged Tip1-Tea2-Mal3 complex, zou het kunnen dat het niet in staat is om tegelijkertijd te binden aan de microtubule tip en de corticale receptor omwille van sterische redenen. Echter, *in vivo* experimenten in onze groep hebben aangetoond dat een chimera eiwit bestaande uit Mal3 gefuseerd met een membraan-bindend domein, wel zou lokaliseren op *S. pombe* polen op een microtubule-afhankelijke manier, vermoedelijk door directe interactie met de microtubule tip [Recouvreur et al. 2016]. Daarom kan de kleine omvang van his-tagged Mal3 niet de reden zijn dat we geen duidelijke afzettingen observeren. Het lijkt erop dat het vermogen van Tip1 om clusters te vormen doorslaggevend is voor een succesvolle afzetting op de wand. Dit is interessant, omdat polariteits markers van *S. pombe* in clusters in het plasmamembraan bleken te zitten [Dodgson et al. 2013]. Onze resultaten suggereren dat clustering die plaatsvindt op een microtubule tip de afzetting van eiwitten op het plasma membraan vergroot, waarmee een extra functionaliteit wordt toegekend aan de clusters die *in vivo* zijn waargenomen.

In dit proefschrift hebben we verder onderzocht of microtubules die vrij zijn om zichzelf te organiseren in de langgerekte micro-putjes bij voorkeur his-tagged Tip1 naar de polen van de putjes brengen en een gepolariseerd corticaal patroon bewerkstelligen. Hoewel microtubule gericht langs de langste as van micro-putjes overheersten, vertoonden slechts weinig putjes een gepolariseerd patroon. Het ontbreken van positieve feedback in ons systeem kan de reden zijn dat polariteit niet overheerste. Het was verrassend om te zien dat microtubuli met elkaar interfereerden en problemen hadden om de cel-polen te bereiken in de micro-putjes waarin microtubuli zeer dicht op elkaar zaten. Interessant is dat dezelfde Tea2-Tip1 pakketten die de afzetting van his-tagged Tip1 kunnen vergemakkelijken, ook het langs elkaar glijden van microtubuli zou kunnen veroorzaken, wat leidt tot een stabiele configuratie bestaande uit lagen van microtubuli met de plus uiteindes gericht naar het midden van de cel. Deze configuratie is niet wenselijk omdat het eiwit afzettingen op de polen van de cel onbewijsbaar maakt. om dit fenomeen te voorkomen, voegden we het eiwit Ase1 toe dat microtubuli bundelt en de motor dynein die naar het min-uiteinde beweegt. De gecombineerde werking van deze twee eiwitten zou dynamische, anti-parallelle microtubule bundels vormen met de plus eindes aan

het uiteinde van de bundels. Dit resulteerde in gepolariseerde afzetting van his-tagged Tip1 in langwerpige micro-putjes.

Deze methode die is ontwikkeld voor micro-putjes met selectieve functionalisering van oppervlakken kan ook worden toegepast om microtubule-cortex interacties die worden geregeld door corticale eiwitten te bestuderen. Als voorbeeld tonen we verkennende experimenten waarin CLASP2 α gebonden aan de wanden microtubuli leek te stabiliseren als het plus einde contact maakte. De studie die is uitgevoerd is nog niet dooslaggenvend en verdere condities moeten worden uitgetoet.

De andere opstelling gaat twee stappen verder richting de *in vivo* situatie van polariteit. Het voegt beperking van de ruimte toe en staat diffusie van de corticale receptor toe. De methode bestaat uit water-in-olie emulsie druppeltjes waarin microtubuli kunnen groeien en via his-tagged Tip1 een interactie kunnen aangaan met lipiden gefunctionaliseerd met Tris-Ni(II)-NTA op het water-olie oppervlak. Om langwerpige druppels (*S. pombe*-achtige vormen) te verkrijgen, hebben we een microfluidics methode aangepast die bestaat uit microkamers waar druppels in worden gedruwd om ze te vervormen naar de vorm van de kamers [Boukellal et al. 2008] naar kleine *S. pombe* afmetingen. We hopen dat deze methode nuttig zal zijn voor het bestuderen van het ontstaan van polariteit en de organisatie van microtubuli in een niet-sferische omgeving.

—

—

DANKWOORD

I started the Ph. D. thinking it would be a regular job from 9 to 5 and 4 years later you wrap it in a book and they call you a 'doctor'. It was far from that. Not just because it has been 6 years, but definitely because the Ph. D. has become a definition of who I am. I would not have taken 2 extra years if I would have been able to give up on playing on the lab with the developed tools or get a better analysis of the measurements obtained. How things came to this, was definitely because of a crazy project too challenging to let pass on. I would like to thank Marileen for such an exciting project. I think I learned a broader variety of techniques than most Ph. D.s which fulfilled my technological side. Moreover you gave me the freedom to often deviate for months and try new, not always profitable, things. I could often feel like an artist designing my *in vitro* cell were microtubules paint the walls with proteins. Although the paintings never turned exactly how we would have liked them to be.

I could also say that the naïve me of 6 years ago chose AMOLF before choosing the project. That did not deceive. Some former colleagues had mentioned how AMOLF self-organizes. It is true. From cleaning up the cafeteria after a PV event to designing fun activities for the 'open dag' or bringing preparations for thesis sketches out of hands. AMOLF people push things forward with initiative and without obligation. Just because it is cool. And it is awesome.

I would like to thank Roland, Hans, Dimitry and Andries for never saying 'you cannot do that', but rather 'let me think how we can achieve that' or 'that's not what you want, we can do better'.

Thank you Willem for the help after 'ups, I broke a window' came out. Thank you Wouter, Anouk, Tarik, Gijsje and Hans for letting me keep a labcoat in AMOLF after the moving.

Thank you Pieter-Rein, Bela, Gijsje, Sander, Pierre and Olga for mentoring and care. Thank you Pierre, Filipe, Niels, Marion, Wiet, Andrew, Chris, Laurens, Thomak, Marina, Simona, Michel, Björn, Brian, Iza, Milena, Eva, Karin, Mirjam, Jochen, Stephan, Maga, Noreen, Stef, Bob, Florian, Oleg, Joris, Matijn, Agatha, Keita, Simone, Bart, Michele, Adi, Nicola, Jacopo, Georges, Sevastian, Cristina, Benjamin, Marjolein, Fatemeh, Vanda, Andrej, Milan, Hinke, André, Hinko and many others I miss for all the chill-out moments in and out of the lab. Thank you Felipe and Martin for the nice times.

Thank you Pauline, Feng, Ioana, José, Milena, and Jeanette for the relaxing times in trips around the world and for the ones to come. Also thank you for putting up with my endless complains and cheering me tirelessly when life would not 'polymerize'.

Thank you Lutz and Sophie for being my adoptive family in Herschelstraat where Movy was our adoptive cat.

Thank you Jolijn for all the immense care and help since I came to Delft. Also thank you Erwin and Sacha for all the help when moving in.

Moving to Delft was not desired and therefore tough. However, many people cheered me greatly with their kindness over my multiple frustrations. Thank you Marek, Eugene, Víctor, Roland, Dominik, Yera, Jonás, Alicia, Pauline, Huong, Andrew, Fabrizio, Vanesa, Adi, Mahi, Siddharth, Yaron, Richard, Mariana, Maarten, Sumit, Orkide, Pavel, Jacob, Esther, Christophe, Lidewij, Sacha, Maga, Stef, Marian, Gesa, Roland, Maurits and Louis. Also thank you to all the new comers, who made that eventually I felt part of Delft. Thank you Da, Benjamin, Greg, Sergii, Anthony, Fede, Johannes, Anne, Andrea, Vladimir, Kim and many others.

Also, thank you very much Yuka for all the nice brunches, cultural exchange, and friendship.

Gràcies a tots aquells que m'heu visitat durant aquests anys. Sovint he estat molt ocupada, però que una fracció de 'casa' vingúes als Països Baixos ha estat molt important per a mi i m'ha fet tirar endavant amb molta més il·lusió. Mercès Javi, Juanma, Juanmi, Villa, Penya, Helen, Cristina, Gemma, Fede, Emmeric, Paz, Marta, Montse, Maria, Andreu i Monika. Gràcies pel vostre suport, igual que als que des de casa sempre m'heu rebut de nou amb un somriure. Gràcies Albert, Marta, Saray, Joan, Kriz, Toni, *fisiquines* i *calaixeros*.

I per acabar, moltes gràcies pares i germans per tot el suport que sempre m'heu donat. Jo no sóc res sense el vostre suport i amor. Sovint us sentia al meu cap dient '¡vinga Núria!' i m'animava a donar el millor de mi.

CURRICULUM VITÆ

Núria TABERNER CARRETERO

02-04-1985 Born in Mataró, Catalonia.

EDUCATION

1989–2003 Col·legi Salesians Sant Antoni de Padua, Mataró
IES Thos i Codina, Mataró

2003–2009 Undergraduate in Physics
Universitat de Barcelona (Spain)

2007–2008 International Erasmus exchange program, in Engineering Physics
Kungliga Tekniska Högskolan, Stockholm (Sweden)

2009–2010 Master in Biophysics
Universitat de Barcelona (Spain)

2010 Technician
Ipsen Pharma , Sant Feliu de Llobregat (Spain)

2010–2016 Ph.D. Biophysics
TU Delft & FOM institute AMOLF
Thesis: A minimal system to establish microtubule-based
cell polarity in vitro
Promotor: Prof. dr. M. Dogterom

—

—

LIST OF PUBLICATIONS

4. **N. Taberner**, M. Dogterom *Microtubule-based deposition of polarity proteins to bio-mimetic cortices*, [in preparation].
3. **N. Taberner**, A. Lof, S. Roth, D. Lamers, H. Zeijlemaker, M. Dogterom *In vitro system for the study of microtubule-based cell polarity in fission yeast*, *Methods in Cell Biology* **128**, 1-22 (2015).
2. C. Valéry, S. Deville-Foillard, C. Lefebvre, **N. Taberner**, P. Legrand, F. Meneau, C. Meriadec, C. Delvaux, T. Bizien, E. Kasotakis, C. Lopez-Iglesias, A. Gall, S. Bressanelli, M.H. Le Du, M. Paternostre, & F. Artzner *Atomic view of the histidine environment stabilizing higher-pH conformations of pH-dependent proteins*, *Nature Communications* **6**, 7771 (2015).
1. **N. Taberner**, G. Weber, C. You, R. Dries, J. Piehler, M. Dogterom *Reconstituting Functional Microtubule-Barrier Interactions*, *Methods in Cell Biology* **120**, 69-90 (2014).